Rockefeller University
Digital Commons @ RU

Student Theses and Dissertations

2019

In Vitro, In Vivo, and In Silico Studies of Reticulospinal Circuits and Generalized Arousal

Adele Bubnys

Follow this and additional works at: https://digitalcommons.rockefeller.edu/student_theses_and_dissertations

 Part of the Life Sciences Commons

Recommended Citation

Bubnys, Adele, "In Vitro, In Vivo, and In Silico Studies of Reticulospinal Circuits and Generalized Arousal" (2019). *Student Theses and Dissertations*. 500.
https://digitalcommons.rockefeller.edu/student_theses_and_dissertations/500

This Thesis is brought to you for free and open access by Digital Commons @ RU. It has been accepted for inclusion in Student Theses and Dissertations by an authorized administrator of Digital Commons @ RU. For more information, please contact nilovao@rockefeller.edu.

IN VITRO, IN VIVO, AND *IN SILICO* STUDIES OF RETICULOSPINAL CIRCUITS AND GENERALIZED AROUSAL

A Thesis Presented to the Faculty of

The Rockefeller University

in Partial Fulfillment of the Requirements for

the degree of Doctor of Philosophy

by

Adele Bubnys

June 2019

© Copyright by Adele Bubnys 2019

IN VITRO, IN VIVO, AND *IN SILICO* STUDIES OF RETICULOSPINAL CIRCUITS AND GENERALIZED AROUSAL

Adele Bubnys, Ph.D.

The Rockefeller University 2019

Generalized arousal (GA) is a fundamental force in the nervous system that alerts an individual to abrupt changes in its environment. A state of high GA is operationally defined by increases in an animal's a.) locomotor output, b.) responsiveness to sensory stimuli, and c.) emotional reactivity. Previous studies have identified the nucleus gigantocellularis (NGC), a small group of large-bodied neurons in the hindbrain reticular formation, as a potential neuronal substrate for GA. These neurons are responsive to a wide range of sensory modalities and have diverse projections that target both forebrain areas and motor effectors directly within the spinal cord, thereby facilitating rapid responses to sensory stimulation. Here, we used three different approaches to study the role of GA in driving and modulating mammalian motor activity: *in silico* modeling of GA circuits, *in vitro* culture of a reticulospinal circuit, and *in vivo* behavioral assays of circadian transitions in GA.

In our *in silico* study, we constructed a variety of computational models of the generalized arousal circuit and asked how modifying specific aspects of the NGC and its connectivity would influence the responsiveness of motor effectors in the circuit to arousing sensory stimuli. These models reveal that an NGC with a homogeneous microstructure that integrates all inputs equally and bifurcating projections that simultaneously target limbic and spinal areas is most effective at transducing an arousing sensory signal.

We then chose to focus specifically on hindbrain Chx10^{+} neurons, a population of spinally projecting neurons localized to the NGC, and developed an *in vitro* system to culture

these neurons both as an isolated population and together with spinal motor neurons. Under these conditions, $Chx10^{+}$ neurons develop a cell-type specific pattern of robust network bursts that they can impose on otherwise irregularly spiking motor neurons, thereby generating a functional reticulospinal connection. The activity of $Chx10^{+}$ neurons was inhibited $AMPA_R$ blockers, indicating that their bursts are generated by a synaptic mechanism. Furthermore, we identified a subset of $Chx10^{+}$ neurons that respond to the arousal neuromodulators orexin and norepinephrine, highlighting these neurons' role in communicating arousal signals to the spinal cord.

As these two studies have demonstrated the intimate link between GA and motor output, we then used an *in vivo* behavioral assay of voluntary motor activity to study the dynamics of circadian transition in arousal levels in mice. We found that despite the intrinsic noisiness and variability of mouse behavior, these transitions follow a remarkably lawful sigmoidal curve that could be robustly fit to a logistic equation with only three parameters and shows time reversibility between the low-to-high and high-to-low arousal transitions. In addition to demonstrating how complex behavior can be reduced to a relatively simple mathematical form, this new curve fitting paradigm allowed us to quantify how different behavioral conditions affect arousal transitions in greater detail than ever before.

ACKNOWLEDGMENTS

This work would not have been possible without the invaluable support and advice from members of the Pfaff lab and the Rockefeller community at large. I would particularly like to thank my advisor Donald Pfaff for affording me the opportunity to work in his lab and always encouraging me to pursue my interests and intuitions around the data. I would also like to thank Inna Tabansky for providing the initial inspiration and framework for my *in vitro* work and for consistently offering excellent advice and support on all of my projects throughout these past five years. Thanks also to my thesis committee members Bruce McEwen, Mary Beth Hatten and George Reeke for urging me to try out new avenues of enquiry that I otherwise would not have considered, and to my external examiner Hynek Wichterle for taking the time to review my work. Dr Hatten went above and beyond her responsibilities as a member of my FAC committee in offering many resources from her lab in support of my cell culture work. George Reeke also provided excellent support and training in building computational models of arousal systems.

Several current and former members of the Pfaff lab assisted in the collection and interpretation of the data presented in this thesis. Hagar Kandel assisted in a large portion of the cell culture, Nadera Rahman and Olivia Le Moene performed many of the generalized arousal assay experiments, and Lee-Ming Kow provided important training and advice for the patch clamp electrophysiology experiments.

I am also very thankful to Rockefeller's many world class resource centers, especially the flow cytometry resource center and the bio-imaging resource center. Special thanks to the outstanding FCRC technicians Selam Tadesse, Songyan Han, and Stanka Semova for performing the FACS sorts that were essential for my cell culture work. Thanks also to Carlos Rico and Christina Pyrgaki from BIRC for their training and advice in calcium imaging.

Lastly, I am very grateful for the unwavering support of my family and friends throughout these past few years. You encouraged me to pursue my passion for biology from the start and helped me keep everything in perspective through the seemingly endless rounds of troubleshooting and failed experiments. These past few years have been wonderful and I'm very excited to see where this journey will lead me next.

TABLE OF CONTENTS

LIST OF FIGURES

LIST OF TABLES

LIST OF ABBREVIATIONS

12/12: 12-hour light/dark schedule

5/10: Five and dime light/dark schedule

5HT: Serotonin

ACh: Acetylcholine

AIN: "arousal sensory input" region of simulated neurons

ANS: Autonomic nervous system

CCK: Cholecystokinin

CFP: Cyan fluorescent protein

Chx10: Ceh-10 Homeodomain-Containing Homolog

CIN: "output onto spinal central pattern generator" region of simulated neurons

CnF: Cuneiform nucleus

CNS: Cortical network simulator

CPG: central pattern generator

CPv: Caudate putamen

CRH: Corticotrophin releasing hormone

DA: Dopamine

DD: Constant darkness

dIN: Dorsal interneuron

EEG: electroencephalogram

EIN: "extensor inhibitory interneuron" region of simulated neurons

EMG: electromyogram

EPSP: Excitatory postsynaptic potential

EXT: "extensor" region of simulated neurons

FACS: Fluorescence activated cell sorting

FIN: "flexor inhibitory interneuron" region of simulated neurons

FLX: "flexor" region of simulated neurons

GA: Generalized Arousal

GAD: Glutamic acid decarboxylase

GFP: Green fluorescent protein

GNX: Gonadectomized mice

GPCR: G-protein coupled receptor

HACTV: Horizontal distance moved

high/low: High to low arousal transition

k: Transition curve slope

L: Transition curve height

LC: Locus Coeruelus

LCR: "Locus Coeruleus" region of simulated neurons

LD: 12-hour light/dark schedule

LIS: “limbic system” region of simulated neurons

low/high: Low to high arousal transition

LPGi: Lateral paragigantocellular nucleus

M-cell: Mauthner cell

MCH: Melanin concentrating hormone

MCR: “motor circuit” region of stimulated neurons

MEA: Multi-electrode array

MLR: Mesencephalic locomotor region

MRRN: Medial rhombencephalic reticular nucleus

MTR: “motor input” region of simulated neurons

NAc: Nucleus accumbens

NGC: Nucleus Gigantocellularis

NREM: Non-rapid eye movement sleep

nt: inhibitory signal transduction threshold

OxA: Orexin A

OxB: Orexin B

POA: Preoptic nucleus

PPN: Pedunculopontine nucleus

pt: excitatory signal transduction threshold

REM: Rapid eye movement sleep

rmse: root mean squared error

SCN: Suprachiasmatic nucleus

SNc: Substantia nigra pars compacta

SPZ: Subparventricular zone

st: spike threshold

t: Transition curve onset

TMN: Tuberomammillary nucleus

TOTDIST: total distance moved

VACTV: Vertical distance moved

VGAT: Vesicular GABA transporter

VMH: Ventro-medial hypothalamus

VTA: Ventral tegmental area

Chapter 1. Introduction to Generalized Arousal

1.1 Generalized arousal

The circuits associated with fundamental behaviors like feeding, aggression, and sexual behavior are typically studied in isolation from one another. However, up to a third of the variation in the arousal component of these behaviors can be attributed to a generalized element (Garey 2003). This component is colloquially referred to as "generalized arousal", a concept first suggested by the data of Moruzzi in 1949. Generalized arousal functions as a set of signals that (i.) alert cortical areas to sudden changes in the outside world and (ii.) facilitate rapid and adaptive behavioral responses (Moruzzi 1949).

A constant, low level of generalized arousal is necessary to maintain a conscious state, but spikes in this arousal signal provide a means to alert an animal to danger in its environment. High generalized arousal is characterized by increases in motor activity, heightened sensitivity to sensory stimuli across modalities, and emotional reactivity (Calderon 2016). Generalized arousal systems are thought to operate near a phase transition such that any kind of sensory input can trigger a rapid, nonlinear amplification of activity in the neuronal substrate to drive the animal into a high arousal state (Pfaff 2007, Proekt 2012).

Since danger in the world can present itself in the form of any number of stimuli, the theoretical neuronal substrate that mediates generalized arousal should be responsive to many categories of sensory stimuli and rapidly convey this signal throughout the brain and spinal cord to prime the animal for behavioral response. The hindbrain reticular formation has long been associated with behavioral arousal, going back to Bremer's pioneering studies that showed that severing the connection between the reticular formation and cortex in cats caused their cortical EEG to switch from a waking state to a sleep-like pattern (Bremer 1937).

Within the medullary reticular formation, a localized group of very large neurons known as the nucleus gigantocellularis (NGC) is ideally positioned to act as the primary substrate for integrating sensory stimuli and transforming them into generalized arousal signals to be rapidly broadcast throughout the rest of the nervous system (Pfaff 2012) (figure 1). During chronic recordings in awake, freely moving animals, neurons in NGC showed excitatory responses to all sensory modalities tested: tactile, visual, auditory, vestibular, and olfactory stimuli and most individual NGC neurons responded to more than one of these sensory modalities (Martin 2010). Activation of the NGC precedes changes in the power of both the peripheral EMG and cortical EEG associated with increases in arousal (Martin 2010). This area is also known to stimulate the acoustic startle response, a fast muscle twitch reflex that protects an individual from sudden bodily attack and helps prime it for a fight or flight response (Koch 1999).

Despite the restricted location of NGC cell bodies, this reticular formation cell group has diverse and far-ranging ascending projections to midbrain and forebrain areas associated with arousal (Jones 1985), and descending reticulospinal projections that support rapid transmission of generalized arousal signals. NGC neurons tend to form clusters that are organized on the basis of their projection targets. Neurons with ascending projections reside primarily in the caudal half of the NGC and descending neurons reside in the rostral half, although neurons with both projection types were identified throughout the NGC (Martin 2011). Despite evidence of some sort of topographic organization, a small yet significant subpopulation of NGC neurons have bifurcating projections that simultaneously target the midbrain and spinal cord (Martin 2010, Kandel, Chen, and Pfaff, unpublished data).

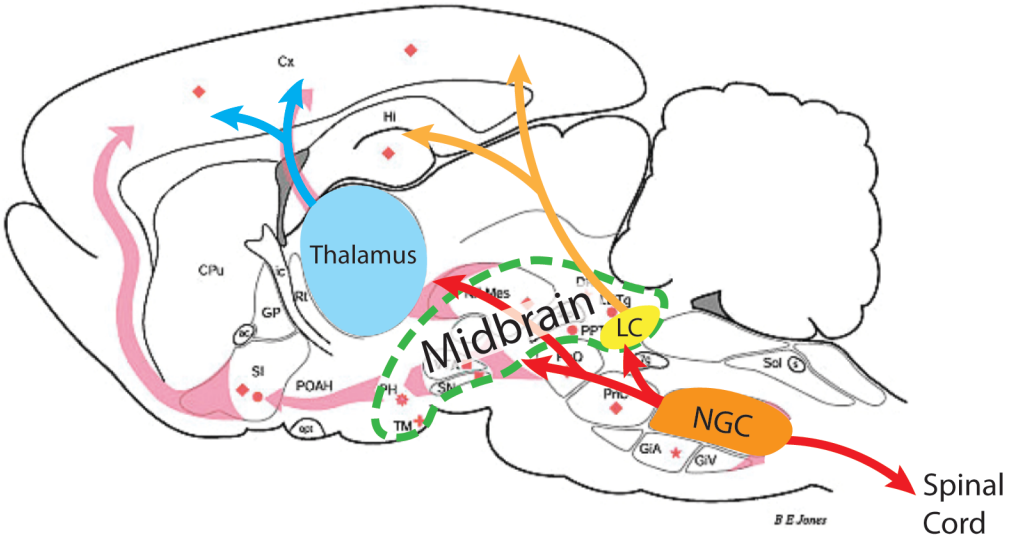

Figure 1. Neuroanatomy of the Nucleus Gigantocellularis

Innervation pattern of the Nucleus Gigantocellularis (NGC). Prominent ascending projections from the NGC target the midbrain (outlined in green), Locus Coeruleus (LC), and thalamus (light blue), descending NGC projections target the spinal cord. Figure adapted from Jones (2003).

Among the ascending targets of the NGC are the midbrain reticular formation, zona incerta, locus coerleus, and central thalamus. The majority of these neurons express mRNA associated with a GABAergic identity, including GAD65 and GAD67 (Martin 2011). The NGC neurons that project to the thalamus are highly integrated with neighboring vasculature and could convey environmental signals to the thalamus via this neurovascular coupling (Tabansky 2018). Thalamic activation is in turn associated with arousal (Schiff 2007, Keenan 2015). Deep brain stimulation of this area is sufficient to restore a comatose patient to consciousness (Schiff 2007) and stimulation of the ventrolateral nucleus of the thalamus induces short-term plasticity in the thalamocortical pathway, thereby providing a mechanism for behavioral state-dependent modulation of ascending information flow via this pathway (Castro-Alamancos 1996).

Notably, the NGC is a major source of excitatory afferents to the locus coeruleus (LC), the primary source of noradrenergic innervation in the cortex. Stimulation of this NGC to LC pathway induces reorientation towards a stimulus (Sara 2012). Activation of these basal pathways originating in the thalamus and LC is generally associated with automatic responses to immediate stimuli, while cortical circuits mediate voluntary behaviors. However, in some situations basal circuits can inhibit cortical circuits to effectively override voluntary motor control and thereby speed up reflexive behavioral responses to salient stimuli (Trofimova 2016).

A sizable fraction of reticulospinal projections originate in the NGC (Peterson 1979, Martin 2010, Oueghlani 2018). These descending NGC neurons are primarily glutamatergic and express the vesicular glutamate transporter VGluT2 (Martin 2011). Selective activation of these $VGluT2^{+}$ neurons elicits muscle contractions and modulates locomotor rhythm (Lemieux 2019).

Some parallels have been drawn between the reticulospinal function of the NGC and large-bodied Mauthner cells (M-cells) in fish and amphibians (Pfaff 2012). These cells have sensory integrative capacity and, as first responders for initiating behavior, firing of M-cells is

necessary and sufficient to drive the C-start escape response in fish (Korn 2005). Much like M-cells, NGC neurons provide direct glutamatergic innervation to spinal locomotor networks in mammals (Hagglund 2010). Stimulation of these reticulospinal projections is sufficient to induce locomotion (Oueghlani 2018) and there is evidence that NGC reticulospinal neurons mediate and modulate mesencephalic locomotor region (MLR) inputs to motor pools (Gatto 2018).

1.2 Our approach to the study of generalized arousal

Generalized arousal systems derive their importance from the near-universality by which they influence the activation of a wide range of behaviors across vertebrate species. The most celebrated aspects of neuroscience during the past decades, on the other hand, have focused on specific neurobiological systems. For instance, much progress has been made on the sensory side in understanding the specificity of coding in the visual cortex, and on the motor side in studying specific signaling from the vestibular nuclei and vestibulospinal projections to motoneurons. Thus, "non-specific" phenomena like generalized arousal have received comparatively little attention.

In this work, we have used three different approaches to study generalized arousal and its relationship to motor output: neuronal modeling, molecular developmental neuroscience, and quantitative work with mouse behavior. These studies are thematically linked, but we have tried to avoid drawing simplistic connections between them. That said, reticulospinal connections analogous to those we have created *in vitro*, are referred to explicitly in our neuronal modeling *in silico*, and they are surely involved in the mouse behavioral activation *in vivo,* which we have quantified in the form of a simple equation. But regardless of the implicit connections between the three major components of this thesis, each stands on its own.

Chapter 2. Computational Modeling of Generalized Arousal

2.1 Computational Modeling

We hypothesize that the dynamics of generalized arousal circuitry centered on the NGC are optimized to maximize rapid and efficient behavioral response to sensory stimulation. We chose to use computational modeling to study these dynamical mechanisms in a novel way by constructing a prototypical NGC arousal circuit and then systematically modifying five different features of the circuitry to determine the manner in which these features might drive significant changes in model output, thought of as behavioral responsiveness to arousing stimuli.

Computational models have been used to test hypotheses about how information processing occurs in the nervous system, how topology affects nervous system function, and to integrate experimental findings within a larger conceptual framework of nervous system function. There is a significant body of work describing how even randomly interconnected neuronal networks can process complex stimuli with proper tuning. Rosenblatt's seminal work on the perceptron was the first example of such a nervous system simulation (Rosenblatt 1958). He showed that a randomly connected network of simple simulated neurons could learn to discriminate between complex visual stimuli and suggested that the memory of the resulting perception is distributed throughout the network. Later work by Edelman and colleagues paired a simulated multilayered network of randomly interconnected neurons with a robot and showed that a network of this sort could be trained to track an object in visual space and perform other tasks in a world of complex stimuli by applying principles of re-entrant signaling to impose value functions on patterns of activity that yield adaptive behavioral output (Edelman 1993; Krichmar & Reeke 2006). This same principle of re-entrant signaling has been used in models of visual cortical areas to show how an object's disparate features may be bound together into a single cohesive perception (Tononi 1992), and to show how distant cortical regions may generate coherent oscillations (Sporns 1989).

Other computational modeling studies have instead focused on how the topology of neuronal networks affects their processing capacity. Strogatz's modeling of "small world" networks showed that having a combination of regularly organized connections between neighboring neurons and more randomly assigned connections between distant neurons yielded improved signal propagation speed, computational power, and synchronizability than having exclusively short range or long-range connectivity schemes (Watts 1998). This principle may be particularly relevant in structures like the reticular formation that combine long axon tracts that project to distant brain regions with much smaller and denser dendritic arbors that only innervate their immediate vicinity (Scheibel and Sheibel 1967). Indeed, modeling the specific interconnectivity of the reticular formation shows that its structure obeys the principles of a small-world network (Humphries 2006). Modeling of interaction networks in biology is not limited to the nervous system. Similar concepts of topology and network complexity have been tested in models of gene interaction networks and demonstrate that optimizing connection strengths between network nodes can yield greater information processing capacity than merely increasing the gross number of nodes (Tikhonov 2016).

Ultimately the goal of many of these simulations is to move towards increasingly realistic models of the intact nervous system with respect to the latest experimental findings. The spinal cord is a particularly amenable system for this sort of approach because patterns of neuronal activity can be most readily associated with specific behavioral outputs. Beginning with Graham and Brown's model of a hemicenter central pattern generator that showed how two reciprocally connected "flexor" and "extensor" areas could generate alternating bursts of activity that underlie limb movement (Graham 1913), models of spinal microcircuits have become increasingly complex to incorporate the expanding diversity of interneuron subtypes identified in the spinal cord (Rybak 2015). These models try to account for the specific behavioral deficits observed

when certain interneuron subtypes are ablated and for the wide variety of locomotor gaits that are observed *in vivo* (Ausborn 2019).

2.2 Modeling generalized arousal

Compared to the cortex and spinal cord, the reticular core of the brainstem has received relatively little attention in the field of computational modeling. To our knowledge there have been no studies applying such modeling approaches to generalized arousal circuits. In preliminary work we showed that, in principle, there is no obstacle to modeling generalized arousal circuity and that model outputs can reflect circuitry in an orderly way.

In the present study, we use *in silico* modeling of generalized arousal circuitry to test the hypothesis that the structure of the arousal circuit associated with the medullary reticular nucleus gigantocellularis (NGC) can be optimized to generate rapid responses to arousing stimuli. We focused on five features of the NGC and associated areas in particular and asked whether altering or removing any of these features has significant consequences on how quickly the arousal circuit generates a behavioral response to sensory input. These features include (1) reciprocal connectivity between the NGC and Locus Coeruleus, (2) the presence of bifurcating axons in the NGC with simultaneously ascending and descending projections throughout the nervous system, (3) the presence of excitatory and inhibitory interneurons within the NGC that have local connectivity, (4) the dedicated input-output architecture of the LC and how it affects its reciprocal connections to the NGC, and (5) the presence of multiple corticospinal tracts that send motor command signals to the spinal cord in parallel with reticulospinal projections from the NGC.

2.3 Overview of modeling methods

For the following simulations, we used the program “CNS” (Cortical Network Simulator) provided by G. Reeke (Reeke & Edelman 1987; Reeke 2016). Nervous system simulations are

constructed in CNS in a hierarchical fashion to emulate the organization of the cortex. Individual cells are organized into rectangular arrays called groups, analogous to cortical columns. These are further arranged into larger arrays called regions. Groups and regions may contain multiple cell types; control over cell outputs and statistical options is consolidated over the entire cell type.

Individual cells may be modeled as rate-coded or spiking neurons. The scalar state of a rate-coded neuron represents its spike rate, while a spiking neuron's state represents its membrane potential. We chose to model our neurons as simple spiking ("Integrate and Fire") cells to capture more of the dynamics of the neural network in a computationally efficient manner. Simple spiking cells integrate all specified excitatory and inhibitory inputs and spike if this value exceeds a predetermined threshold, immediately going into a refractory period of predetermined length during which the cell does not accept any inputs. Subthreshold inputs do not contribute to the cell's internal state. Membrane potential decay is modeled by a simple exponential function. The basic equation for a simple spiking neuron is as follows:

Equation 1. $V_m(i,t) = \{[(A + M)\Phi(Is) + P] + N + W\}\Phi(D)$

Equation 2. $\Phi(x) = 1-2*(x^2)+(x^4)$

$V_m(i,t)$ is the membrane potential of cell i at time t. The variables A and M represent total input from specific and modulatory connections (see below), respectively. Is is shunting inhibition applied as a sigmoidal function $\Phi(x)$ described in equation 2. P is stimulation applied using an external probe, N is Gaussian noise, W is the information passed on from the previous time point after decay has been applied ($W = \omega Vm(i,t-1)$ where ω is a constant decay factor corresponding to $e^{-\Delta t/\tau}$ for some decay time τ), and D is synaptic depression. The signals in square brackets in equation 1 must either exceed a positive threshold, 'pt' for excitatory inputs or be lower than a negative threshold, 'nt' for inhibitory inputs in order for signal transduction to

occur. Once the signal has crossed one such threshold, a scalar multiplier is applied for further modification. V_m must exceed a threshold, 'st', for the cell to emit a spike. All activity values are on an arbitrary mV scale with 0 as equilibrium rest potential.

CNS is capable of modeling several types of connections between individual neurons and groups or regions of cells. We primarily used modulatory and specific connections for the following simulations. Modulatory connections modulate the responses of all cells in the specified target region according to the mean of the activity of a source region, multiplied by a modifier.

Specific connections can be assigned between individual neurons according to a variety of organizational schemes. For the following simulations, we generated these connections using a “crow’s foot” model to represent a given neuron’s dendritic arbor. For computational reasons, connections are generated as a list of sources for each target cell rather than as a list of targets for each source cell. For each target neuron, a dendritic arbor is generated by first selecting a neuron randomly from within the specified source region to serve as an input source. Other source neurons are then selected randomly from a rectangular area of user specified dimensions surrounding the first source neuron. The percentage of these connections that is excitatory or inhibitory is specified, and then the subsequent sum of the inputs is passed on to the target cell according to the thresholds for simple spiking cell activation.

In CNS, time steps for a simulation are divided into two categories, cycles and trials. Trials correspond to the interval during an experiment when a stimulus is applied and remains unchanged. Each trial can consist of multiple cycles, evaluations of network responses needed to equilibrate with the current stimulus. The primary way in which the computations happening within trials and cycles differs in our simulations is by which value of the ω decay parameter is applied. The variable ω_2 is applied when calculating the activity from cycle to cycle within a

trial, while the variable ω_1 is only applied when calculating activity from trial to trial, generally corresponding to a longer time between trials than the time for a cycle.

All of the following simulations study the relationship between stimulatory input and model output depending on circuit configuration. CNS includes several mechanisms for the application of external stimulation during a simulation run. We chose to use the CNS noise function as a relatively simple and straightforward way to stimulate entire groups and regions of neurons with a constant amount of input. Noise input is applied to a percentage of neurons within a region according to the parameter "frac", and its strength is determined from a normal distribution with a user-provided mean and sigma. We generally applied the noise stimulation uniformly across all neurons in a given group by setting frac to 1 and sigma to 0, while varying the mean.

2.4 Generating a model of a hemicenter central pattern generator

The goal of this simulation was to construct a central pattern generator circuit that would, with increasing locomotor drive, generate left-right alternating bursts of activity in flexor and extensor regions. These bursts represent the coordinated activation of networks of spinal motor neurons and inhibitory interneurons required to generate basic limb movements. The overall architecture and connectivity scheme of this model was based on the classical hemicenter CPG (Brown 1914, Lundberg 1981, McCrea 2007).

We built the model with five regions: "motor input" (MTR), "flexor" (FLX), "extensor" (EXT), "flexor inhibitory interneurons" (FIN), and "extensor inhibitory interneurons" (EIN). Each of these regions contains 100 neurons arranged in a 10 by 10 lattice. We used simple spiking cells and adjusted their positive signal transduction threshold (pt), spike threshold (st), ω_1 and ω_2 decay parameters within each region to yield the desired circuit behavior. The circuit configuration is diagrammed in figure 2a. We went through several iterations in order to generate

a set of parameters to yield the desired hemicenter behavior. The parameters used in each iteration are listed in table 1.

To start, we sought to optimize the behavior of each side of the hemicenter in isolation to generate bursts of activity interspersed with periods of quiescence. To do this, we turned off all excitatory inputs from MTR to the EXT half of the oscillator, gave the MTR region a constant excitatory noise input, and tuned the subsequent parameters encoding the strength of the connections between FLX and FIN and the excitability of the neurons within these regions. The parameters that gave optimal behavior for the circuit are shown in table 1: trial 1 and the raster plot showing the activity of each region during a simulation with these parameters is shown in figure 2b.

Then, we introduced excitation of the extensor half of the circuit containing the EXT and EIN regions and adjusted this same set of parameters to yield alternating bursts between the flexor and extensor (figure 2c). Although the specific combination of simulation parameters outlined in table 1: trial 2 yielded alternating bursts of flexor and extensor activity, this behavior fell apart when the excitatory noise inputs to the MTR region were altered. In order to improve the robustness of flexor/extensor alternation and allow for changes in burst frequency with increasing motor drive, we varied a number of parameters more systematically to explore their effect on circuit behavior.

Figure 2. The hemi-center CPG model.

a, setup of the hemi-center central pattern generator. The five regions "motor input" (MTR), "flexor" (FLX), "extensor" (EXT), "flexor inhibitory interneurons" (FIN), and "extensor inhibitory interneurons" (EIN), containing 100 neurons each are connected by excitatory (→) and inhibitory (⊣) modulatory connections. Tonic noise input is provided to all cells of MTR, EXT, and FLX, indicated with (↯). **b-h**, spiking activity of all five regions of the hemi-center CPG for different combinations of parameters for inter-region connectivity and cell properties, modified with the goal of generating bursts of activity alternating between the FLX and EXT sides of the CPG. ***b***, Trial 1: optimized parameters for inputs to just the FLX/FIN half of the circuit to yield bursts of activity in FLX. ***c***, Trial 2: the result of incorporating the EXT/EIN half of the circuit and adjusting the parameters to yield bursts that alternate between the FLX/FIN and EXT/EIN halves of the circuit. ***d***, Trial 3: improving the robustness of CPG alternating activity by applying direct noise stimulation to FIN and EIN. ***e***, Trial 4: further improving the robustness of CPG activity by adjusting the EIN-to-FLX and FIN-to-EXT inhibitory connection strengths. ***f***, Trial 5: adding direct noise stimulation to FLX and EXT yields poorer outcomes than in the previous trials. ***g***, Trial 6: adjusting the positive signal transduction threshold of FIN and EIN to 120 yielded a poor outcome. ***h***, Adjusting the positive threshold for FIN and EIN to 30 yielded better alternating burst activity.

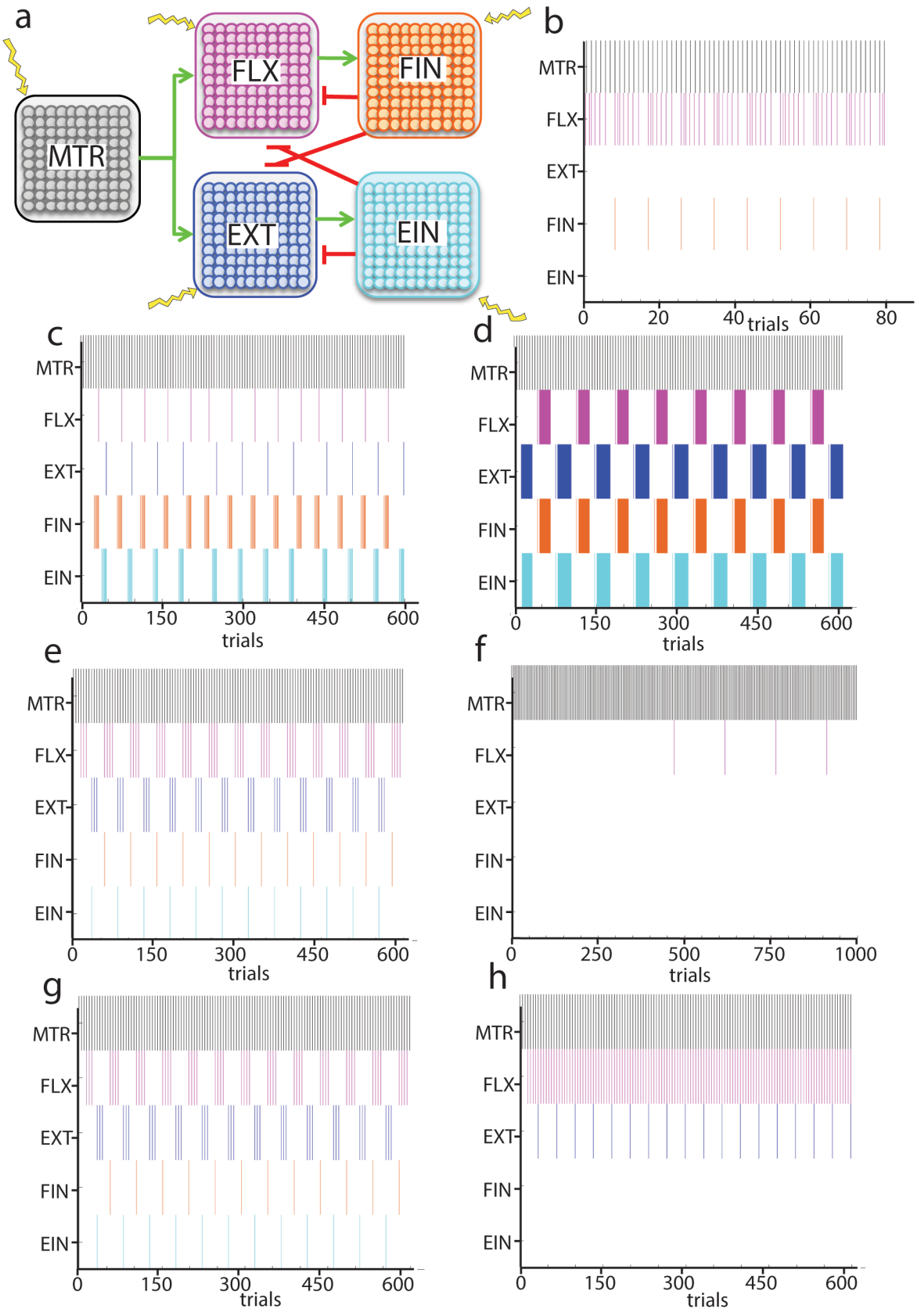
a
MTR
FLX
FIN
EXT
EIN
b
MTR
FLX
EXT
FIN
EIN
0
20
40
trials
60
80
c
MTR
FLX
EXT
FIN
EIN
0
150
300
450
600
trials
d
MTR
FLX
EXT
FIN
EIN
0
150
300
450
600
trials
e
MTR
FLX
EXT
FIN
EIN
0
150
300
450
600
trials
f
MTR
FLX
EXT
FIN
EIN
0
250
500
750
1000
trials
g
MTR
FLX
EXT
FIN
EIN
0
150
300
450
600
trials
h
MTR
FLX
EXT
FIN
EIN
0
150
300
450
600
trials

Table 1. Parameters for modeling the hemicenter central pattern generator

region	parameter	Trial 1	Trial 2	Trial 3	Trial 4	Trial 5	Trial 6a	Trial 6b	Trial 7
MTR	noise input	20	10	10	10	10	10	10	0-50
	MTR to EXT	0	1	1	1	1	1	1	1
	MTR to FIN	1	1	1	1	1	1	1	1
	ω1	1	1	1	1	1	1	1	1
	ω2	0.8	0.8	0.8	0.8	0.8	0.8	0.8	0.8
	pt	0	120	120	120	120	120	120	120
	st	49	49	49	49	49	49	49	49
FLX	noise input	0	0	0	0	-3	0	0	0
	FLX to FIN	1	1	1	1	1	1	1	1
	ω1	1	1	1	1	1	1	1	1
	ω2	0.8	1	1	1	1	1	1	1
	pt	0	120	120	120	120	120	120	120
	st	49	49	49	49	49	49	49	49
EXT	noise input	0	0	0	0	-3	0	0	0
	EXT to EIN	1	1	1	1	1	1	1	1
	ω1	1	1	1	1	1	1	1	1
	ω2	0.8	1	1	1	1	1	1	1
	pt	0	120	120	120	120	120	120	120
	st	49	49	49	49	49	49	49	49
FIN	noise input	0	0	-5	-5	-5	-5	-5	0
	FIN to FLX	-2	0	0	0	0	0	0	0
	FIN to EXT	0	-4	-4	-0.2	-0.2	-0.2	-0.2	-1
	ω1	1	1	1	1	1	1	1	1
	ω2	1	1	1	1	1	1	1	1
	pt	120	30	30	30	30	30	120	30
	st	49	49	49	49	49	49	49	49
EIN	noise input	0	0	-5	-5	-5	-5	-5	0
	EIN to EXT	-2	0	0	0	0	0	0	0
	EIN to FLX	0	-4	-4	-0.2	-0.2	-0.2	-0.2	-1
	ω1	1	1	1	1	1	1	1	1
	ω2	1	1	1	1	1	1	1	1
	pt	120	30	30	30	30	30	120	30
	st	49	49	49	49	49	49	49	49
trials		80	600	600	600	1000	600	600	100
cycles per trial		4	4	4	4	4	4	4	4

First, in addition to the noise stimulation applied to MTR, we tried applying direct noise stimulation to FIN and EIN at different values varying from -15 to 10. A noise input value of -5 to these regions yielded the greatest improvement to the flexor/extensor alternation behavior (figure 2d, table 1: trial 3).

Then, we adjusted the connection strengths for the EIN-to-FLX and FIN-to-EXT inhibitory connections, varying the values of these parameters from -3 to -0.1. A connection strength of -0.2 yielded the result closest to flexor/extensor alternation (figure 2e, table 1: trial 4).

After that, we tried applying noise inputs to FLX and EXT from -10 to 10 with the expectation that this might change burst frequency but found that any direct noise inputs to these regions completely broke the flexor/extensor alternation of the circuit (figure 2f, table 1: trial 5). So, this input was removed in subsequent simulations.

For the next trial, we adjusted the positive signal transduction threshold of FIN and EIN from 30 to 120 and found that a value of 30 yielded better flexor/extensor alternation (figure 2g, table 1: trial 6a) than a positive threshold of 120 (figure 2h, table 1: trial 6b).

Having established some preliminary values for the inter-region connection strengths and spike thresholds, we again iterated through different combinations of noise inputs to FLX and EXT, and inhibitory FIN-to-EXT and EIN-to-FLX connection strengths and found a combination of parameters that generated faster “steps” as motor drive was increased (figure 3, table 1: trial 7).

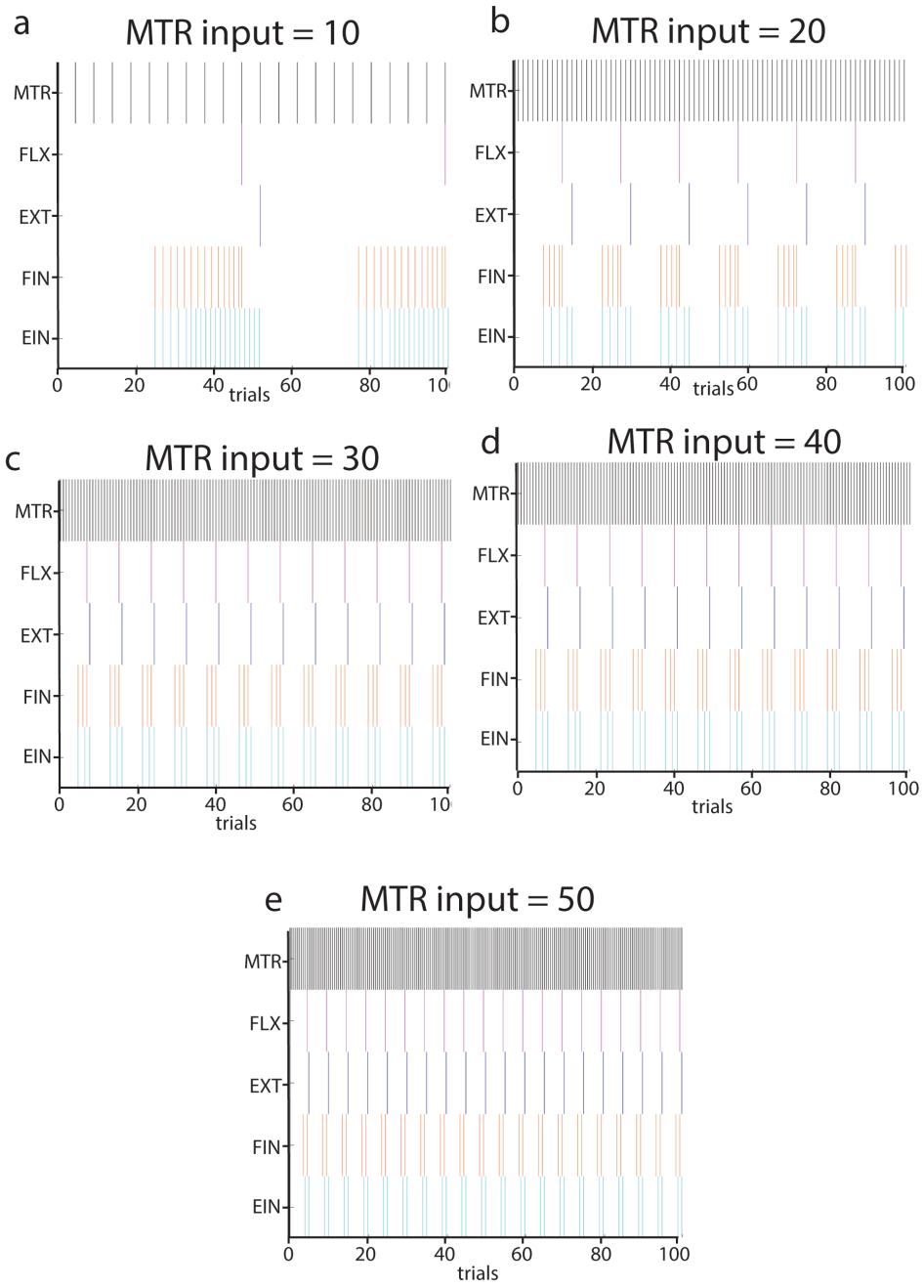

Figure 3. Frequency of flexor/extensor bursts increases with progressively higher inputs to motor control region.

a-e, Raster plots of the activity of each region in the hemi-center CPG (diagrammed in figure 2a) with different noise inputs to the MTR region uniformly applied throughout each simulation. Noise input to MTR is set to ***a***, 10, ***b***, 20, ***c***, 30, ***d***, 40, and ***e***, 50. The other parameters used in this series of simulations are listed in table 1: trial 7.

2.5 Model 1: How does the connectivity between the NGC and Locus Coeruleus affect responses to arousal?

The Locus Coeruleus (LC) is the primary source of noradrenaline in the frontal cortex, and thus an important driver of cortical arousal (Berridge 2003). There is significant neuroanatomical evidence that it is a major innervation target of the nucleus gigantocellularis (NGC) (Sara 2012, Ennis 1988). The NGC in turn is also the target of noradrenergic innervation from the LC (Jones 1985, McBride 1976). We used computational modeling to explore the ramifications of having recurrent connectivity between these two important arousal centers and whether this would improve the responsiveness of the circuit to arousing external stimuli.

2.5.1 Methods

This model was constructed with three regions, “arousal sensory input” (AIN), “nucleus gigantocellularis” (NGC), and “Locus Coeruleus” (LCR) providing input to the hemicenter central pattern generator consisting of the five regions MTR, FLX, EXT, FIN, EIN already described. The regions AIN, NGC, and LCR consist of 100 simple spiking neurons arranged in a 10 by 10 lattice. The parameters used for each region in this model are listed in table 2. The connectivity of this circuit is shown in figure 4a. The NGC and LCR both send modulatory inputs to the hemicenter CPG via the region MTR, while NGC in turn receives modulatory input from AIN.

Table 2. Parameters for model 1

Region	Parameter	Model 1.1	Model 1.2	Model 1.3	Model 1.4
AIN	noise input	0-25	0-25	0-25	0-25
	AIN to NGC	1	1	1	1
	ω1	1	1	1	1
	ω2	0.8	0.8	0.8	0.8
	pt	0	0	0	0
	nt	0	0	0	0
	st	49	49	49	49
LCR	noise input	0-50	0-50	0-50	0-50
	LCR to NGC	0	1	0	1
	LCR to MTR	1	1	1	1
	ω1	1	1	1	1
	ω2	1	1	1	1
	pt	30	30	30	30
	nt	0	0	0	0
	st	49	49	49	49
NGC	NGC to LCR	0	0	1	1
	ω1	1	1	1	1
	ω2	1	1	1	1
	pt	30	30	30	30
	nt	0	0	0	0
	st	49	49	49	49
MTR	MTR to EXT	1	1	1	1
	MTR to FIN	1	1	1	1
	ω1	1	1	1	1
	ω2	0.8	0.8	0.8	0.8
	pt	120	120	120	120
	st	49	49	49	49
	noise input	0	0	0	0
FLX	FLX to FIN	1	1	1	1
	ω1	1	1	1	1
	ω2	1	1	1	1
	pt	120	120	120	120
	st	49	49	49	49
	noise input	0	0	0	0
EXT	EXT to EIN	1	1	1	1
	ω1	1	1	1	1
	ω2	1	1	1	1
	pt	120	120	120	120
	st	49	49	49	49
	noise input	0	0	0	0
FIN	FIN to FLX	0	0	0	0
	FIN to EXT	-1	-1	-1	-1
	ω1	1	1	1	1
	ω2	1	1	1	1
	pt	30	30	30	30
	st	49	49	49	49
	noise input	0	0	0	0
EIN	EIN to EXT	0	0	0	0
	EIN to FLX	-1	-1	-1	-1
	ω1	1	1	1	1
	ω2	1	1	1	1
	pt	30	30	30	30
	st	49	49	49	49
trials		100	100	100	100
cycles per trial		4	4	4	4

Figure 4. Circuit arrangement for model 1.

a, Model 1.4: the circuit contains eight regions, "arousal sensory input" (AIN), "nucleus gigantocellularis" (NGC), and "Locus Coeruleus" (LCR), "motor input" (MTR), "flexor" (FLX), "extensor" (EXT), "flexor inhibitory interneurons" (FIN), and "extensor inhibitory interneurons" (EIN) of 100 neurons each, connected by excitatory (→) or inhibitory (⊣) modulatory connections. Different amounts of external stimulation are applied to AIN and LCR in each simulation run (↯).

b-d, Different modifications on the connection strengths between regions of the circuit used in subsequent iterations of the model. ***b***, model 1.1: all recurrent connections between the LCR and NGC regions are set to 0, the remaining excitatory connections are all set to 1. ***c***, model 1.2: the connection from the NGC to LCR is set to 0. ***d***, model 1.3: the connection from the LCR to NGC is set to 0.

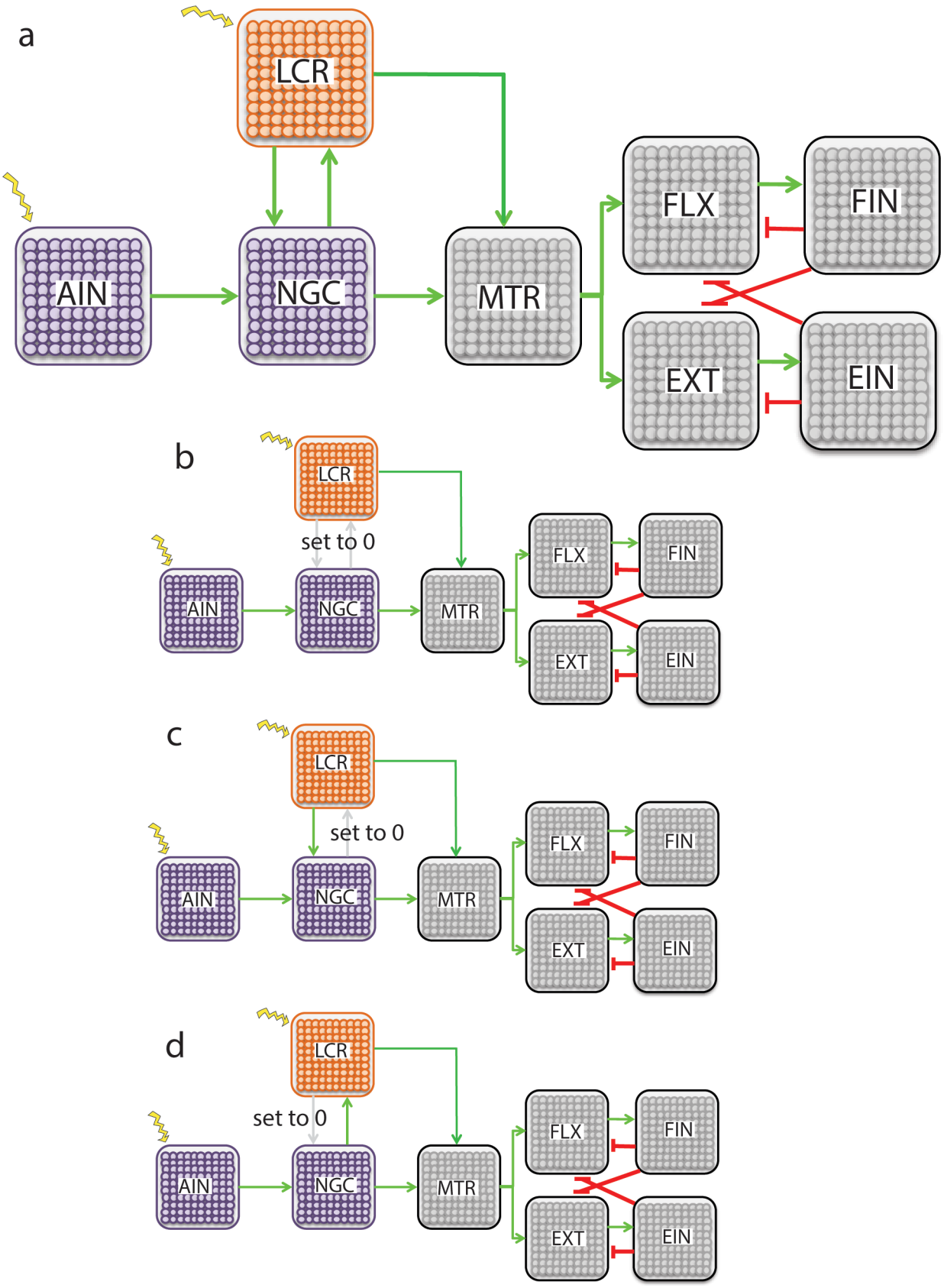
a
LCR
AIN
NGC
MTR
FLX
FIN
EXT
EIN
b
LCR
set to 0
AIN
NGC
MTR
FLX
FIN
EXT
EIN
c
LCR
set to 0
AIN
NGC
MTR
FLX
FIN
EXT
EIN
d
LCR
set to 0
AIN
NGC
MTR
FLX
FIN
EXT
EIN

Each set of simulations was run for 100 trials, with 4 cycles per trial. During each set of trials noise stimulation was applied to AIN and LCR. This stimulation strength was independently varied from 0 to 25 in AIN and 0 to 50 in LCR, so that all combinations of AIN and LCR activity were covered. The output of the circuit was measured as the number of spikes generated by EXT, representing CPG activity.

Four different connectivity patterns were tested within this model framework. In the first (model 1.1), the recurrent connection strengths from NGC to LCR were set to 0 to model an arousal circuit in the absence of any communication between the hindbrain and midbrain (figure 4b). In the second set of simulations (model 1.2), we set the LCR to NGC modulatory connection strength to 1, while keeping the NGC to LCR connection at 0 to model an arousal system containing only ascending hindbrain inputs to the midbrain (figure 4c). Then, in model 1.3 we switched the connection strengths such that the NGC to LCR connection had strength of 1 and the LCR to NGC connection was at 0 (figure 4d). Finally, in model 1.4 we tested the effects of including recurrent connections between the hindbrain and midbrain arousal systems by setting the NGC to LCR and LCR to NGC connection strengths to 1 (figure 4a).

Data for this model (in the appendix)

Appendix 1: CNS control file for model 1

Appendix 2: Results for model 1.1

Appendix 3: Results for model 1.2

Appendix 4: Results for model 1.3

Appendix 5: Results for model 1.4

Figure 5. Results of simulations of model 1.

a-d overall landscape of CPG responses to different combinations of tonic stimulation of LCR and AIN regions for the four variations on model 1. ***a***, An arousal circuit with no connections between the LCR and NGC regions (model 1.1, figure 4b). ***b***, an arousal circuit with a connection from the LCR to NGC (model 1.2, figure 4c). ***c***, an arousal circuit with a connection from the NGC to LCR (model 1.3, figure 4d). ***d***, an arousal circuit with bidirectional connections between the NGC and LCR (model 1.4, figure 4a).

e-f responses of each model to different amounts of LCR stimulation when AIN stimulus is kept constant. ***e***, responses at low arousal (AIN input = 0), ***f***, responses at intermediate arousal (AIN input = 10mV), ***g***, responses at high arousal (AIN input = 20mV).

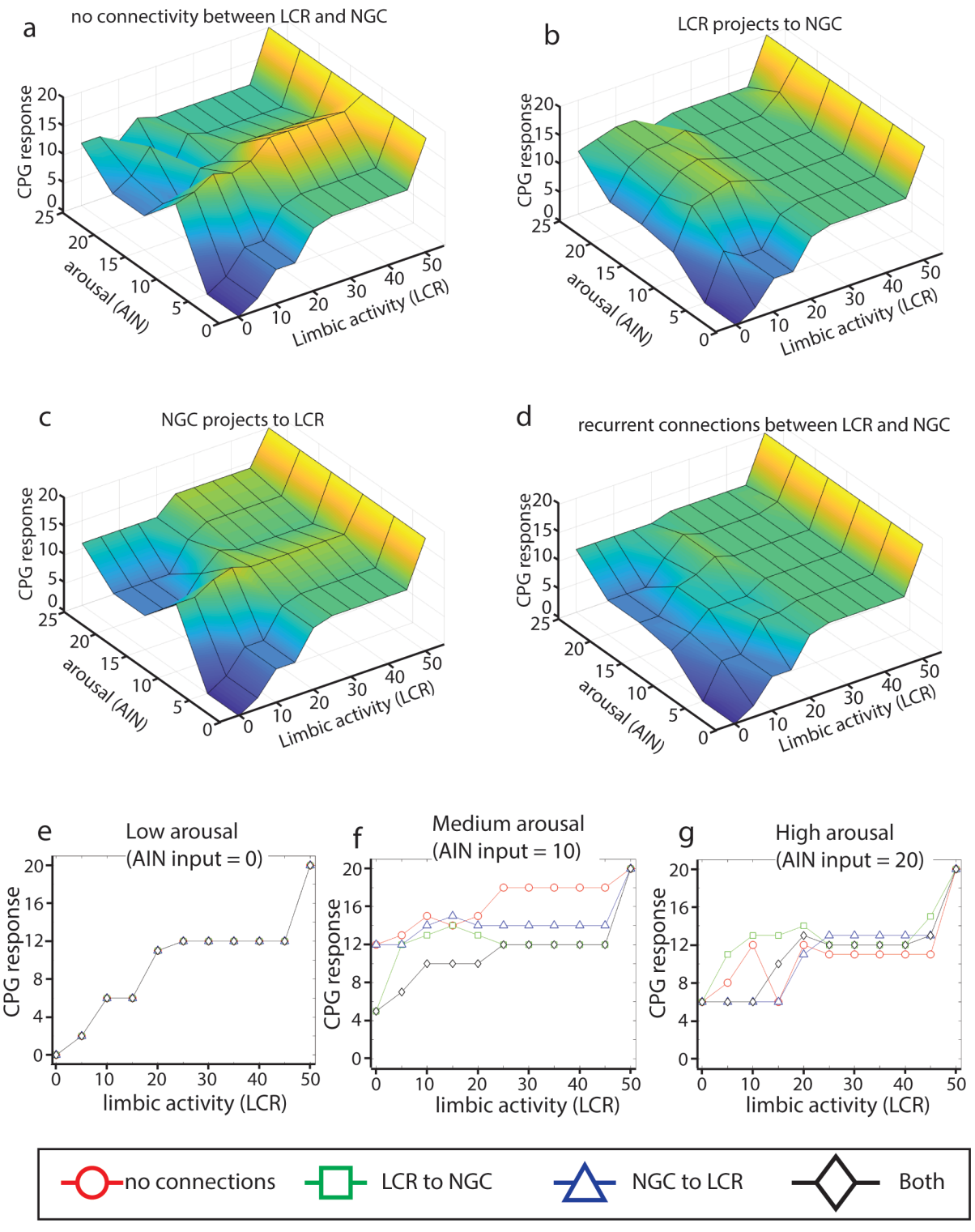
a
no connectivity between LCR and NGC
b
LCR projects to NGC
c
NGC projects to LCR
d
recurrent connections between LCR and NGC
CPG response
arousal (AIN)
Limbic activity (LCR)
e
Low arousal
(AIN input = 0)
f
Medium arousal
(AIN input = 10)
g
High arousal
(AIN input = 20)
limbic activity (LCR)
no connections
LCR to NGC
NGC to LCR
Both

2.5.2 Results

Overall, the response landscapes of the circuit configurations for model 1.1 and model 1.3 (figure 5a,c) are similar to each other, while the responses for models 1.2 and 1.4 are more similar to one another than to the other two models (figure 5b,d). This suggests that when recurrent connectivity between the NGC and LCR is introduced, the LCR-to-NGC connection has the greater influence over the ultimate behavior of the circuit.

The responses of all four models to different levels of LCR stimulation are exactly the same in the "low arousal" case when there is no stimulation applied to AIN (figure 5e). However, as the amount of arousal input to the circuit is increased, differences between the four models' responses to LCR stimulation begin to arise. At "intermediate arousal" when AIN gets 10mV of tonic stimulation, all of the models show greater CPG response as LCR activity increases. Although the level of evoked CPG activity is highest in the circuit with no connectivity between the LCR and NGC, this circuit has a shallower dynamic range of response to varying levels of LCR input than the circuit with recurrent LCR and NGC connections (figure 5f). At high levels of arousal (AIN input = 20mV), the responses of each model to increasing levels of LCR stimulation tend to flatten out, suggesting a decreased sensitivity to LCR activity, particularly at higher levels (figure 5g). In the model with a one-way LCR to NGC connection, the best dynamic range of CPG response came at low levels of LCR stimulation, whereas for the models with either just the NGC to LCR connection or recurrent connections had a better dynamic range at intermediate LCR stimulation levels. The model with no connectivity did not have a linear relationship between LCR stimulation and CPG response, mostly due to a peak at 10mV of LCR stimulation.

2.5.3 Conclusions

These experiments reveal that the presence of connections between the NGC and LC may not necessarily potentiate motor behavior uniformly at all levels of arousal and corticospinal drive. And, for that matter, increasing arousal input does not drive motor responses in a linear or even monotonic fashion. We observed the greatest difference in responses among the different models at intermediate arousal input levels.

At these intermediate arousal levels, the circuit with recurrent connectivity between the brainstem NGC and midbrain LC had the greatest dynamic range of responses to limbic activity. Even though this circuit started off at a lower level of responsiveness to LC activity than the versions without NGC and LC interconnectivity, it was more sensitive to small changes in LC activity. This suggests that one function of recurrent LC to NGC connectivity may be to maintain the power of top-down voluntary motor control even when arousal drive is high.

2.6 Model 2: What if the NGC contains neurons with ascending, descending, or bifurcating axons?

A subset of neurons within the nucleus gigantocellularis have been found to have bifurcating axons that project simultaneously to both midbrain arousal nuclei and the spinal cord (Valverde 1961). The presence of these bifurcating NGC neurons supports the hypothesis that this nucleus integrates behavioral arousal throughout the nervous system, since they would provide a plausible pathway whereby NGC activation rapidly affects a wide swath of the brain and spinal cord (Pfaff 2012). We constructed the following circuit models in order to study the effect that bifurcating neurons in the NGC may have on behavioral responsiveness to arousal and limbic activation compared to cases where the NGC has only ascending projections to the limbic system or descending projections to the spinal cord.

2.6.1 Methods

The circuit consists of five distinct regions: “arousal sensory input” (AIN), “nucleus gigantocellularis” (NGC), “limbic system” (LIS), “motor circuit” (MCR), and “output onto spinal central pattern generator” (CIN). Apart from the NGC, all four other regions contain 100 cells each, arranged in a 10 by 10 rectangular lattice. The NGC region is further subdivided into three groups, NGC_A, NGC_B, and NGC_C that each contain 30 cells arranged in a 10 by 3 rectangular lattice. The parameters used for each region in this model are listed in table 3. A schematic of the modeled circuit is shown in figure 6a. Notably, the three groups within the NGC region have different connectivity patterns. NGC_A represents ascending projections from the hindbrain to midbrain; this group has a modulatory connection to MCR. NGC_C represents descending projections from the midbrain to the spinal cord; this group has a modulatory connection to CIN. NGC_B represents bifurcating axons from the hindbrain to midbrain and spinal cord; this group has modulatory connections to both MCR and CIN.

Each set of simulations was run for 20 trials, with 4 cycles per trial. During each set of trials, noise stimulation was applied to AIN and LIS. Stimulation strength in both of these regions was independently modulated from 0 to 50 in each region to cover all combinations of AIN and LIS stimulation. Output was measured as the number of cycles and trials required for CIN to reach spike threshold and begin firing action potentials. Because ω_2 was set to 1, there was no decay of activity once CIN had reached threshold, so it continued to fire at full speed until the end of the simulation (figure 6b). Thus, for this and all following models, the z and y-axes are effectively flipped such that a better motor response is represented by a lower CIN time to response value.

Three different circuit conditions were tested in this model. In the first (model 2.1), the modulatory connection strength from NGC_A to MCR was set to 1, while all other outputs from

NGC_B and NGC_C were set to 0 to model a circuit containing purely ascending hindbrain projections (figure 6c). In the second condition (model 2.2), the modulatory connection strength from NGC_C to CIN was set to 1 which all other NGC outputs were 0 to model purely descending hindbrain projections (figure 6d). In the third condition (model 2.3), the modulatory outputs from NGC_B to MCR and CIN were set to 1, while NGC_A and NGC_C output were set to 0 to model bifurcating hindbrain projections (figure 6e).

Data for this model (in the appendix):

Appendix 6: CNS control file for model 2

Appendix 7: Results for model 2.1

Appendix 8: Results for model 2.2

Appendix 9: Results for model 2.3

2.6.2 Results

Figure 7 shows the results of applying different amounts of stimulation to LIS and AIN in circuits with ascending NGC projections only (figure 7a), descending NGC projections only (figure 7b), and bifurcating NGC projections (figure 7c). For all three of these cases, increasing levels of arousal and limbic stimulation decrease the latency to CPG response, reflecting quicker response times in the system. In the absence of limbic input, all three versions of the circuit have identical responses to arousal stimulation (figure 7d). However, when limbic input is increased, the effect of the different NGC projection schemes becomes more apparent (figure 7e). Having a bifurcating NGC leads to shorter response latencies to arousal stimulation at all levels, while the circuit with an NGC that has only ascending projections has the slowest response latency to arousal stimulation. The same effect holds true across different levels of limbic stimulation when arousal is kept constant at 0 (figure 7f) or 10mv (figure 7g).

Table 3. Parameters for model 2

Region	Parameters	Model 2.1	Model 2.2	Model 2.3
AIN	noise input	0-50	0-50	0-50
	AIN to NGCa	1	1	1
	AIN to NGCb	1	1	1
	AIN to NGCc	1	1	1
	pt	120	120	120
	nt	0	0	0
	st	49	49	49
	ω1	1	1	1
	ω2	1	1	1
NGCa	NGCa to MCR	1	0	0
	pt	120	120	120
	nt	0	0	0
	st	49	49	49
	ω1	1	1	1
	ω2	1	1	1
NGCb	NGCb to MCR	0	0	1
	NGCb to CIN	0	0	1
	pt	120	120	120
	nt	0	0	0
	st	49	49	49
	ω1	1	1	1
	ω2	1	1	1
NGCc	NGCc to CIN	0	1	0
	pt	120	120	120
	nt	0	0	0
	st	49	49	49
	ω1	1	1	1
	ω2	1	1	1
LIS	noise input	0-50	0-50	0-50
	LCR to MCR	1	1	1
	pt	120	120	120
	nt	0	0	0
	st	49	49	49
	ω1	1	1	1
	ω2	1	1	1
MCR	MCR to CIN	1	1	1
	pt	120	120	120
	nt	0	0	0
	st	49	49	49
	ω1	1	1	1
	ω2	1	1	1
CIN	pt	120	120	120
	nt	0	0	0
	st	49	49	49
	ω1	1	1	1
	ω2	1	1	1
trials		20	20	20
cycles per trial		4	4	4

Figure 6. Circuit arrangement and behavior of model 2.

a, arrangement of the circuit. This model contains five regions, "arousal sensory input" (AIN), "nucleus gigantocellularis" (NGC), "limbic system" (LIS), "motor circuit" (MCR), and "output onto spinal central pattern generator" (CIN). The regions AIN, MCR, LIS, and CIN contain 100 neurons each, while NGC is divided into three groups of 30 neurons each, NGC_A, NGC_B, and NGC_C. All inter-region connections (→) are excitatory and tonic input is applied to AIN and LIS in each simulation (↯). ***b***, example output of CIN region from a circuit simulation in which AIN stimulation is 0 and LIS stimulation is 2. Raster plot shows constant tonic spiking arising after 3 trials as the mean membrane voltage of CIN cells increases over the course of the simulation and eventually saturates at 130mV when the cells begin spiking (indicated with →). The fewer trials elapse before CIN activation, the more responsive the circuit.

c-e, Different modifications on the connectivity of the three sub-regions of the NGC to MRC and CIN. ***c***, only projections from NGC_A to MCR turned on (model 2.1). ***d***, only projections from NGC_C to CIN turned on (model 2.2). ***e***, only projections from NGC_B to MCR and CIN turned on (model 2.3).

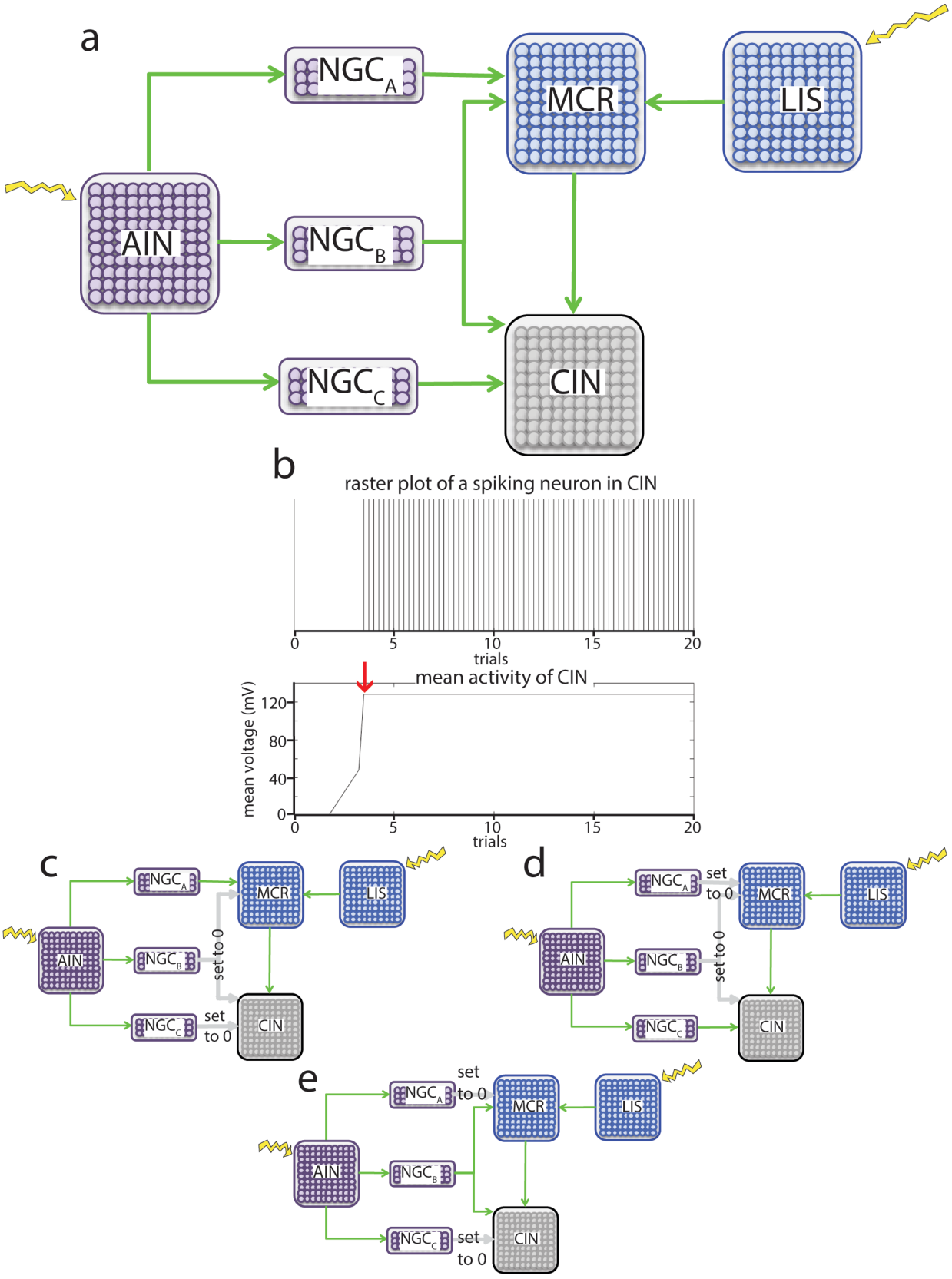
a
NGC_A
MCR
LIS
AIN
NGC_B
NGC_C
CIN
b
raster plot of a spiking neuron in CIN
0
5
10
15
20
trials
mean activity of CIN
mean voltage (mV)
120
80
40
0
c
set to 0
d
e

Figure 7. Results of simulations of model 2.

a-c overall landscape of CIN responses to different combinations of tonic stimulation of LIS and AIN regions for the three variations on model 2, we used a measure of how many cycles in a given simulation it takes for CIN to begin spiking (figure 6b) as the output of this and all subsequent models. ***a***, NGC region has ascending projections to MTR only (model 2.1, figure 6c). ***b***, NGC region has descending projections to CIN only (model 2.2, figure 6d). ***c***, NGC region has bifurcating projections to MTR and CIN (model 2.3, figure 6e).

d-g responses of each model to different amount of LIS or AIN stimulation when stimulation to other the target region is kept constant. ***d***, responses to AIN stimulation at low limbic activity (LIS input = 0), ***e***, responses to AIN stimulation at high limbic activity (LIS input = 10mV), ***f***, responses to LIS stimulation at low arousal (AIN input = 0), ***g***, responses to LIS stimulation at high arousal (AIN input = 10mV).

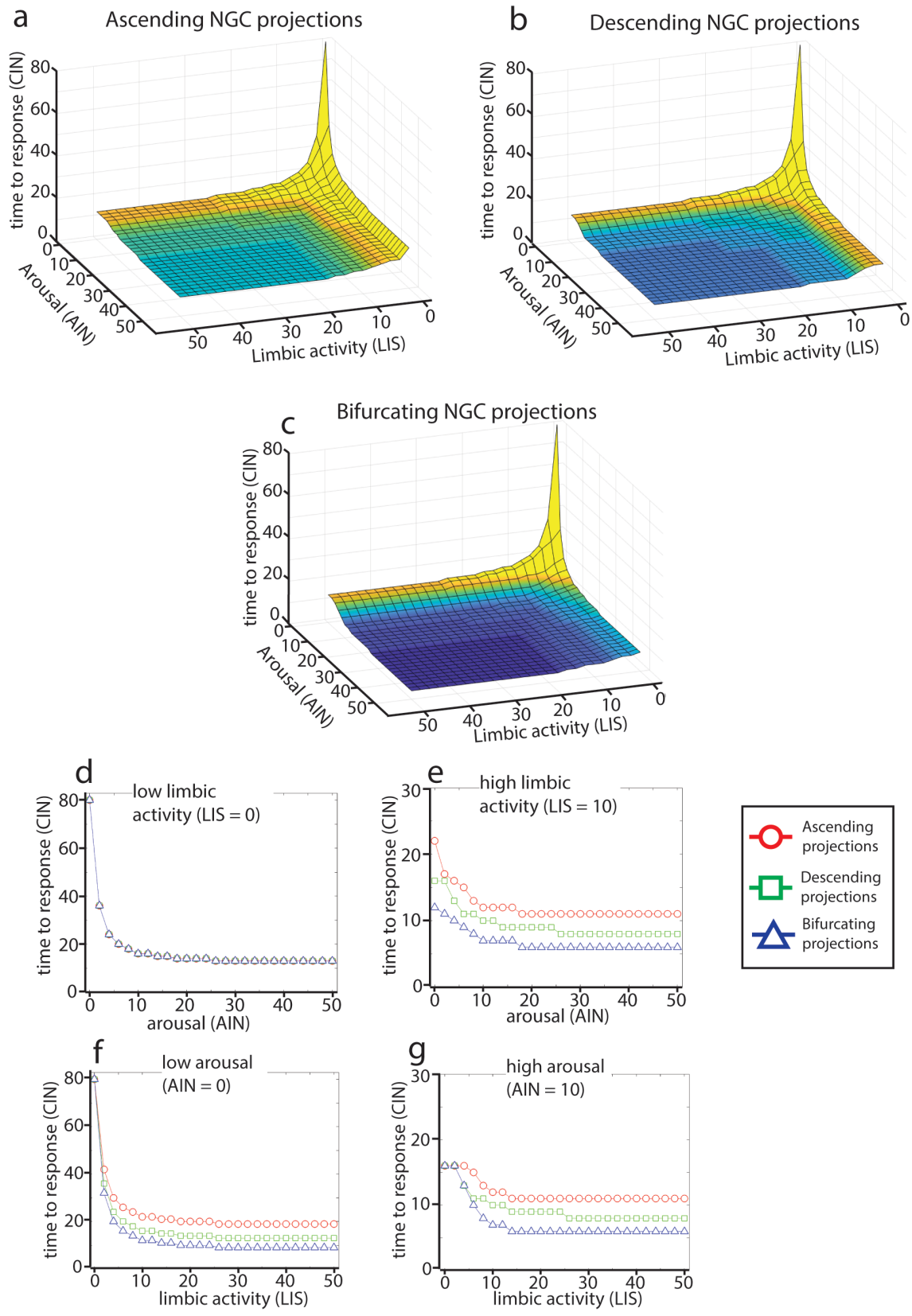
a
Ascending NGC projections
time to response (CIN)
Arousal (AIN)
Limbic activity (LIS)
b
Descending NGC projections
c
Bifurcating NGC projections
d
low limbic activity (LIS = 0)
arousal (AIN)
e
high limbic activity (LIS = 10)
Ascending projections
Descending projections
Bifurcating projections
f
low arousal (AIN = 0)
limbic activity (LIS)
g
high arousal (AIN = 10)

2.6.3 Conclusions

The responsiveness of all these circuits plateaus with increasing amounts of arousal or limbic stimulation, but the response latency values that each configuration converges on are different. This suggests that having a bifurcating NGC increases the maximum responsiveness of the system but doesn't change the relationship between arousal input and behavioral response. Thus, bifurcating projections from the NGC to the spinal cord and midbrain appear to increase the speed at which an arousing stimulus is propagated throughout the nervous system.

It is perhaps not surprising that the model with a bifurcating NGC should yield such improvements to behavioral responsiveness. Since this model sends modulatory input to both the MCR and CIN regions, this results in a larger amount of overall activation in the system relative to the models with only ascending or descending NGC outputs. We speculate that in the intact nervous system, such bifurcation of the NGC serves to more rapidly propagate an arousal signal throughout many regions of the brain associated with locomotor drive, which all ultimately converge on motor effectors in the spinal cord and summate to push these motor circuits over their behavioral activation threshold more rapidly during a state of high generalized arousal.

2.7 Model 3: What if there are local excitatory or inhibitory connections within the NGC?

In the previous circuit models, each simulated neuronal region only received excitatory or inhibitory input from cells located in a different region, without any synapses between neurons within the same region. However, the reticular formation also contains inhibitory interneurons with exclusively local connectivity and excitatory neurons that are known to have a mixture of local and long-range connections. GABAergic neurons in the reticular formation have been implicated in driving behavioral state changes (Minert 2017). The following model elaborates on the circuit structure introduced in model 2 by incorporating different combinations of excitatory

or inhibitory connections between neurons within the NGC region in order to explore the functional consequences of such local connectivity on the overall responsiveness of the arousal circuit.

2.7.1 Methods

This model is a modified version of model 2 and contains the same five regions: “arousal sensory input” (AIN), “nucleus gigantocellularis” (NGC), “limbic system” (LIS), “motor circuit” (MCR), and “output onto spinal central pattern generator” (CIN). The regions AIN, LIS, MCR, and CIN contain 100 cells each arranged in a 10 by 10 grid. NGC is split up into two groups, NGC_1 and NGC_2 of 50 cells arranged in a 5 by 10 grid. NGC_1 projects to MCR, representing ascending hindbrain to midbrain projections, while NGC_2 projects directly to CIN and represents hindbrain connections to the spinal cord. The parameters used for each region in this model are listed in table 4. A detailed schematic of the connectivity of this model circuit is shown in figure 8.

In addition to the aforementioned modulatory connections between regions, we also incorporated specific local connections among neurons within NGC_1 and NGC_2. These specific connections were assigned randomly; for a given neuron in each of these regions, a number of other neurons within that same region were selected at random to input to it. All connections were assigned to have a strength of 1 with a standard deviation of 0, and the percentage of these connections that were excitatory rather than inhibitory was set between 0 and 100%.

Each simulation was run for 20 trials with 4 cycles per trial. During each set of trials, noise stimulation was applied to AIN and LIS. Stimulation strength in both of these regions was independently modulated from 0 to 30 in each region to cover all combinations of AIN and LIS stimulation. Output was measured as the number of cycles and trials required for CIN to reach spiking threshold. We tested the effects of modifying the parameters for the specific connections

within NGC_1 and NGC_2, including the number of connections per cell (varied from 5 to 25) and the percentage of connections that are excitatory rather than inhibitory (varied from 0% to 100%). For illustrative purposes, we chose to focus on the effects of the balance between excitatory and inhibitory recurrent excitation when there are 20 connections per cell and the percentage of excitatory connections is 0%, 40%, or 100%.

Data for this model (in the appendix):

Appendix 10: CNS control file for model 3

Appendix 11: Results for 0% excitatory connections

Appendix 12: Results for 40% excitatory connections

Appendix 13: Results for 100% excitatory connections

Table 4. Parameters for model 3

Regions	Parameters	Model 3.1	Model 3.2	Model 3.3	Model 3.4
AIN	noise input	0-30	0-30	0-30	0-30
	AIN to NGC1	1	1	1	1
	AIN to NGC2	1	1	1	1
	ω1	1	1	1	1
	ω2	1	1	1	1
	pt	120	120	120	120
	nt	0	0	0	0
	st	49	49	49	49
NGC1	NGC1 to MCR	1	1	1	1
	number of local connections	0	20	20	20
	percent excitatory local conns	na	1	0	0.4
	ω1	1	1	1	1
	ω2	1	1	1	1
	pt	120	120	120	120
	nt	0	0	0	0
	st	49	49	49	49
NGC2	NGC2 to CIN	1	1	1	1
	number of local connections	0	20	20	20
	percent excitatory local conns	na	1	0	0.4
	ω1	1	1	1	1
	ω2	1	1	1	1
	pt	120	120	120	120
	nt	0	0	0	0
	st	49	49	49	49
LIS	noise input	0-30	0-30	0-30	0-30
	LIS to MCR	1	1	1	1
	ω1	1	1	1	1
	ω2	1	1	1	1
	pt	120	120	120	120
	nt	0	0	0	0
	st	49	49	49	49
MCR	MCR to CIN	1	1	1	1
	ω1	1	1	1	1
	ω2	1	1	1	1
	pt	120	120	120	120
	nt	0	0	0	0
	st	49	49	49	49
CIN	ω1	1	1	1	1
	ω2	1	1	1	1
	pt	120	120	120	120
	nt	0	0	0	0
	st	49	49	49	49
trials		20	20	20	20
cycles per trial		4	4	4	4

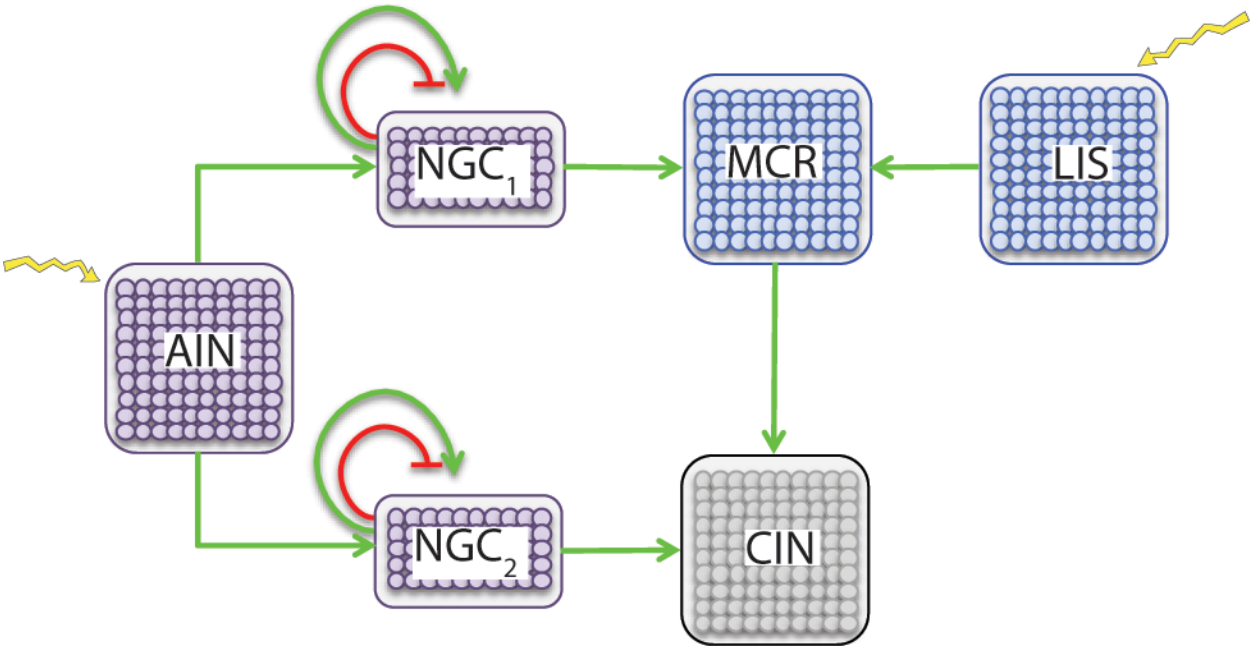

Figure 8. Circuit arrangement of model 3.

The model contains five regions, "arousal sensory input" (AIN), "nucleus gigantocellularis" (NGC), "limbic system" (LIS), "motor circuit" (MCR), and "output onto spinal central pattern generator" (CIN). The regions AIN, MCR, LIS, and CIN contain 100 neurons each, while NGC is split into two groups, NGC_1 and NGC_2 with 50 neurons in each. Connections between regions (→) are all excitatory and modulatory. Connections within NGC_1 and NGC_2 are a mix of excitatory (→) and inhibitory (–|) specific connections between randomly assigned neurons within the same group (curved arrows). Tonic excitation was applied to AIN and LIS (↯) during each round of simulations.

2.7.2 Results

In the absence of any recurrent local connections within the NGC, both arousal and limbic inputs contribute to CIN response to the same degree, yielding a symmetrical response landscape (figure 9a, model 3.1). With the addition of local excitatory connections within NGC_A and NGC_B, the balance of power is shifted in favor of arousal input, with limbic input only exerting an effect on CPG response when arousal is very low, leading to an asymmetrical response landscape (figure 9b, model 3.2). If instead NGC_A and NGC_B contain local inhibitory connections, low levels of limbic activity limit the effect that arousal stimulation has on CIN response such that maximum CIN responsiveness is only reached when arousal and limbic stimulation levels are high (figure 9c, model 3.3). Where NGC_A and NGC_B contain a mixture of excitatory and inhibitory local connections, a local minimum emerges in the response landscape when limbic stimulation is low such that intermediate levels of arousal yield faster CIN responses than either high or low levels of arousal (figure 9d, model 3.4).

At low levels of arousal, the presence of local connectivity within the NGC has no effect on behavioral output in response to limbic activation (figure 9e). Differences between the four models only arise at higher levels of arousal. The mixed local connections model has the greatest dynamic range of responses to limbic stimulation and the models with none or purely excitatory local NGC connections have a nearly flat relationship between limbic stimulation and behavioral response since high arousal has already saturated the circuit (figure 9f). In the absence of limbic input, the models with none, purely excitatory, or purely inhibitory local NGC connections display increased CIN response as arousal rises, whereas the mixed connections model has no response to arousal at any level (figure 9g). When limbic activity is high, all of the models have a positive relationship between arousal and behavioral response, with the responsiveness of the mixed connections model falling in between the purely excitatory and purely inhibitory models

(figure 9i). However, at intermediate limbic activity, a local minimum arises within the mixed connections model such that very low or very high arousal yields poorer behavioral response times than intermediate levels of arousal (figure 9h).

A closer look at the mechanisms underlying this local minimum reveals that the timing of CIN activation depends on having the sum of inputs from the MCR and NGC regions reach a threshold value. At intermediate limbic activation and low arousal levels, CIN activation is driven solely by limbic input, with arousal's contributions coming too late to make a significant difference in the time it takes for CIN to reach its activation threshold (figure 10a). As arousal input increases, it summates with the limbic contributions to allow CIN to reach spike threshold sooner, resulting in better response times (figure 10b). However, increased NGC activity driven by arousal also increases the degree of recurrent inhibition within this region, which causes the NGC to begin to have a dampening effect on CIN activity. Therefore, in this case high levels of arousal input paradoxically cause CIN to become less responsive to stimulation (figure 10c).

2.7.3 Conclusions

Predictably, we observe that adding local excitatory connections to the NGC tends to potentiate the circuit's response to arousal stimuli, whereas local inhibitory connections decrease the responsiveness of the circuit. It is only when we incorporate a mixture of local excitatory and inhibitory connections within the NGC that the circuit develops fundamentally new properties, such as a local minimum of excitability at intermediate levels of arousal and limbic activation.

According to the Yerkes-Dodson effect, the relationship between arousal and behavioral facilitation follows an inverted U-shaped curve such that very low and very high arousal are less effective than intermediate arousal. The computational models described here reveal that one way to generate this kind of relationship is through a combination of local excitatory and inhibitory feedback within an arousal integrator such as the NGC.

Figure 9. Results of simulations of model 3.

a-d overall landscape of CIN response latencies to different combinations of tonic stimulation of LIS and AIN regions for the four variations on model 3 (figure 8). ***a***, NGC_A and NGC_B have no local connections, ***b***, NGC_A and NGC_B have excitatory local connections, ***c***, NGC_A and NGC_B have inhibitory local connections, ***d***, NGC_A and NGC_B have a mixture of excitatory and inhibitory local connections.

e-i responses of each model to different amounts of LIS or AIN stimulation when stimulation to other target is kept constant. ***e***, responses to LIS stimulation at low levels of arousal (AIN input = 0), ***f***, responses to LIS stimulation at high levels of arousal (AIN input = 30mV). ***g***, responses to AIN stimulation at low limbic activity levels (LIS input = 0), ***h***, responses to AIN stimulation at intermediate limbic activity levels (LIS input = 12mV), ***i***, responses to AIN stimulation at high limbic activity levels (LIS input = 30mV).

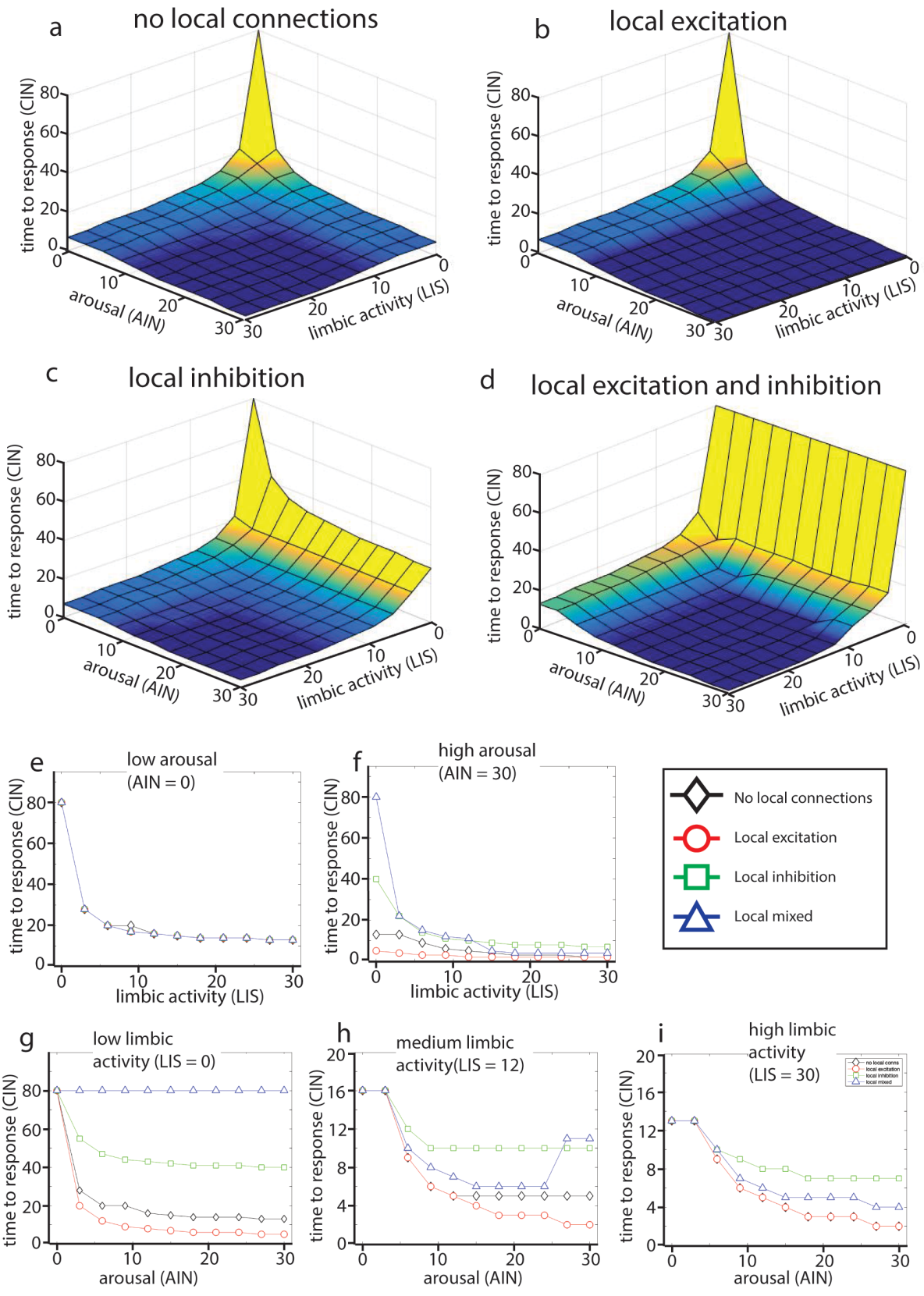
a
no local connections
b
local excitation
c
local inhibition
d
local excitation and inhibition
time to response (CIN)
arousal (AIN)
limbic activity (LIS)
e
low arousal
(AIN = 0)
f
high arousal
(AIN = 30)
No local connections
Local excitation
Local inhibition
Local mixed
g
low limbic
activity (LIS = 0)
h
medium limbic
activity(LIS = 12)
i
high limbic
activity
(LIS = 30)

Figure 10. Mechanism for how the CNS program generates a local minimum in mixed connections model 3.

a, at low arousal, input from the limbic system LIS (—) causes the motor effector CIN (—) to reach threshold (—) and eventually begin spiking (☆). ***b***, as arousal increases, NGC activation begins sooner and combined NGC (—) and limbic inputs cause the motor effector to begin spiking. ***c***, at high arousal the peak in NGC activity happens too soon and inhibitory NGC input prevents the motor effector from immediately reaching spiking threshold.

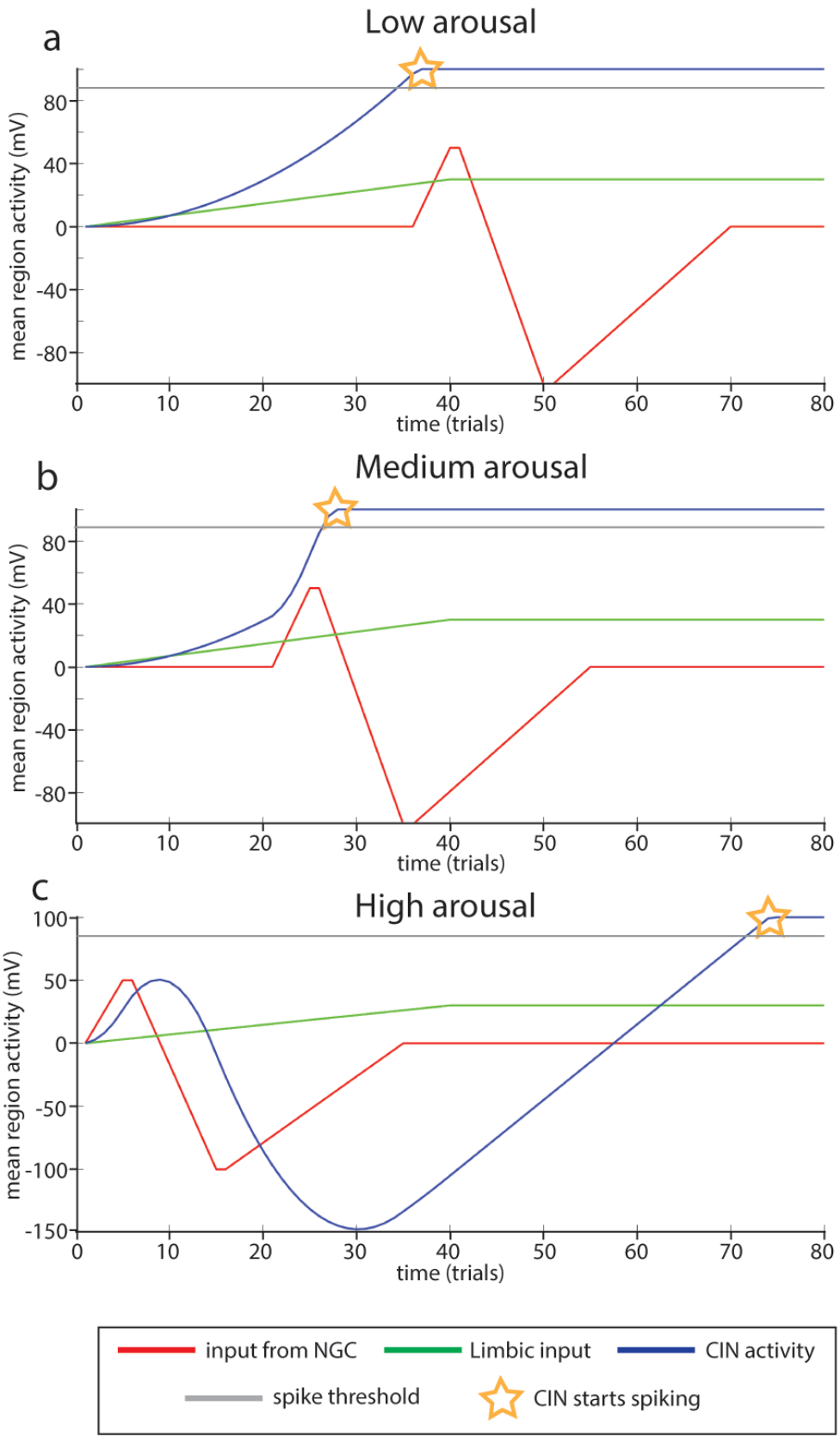
a
Low arousal
mean region activity (mV)
80
40
0
-40
-80
0
10
20
30
40
50
60
70
80
time (trials)
b
Medium arousal
mean region activity (mV)
80
40
0
-40
-80
0
10
20
30
40
50
60
70
80
time (trials)
c
High arousal
mean region activity (mV)
100
50
0
-50
-100
-150
0
10
20
30
40
50
60
70
80
time (trials)
input from NGC
Limbic input
CIN activity
spike threshold
CIN starts spiking

2.8 Model 4: What if the Locus Coeruleus or NGC are subdivided?

Our previous model circuits treated the LCR and NGC as homogeneous structures that integrated all received inputs together to generate a single level of output activation. However, there is evidence that the Locus Coeruleus actually contains an organized input-output architecture that keeps ascending and descending circuits relatively segregated from each other (Schwarz 2015a,b). Thus, for the following series of models, we asked whether splitting the LCR or the NGC into descending and ascending streams would have a significant effect on behavioral responsiveness to arousal and limbic activation.

2.8.1 Methods

This model was constructed with six groups: "sensory input" (AIN), "nucleus gigantocellularis" (NGC), "limbic system" (LIS), "motor circuits" (MCR), "Locus Coeruleus" (LCR), and "input to central pattern generator" (CIN). Each group contains 100 neurons arranged in a 10 by 10 lattice. The parameters used for each region in this model are listed in table 5. Noise stimulation was applied uniformly to AIN and LIS with a sigma of 0. The strength of this stimulation was independently modulated from 0 to 10 in AIN and 0 to 50 in LIS to cover all possible combinations of AIN and LIS activity and their effect on CIN activity. Each simulation was run for 10 trials, with 4 cycles per trial.

In the first set of simulations (model 4.1), all regions contained only one group (figure 11a). In the second set of simulations (model 4.2), the LCR region was split into two groups containing 50 neurons each. LCR_A, the ascending stream, received modulatory inputs from the NGC and projected to LIS. LCR_B, the descending stream, received modulatory inputs from the LIS and projected to NGC. All of these connections had strength 1 and sigma 0 (figure 11b). In the third set of simulations (model 4.3), the NGC was split into two sub-regions. NGC_A, the ascending stream, received modulatory inputs from AIN and projected to LCR. NGC_B, the

descending stream, received modulatory inputs from LCR and projected to CIN. Again, all of these modulatory connections had strength 1 and sigma 0 (figure 11c). In the fourth simulation configuration (model 4.4), both the NGC and LCR were split into two groups of 50 neurons apiece. NGC_A received modulatory inputs from AIN and projected to LCR_A. LCR_A in turn projected to LIS. LCR_B received modulatory inputs from LIS and projected to NGC_B, which in turn projected to CIN (figure 11d).

Data for this model (in the appendix):

Appendix 14: CNS control file for model 4.1 (no split regions)

Appendix 15: Results for model 4.1

Appendix 16: CNS control file for PFC2 (split LC) (model 4.2)

Appendix 17: Results for split LC (model 4.2)

Appendix 18: CNS control file for PFC3 (split NGC) (model 4.3)

Appendix 19: Results for split NGC (model 4.3)

Appendix 20: CNS control file for PFC4 (split LC and NGC) (model 4.4)

Appendix 21: Results for split LC and NGC (model 4.4)

Table 5. Parameters for model 4

Region	Parameters	Model 4.1	Region	Parameters	Model 4.2	Region	Parameters	Model 4.3	Region	Parameters	Model 4.4
AIN	noise input	0-10	AIN	noise input	0-10	AIN	noise input	0-10	AIN	noise input	0-10
	AIN to NGC	1		AIN to NGC	1		AIN to NGCa	1		AIN to NGCa	1
	pt	120		pt	120		pt	120		pt	120
	nt	0		nt	0		nt	0		nt	0
	st	49		st	49		st	49		st	49
	ω1	1		ω1	1		ω1	1		ω1	1
	ω2	1		ω2	1		ω2	1		ω2	1
NGC	NGC to LCR	1	NGC	NGC to LCRb	1	NGCa	NGCa to LCR	1	NGCa	NGCa to LCRa	1
	NGC to CIN	1		NGC to CIN	1		pt	120		pt	120
	pt	120		pt	120		nt	0		nt	0
	nt	0		nt	0		st	49		st	49
	st	49		st	49		ω1	1		ω1	1
	ω1	1		ω1	1		ω2	1		ω2	1
	ω2	1		ω2	1	NGCb	NGCb to CIN	1	NGCb	NGCb to CIN	1
LIS	noise input	0-50	LIS	noise input	0-50		pt	120		pt	120
	LIS to MCR	1		LIS to MCR	1		nt	0		nt	0
	LIS to LCR	1		LIS to LCRa	1		st	49		st	49
	pt	120		pt	120		ω1	1		ω1	1
	nt	0		nt	0		ω2	1		ω2	1
	st	49		st	49	LIS	noise input	0-50	LIS	noise input	0-50
	ω1	1		ω1	1		LIS to MCR	1		LIS to MCR	1
	ω2	1		ω2	1		LIS to LCR	1		LIS to LCR	1
MCR	MCR to CIN	1	MCR	MCR to CIN	1		pt	120		pt	120
	pt	120		pt	120		nt	0		nt	0
	nt	0		nt	0		st	49		st	49
	st	49		st	49		ω1	1		ω1	1
	ω1	1		ω1	1		ω2	1		ω2	1
	ω2	1		ω2	1	MCR	MCR to CIN	1	MCR	MCR to CIN	1
LCR	LCR to NGC	1	LCRa	LCRa to NGC	1		pt	120		pt	120
	LCR to LIS	1		pt	120		nt	0		nt	0
	pt	120		nt	0		st	49		st	49
	nt	0		st	49		ω1	1		ω1	1
	st	49		ω1	1		ω2	1		ω2	1
	ω1	1		ω2	1	LCR	LCR to NGCb	1	LCRa	LCRa to LIS	1
	ω2	1	LCRb	LCRb to LIS	1		LCR to LIS	1		pt	120
CIN	pt	120		pt	120		pt	120		nt	0
	nt	0		nt	0		nt	0		st	49
	st	49		st	49		st	49		ω1	1
	ω1	1		ω1	1		ω1	1		ω2	1
	ω2	1		ω2	1		ω2	1	LCRb	LCRb to NGCb	1
trials		20	CIN	pt	120	CIN	pt	120		pt	120
cycles per trial		4		nt	0		nt	0		nt	0
				st	49		st	49		st	49
				ω1	1		ω1	1		ω1	1
				ω2	1		ω2	1		ω2	1
			trials		20	trials		20	CIN	pt	120
			cycles per trial		4	cycles per trial		4		nt	0
										st	49
										ω1	1
										ω2	1
									trials		20
									cycles per trial		4

Figure 11. Circuit configurations for model 4.

All configurations contain the six regions "arousal sensory input" (AIN), "nucleus gigantocellularis" (NGC), "limbic system" (LIS), "motor circuits" (MCR), "Locus Coeruleus" (LCR), and "input to central pattern generator" (CIN) with 100 neurons in each, unless otherwise noted. Connections between regions (→) are of the excitatory modulatory type, tonic excitation was applied to AIN and LIS (↯) during each round of simulations. ***a***, configuration for the first set of simulations, NGC and LCR are single groups (model 4.1), ***b***, configuration for the second set of simulations (model 4.2), LCR is divided into two groups, LCR_A and LCR_B, with 50 neurons in each. LCR_A is part of the "descending" stream from LIS to NGC. LCR_B is part of the "ascending" stream from NGC to LIS. ***c***, configuration for the third set of simulations (model 4.3), NGC is divided into two groups, NGC_A and NGC_B, with 50 neurons in each. NGC_A is part of the "ascending" stream from AIN to LCR. NGC_B is part of the "descending" stream from LCR to CIN. ***d***, configuration for the fourth set of simulations (model 4.4), NGC and LCR are each divided into two groups, NGC_A, NGC_B, LCR_A, and LCR_B with 50 neurons in each. NGC_A and LCR_A are part of the "ascending" stream from AIN to LIS. NGC_B and LCR_B are part of the "descending" stream from LIS to CIN.

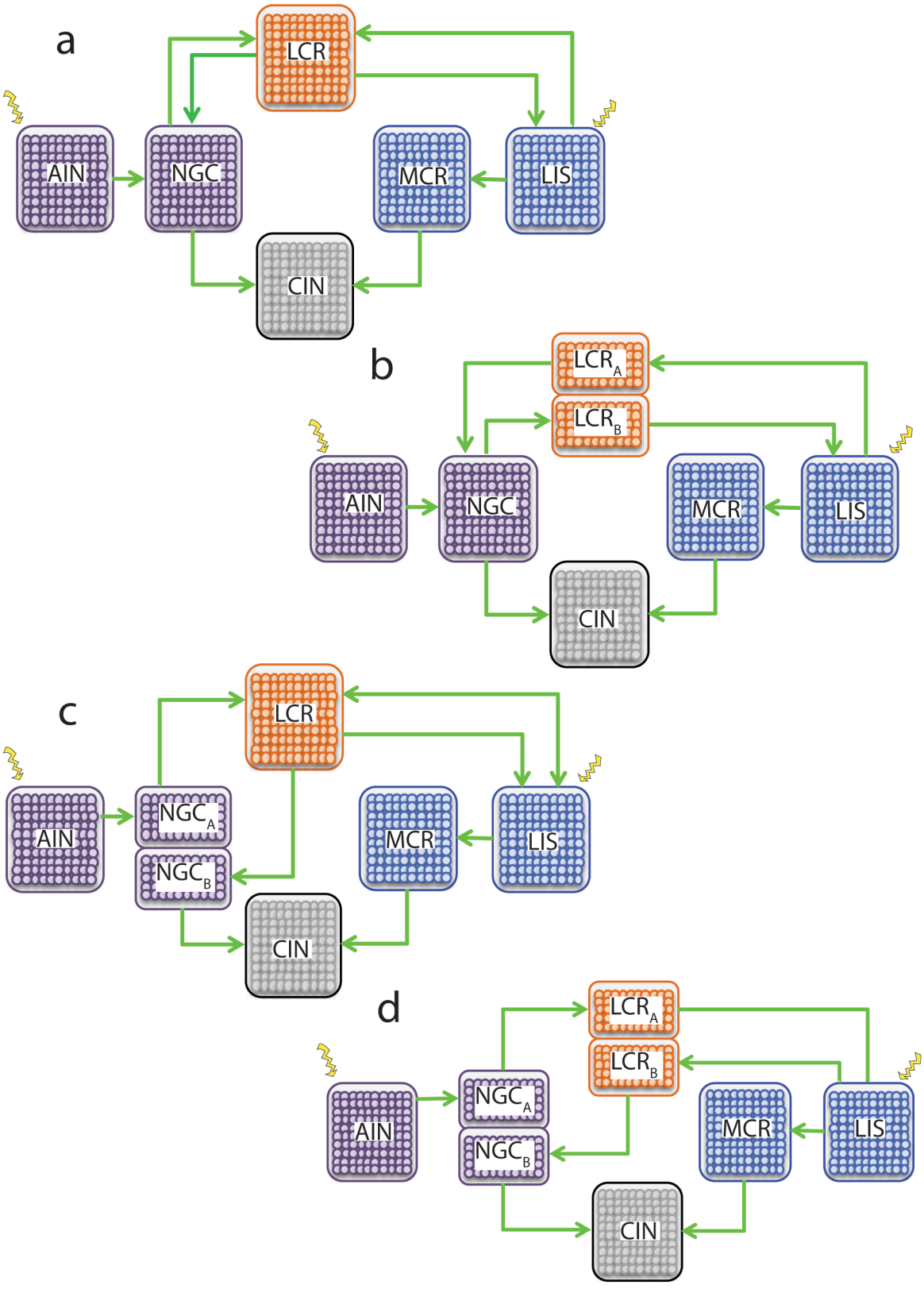
a
LCR
AIN
NGC
MCR
LIS
CIN
b
LCR_A
LCR_B
AIN
NGC
MCR
LIS
CIN
c
LCR
AIN
NGC_A
NGC_B
MCR
LIS
CIN
d
LCR_A
LCR_B
AIN
NGC_A
NGC_B
MCR
LIS
CIN

2.8.2 Results

Dividing the LCR into two sub-regions, one exclusively dedicated to "descending" input from LIS to NGC and the other dedicated to "ascending" input from NGC to LIS has no effect on the responses of the behavioral output region CIN to all combinations of limbic stimulation to the LIS and arousal stimulation to the AIN (figure 12b), compared to the default case where the LCR is a single region that receives both ascending and descending inputs (figure 12a). However, dividing the NGC into two sub-regions exclusively dedicated to "ascending" projections from AIN to LCR and "descending" projections from LCR to CIN makes the circuit slightly less responsive to arousal (figure 12c). This change is particularly apparent when limbic activity is low. Having separate ascending and descending streams within the NGC and LCR together has the greatest effect on circuit behavior; the circuit does not respond to arousal at all except for when there is no limbic activation (figure 12d).

When arousal is low, all of these circuit configurations have the same response to limbic stimulation (figure 12e). As arousal is increased, the models with a split NGC perform slightly worse in response to limbic input, but overall follow the same response function as the models without any subdivisions (figure 12f). Differences in these circuits become more apparent when looking at the effects of changing arousal input when limbic activity is low. The models without a divided NGC require less arousal input to become active and achieve a faster behavioral response at high arousal than the circuits with a split NGC (figure 12g). The same trend holds true for the effects of arousal when limbic activity is high (figure 12h).

2.8.3 Conclusions

Although the effects of dividing the NGC and LCR into articulated input-output streams are fairly subtle, we observe that dividing the NGC in this way has a deleterious effect on circuit responsiveness, particularly to increasing levels of behavioral arousal. This suggests that

structuring the NGC like a sensory integrator that takes into account inputs from throughout the nervous system in generating an arousal signal improves behavioral responsiveness to arousal. On the other hand, dividing the LCR had no effect on the circuit's responsiveness to arousal or limbic stimuli. Perhaps having this kind of articulated circuitry within the Locus Coeruleus is of greater consequence to its targets within the forebrain.

Figure 12. Results of simulations of model 4.

a-d overall landscapes of CIN response latencies to different combinations of tonic stimulation of LIS and AIN regions for the four variations on model 4. ***a***, baseline case where the NGC and LCR integrate all ascending and descending inputs (figure 11a). ***b***, LCR has been split into sub-regions dedicated to "ascending" and "descending" projections (figure 11b). ***c***, NGC has been split into sub-regions (figure 11c). ***d***, NGC and LCR have both been split into sub-regions (figure 11d).

e-h responses of each model to different amounts of LIS or AIN stimulation when stimulation to the other target is kept constant. ***e***, responses to LIS stimulation at low arousal (AIN input = 0), ***f***, responses to LIS stimulation when arousal is high (AIN input = 10 mV), ***g***, responses to AIN stimulation when limbic activity is low (LIS input = 0), ***h***, responses to AIN stimulation when limbic activity is high (LIS input = 40 mV).

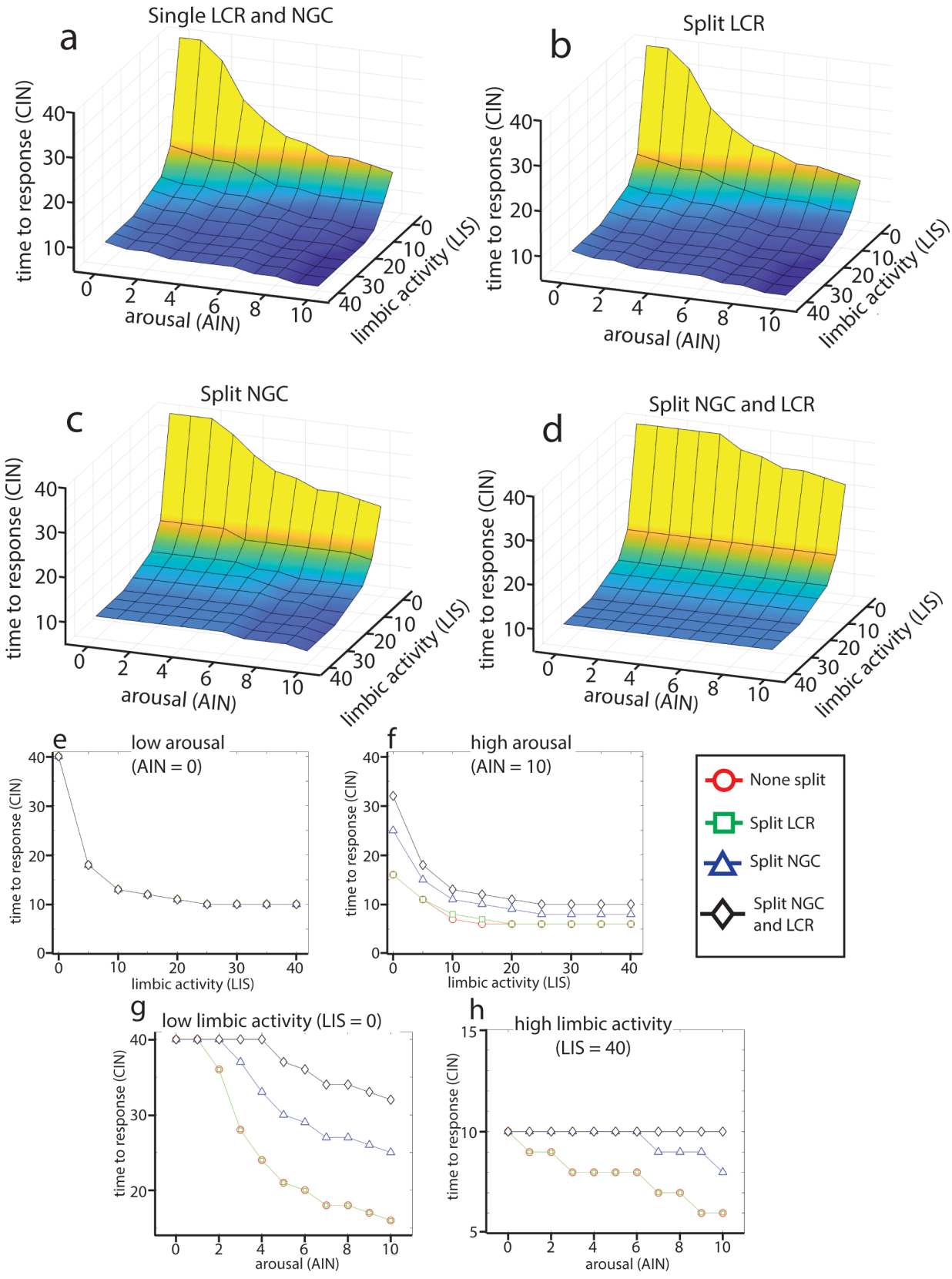
a
Single LCR and NGC
time to response (CIN)
arousal (AIN)
limbic activity (LIS)
b
Split LCR
c
Split NGC
d
Split NGC and LCR
e
low arousal
(AIN = 0)
f
high arousal
(AIN = 10)
None split
Split LCR
Split NGC
Split NGC
and LCR
g
low limbic activity (LIS = 0)
h
high limbic activity
(LIS = 40)

2.9 Model 5: What if there are multiple descending motor control circuits?

All of our previous models represented descending motor commands originating in the cortex and limbic system as a single stream of information projecting to the spinal cord. In lower vertebrates such as lampreys, the primary source of descending motor control is mediated through the mesencephalic locomotor area (MLR), so such a representation is generally accurate (Dubuc 2008). Though the MLR still plays an important role in motor control in mammals, an increasing proportion of motor commands are conveyed to the spinal cord via parallel pathways that originate in sensorimotor cortex (Grillner 2008). We sought to incorporate a more "mammalian" version of motor control into our arousal circuit model by adding a second source of cortico-limbic input in parallel with the first to explore how this second descending motor control pathway affects the contributions of arousal on behavioral responsiveness.

2.9.1 Methods

This model is a modification of model 3 and contains all of the same regions and connectivity as that circuit: "arousal sensory input" (AIN), "nucleus gigantocellularis" (NGC_A and NGC_B), "limbic system" (LIS), "motor circuit" (MCR), and "output onto spinal central pattern generator" (CIN). NGC_A and NGC_B contain recurrent connections assigned using the same scheme as in model 3, with 20 connections per neuron and an excitation/inhibition ratio of 40:60. In addition to these regions, a second parallel forebrain influence was added in the form of the two regions "limbic input 2" (LIS_2) and "motor circuit 2" (MCR_2). There are modulatory connections between LIS_2 and MCR_2, between MCR_2 and CIN, and between NGC_A and MCR_2. The parameters used for each region in this model are listed in table 6.

Each simulation was run for 20 trials, with 4 cycles per trial. During each set of trials, noise stimulation was applied to AIN, LIS_1 and LIS_2. The same level of stimulation was applied to LIS_1 and LIS_2; this was modulated from 0 to 30. Stimulation applied to AIN was

independently modulated from 0 to 30 and all combinations of LIS_1/LIS_2 and AIN stimulation levels were tested in each round of simulations. As before, the output of the model was measured as the number of trials and cycles required for CIN to begin spiking.

Using this framework, we tested a few variations on the aforementioned circuit configuration. In the first set of simulations (model 5.1), we modeled a circuit with a single forebrain input from LIS_1 and MCR_1 (figure 13a). For the next simulation set (model 5.2), we added in a second, parallel limbic system input in the form of LIS_2 and MCR_2, which are connected to CIN with modulatory inputs as diagrammed in figure 13b. In a third set of simulations (model 5.3), we tested how the ascending arousal stream contributed to circuit activity by removing the descending arousal stream and setting the NGC_B to CIN connection strength to zero (figure 13c). In the fourth set of simulations (model 5.4), we similarly tested the role of the descending arousal stream in this circuit in the absence of an ascending stream by setting the NGC_A to MCR_1 and NGC_A to MCR_2 connection strengths to zero (figure 13d).

Data for this model (in the appendix):

Appendix 22: CNS control file for model 5

Appendix 23: Results for model 5.1

Appendix 24: Results for model 5.2

Appendix 25: Results for model 5.3

Appendix 26: Results for model 5.4

Table 6. Parameters for model 5

Region	Parameters	Model 5.1	Region	Parameters	Model 5.2	Model 5.3	Model 5.4
AIN	noise input	0-30	AIN	noise input	0-30	0-30	0-30
	AIN to NGCa	1		AIN to NGCa	1	1	1
	AIN to NGCb	1		AIN to NGCb	1	1	1
	pt	120		pt	120	120	120
	nt	0		nt	0	0	0
	st	49		st	49	49	49
	ω1	1		ω1	1	1	1
	ω2	1		ω2	1	1	1
NGCa	NGCa to MCR1	1	NGCa	NGCa to MCR1	1	1	0
	number of local connections	20		NGCa to MCR2	1	1	0
	percent excitatory local conns	0.4		number of local connections	20	20	20
	pt	120		percent excitatory local conns	0.4	0.4	0.4
	nt	0		pt	120	120	120
	st	49		nt	0	0	0
	ω1	1		st	49	49	49
	ω2	1		ω1	1	1	1
NGCb	NGCb to CIN	1		ω2	1	1	1
	number of local connections	20	NGCb	NGCb to CIN	1	0	1
	percent excitatory local conns	0.4		number of local connections	20	20	20
	pt	120		percent excitatory local conns	0.4	0.4	0.4
	nt	0		pt	120	120	120
	st	49		nt	0	0	0
	ω1	1		st	49	49	49
	ω2	1		ω1	1	1	1
LIS1	noise input	0-30		ω2	1	1	1
	LIS1 to MCR1	1	LIS1	noise input	0-30	0-30	0-30
	pt	120		LIS1 to MCR1	1	1	1
	nt	0		pt	120	120	120
	st	49		nt	0	0	0
	ω1	1		st	49	49	49
	ω2	1		ω1	1	1	1
MCR1	MCR1 to CIN	1		ω2	1	1	1
	pt	120	MCR1	MCR1 to CIN	1	1	1
	nt	0		pt	120	120	120
	st	49		nt	0	0	0
	ω1	1		st	49	49	49
	ω2	1		ω1	1	1	1
CIN	pt	120		ω2	1	1	1
	nt	0	LIS2	noise input	0-30	0-30	0-30
	st	49		LIS2 to MCR2	1	1	1
	ω1	1		pt	120	120	120
	ω2	1		nt	0	0	0
trials		20		st	49	49	49
cycles per trial		4		ω1	1	1	1
				ω2	1	1	1
			MCR2	MCR2 to CIN	1	1	1
				pt	120	120	120
				nt	0	0	0
				st	49	49	49
				ω1	1	1	1
				ω2	1	1	1
			CIN	pt	120	120	120
				nt	0	0	0
				st	49	49	49
				ω1	1	1	1
				ω2	1	1	1
			trials		20	20	20
			cycles per trial		4	4	4

Figure 13. Circuit configuration for model 5.

All configurations contain the five regions "arousal sensory input" (AIN), "nucleus gigantocellularis" (NGC), "limbic system" (LIS), "motor circuit" (MCR), and "output onto spinal central pattern generator" (CIN). The regions AIN, LIS, MCR, and CIN contain 100 neurons each, while NGC is split into two groups, NGC_A and NGC_B with 50 neurons in each. Regions are connected by excitatory modulatory connections (→). NGC_A and NGC_B also have specific excitatory (→) and inhibitory (⊣) connections between random neurons within the same group (curved arrows). External stimulation (↯) was applied to AIN, LIS_1, and LIS_2, where applicable, during each set of simulations. ***a***, configuration for model 5.1. There is only one limbic stream (LIS_1 and MCR_1) projecting to CIN. ***b***, configuration for model 5.2. A second stream of limbic input (LIS_2 and MCR_2) has been added in parallel to the first limbic stream (LIS_1 and MCR_1). ***c***, configuration for model 5.3. Descending connections from NGC_B to CIN have been set to 0. ***d***, configuration for model 5.4. Ascending connections from NGC_A to MCR_1 and MCR_2 have been excluded. ***e***, configuration for model 5.5. The second limbic stream (LIS_2 and MCR_2) has been removed, and the ascending connection from NGC_A to MCR has been set to 0.

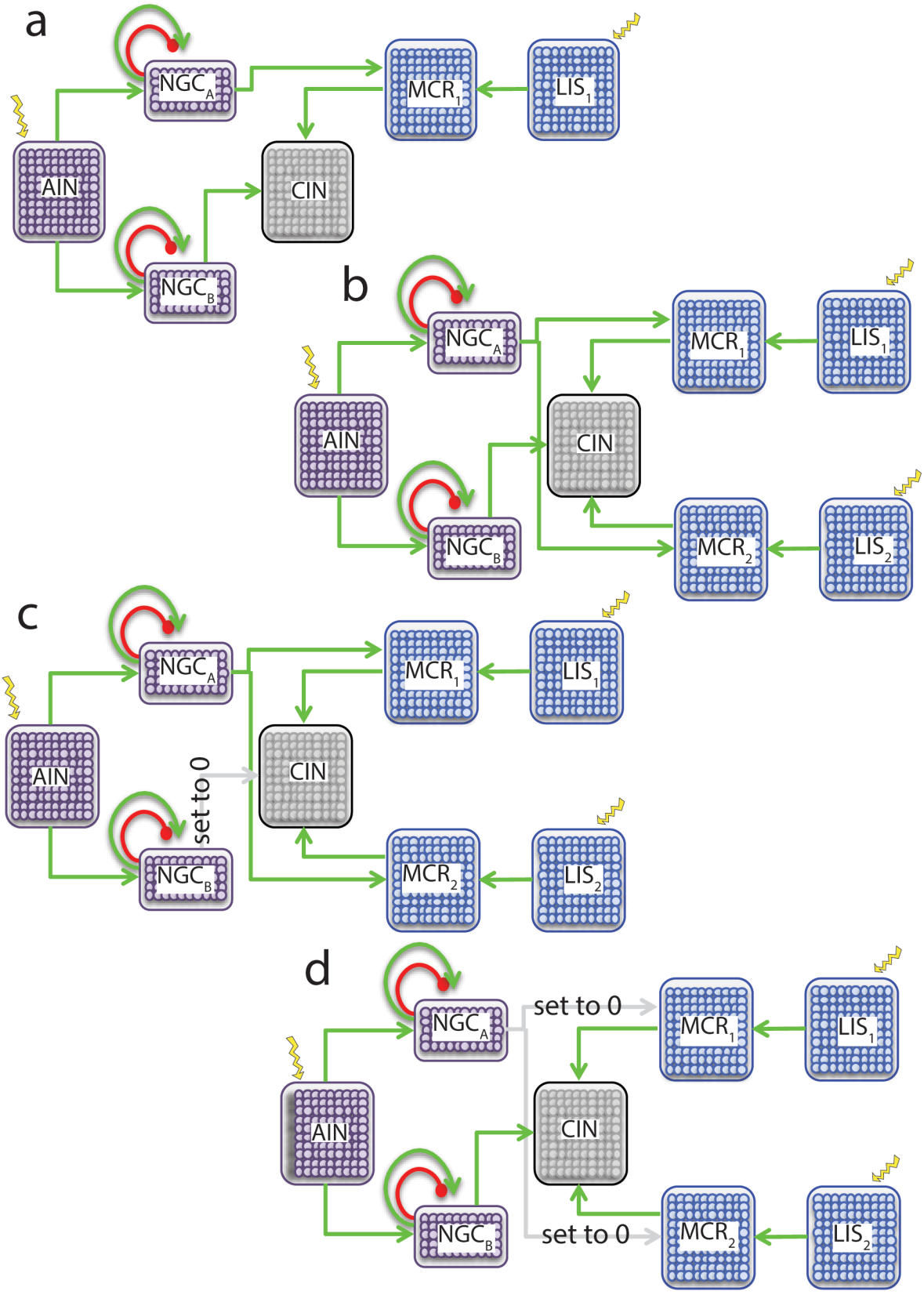
a
NGC_A
MCR_1
LIS_1
AIN
CIN
NGC_B
b
NGC_A
MCR_1
LIS_1
AIN
CIN
NGC_B
MCR_2
LIS_2
c
NGC_A
MCR_1
LIS_1
AIN
set to 0
CIN
NGC_B
MCR_2
LIS_2
d
NGC_A
set to 0
MCR_1
LIS_1
AIN
CIN
NGC_B
set to 0
MCR_2
LIS_2

2.9.2 Results

When we took the circuit from model 3.4 (figure 13a) and added a second set of limbic system inputs in the form of the regions LIS_2 and MCR_2 (figure 13b), this circuit lost much of its responsiveness to arousal (figure 14a,b), although times to first response remained low when limbic activity was high. When we further dissected the contributions of the ascending and descending NGC projections to the circuit's responses to increasing arousal, we found that getting rid of the ascending projection from NGC_A to MCR_1 and MCR_2 caused the circuit to lose its sensitivity to arousal entirely (figure 14c,d). All of these circuits retained broadly similar responses to limbic stimulation via LIS_1 and LIS_2 at high and low levels of arousal (figure 14e,f). Adding a second descending motor pathway did not appear to alter the circuit's overall relationship between arousal and CIN behavioral output at different levels of limbic activation, but it did decrease the dynamic range of the response, effectively muting the circuit's sensitivity to brainstem arousal (figure 14g-i).

2.9.3 Conclusions

These results show that adding a second cortico-spinal pathway strongly occludes the contributions of arousal to behavior when that pathway is active, as the balance of power is shifted in favor of limbic modulation. What little power the brainstem arousal machinery has over behavior is mediated through ascending projections of the NGC to corticolimbic areas. We observe that as the nervous system undergoes encephalization and becomes increasingly complex, the role that brainstem arousal circuits underlying basic survival instincts play proportionally shrinks during voluntary motor activities, allowing for greater flexibility in behavioral repertoires.

Figure 14. Results of simulations of model 5.

a-d overall landscapes of CIN response latencies to different combinations of tonic stimulation of LIS and AIN regions for the four variations on model 5. ***a***, baseline case where there is a single limbic stream to CIN (figure 13a), ***b***, a second limbic stream has been added in parallel to the first (figure 13b), ***c***, there are two limbic streams and the NGC only has ascending projections to both motor control regions (figure 13c), ***d***, the NGC only has descending projections to CIN (figure 13d).

e-i responses of each model to different amounts of LIS or AIN stimulation when stimulation to the other target is kept constant. ***e***, responses to LIS stimulation at low arousal (AIN input = 0), ***f***, responses to LIS stimulation when arousal is high (AIN input = 30 mV), ***g***, responses to AIN stimulation when limbic activity is low (LIS input = 0), ***h***, responses to AIN stimulation at intermediate limbic activity (LIS input = 12 mV), ***i***, responses to AIN stimulation when limbic activity is high (LIS input = 30mV).

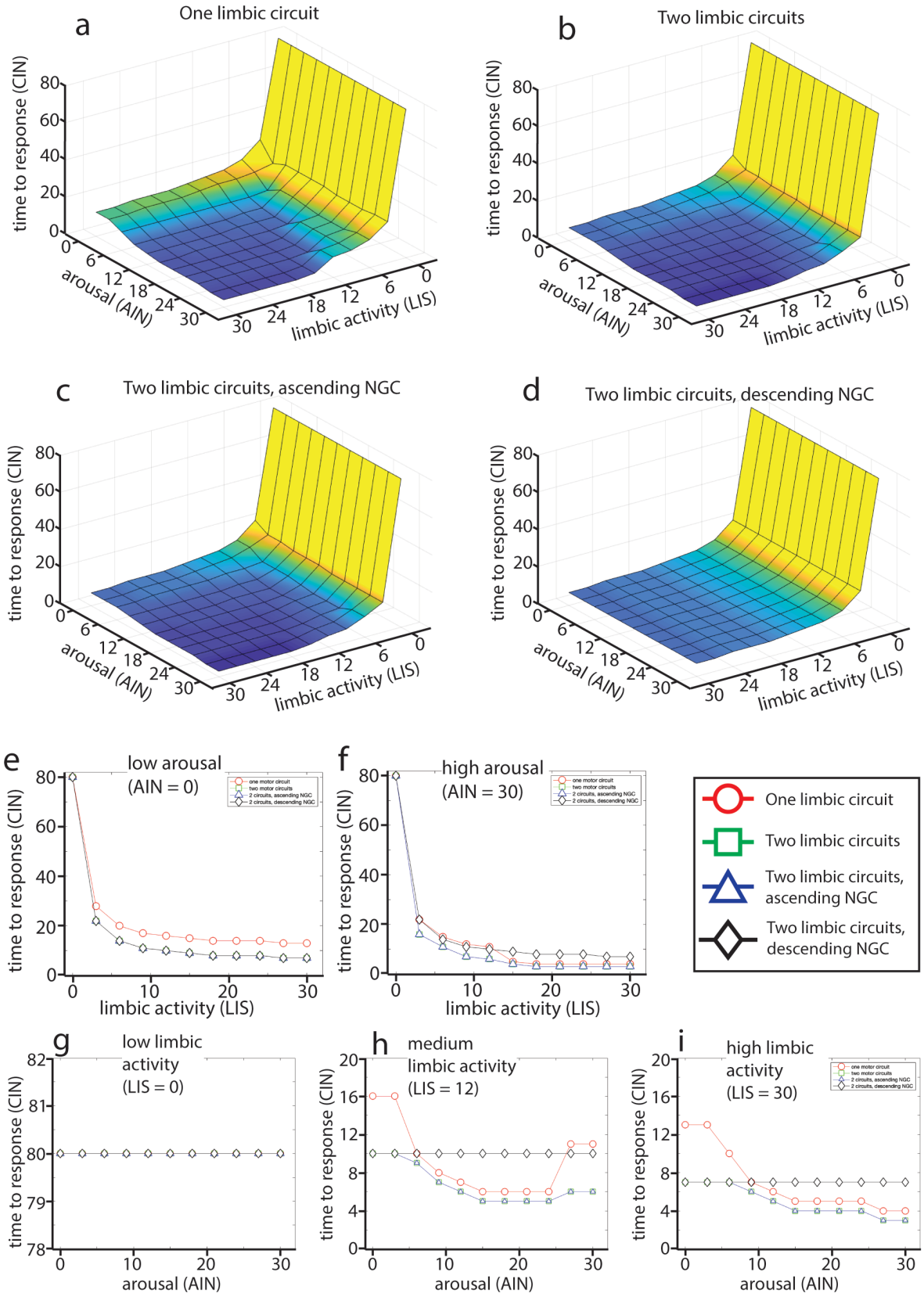
a
One limbic circuit
b
Two limbic circuits
c
Two limbic circuits, ascending NGC
d
Two limbic circuits, descending NGC
time to response (CIN)
arousal (AIN)
limbic activity (LIS)
e
low arousal
(AIN = 0)
f
high arousal
(AIN = 30)
limbic activity (LIS)
One limbic circuit
Two limbic circuits
Two limbic circuits, ascending NGC
Two limbic circuits, descending NGC
g
low limbic activity
(LIS = 0)
h
medium limbic activity
(LIS = 12)
i
high limbic activity
(LIS = 30)
arousal (AIN)

2.10 Discussion

In this series of computational modeling experiments, we sought to address the hypothesis that the structure of the generalized arousal circuit centered on the nucleus gigantocellularis (NGC) of the hindbrain reticular formation is optimized to yield maximum behavioral responses to arousing stimuli. This circuit optimization could take the form of decreasing the threshold for sensory stimulation required to yield a behavioral response or amplifying the level of behavioral activation induced by a given stimulus.

We emphasize that in setting up these models we had to achieve a balance between clearly defined abstract questions and devotion to real-world neuroanatomical details. For this preliminary approach to reticular formation and generalized arousal modeling we favored the former, but recognize that, as more and more labs encounter this subject, the broad set of issues we took on will be subdivided such that high-resolution neuroanatomy and biophysics can be taken into account.

We chose to focus on five features of the NGC arousal circuit and asked whether building models that incorporate these features yield better circuit responsiveness to arousing stimuli compared to models without them. These features included recurrent connectivity between the NGC and the midbrain Locus Coeruleus (LC), bifurcating axons within the NGC with simultaneously ascending and descending projections to distal parts of the nervous system, local connectivity among neighboring neurons within the NGC, specific input-output architecture in the NGC and the associated LC, and additional cortico-spinal pathways that project to the spinal cord in parallel to reticulospinal projections originating in the NGC.

Overall, we found that some of these features improved the performance of the arousal circuit in response to sensory stimuli, while others shifted the balance of power to favor the influence of cortico-limbic systems. In particular, when we modeled a version of NGC with

bifurcating projections, we observed a shift towards faster behavioral responses to the amount of sensory stimulation without a concurrent change in the absolute stimulus threshold for behavioral activation compared to similar models of an NGC with exclusively ascending or descending projections (figure 7e). Incorporating excitatory local connections within the NGC also yielded faster behavioral responses to arousing stimuli without altering the sensory threshold compared to models with inhibitory local connections, or no local connectivity at all (figure 9g,i). If the NGC is modeled as a homogeneous region that integrates all of its inputs together to generate a single activity value for its output, we observe improvements in both the speed of behavioral response to arousal and in the behavioral response threshold compared to models in which the NGC was divided into separate input-output streams (figure 12g).

By contrast, we found that adding recurrent connectivity between the NGC and LC yielded a circuit that lost much of its sensitivity to arousing stimuli, particularly at higher levels of limbic activity within the LC (figure 5d). Similarly, incorporating additional cortico-spinal pathways in parallel with the NGC reticulospinal pathway decreased the circuit's sensitivity to arousal (figure 14i).

In our models that incorporate recurrent NGC and LC connectivity or multiple cortico-spinal pathways, the resulting behavioral output of the circuit is increasingly influenced by limbic inputs. Cortico-limbic arousal circuits are generally associated with greater analytic and contextual processing of stimuli while more basal circuits generate automatic, stereotyped behaviors that sacrifice cognitive flexibility in favor of speed and robustness (Trofimova 2016). The evolutionary trend towards greater cognitive flexibility in higher vertebrates can be mirrored by the shift in generalized arousal circuits from the reticulospinal Mauthner cell in fish and amphibians that rapidly and efficiently drives the highly stereotyped C-start escape response when stimulated, to the bifurcating nucleus gigantocellularis in mammals that combines

reticulospinal projections with ascending connections to higher cortical areas associated with complex behavior.

On the other hand, the mammalian NGC retains some features that promote its arousing function. Having excitatory local connectivity within the NGC, for instance, led to faster behavioral responses to arousing stimuli in our models. Such a mixture of local connectivity between neighbors combined with long range axons that project widely to distal targets is characteristic of the reticular formation (Pfaff 2017), and studies of small-world networks with a combination of local and distal connections suggests that such a scheme improves signal propagation speed (Watts 1998). Within our models, this connectivity scheme has clear consequences for generalized arousal. While having excitatory local connections improves reactivity to arousal, increasing the proportion of local connections that are inhibitory decreases response times to arousing stimuli without changing the absolute threshold for response. This suggests that adjusting the synaptic weights of local connections within the NGC could be a potential mechanism for tuning an animal's sensitivity to arousing stimuli.

Our modeling also demonstrates that having an undifferentiated architecture within the NGC in which all inputs to this nucleus contribute to its arousal signal output yields improved arousal function over a variation of the NGC that has a defined input-output architecture. This suggests that the NGC's function as a sensory integrator is important for generalized arousal. Danger in the environment can take many forms, so an arousal signal needs to take all sensory modalities into account.

2.10.1 Outlook and Caveats

To our knowledge, this is the first attempt at computational modeling of generalized arousal circuitry. We confirm that certain features of the NGC are salient for this area's function as the neural substrate for generalized arousal. These models have in turn opened up a few

potential avenues for future experiments aimed at better understanding how generalized arousal functions in the brain. For instance, we identify a potential mechanism for tuning the magnitude of behavioral responses to arousal by modulating the ratio of excitatory and inhibitory synapses among local interneurons within and adjacent to the NGC. We propose future experiments aimed at first identifying the nature of local connectivity within the NGC and then using chemogenetic tools to modulate the strength of these synapses. We hypothesize that changing the strength of interneuron synapses within the NGC would have significant effects on arousal-associated behaviors that tune according to the degree of local inhibition and excitation.

Our modeling experiments also suggest that a lack of specific input-output architecture is important for NGC function. A number of viral genetic tracing tools have been used to great effect in tracing the relationship between neurons that project to the Locus Coeruleus and its subsequent targets to show that projections from the LC to specific areas typically originate from LC neurons that receive similar inputs (Schwarz 2015a,b). It would be interesting to employ such tools to determine whether the NGC also has topographic organization within its range of inputs and outputs. We hypothesize that since the primary role of the NGC is in the integration of many sensory inputs to generate a nonspecific generalized arousal signal that potentiates a wide range of behaviors, this nucleus should lack the sort of specific input-output architecture that has been identified within the LC.

Despite the fact that we derived some salient conclusions about arousal from our modeling efforts, these models cannot capture the full diversity and complexity of generalized arousal circuitries. We chose to focus exclusively on the NGC's projections to the spinal cord and Locus Coeruleus while ignoring the wealth of other projections it has to other thalamic and limbic areas, which may or may not be modulated in the same way. Also, all cells of each type had identical thresholds, decay parameters, and connection strengths. It would be interesting to

see whether small variations in these parameters within a region might provide enhanced specificity to different inputs. We also note that we used activation of the NGC's reticulospinal projections to the spinal cord in response to sensory stimulation as our readout of arousal-induced behavior. Increased sensitivity to sensory stimuli is one of the main features of a highly aroused state, but our models do not represent the effects of generalized arousal on emotional reactivity, another important arousal criterion.

Furthermore, our representation of inputs to the NGC as a single variable of stimulatory input to this entire region also does not capture the full complexity of this circuit. In addition to receiving information about the outside world from sensory areas and adjacent vasculature, the NGC is also a target of neuromodulator systems such as the orexinergic lateral hypothalamus and the noradrenergic Locus Coeruleus that play diverse roles in regulating and reporting behavioral state (Ennis 1988, Yang 2017). These inputs provide an important readout of the brain's current arousal state that may in turn affect the arousal signal output of the NGC.

In conclusion, the modeling experiments described in this chapter have laid a foundation for the study of generalized arousal both as a neuroanatomical, neurophysiological and control systems problem. Ultimately, our goal is to integrate neurobiological and behavioral data to build increasingly realistic models of generalized arousal in order to better understand how animals are able to select adaptive responses from a wide behavioral repertoire in the face of a changing and complex world.

These models have explored the concept that the strongest behavioral effects of generalized arousal are mediated by direct connections between the reticular formation NGC and the spinal cord. So, what are the physiological properties of the NGC neurons that constitute these reticulospinal projections? How do they drive behavior? And, how are these neurons integrated within the larger context of behavioral arousal systems? We aim to address these

questions in the following chapters using *in vitro* methods to construct a reticulospinal circuit in a dish and *in vivo* methods to quantify the dynamics of the behavioral changes associated with the transition from a low to a high arousal state.

Chapter 3. Behavioral Arousal Systems

3.1 Review of behavioral arousal systems

In life, generalized arousal (GA) systems as we know them contribute to nearly all motivated behaviors. This means that the neuronal substrate for GA both contacts and is a target of the many neuromodulator systems that regulate different aspects of behavioral arousal, including sleep/wake regulation, attention, feeding, sexual behaviors, aggression, and fear responses. Due to the fundamental nature of the behaviors they regulate, there is a great deal of redundancy and connectivity between these arousal neuromodulator systems. Here, we review some of the major arousal neuromodulators, their patterns of innervation, and implications for behavior.

3.1.1 Norepinephrine

The Locus Coeruleus (LC) is the nexus of the noradrenergic system in the central nervous system, providing the vast majority of norepinephrine to diffuse areas throughout the brain. This relatively small nucleus of the midbrain contains only a few thousand neurons but receives a diverse array of afferent inputs from other brain regions including the nucleus gigantocellularis (NGC) of the medullary reticular formation and its neighbor, the nucleus paragigantocellularis, as well as the central nucleus of the amygdala, the vagus nerve by way of the solitary tract, and the prefrontal cortex. Of these afferents, the NGC provides the majority of excitatory input to the LC. There is evidence that parallel NGC inputs to the LC and autonomic nervous system mediate the behavioral orienting response in response to arousing stimuli. Acute stressors also activate the LC, and chronic stress has been found to strengthen the connections between the amygdala and LC (Sara 2012). Although the LC only receives sparse input from the forebrain, the positive feedback loop established by reciprocal connections between these areas has been implicated in mediating the gain modulation of sensory-evoked responses in various sensory cortices (Berridge 2003).

Noradrenergic neurons originating in the LC innervate a variety of brain regions associated with neurmodulation and behavioral arousal, including the cerebral cortex, spinal cord, thalamus, hypothalamus, and basal forebrain (Jones 2003). There is a large body of literature detailing the role of norepinephrine in the forebrain and how it influences attention and arousal. LC activation is associated with the expectation of an unpredictable stimulus and phasic LC activation promotes reorganization of behavioral circuits in the forebrain that promotes switching between tasks (Zitnik 2015). Tonic adrenergic input, on the other hand, is associated with a distractible state. This firing pattern is often activated when the utility of the current behavior drops, thus facilitating a switch to an alternate, more rewarding task (Aston-Jones 2005). Such reward-based calculations have been shown to be mediated in part by inputs to the LC from the anterior cingulate and orbitofrontal cortices. The LC also projects to the ventro-medial hypothalamus (VMH), a region associated with the lordosis circuit (Devidze 2006). Noradrenergic signaling mediated by α1B adrenergic receptors in the VMH is estrogen-dependent, thereby gating the expression of lordosis behaviors (Lee 2006). There is also evidence that in addition to receiving dense innervations from NGC, LC also has reciprocal projections to this brainstem arousal nucleus (Jones 1985, McBride 1976). Thus, the diverse projections of the noradrenergic system are implicated in a wide array of arousal-related behaviors.

Optogenetic stimulation of all noradrenergic neurons of the LC is sufficient to drive a sleep to wake transition in mice, while high frequency stimulation in awake animals causes reversible behavioral arrest (Carter 2010). But although the LC was initially thought to be a largely homogeneous structure, an increasing body of evidence suggests that it contains a surprisingly large degree of internal organization. Retroviral tracing studies of the relationship between LC afferent and efferent projections reveals a modular structure of LC microcircuits

(Schwarz 2015a,b). These different LC microcircuits appear to have distinct behavioral functions. For instance, LC efferents to the basal/lateral nuclei of the amygdala are selectively activated during the acquisition of a fear conditioning response, while efferents to the infralimbic region of the medial pre-frontal cortex are more active during fear extinction after conditioning. However, both of these circuits are activated indiscriminately with a sufficiently strong unconditioned shock stimulus (Uematsu 2017). This suggests that the Locus Coeruleus has a much more complex function that toggles between a discrete patterned coding mode that mediates emotional learning and a more generalized "broadcast" mode that mediates generalized arousal depending on the behavioral context.

3.1.2 Dopamine

Neurons producing the neuromodulator dopamine reside primarily in the A11 nucleus of the dorsal hypothalamus, the ventral tegmental area (VTA), and substantia nigra pars compacta (SNc). The ventral mesencephalic dopamine system, consisting of the VTA and SNc, plays a pivotal role in motivation, reward, learning, and locomotor control. Stimulation of these mesencephalic nuclei promotes behavioral arousal and attention, and exploratory behaviors associated with rewarding stimuli (Jones 2003). This dopaminergic circuit is central to the incentive salience model of motivation behavior. According to this model, separate circuits are responsible for encoding "wanting" versus "liking" of a reward. Certain addictive drugs are known to specifically sensitize the "wanting" circuits while desensitizing "liking" circuits by the incentive sensitization model of addiction. Stimulating inputs to the dopaminergic VTA from the lateral hypothalamus increases reward seeking without altering the hedonic value of the reward, a key feature of the hypothesized "wanting" circuit (Berridge 2003)

Dopaminergic neurons in the VTA and SNc perform this incentive salience computation by encoding the mismatch between expectation and reward. This is done by a two-part response

wherein a reward-predicting cue elicits a non-specific short latency response, followed by a second response upon reward presentation. The firing rate increases for rewards that are greater than expected and decreases for rewards that are less than expected or fail to arrive at all. Such mismatch between expectation and results is a primary driver of reward-based learning (Schultz 1996). Thus, dopaminergic signaling encodes the economic utility of a reward by integrating information about homeostatic need, satiety, risk, and effort (Schultz 2017). The wide-ranging inputs required to generate accurate reward value assessments are reflected in the diverse afferents and efferents of the VTA and SNc.

Although there is a great amount of overlap between the afferents of the SNc and VTA, the SNc preferentially receives inputs from somatosensory and motor cortices, subthalamic nuclei, and the autonomic nervous system (ANS). This is consistent with the SNc's short latency responses to appetitive and aversive stimuli, while ANS inputs provide information about the state of the periphery. The VTA, on the other hand, gets strong inputs from the lateral hypothalamus, which plays a role in coding for stimulus value (Watabe-Uchida 2012). Within the VTA, GABAergic and dopaminergic neurons have slightly different wiring patterns consistent with their distinct patterns of activation and behavioral effects. While dopaminergic VTA neurons are innervated by orexin, oxytocin, and vasopressin-releasing neurons on the lateral and paraventricular hypothalamus, GABAergic VTA neurons get preferential inputs from the anterior cortex and central nucleus of the amygdala (Beier 2015). This is consistent with the GABAergic VTA's role in conditioned place aversion (Tan 2012).

Dopaminergic afferents to the nucleus accumbens are a well-characterized aspect of the incentive salience reward circuit (Berridge 2003). But this system also plays a role in motor action selection by way of ascending projections to "planning" areas of the prefrontal cortex. These targets are generally distinct from those innervated by noradrenergic neurons and are

thought to suppress the scanning attention state in favor of action selection (Tromifova 2016). The VTA and SNc are also known to project to brainstem motor areas to affect locomotor activity more directly. For instance, SNc projections to the pedunculopontine nucleus act to suppress muscle tone (Kim 2017). The VTA and SNc are also both known to project to the mesencephalic locomotor region (MLR) and increase the excitability of motor circuits. Notably, these descending projections are much more prominent in lampreys and other lower vertebrates, while in mammals an increasing fraction of VTA and SNc neurons project to striatal areas, likely reflecting the expanded role of cortical areas in the control of locomotion (Ryczko 2016).

Dopamine also has an important role in regulating the rhythmic activation of spinal central pattern generators, as low concentrations increase locomotor rhythm while progressively higher concentrations decrease and finally halt locomotor output altogether. In this case, the predominant source of spinal dopamine is actually the A11 nucleus of the dorsal hypothalamus, which is distinct from the mesencephalic circuit (Sharples 2014). One of the prominent inputs to A11 comes from the suprachiasmatic nucleus, thus providing a mechanism of circadian control over locomotion.

In addition to its role in motivation and reward, the mesencephalic dopamine circuit is also associated with behavioral arousal, although this role was obfuscated for many years by the finding that the firing rates of dopaminergic nuclei did not correlate with sleep and wake states (Trulson 1981). This led to the widespread belief that the dopaminergic system is only involved in mediating behavioral arousal and has no effect on wakefulness (Saper 2010). However, more recent evidence indicates that the dopaminergic system is more involved in arousal than previously thought.

The mesencephalic dopamine nuclei have reciprocal connections to many brainstem nuclei associated with arousal, including the dorsal raphe, locus coeruleus, pedunculopontine and

laterodorsal tegmental nuclei, the tuberomammillary nucleus of the posterior hypothalamus, and the lateral hypothalamus (Monti 2007, Taylor 2016). Furthermore, many drugs that promote wakefulness are known to have an effect on the dopaminergic system. For instance, an amphetamine-like drug used to treat excessive daytime sleepiness in narcolepsy patients increases extracellular dopamine (Wisor 2001). Systemic application of D_1 receptor agonist induces behavioral arousal while reducing REM and slow wave sleep duration (Monti 2007).

Optogenetic stimulation of dopaminergic neurons of the VTA is sufficient to wake up mice under isofluorane anesthesia (Taylor 2016). Chemogenic silencing of the VTA, on the other hand, suppresses wakefulness even when the animal is in the presence of salient stimuli (Ebon-Rothschild 2016). This pharmacological manipulation also promotes nest-building behavior prior to sleep, which suggests that it affects sleep circuitry on a more executive level. Increases in VTA-DA neuron Ca^{2+} activity immediately preceded transitions from NREM to REM sleep or waking states, while decreases in activity precede the wake to NREM sleep transition (Eban-Rothschild 2016). VTA projections to the nucleus accumbens (NAc) appear to be most instrumental in the dopaminergic control of long-term arousal. Lesions to the shell of the nucleus accumbens have been found to increase arousal and disrupt sleep (Qiu 2012).

Thus, given their role in reward and arousal, mesencephalic dopamine circuits have been hypothesized to integrate motivation information in order to determine the appropriate arousal level to allocate.

3.1.3 Serotonin

Serotonergic neurons primarily reside in the medial and dorsal raphe nuclei. These regions receive innervation from the hypothalamus, cerebral cortex, basal ganglia, midbrain, and striatum and in turn project reciprocally to many of these same areas (Steckler 1995, Dorocic 2014, Hasegawa 2017). Serotonin signaling has been implicated in a wide variety of behaviors

including feeding, sex (Haensel 1991), aggression (Ferrari 2003), thermoregulation, endocrine regulation, motor activity (Sharples 2014), pain modulation, learning and memory (Koscis 2006), and mood. Given serotonin's widespread influences, drugs regulating neuronal serotonin levels have emerged as important players in the psychopharmacology field (Olivier 2015).

Reward processing areas such as the VTA and NAc number among the more prominent afferents of the dorsal raphe. Serotonergic dorsal raphe neurons themselves appear to encode rewarding stimuli. These cells fire in response to rewarding stimuli and remain silent in the presence of aversive stimuli (Li 2016) and optogenetic stimulation of this population has been found to be rewarding across a variety of tasks (Liu 2014). Dorsal raphe neurons fire tonically upon the presentation of a reward-predicting cue and continue to do so until the reward is finally presented (Li 2016). Thus, the serotonergic system appears to encode different aspects of reward from the dopaminergic system and these neurons may promote patience in waiting for expected rewards.

Dorsal raphe activity has also been correlated with sleep/wake states, as these neurons are most active during waking, less so during slow-wave sleep, and are silent during REM sleep (Jones 2003). Lesions of the raphe cause sleep loss in cats that can be remedied by systemic serotonin doses (Portas 2000). The dorsal raphe innervates REM sleep producing areas including the pendunculopontine tegmental nucleus and mesencephalic tegmentum, and serotonin levels in these areas have been found to correlate with sleep/wake state, suggesting the serotonin may play a role in inhibiting REM sleep. Direct injections of serotonin into the cholinergic nucleus basalis decrease the gamma-EEG and overall REM sleep levels without altering the amount of waking or slow wave sleep, which suggests that serotonin plays more a supportive role in sleep by modulating cholinergic circuits (Cape 1998). Orexinergic projections to the dorsal raphe have

also been found to suppress cataplexy in an orexin receptor-deficiency model of narcolepsy by way of raphe projections to the amygdala (Hasegawa 2014, Hasegawa 2017).

Serotonergic activity is generally associated with a quiet and satiated waking state (Jones 2003). Systemic depletion of serotonin using P-chlorophenylalanine (PCPA) reduces rhythmic slow wave activity in the hippocampus and low-voltage fast-wave activity in the cerebral cortex that are associated with an aroused state. However, these effects were only apparent when serotonin depletion was paired with cholinergic inhibition by atropine injection (Vanderwolf 1986). Indeed, the role of serotonin in arousal is relatively modest compared to other major neuromodulators like acetylcholine and norepinephrine. It appears that serotonin may primarily affect behavioral arousal by modulating cholinergic activity (Steckler 1995, Cape 1998).

3.1.4 Acetylcholine

The cholinergic system is closely associated with cortical activation and arousal. The two primary sources of cholinergic neurons in the central nervous system are the ponto-mesencephalic tegmentum and the basal forebrain. Ponto-mesencephalic cholinergic neurons are located within the laterodorsal tegmental and pedunculopontine tegmental nuclei of the reticular formation and their long dendrites constitute one of the major ascending pathways of the reticular activating system. These neurons project to a number of midbrain and forebrain nuclei including the substantia nigra, thalamus, hypothalamus, basal forebrain, and medial prefrontal cortex (Steckler 1995). Descending ponto-mesencephalic projections are also known to contact spinal and reticulospinal systems involved in REM sleep. Consistent with their neuroanatomy, stimulation of ponto-mesencephalic cholinergic neurons is associated with increases in cortical and thalamic activation and these neurons are known to be most active during states of wakefulness or REM sleep (Jones 2003).

The cholinergic basal forebrain acts as an extrathalamic relay between the brainstem and frontal cortex. Much like the ponto-mesencephalic system, it is known to suppress delta and slow wave sleep patterns in the forebrain and increase fast gamma and rhythmic theta EEG patterns associated with wakefulness. There is evidence that the role of the basal forebrain goes beyond merely potentiating cortical arousal, as this circuit is known to promote learning and memory, alter cognitive task accuracy, and act in concert with the dopaminergic system to reinforce rewarding behavior (Jones 2004). The basal forebrain receives inputs from brainstem and hypothalamic arousal systems and is known to respond to glutamate, dopamine, histamine, and orexins. The orexinergic lateral hypothalamus projects to the basal forebrain and the existence of reciprocal connections suggests that the basal forebrain may interact with the orexin system to promote arousal. But orexinergic dendrites contact only glutamatergic and GABAergic neurons in the basal forebrain, indicating that the relationship between the orexin and cholinergic systems is likely more complicated than just a positive feedback loop (Agostinelli 2016).

The basal forebrain contains a mixture of glutamatergic, GABAergic, and cholinergic neurons that each contribute differently to cortical arousal. $ChAT^+$ cholinergic, $VGluT2^+$ glutamatergic, and parvalbumin expressing (PV^+) GABAergic neuron activation promotes wakefulness in favor of slow wave sleep with varying degrees of efficacy. Somatostatin expressing (SOM^+) GABAergic neurons, on the other hand, promote slow wave sleep and exert an inhibitory effect on the other basal forebrain populations (Xu 2015).

Levels of acetylcholine (ACh) are tightly controlled among targets in the cortex, which suggests that the cholinergic circuits innervating these regions have segregated inputs and outputs. Indeed, there is some segregation of basal forebrain input-output relationships. For instance, inputs from various parts of caudate putamen (CPv) to the basal forebrain are topographically organized such that medial CPv inputs are targeted to orbitofrontal cortex while

caudal CPv inputs specifically target the amygdala. Such microcircuits are important for specific cognitive operations, while the more overlapping cholinergic circuits convey broader information about arousal state changes (Gielow 2017). The timing of ACh release into basal forebrain targets is also task dependent. Changes in tonic ACh levels in the cortex and hippocampus predict sleep to wake transitions while phasic ACh release in these regions is associated with performance on a working memory task (Ruivo 2017). These lines of evidence suggest a two-fold function of the cholinergic basal forebrain: that it regulates the overall level of cortical arousal while also targeting specific cortical regions associated with reward, learning and memory, and somatosensory feedback.

3.1.5 Histamine

The sole source of histamine in the brain is the tuberomammillary nucleus (TMN) of the posterior hypothalamus. This nucleus receives particularly dense innervation from the infralimbic cortex, lateral septum, preoptic nucleus, and adrenergic, noradrenergic, and serotonergic nuclei of the brain stem. In turn, some of the major targets of TMN projections include the cerebral cortex, amygdala, substantia nigra, and striatum, with other less dense but similarly notable projections to the hippocampus, thalamus, retina, and spinal cord (Haas 2003, Haas 2008).

Consistent with the diverse range of histaminergic TMN targets, histamine receptors are expressed widely throughout the brain and periphery. The family of histamine GPCRs includes four subtypes. H1 receptors are the target of classical antihistamines and mediate the excitatory effects of histamine throughout the central nervous system. H2 receptors yield similarly excitatory effects, though these generally serve to potentiate neuronal responses to other stimuli rather than histamine on its own. H3 receptors are autoreceptors found on histaminergic, glutamatergic, cholinergic, and adrenergic neurons that yield an inhibitory effect that restricts

neurotransmitter release. H4 receptors are primarily found in the peripheral nervous system and have limited expression in the central nervous system.

The identification of neurons within the posterior hypothalamus that are selective for different behavioral states provided some initial clues as to the role of the histamine system in arousal. So-called "REM-off" neurons in the posterior hypothalamus include histaminergic neurons of the TMN. These cells exhibit slow tonic firing during waking, which decreases in slow-wave sleep, and are completely silenced during REM sleep (Jin 1989, Steininger 1999). Histidine decarboxylase knockout mice, which cannot produce histamine, were shown to sleep more, have decreased cortical EEG power in the θ range, and a shorter sleep latency following behavioral stimulation than wild-type controls (Parmentier 2002). Optogenetic silencing of histaminergic neurons similarly promotes slow-wave sleep (Fujita 2012). Although histamine levels in the central nervous system vary across the circadian cycle, these levels were not affected by sleep deprivation, which suggests that the histaminergic system is involved in circadian sleep rather than homeostatic sleep drive (Strecker 2002).

Projections from the preoptic nucleus (POA) to the TMN have been especially implicated in regulating histamine's role in sleep/wake cycle control. Chung *et al* found that selective optogenetic stimulation of GABAergic POA→TMN neurons in mice increases the time spent in slow-wave and REM sleep, while silencing this same population has the opposite effect. On the other hand, stimulation of glutamatergic POA→TMN neurons promotes wakefulness. Of the $GABA^{POA\rightarrow TMN}$ neurons, certain subpopulations were found to express sleep promoting corticotrophin releasing hormone (CRH) and cholecystokinin (CCK), as well as Tac1, which encodes Substance P, and P_{dyn}, which encodes opioid peptides like dynorphin A. Selective stimulation of the CRH^{+} or CCK^{+} $GABA^{POA\rightarrow TMN}$ neurons increases slow-wave and REM sleep, while stimulation of the $Tac1^{+}$ or P_{dyn}^{+} neurons only promotes slow-wave sleep. These results

suggest that there are different subpopulations of $GABA^{POA \rightarrow TMN}$ neurons that are selective for REM versus slow-wave sleep (Chung 2017).

The TMN is also a major target of innervation from the neighboring orexinergic lateral hypothalamus (Haas 2008). These orexinergic projections are thought to stabilize sleep/wake states, and the application of orexin to the TMN has an excitatory effect on histaminergic neurons (Yamanaka 2003).

Injections of the $GABA_A$ receptor agonist muscimol to the posterior hypothalamus were also shown to increase slow-wave sleep (Lin 1989). A large proportion of histaminergic neurons co-express GAD enzymes, so GABAergic transmission likely plays a significant role in the histamine circuit's regulation of arousal. Yu *et al* found that siRNA knockdown of VGAT in histaminergic neurons resulted in increased wakefulness and hyperactivity. Optogenetic stimulation of histaminergic projections to medium spiny and pyramidal neurons induced G_{Tonic}, a hyperpolarizing current generated by the activation of $GABA_A$ receptors. These findings suggest a two-fold function of GABA co-transmission in the histamine system. First, that GABA serves as a brake to histamine circuit overactivation, and second that this neurotransmitter may sharpen cognitive responses via G_{Tonic}, which increases the stringency of the timing of coincident EPSPs required to drive cortical neuron responses (Xu 2015).

In addition to their well-documented role in the regulation of sleep, histamine circuits have also been implicated in the generation of motivated behaviors (Torrealba 2012). TMN activation is associated with animals waking up in anticipation of an expected meal, though it is independent of the presence or absence of food (Inzunza 2000). Histamine decarboxylase knockout mice also have decreased levels of novelty-induced arousal. It has been found that inputs from the infralimbic cortex to the TMN are essential for this appetitive function of the histaminergic system and that in turn histamine acts on the dopamine system to influence

motivated behavior. Selective histamine application to the nucleus accumbens increases exploratory behavior (Orofino 1999), whereas histamine in the ventral hippocampus decreases exploration and anxiety levels (Ruarte 1997). Furthermore, there is a negative correlation between histamine receptor ligand binding and apathy scores in patients with depression, schizophrenia, and Alzheimer's, though the detailed mechanistic links between these pathologies and histamine system dysfunction have yet to be fully explored (Torrealba 2012).

Histamine is also known to influence energy regulation, feeding, and sexual behaviors. There is strong histaminergic innervation of the hypothalamus and histamine mediates the effects of leptin on feeding (Morimoto 1999), though since histaminergic neurons do not express leptin receptors, this is thought to be indirectly regulated by α-MSH^{+} neurons, which project to the TMN (Fekete 2003). Histamine projections to the ventro-medial hypothalamus also play a role in controlling lordosis behavior in concert with norepinephrine and encephalin (Devidze 2006, Martin 2011). Thus, the histamine system serves as an important unifying component of many forms of behavioral arousal.

3.1.6 Orexin

Orexin A (OxA) and Orexin B (OxB), also known as hypocretin 1 and 2 respectively, were first identified as a pair of neuropeptides produced in the hypothalamus that have a generally neuroexcitatory effect and promote feeding behavior (DeLecea 1998, Sakurai 1998). Since their discovery, the central role of orexins in regulating behavioral arousal has been further elucidated. OxA and OxB are processed from the same precursor, prepro-orexin and activate a pair of related G-protein coupled receptors. Orexinergic neurons are located adjacent to the fornix at premammillary levels of the hypothalamus and project to other arousal related neuromodulatory circuits including noradrenergic, cholinergic, and histaminergic nuclei (Jones 2003). This neuroanatomical connectivity pattern hints at orexin's role in modifying other

arousal circuits and lowering the arousal threshold for a variety of behaviors, including locomotion, energy balance and reward seeking, sleep, narcolepsy, and emotional learning.

Orexin circuit activation is closely associated with locomotor behaviors. Blocking OxA receptors throughout the brain results in a hypoactive phenotype (Kim 2017). Neurons in the mesencephalic locomotor region (MLR) express orexin receptors (Sherman 2015). Orexin neurons in the lateral hypothalamus have also been found to stimulate neighboring $GAD65^{+}$ neurons, which show bursts activity prior with running bouts (Kosse 2017).

Much like the OxA receptor block, ablating orexin neurons blocks the increased wakefulness and motor activity brought on by fasting. Applying a dopamine antagonist similarly attenuates these orexin or fasting-induced behavioral changes, suggesting a role for an orexin-dopamine circuit in energy balance. Glucose and leptin have been found to inhibit orexin neurons, while ghrelin exerts an excitatory effect (Yamanaka 2003). Furthermore, the lateral hypothalamus receives innervation from the arcuate nucleus, which contacts the blood-brain barrier and provides a potential route whereby bloodstream metabolic factors could affect the orexin circuit (Elias 1998). Orexin neurons in the lateral hypothalamus are intermingled with melanin concentrating hormone (MCH) producing neurons and there is some evidence of cross-talk between these two populations (Adamantidis 2008). MCH deficiency causes leanness and increases metabolic rate. However, orexin neuron ablation results in only modest decreases in food intake, likely since orexin mediates arousal afferents on feeding circuits, which increase the likelihood of a behavior without directly driving it. Orexinergic projections to the nucleus accumbens, ventral tegmental area, and prefrontal cortex also imply a role in for this neuromodulator in driving drug-seeking behavior (Boutrel 2005).

Perhaps the most well studied aspect of the orexin circuit is its role in sleep and subsequent dysfunction in narcolepsy. Intracerebroventricular injection of OxA during the

natural sleep phase in rats results in increased arousal 2 to 3 hours later (Piper 2000). Orexin neurons in the dorsomedial hypothalamus receive innervation from the suprachiasmatic nucleus and the strong downstream orexinergic innervation of the locus coeruleus has been shown to mediate circadian activity in this area (Gompf 2008). Applying OxA directly to the locus coeruleus suppresses REM sleep while increasing wakefulness (Bourgin 2000).

Narcolepsy type 1 is associated with a progressive loss of orexin neurons that leads to dysregulation of sleep/wake cycles and cataplexy, the sudden loss of muscle tone brought on by extreme positive emotion. Loss of orexin inputs to the locus coeruleus is implicated in mediating the sleep/wake deficiencies associated with this condition. Restoring OxA receptor expression in noradrenergic neurons of the LC in a mouse model of narcolepsy markedly increases waking episode duration. In parallel, restoring OxB receptor expression in the serotonergic dorsal raphe nucleus prevents cataplexy-like episodes without altering sleep/wake balance in narcoleptic mice (Hasegawa 2014). These dorsal raphe neurons project to and inhibit the lateral/basolateral amygdala in normal conditions to prevent cataplexy (Hasegawa 2017).

Orexin inputs to the locus coeruleus have also been implicated in a fear conditioning circuit by way of adrenergic projections to the lateral amygdala. Stimulating this circuit prior to administering a conditioned fear paradigm has been found to strengthen aversive memory formation (Sears 2013). Since the locus coeruleus is one of the major afferents of the orexin circuit and is itself the nexus of the noradrenergic circuit, it is likely that orexin modulates a number of other behaviors associated with this nucleus, the breadth of which is still not fully appreciated.

Due to its myriad of projections to other neuromodulatory systems, it has been suggested that rather than mediating behavioral arousal directly, orexin acts as an “alarm” that can lower the arousal threshold for other systems. Notably, orexin cells appear to project selectively to

noradrenergic locus coeruleus neurons that in turn project to the medial prefrontal cortex, suggesting a potential role in gain modulation of sensory evoked cortical responses. Also, OxA receptors have been found in the medullary nucleus gigantocellularis, a region strongly associated with the behavioral orienting response (Yang 2017). These neuroanatomical and behavioral findings establish orexin as an important part of arousal neurocircuitry that binds together disparate neuromodulatory systems.

3.2 Reticulospinal circuits

The effects of the aforementioned arousal neuromodulator systems on behavioral expression are gated by the reticulospinal system, which originates in the brainstem reticular formation and sends motor commands to the spinal cord. Since the central pattern generator circuits in the spinal cord are only capable of the most basic instantiation of motor programs, much of the information regarding action selection and start and stop signals is relayed via this tract.

The importance of glutamatergic efferents from the brainstem in motor control has been amply demonstrated by ex-vivo brainstem-spinal cord preparations in rodents that maintain a locomotor-like pattern of dorsal root activation but lose this rhythmicity when the connection to the brainstem is severed (Smith 1987). The brainstem locomotor control system originates in the mesencephalic locomotor region (MLR), which sits at the juncture between the midbrain and hindbrain and continues through the reticular formation to contact spinal central pattern generator circuits to induce and regulate locomotion. These circuits are perhaps best understood in the lamprey, but they are highly conserved across all vertebrates, including mammals.

Repetitive motor programs such as walking and swimming are executed by spinal central pattern generators (CPGs), networks of reciprocally connected excitatory and inhibitory interneurons that produce rhythmic activation of motor neuron pools. These CPGs can

themselves adapt directly to perturbations relayed to them by sensory feedback signals, but generally do not exert sophisticated control over locomotion. Reticulospinal neurons originating in the hindbrain reticular formation provide the principle glutamatergic excitatory drive to these spinal CPGs. These neurons integrate postural information from vestibular nuclei and locomotor drive signals from the mesencephalic and diencephalic locomotor regions in order to initiate, halt, and control the speed of locomotion.

Upstream of the reticular system, the midbrain mesencephalic locomotor region (MLR) integrates inputs from forebrain and limbic motor areas to elicit goal-directed locomotion. MLR neurons do not directly contact the spinal cord, and thus require reticulospinal neurons to relay their signals to spinal CPGs. In order to prevent inappropriate movements, the MLR is kept tonically inhibited by the pallidum. A motor action can only be initiated if this inhibition is lifted by the striatum, which has electrophysiological properties that lend it a high activation threshold and therefore acts as a filter for cortical and thalamic inputs. Dopamine plays a key role in modulating the threshold of striatal neurons. When dopamine levels are too low, as in Parkinson's disease, it can become difficult to initiate any sort of voluntary movements, whereas excess dopamine can lead to hyperkinesia. Further upstream, the basal ganglia and the thalamus are required for goal-directed movement. Decerebrate cats and rabbits may retain relatively complex behaviors, including orienting towards a stimulus, seeking out food, and displaying sham rage as long as innervation from these two regions remains intact (Grillner 2008).

3.2.1 The Mesencephalic Locomotor Region

The mesencephalic locomotor region (MLR) sits at the juncture between the midbrain and the hindbrain and is a particularly important hub in the reticulospinal system. This region integrates inputs from the central nervous system and periphery to elicit goal-directed movement. This information is relayed to reticulospinal neurons as a graded signal to generate a variety of

speeds (Dubuc 2008). The MLR is split into two major nuclei, the pedunculopontine nucleus (PPN) and the cuneiform nucleus (CnF). Glutamatergic neurons of the CnF promote escape behavior (Caggiano 2018). Optogenetic stimulation of this region is sufficient to initiate locomotion at a wide variety of speeds depending on the frequency of stimulation (Josset 2018). The PPN, on the other hand, appears to be more involved in exploratory behaviors. Stimulation of this region can initiate locomotion but does not allow the animal to attain high speeds (Caggiano 2018). Both of these nuclei project to brainstem reticulospinal neurons, though the CnF also projects to the PPN.

3.2.2 Brainstem Reticulospinal Neurons

The MLR relays locomotor signals to the spinal cord via glutamatergic reticulospinal neurons in the medial reticular formation. Through retrograde tracing, spinally-projecting neurons have been identified in the medullary gigantocellular nucleus, lateral paragigantocellular nucleus, intermediate trigeminal nucleus, and the spinal trigeminal nucleus (Ouleghani 2018). These reticulospinal neurons do not just passively relay information from the MLR, they themselves can induce rapid escape in response to direct sensory feedback. There has been much focus recently on identifying the particular populations of reticulospinal neurons involved in the initiation and cessation of movement in lampreys, fish, and rodents.

In the lamprey, Muller and Mauthner cells act as command neurons that initiate locomotion, especially rapid escape responses that bypass the MLR (Korn 2005). Mauthner cell activation has been found to be necessary and sufficient to induce the C-start escape response in fish and these neurons are considered to be an evolutionary precursor to the mammalian medullary gigantocellular nucleus (Pfaff 2006).

Within the hindbrain of higher vertebrates, excitatory V2a interneurons have been implicated in the initiation of locomotion. This class of neurons, which expresses the

transcription factors Chx10 and Lhx3, are found throughout the spinal cord as well as the rostral and caudal hindbrain. In zebrafish, optogenetic stimulation of hindbrain V2a neurons initiates naturalistic swimming while their inactivation halts ongoing swimming bouts. These V2a hindbrain neurons exist as two separate populations. The "small" V2a reticulospinal neurons found in the caudal hindbrain provide tonic excitation to locomotor circuits and the rostral hindbrain; these neurons do not fire rhythmically. Larger "magnocellular" V2a neurons in the medial hindbrain do fire rhythmically in time with the ventral root burst and are proposed to play an integral role in patterning rhythmic swimming circuits (Kimura 2013). In developing *Xenopus* tadpoles, Soffe *et al* identified an analogous population of excitatory dorsal interneurons (dINs) extending from the spinal cord to the hindbrain. The most rostral portion of this population is localized to the $Chx10^{+}$ dorsal hindbrain and drives sensory-evoked swimming bouts in a rhythmic fashion. Spikes from these dINs precede each cycle of swimming circuit neuron activity in a manner consistent with driving rhythmic activity (Soffe 2009, Li 2019).

In mammals, hindbrain V2a neurons are localized within and adjacent to the lateral paragigantocellular nucleus (LPGi), an area that when stimulated produces naturalistic locomotion in mice (Capelli 2017). V2a neurons were found to express cFOS following bouts of locomotor activity in a manner consistent with their role in the initiation of locomotion (Bretzner 2013). These neurons also undergo an increase in calcium activity in response to stimulation of the CnF of the MLR, and a mixture of excitatory and inhibitory calcium responses to stimulation of the PPN of the MLR. Developmental ablation of these neurons results in irregular respiratory rhythms in newborn mice, again consistent with their role in rhythm generation in fish (Crone 2012). However, optogenetic stimulation of hindbrain V2a neurons halts ongoing bouts of locomotion and their inactivation decreases spontaneous stopping (Bouvier 2015). So, the role of

V2a neurons in the mammalian system appears to also include a “stop” function in addition to providing rhythmic drive to CPGs.

Other reticulospinal neurons have been identified in the lamprey and mouse that halt locomotion. A subset of neurons within the lamprey MLR project to downstream reticulospinal “stop” neurons within the medial rhombencephalic reticular nucleus (MRRN). Stimulation of either these MLR neurons or their MRRN targets is sufficient to halt ongoing locomotion (Juvin 2016, Gratsch 2019). The MRRN “stop” neurons are thought to be analogous to the mammalian V2a “stop” neurons. In rodents, inhibitory GABAergic and glycine-ergic neurons of the LPGi also appear to play a role in halting locomotion (Capelli 2017). These neurons have only local projections within the LPGi, and so are likely to function by inhibiting their excitatory neighbors that drive locomotion.

Reticulospinal neurons are also known to be important for the acoustic startle response, a behavioral arrest and fast muscle twitch reflex in response to a loud auditory stimulus that prepares an animal for a potential fight or flight response (Koch 1999). This seemingly simple behavior integrates a wide variety of sensory, brain state, and learning information to modulate response sensitivity and amplitude. Giant neurons of the caudal pontine reticular nucleus, including V2a neurons have been implicated in this response, suggesting yet another role for V2a stop neurons (Kim 2017).

3.2.3 Neuromodulators and motor control

Although the reticulospinal system is primarily glutamatergic, several neuromodulators are known to exert effects on the spinal cord and hindbrain motor circuitry. These include dopamine, serotonin, norepinephrine, and orexin.

Dopamine in the basal ganglia plays a critical modulatory role on the excitability of the striatum and subsequent disinhibition of the MLR to initiate movement (Ryczko 2016).

Additionally, dopaminergic neurons in the A11 nucleus of the posterior hypothalamus innervate the spinal cord and modulate CPG activity. This spinal dopamine is required for the stable bursting activity of HB9-expressing motor neurons. Furthermore, the A11 nucleus receives innervation from the suprachiasmatic nucleus, suggesting some circadian regulation of dopamine in the spinal cord (Kim 2017, Sharples 2014).

Serotonin (5HT) is one of the classical agents used to induce fictive locomotion in isolated rodent spinal cord preparations. Descending serotonergic input to the spinal cord originates in the parapyramidal region of the medulla, which includes the LPGi. Different serotonin receptors play distinct roles in locomotion. $5HT_7$ receptor antagonists increase step cycle duration and disrupt locomotor rhythm generation, while $5HT_{2A}$ receptor antagonists reduce the amplitude of ventral root bursting without impacting the step cycle rhythm, suggesting that this receptor drives premotor and motor neurons directly (Jordan 2008).

Acetylcholine also plays a role in modulating locomotion. In the lamprey, cholinergic muscarinoceptive brainstem neurons receive inputs from the MLR in parallel with reticulospinal neurons. These neurons act as a positive feedback loop that amplifies and extends the duration of locomotion due to their delayed and sustained activation in response to the MLR (Smetana 2010). Within the rodent MLR, the pedunculopontine nucleus contains some cholinergic neurons that, when stimulated, increase locomotor rhythm, though they cannot initiate locomotion from rest (Josset 2018).

Norepinephrine is known to initiate and modulate locomotor activity and increase motor neuron excitability (Miles 2011, Tartas 2010). Noradrenergic projections to the spinal cord mostly originate from the A5, A6, and A7 nuclei of the brainstem (Miles 2011, Jordan 2008). Much like its role in the rest of the brain (Mather 2016), norepinephrine appears to amplify gain modulation in the spinal cord by enhancing motor neuron bistability (Conway 1988, Lee 1999),

and increasing the frequency dependence of short-term depression in synapses between sensory afferents and motor neurons (Barriere 2008). This neuromodulator also exerts its effects on locomotion at the brainstem level. Reticulospinal neurons have a broadly excitatory response to norepinephrine application (Hölsi 1970), while injection of norepinephrine to the reticular formation decreases reactivity to sensory stimuli without altering the sensory detection threshold (Grossman 1968).

Orexin neurons of the lateral hypothalamus innervate nearly all major motor control centers throughout the brain, including the motor cortex, brainstem, spinal cord, basal ganglia, and the cerebellum (Hu 2018). Orexin knockout mice have decreased levels of voluntary motor activity without showing deficits in initiation and speed. Among its varied roles, orexin appears to increase the excitability of voluntary motor circuits, integrate reward related information from the amygdala with descending locomotor control (Kim 2017), influence postural control by increasing the firing rate of dopamine neurons in the substantia nigra (Liu 2018), and tune cerebellar outputs to become more sensitive to sensory stimuli (Hu 2015). Orexinergic innervation of the brainstem has varied behavioral effects. Injection of orexin into the medullary gigantocellular nucleus results in hindlimb muscle atonia in decerebrate rats while improving sensitivity to external stimuli when injected into the lateral vestibular nucleus (Hu 2015). So, it appears that orexin modulation in the brainstem is state-dependent.

The high level of redundancy and overlap between these behavioral arousal systems in the intact nervous system makes it difficult to precisely dissect the individual contributions of cell types and their projections to overall circuit activity. Developmental ablation of specific components of the arousal circuit can have lethal effects or drive other systems alter their function in order to compensate for the disruption, resulting in a deceptively mild phenotype. To avoid this problem, we opted to take a bottom-up approach to the study of reticulospinal circuits

and generalized arousal by building a reticulospinal circuit in a dish with only the most fundamental components: reticulospinal NGC neurons, and spinal motor neurons. Our goal was to determine whether we could form a functional connection between these two cell types in the dish, and then use this *in vitro* platform to investigate how the NGC reticulospinal circuit interacts with other behavioral arousal systems by interrogating it with some of the aforementioned arousal neuromodulators, orexin and norepinephrine.

Chapter 4. Developing an *in vitro* Reticulospinal Circuit

4.1 Introduction

4.1.1 Building a reticulospinal circuit *in vitro*

In order to derive clinically relevant findings, most *in vitro* disease models seek to incorporate as realistic a mixture of cells from the modeled region as possible. Some of these models have been shown to develop complex patterns of activity similar to their *in vivo* counterparts (Trujillo 2018). To appreciate how the many components of these cultures give rise to such complex emergent properties, it is important to understand to what extent their patterns of activity are constrained by the properties of individual neuronal cell types, and how mixing different subpopulations of neurons might affect the activity of the network.

To create a simple system where we could address how molecularly defined subpopulations of neurons develop network activity, and how these subpopulations interact in co-culture, we selected two neuronal subtypes with a well-defined relationship in the intact nervous system, spinal motor neurons and reticulospinal neurons. Of the subtypes of reticulospinal neurons, we specifically focused on V2a excitatory interneurons expressing the transcription factor Ceh-10 Homeodomain-Containing Homolog (Chx10, also known as Visual System Homeobox 2, or Vsx2).

We hypothesized that the reticulospinal neurons cultured on multi-electrode arrays (MEA) would develop a different pattern of activity than motor neurons, which would be consistent with each subtype having a distinct behavioral role. Because *in vivo* motor neurons are partially controlled by reticulospinal neurons, we further hypothesized that the reticulospinal neurons' activity would come to dominate in a combined co-culture. This would support the idea that patterns observed in neuronal cultures *in vitro* are at least partially governed by cell type-specific electrical and biochemical properties, as opposed to being entirely driven by the relative ratios of excitatory and inhibitory cells.

Here, we report that Chx10$^+$ hindbrain neurons develop synchronized network bursts that differ from the diffuse, unsynchronized activity of motor neurons, and that in co-culture motor neurons are recruited into Chx10$^+$ neuron bursts. We interrogated these reticulospinal cultures with a panel of synaptic blockers and found that network bursts are mediated by an $AMPA_R$-dependent mechanism. We also identified divergent responses in motor and Chx10$^+$ neurons to the α_1 adrenoreceptor agonist L-phenylephrine and found that a subset of Chx10$^+$ neurons are modulated by the two orexin isoforms.

4.1.2 Multi electrode array studies

Multi-electrode arrays (MEAs), tissue culture dishes that integrate grids of dozens to hundreds of small planar extracellular electrodes, are a powerful method for *in vitro* neuroscience as they allow the long term, non-invasive, and simultaneous recording of dissociated neuronal cultures. This tool has been used to study the mechanisms of spike synchronization in cortical and hippocampal neuron networks (Wagenaar 2005, Esposti 2009, Maheswaranthan 2012, Lonardoni 2017), for high-throughput testing of the effects of toxins and therapeutic drugs on cell cultures (Clements 2014, Jenkinson 2017), and as a platform for the development of organotypic cultures that probe the interactions between multiple brain regions (Dauth 2017, Soscia 2017, Sarkar 2018).

One prominent feature of neurons cultured on MEAs is the emergence of regular bursts of high spiking activity that are coordinated across many, and often all, recorded channels. These so-called network bursts have been found to consistently arise in cultures taken from the mammalian cortex (Van Pelt 2005), hippocampus (Li 2007, Li 2009), amygdala (Dauth 2017), and spinal cord (Black 2017). Although cortical neurons *in vivo* are typically characterized by stochastic spike trains that can effectively encode a large amount of information (Shannon 1948), synchronized neuronal bursting has been found to be important in a number of contexts,

including during development as a way to drive activity-dependent pruning of synapses, during slow wave sleep (Schwartz 2015), in the visual cortex as a way to encode statistical regularities within visual stimuli (Vinck 2016), and between discrete cortical regions as a mechanism for the integration of sensory information (Engel 2001, Palva 2005, Singer 1999).

In vitro, neurons are thought to take on the network burst phenotype by default because they lack a source of external sensory input (Wagenaar 2005). Electrical stimulation of such cultures can disrupt the network from a sleep-like pattern of bursting, effectively causing the culture to temporarily "wake up" (Jewett 2015). Such stimulation has also been found to alter the rate of action potential propagation across the network with implications in the regulation of learning and memory (Bakkum 2008). These findings demonstrate that network bursts are not merely an artifact of *in vitro* culture conditions but in many cases reflect important processes of the intact nervous system.

Several groups have used the MEA platform to model interactions between different brain areas, primarily by co-culturing tissue fractions taken from the different regions of interest as spatially segregated populations on the same array. Tissue taken from the prefrontal cortex, hippocampus, and amygdala and cultured on MEAs developed region-specific spike waveforms and patterns of activity. These patterns changed when the different tissue types were co-cultured on a single array and they developed correlated activity that suggested that these regions could communicate with each other *in vitro* (Dauth 2017, Soscia 2017).

It is unclear whether the observed region-specific differences in these studies arose because of variations in the ratio of excitatory to inhibitory interneurons, which computational models have shown has a significant impact on network burst dynamics (Maheswaranathan 2012, Chiappalone 2006, Lonardoni 2017), or differences in the inherent properties of the cell types found within each region. In our reticulospinal cultures, we sought to answer this question

of whether two molecularly defined cell types would develop distinct patterns of network activity *in vitro* by employing rigorous methods for isolating each cell type of interest before culturing and co-culturing them on MEAs.

4.2 Methods

4.2.1 Cell culture

Primary cortical glia were dissected and dissociated using the protocol described in Schlidge *et al* (2013) from Swiss Webster mice at P1-4. Mouse pups were anesthetized on ice, then decapitated. The cortex was separated from the cerebellum and midbrain and the corpus callosum was severed, then the meningeal covering was peeled away. Cortical tissue was dissociated in 10% trypsin (0.25% EDTA, Gibco, 25200-056) and passed through a 35μm filter (Corning, 352235). Cells were cultured on 100mm cell culture dishes treated with 0.1% gelatin (ATCC, PCS-999-027) at a density of ~$5x10^4$ cells/cm^2 and grown at 37°C under standard tissue culture conditions until confluent, usually within 8 days. Glial culture media contained high glucose DMEM (Sigma-Aldrich, 21063-029), 10% heat inactivated fetal bovine serum (ATCC, SCRR-30-2020), and 1% penicillin/streptomycin/antimycotic (Sigma-Aldrich, A5955). Once the glia reached confluence, they were dissociated with trypsin and cultured on sterile 5mm no.1 glass coverslips (Warner, 640700) treated with 1mg/ml Poly-D-Lysine (Millipore, A-003-E) and 1mg/ml laminin (Corning, 354232) in 24-well plates at a density of $5x10^5$ cells/well. Neurons were seeded on this feeder layer of glia once it reached confluence, within about 8 days.

ES-cell derived motor neurons were generated using the protocol described in (Wichterle *et al*., 2002) from the HBG3 ES cell line in which the enhanced green fluorescent protein (eGFP) is expressed under the control of the HB9 promoter (courtesy of Wichterle lab). ES cells were grown in ADFNK media that consisted of 1:1 DMEM/F12 (Millipore, DF-041-B): Neurobasal

(Gibco, 21103049), 10% knock out serum replacement (Gibco, 10828010), 1% penicillin/streptomycin/antimycotic, and 1% GlutaMax supplement (Gibco, 35050061) for 2 days until they formed embryoid bodies. Media was supplemented on day 2 with 1μM retinoic acid (Sigma-Aldrich, R2625) and 1μM smoothened agonist (Calbiochem, 566661). Embryoid bodies were dissociated on day 6 with papain (Worthington, LK003150).

Unsorted motor neurons were plated on 5mm glass coverslips in a 24-well plate on top of a feeder layer of glia at a density of $1x10^6$ cells/well. Motor neurons that underwent FACS sorting were plated on Poly-D-lysine and laminin coated 5mm glass coverslips at a density of $5x10^5$ cells/well. For glial co-culture, sorted motor neurons were seeded on glass coverslips with a feeder layer of astroctyes at a density of $5x10^5$ cells/well. For multi-electrode recordings, standard 60-elecrode multi-electrode arrays (MultiChannel Systems, 890276) were sterilized and then coated with poly-D-lysine and laminin and seeded with $1x10^6$ sorted motor neurons. For glial co-culture on multi-electrode arrays, poly-D-lysine and laminin treated arrays were seeded with $5x10^5$ glial cells that were grown to confluence prior to seeding with $1x10^6$ sorted motor neurons. All motor neurons were cultured at 37°C in 5% carbon dioxide and 95-100% humidity. Media consisted of the BrainPhys neuronal medium (StemCell, 5792) supplemented with 2% NeuroCult SM1 neuronal supplement (StemCell, 5711), 1% N2-supplement (Gibco, 17502048), 1% GlutaMax supplement, 1% pen/strep/antimycotic, 1μM adenosine 3′,5′-cyclic monophosphate, N^6,O2′-dibutyryl-sodium salt (Calbiochem, 28745), 10ng/ml brain-derived neurotrophic factor (BDNF, MACS, 130-093-811), 10ng/ml glial derived neurotrophic factor (GDNF, GoldBio, 1170-14-10), and 1μM ascorbic acid (Sigma-Aldrich, A4403). For the HB9::GFP negative control, ES cell-derived motor neurons were generated in parallel from the E14 ES cell line (courtesy of Hatten lab).

Reticulospinal Chx10$^+$ neurons were dissected from E12.5 mouse embryonic hindbrains using the protocol described in Fantin *et al* (2013) from mice in which the cyan fluorescent protein (CFP) is expressed under the control of the Chx10 promoter (Zhong *et al*, 2010). To produce the cells, a male mouse homozygous for Chx10::CFP (courtesy of Sharma lab) was mated with a Swiss Webster female mouse (Taconic). On E12.5 of the pregnancy, the pregnant female was anesthetized in 5% isofluorane and oxygen and euthanized via cervical dislocation.

For the hindbrain dissection, each embryo was decapitated just rostral to the forelimb and the neural tube was isolated from the rest of the tissue. The developing rhombencephalon (hindbrain) segment corresponding to the position of the reticular formation in adults was excised and trimmed at the rostral and caudal ends. Dissections were performed in ice-cold HBSS buffer (Gibco, 14175-095) supplemented with 1% pen/step/antimycotic, 20mM D-glucose (Sigma-Aldrich, G8769), and 1μM ascorbic acid. Hindbrains were dissociated with papain and sorted using flow cytometry to isolate the Chx10$^+$ subpopulation. For the Chx10::CFP negative control, E12.5 hindbrains were derived from Swiss Webster mouse embryos. Sorted Chx10$^+$ hindbrain neurons were seeded on either 5mm glass coverslips in a 24-well plate or multi-electrode arrays, both prepared with a confluent layer of glia, at a density of 1x10^4 cells/well of coverslips or 4x10^4 cells/array. All Chx10$^+$ hindbrain neurons were cultured at 37°C under standard tissue culture conditions in Neurobasal medium supplemented with 2% SB-27 (Gibco, 17504044), 1% GlutaMax, 1% pen/strep/antimycotic, 1μM Adenosine 3′,5′-cyclic monophosphate, N^6,O2′-dibutyryl-sodium salt, 10ng/ml BDNF, 10ng/ml GDNF, and 1μM ascorbic acid.

For reticulospinal cocultures, sorted HB9::GFP$^+$ motor neurons and Chx10::CFP$^+$ hindbrain neurons were seeded together on a confluent layer of glia on either 5mm coverslips or multielectrode arrays. On coverslips in a 24-well plate, HB9$^+$ neurons were seeded at a density of

$2.5x10^5$ cells/well and $Chx10^+$ neurons were seeded at a density of $1x10^5$ cells/well. On multi-electrode arrays, $HB9^+$ neurons were seeded at a density of $1x10^6$ cells/dish and $Chx10^+$ neurons were seeded at a density of $4x10^5$ cells/dish. Co-cultures were grown in the same supplemented BrainPhys medium used for $HB9^+$ cultures.

4.2.2 Flow Cytometry

All samples were sorted on the basis of fluorescent marker expression on the BD FACSAriaII benchtop flow cytometer with a 100μm nozzle and 20psi sheath pressure. Flow cytometry was performed at the Flow Cytometry Resource Center at Rockefeller University.

To isolate HB9::GFP^+ motor neurons, embryoid bodies derived from HBG3 ES cells were dissociated on day 6 using papain and resuspended in FACS buffer for embryoid bodies that contains phenol-free HBSS supplemented with 2% heat-inhibited horse serum (Gibco, 26050088) and 500U DNAse (Worthington, LK003172). For the GFP negative control, embryoid bodies were derived from E14 ES cells and prepared under parallel conditions. Between 10 and 20nM DAPI (Invitrogen, D1306) was added to each sample as a dead-cell exclusion dye. Each sample was excited by a violet 405nm laser and dead cells were excluded on the basis of emission in the DAPI wavelength 461nm using the 405D filter. Single cells were distinguished from doublets on the basis of forward and side scatter of the sample comparing the scatter area versus width. GFP fluorescence was detected using illumination from a 488nm blue laser equipped with a 535/30nm filter and the gate for GFP^+ cell isolation was set based on a comparison of the GFP fluorescence of the HBG3-derived sample and the E14-derived sample. Typically, 50-60% of input cells from HBG3-derived embryoid bodies expressed GFP.

For Chx10::CFP^+ hindbrain neurons, hindbrains from Chx10::$CFP^{+/-}$ mice were dissociated at E12.5 using papain and resuspended in FACS buffer for hindbrains that contains high glucose phenol-free DMEM supplemented with 10% heat-inactivated fetal bovine serum,

1% pen/strep/antimycotic, and 500U DNAse. For the CFP negative control, hindbrains from Swiss Webster mice were prepared under parallel conditions. Approximately 20nM ToPro3 (Invitrogen, T3605) was added to each sample as a dead-cell exclusion dye. Each sample was excited by a red 640nm laser, dead cells were excluded on the basis of emission in the ToPro3 wavelength using the 640C 670/30nm filter. As with the HB9::GFP^{+} motor neurons, single cells were distinguished from doublets on the basis of forward and side scatter area versus width. CFP fluorescence was detected using illumination from a 445nm blue violet laser equipped with a 490/30nm filter and the gate for CFP^{+} cell isolation was set based on a comparison of the CFP fluorescence of the Chx10::CFP$^{+/-}$-derived sample and the Swiss Webster-derived sample. Typically, 2.5-3% of input cells from Chx10::CFP$^{+/-}$ mouse hindbrains expressed CFP.

4.2.3 Electrophysiology

Coverslips containing neurons cultured on a feeder layer of astrocytes as described above (see Cell Culture methods) for 5 to 10 days were perfused with 1x HEPES-ACSF in the recording chamber (HEPES-ACSF: 135mM NaCl, 10mM HEPES, 10mM glucose, 5mM KCl, 1mM $CaCl_2$-$2H_2O$, 1mM $MgCl_2$) under constant flow (~5ml/minute). All cells were patched using pulled glass pipettes with an R_E of 5 to 12 MΩ filled with a standard internal pipette solution (K-gluconate: 14mM, HEPES-K: 10mM, $NaHCO_3$: 60μM, Mg-ATP: 4mM, Na_2-ATP: 2mM, Na-GTP: 30 μM, sucrose: 8mM, $CaCl_2$: 1mM, EGTA: 5μM). Data were acquired on the MultiClamp 700B (Axon instruments) using ClampEx software. HB9^{+} spinal motor neurons were identified by GFP signal imaged using an Olympus BXS1W1 upright fluorescence microscope equipped with a FITC/EGFP filter (480/535nm ex/em, Chroma). Chx10^{+} hindbrain neurons were identified by CFP signal from an ECFP filter (436/480nm ex/em, Chroma).

Once the patch seal was achieved, the membrane voltage of the neuron was recorded for 1 minute at 1kHz sampling frequency without injecting additional current to measure the spontaneous activity of the neuron (I=0 mode). For current clamp experiments, current was injected to bring V_m to -70mV and current steps were applied in 10pA increments from -10 to 130pA for 1 second duration, returning to -70mV holding potential between steps.

For voltage clamp experiments, the cell was held at -80pA for 100ms before stepping voltage injection from -100 to 150mV in 10mV increments for 100ms, returning to the -80pA holding potential between each step. IV plots were calculated for I_{Na} by subtracting the initial trough in the voltage clamp recording from the steady-state current during voltage step.

Neuromodulators were applied to the cultures during recording by local micropuff. We used 1μM orexin A (Tocris, 205640-90-0) and 1μM orexin B (Tocris, 202801-92-1). A pulled glass pipette was loaded with either 1x HEPES-ACSF control solution or the drug and brought within 10μm of the cell surface. Spontaneous neuron activity was recorded in I=0 mode for 1 minute, then continuous micropuff stimulation was applied for 10 seconds at 10V, a rate of 2.4pps, and a puff duration of 3ms (Grass Medical Instruments). Micropuff stimulation was applied 3 times per recording with a 30 second break between stimuli. Micropuff application of ACSF had no significant effect on spontaneous activity, so was only repeated in initial control experiments.

Data analysis and plotting of patch clamp data was performed using ClampFit and MATLAB (see github.com/abubnys/patch_clamp_analysis for specific scripts used). To generate IV plots of voltage-gated sodium current from voltage-clamp data, the local minimum evoked current within 30ms of voltage step onset was subtracted from the mean current during the last 30ms of the voltage step and plotted against the magnitude of the injected voltage.

4.2.4 Multi-electrode recordings

Multi-electrode arrays were cultured with $HB9^+$ motor neurons or $Chx10^+$ hindbrain neurons as described above (see Cell Culture methods). For the duration of the lifetime of the culture (D3 to D30 days after plating for $Chx10^+$ and D7 to D30 days after plating for $HB9^+$ neurons), spontaneous extracellular activity was recorded using the MEA2100-Lite system (MultiChannel Systems). The array was placed in the recording apparatus and allowed to equilibrate at room temperature for 30 minutes prior to recording for 4 minutes. Data acquisition was performed on MCRack with an input voltage range of -19.5 to +19.5mV and a sampling frequency of 20kHz. Raw electrode data for 60 electrodes were processed through a Bessel 4^{th} order high pass filter with a cutoff at 400Hz. The spike detection threshold was 5 standard deviations below the mean of the filtered recordings. Raw and filtered data, along with spike timestamps were converted to .txt files using MC_DataTool and the resulting files were analyzed in Matlab.

For synaptic blocker and arousal neuromodulator wash-in experiments on the multi-electrode arrays, warmed 1x HEPES-ACSF was perfused through the MEA after the 30 minute equilibration period at ~5ml/minute for 10 minutes. The baseline activity of the MEA was recorded for 2 minutes under the previously mentioned parameters. Then, 100uL of a 10x solution of the drug was slowly perfused in at 50µL/minute for 2 minutes while recording. After 2 minutes the pump was stopped and the steady state activity of the array in the presence of the drug was recorded for 4 minutes. The MEA was washed with 1x HEPES-ACSF at 5ml/minute for 10 minutes in between drug applications. Filtered electrode data was converted using MC_DataTool and analyzed in Matlab. The final concentrations of the drugs used were 20µM CNQX (Tocris, 479347-85-8), 50µM AP5 (Tocris, 79055-68-8), 60µM bicuculline (Tocris,

UN1544), 5μM orexin A (Tocris, 205640-90-0), 5μM orexin B (Tocris, 202801-92-1), and 300μM or 500μM L-phenylephrine (Sigma, P-6126).

Data analysis for perfusion experiments was performed in Matlab (see github.com/abubnys/MEA_perfusion_package for specific scripts used). For initial spike data extraction, the high-pass filtered recordings from each electrode generated by MC_Rack (multichannel systems, Reutlingen, Germany) were converted into .txt format using MC_DataTool (multichannel systems). Spikes were detected in each channel using a manual threshold adjusted to pick up deviations that were approximately five standard deviations below the baseline of the recording and analysis of spike waveforms was used to determine whether one or more neurons was contributing to the observed signal. Spike sorting was performed on these data by plotting the aggregate collection of waveforms from recorded spikes. If this collection of waveforms fell within multiple visually distinguishable distributions, manual thresholds for each distribution were set by drawing a line through the waveforms visually classified as similar and then categorizing all recorded spikes according to whether they cross this threshold line or not. Then, spike rate was calculated for each waveform type by counting the number of spikes that fall within bins of 100ms width and multiplying by 10 to covert to units of Hz.

To facilitate comparison of different spike rates across all recordings, spike rates were smoothed using a cubic spline function, then binned according to the average spike rate in non-overlapping 10s intervals, then normalized to set the average spike rate from the first 10 bins (corresponding to the first 100s of recording) to 1.

To determine if synaptic blocker or orexin wash-in had a dose-dependent effect on the activity of each culture type, normalized spike rate data from each electrode on the MEA that recorded spontaneous neuronal activity were pooled across all drug wash-in trials for a given

culture type. The data corresponding to the period when the drug was washed in (2-4 minutes into the recording) were fit to a linear mixed effects model using the function fitlme() in matlab with the normalized spike rate as the predictor variable and electrode as the random effect:

Equation 3. Drug dose (μM) ~ 1 + normalized spike rate + (1|electrode)

Results from the linear mixed effects model are reported as β, the slope of the spike rate versus drug concentration and the statistical significance p.

4.2.5 Calcium imaging

$HB9^+$, $Chx10^+$, or combined cocultures grown on 5mm coverslips with a feeder layer of glia were loaded with Rhod-3 AM dye according to manufacturer's instructions (Molecular Probes, R10145), then washed with 1x HEPES-ACSF. Calcium imaging was subsequently performed in 1x HEPES-ACSF.

For $Chx10^+$ cultures, calcium reporter dye fluorescence during spontaneous activity was imaged using an inverted spinning disc confocal microscope (Zeiss Axiovert 200) equipped with an EMCCD camera (Andor iXon). Solid state lasers were used for excitation at 443 and 561nm (Spectral Applied) paired with a polychroic filter with 440nm, 491nm, 561nm, and 640nm filters. Imaging acquisition was performed using MetaMorph software. $Chx10^+$ neurons were identified by CFP signal (440/480nm ex/em) and rhodamine3 signal was identified on the Texas Red channel (561/620-60nm ex/em). Calcium imaging data was acquired via time-lapse, with a 150ms interval and 100ms exposure time for 2 minutes.

For $HB9^+$ cultures, HB9/Chx10 cocultures, and astrocyte cultures, spontaneous calcium activity was imaged at room temperature and ambient CO_2 using an Olympus BXS1W1 upright fluorescence microscope equipped with an Evolution QEi digital CCD camera (MediaCybernetics). A 120W mercury vapor short arc bulb was used as the fluorescence light source (X-Cite series 120Q). Imaging acquisition was done using NIS-Elements BR software.

$Hb9^+$ spinal motor neurons were identified by GFP signal using a FITC/EGFP filter (480/535nm ex/em, Chroma) and imaged with an exposure time of 100ms. $Chx10^+$ hindbrain neurons were identified by CFP signal using an ECFP filter (436/480nm ex/em, Chroma) and imaged with an exposure time of 100ms. Rhodamine3 signal was imaged using a CY3/TRITC filter (545/605nm ex/em, Chroma) with an exposure time of 60ms per frame for 40 to 80 seconds.

For experiments involving application of the $AMPA_R$ blocker CNQX, the spontaneous calcium activity of HB9/Chx10 co-cultures in HEPES-ACSF solution was imaged to determine a baseline level of activity. Then, 200µl of a 100x solution of CNQX was injected into the bath for a final drug bath concentration of 40µM. The culture was allowed to equilibrate for five minutes before imaging of spontaneous calcium activity in the presence of the drug. The drug was washed out by replacing 50% of media with fresh HEPES-ACSF in 5 repeated washes, then the culture was allowed to equilibrate for 5 minutes before imaging spontaneous calcium activity to measure recovery of spontaneous activity.

Calcium imaging data for all experiments was analyzed in Matlab (see github.com/abubnys/calcium_imaging_ROI_analysis for specific scripts used). Due to overlap between CFP and GFP emissions spectra, CFP^+ neurons appear on the GFP fluorescence channel and were distinguished from HB9::GFP^+ neurons on the basis of their fluorescence on the CFP channel. ROIs were manually drawn around the cell bodies of identified CFP^+ and GFP^+ neurons and the mean Rhodamine3 fluorescence within the ROI was calculated at each frame of the recording in the Rhod3 channel. Signal from slow calcium waves originating from unlabeled asctrocytes and overlapping with CFP^+ and GFP^+ cell bodies was subtracted from the calcium recordings by normalizing the raw recording according to a moving baseline calculated by smoothing the recording with a cubic spline function.

4.3 Results

4.3.1 Developing reticulospinal cultures

Numerous studies of mixed populations of neurons from various brain regions such as cortex, amygdala, and spinal cord cultured on extracellular multielectrode arrays reveal that these cultures have a strong tendency to develop network bursts, in which many neurons across the cultured network fire all at once in burst periods followed by periods of quiescence (Wagenaar 2006, Black 2017, Dauth 2016, Van Pelt 2005). It is generally believed that the generation of such bursts requires a combination of excitatory and inhibitory interneurons that work in concert to prevent runaway activity (Maheswaranathan 2012, Li 2009, Sternfeld 2017).

We sought to test this hypothesis by purifying neuronal subpopulations, which allowed us to eliminate the confounding effects of mixed populations of neuronal progenitors and inhibitory interneurons of unknown developmental origin. We focused specifically on reticulospinal cultures containing homogeneous populations of spinal motor neurons and hindbrain $Chx10^{+}$ neurons. Hindbrain $Chx10^{+}$ neurons are known to play a role in regulating locomotor gait and breathing rhythm and have descending projections to the spinal cord (Bretzner 2013, Bouvier 2015, Crone 2012), while spinal motor neurons provide direct limb-muscle innervation. Thus, the *in vivo* function of both neuronal subtypes predisposes them to rhythmic bursts.

To isolate pure populations of spinal motor neurons and hindbrain $Chx10^{+}$ neurons, we employed fluorescence activated cell sorting (FACS). We cultured these cell types as single populations and also as a mixed reticulospinal culture. We differentiated HBG3 spinal motor neurons from embryonic stem cells using Wichterle et al's protocol of caudalization followed by ventralization of embryoid bodies to induce the spinal motor neuron identity (Wichterle 2002) (figure 15a). Embryoid bodies were dissociated 4 days after induction and sorted on the basis of HB9::GFP expression using motor neurons differentiated by the same protocol from E14 stem

cells lacking GFP as a negative control (figure 15b,c). Prior to sorting, approximately 40-50% of the embryoid body neurons derived from HBG3 ES cells expressed GFP. FACS enriched this population to >96%. HB9::GFP$^+$ motor neurons were subsequently cultured on a layer of cortical astrocytes to improve axonal outgrowth and network development (figure 15d).

While the sorted HB9$^+$ motor neurons appeared morphologically indistinguishable from unsorted HB9$^+$ motor neurons, it is possible that the sorting affected their electrophysiological activity. We performed whole cell patch clamp on HB9::GFP$^+$ neurons from sorted and unsorted cultures grown in parallel under identical conditions. For HB9$^+$ spinal motor neurons, the average capacitance C_m was 63.05±4.08pF, the membrane resistance R_m was 121.3±22.7MΩ, the access resistance R_a was 27.8±2.85MΩ, and the resting membrane potential V_m was -16.5± 3.5mV. After 7 days in culture, motor neurons in both treatments responded to brief current pulses with spike trains, having a spike threshold around 20pA (figure 15e,f). They developed voltage gated I_{Na} with maximum current evoked at -2±12 mV (figure 15g-i) that was not significantly different between sorted and unsorted populations (Student's 2-tailed T-test p = 0.879). After 13 days in culture, both sorted and unsorted motor neurons also developed spike trains of spontaneous activity (figure 15j).

We then isolated and cultured primary hindbrain neurons expressing the transcription factor Chx10, also using the FACS approach. We sought to assess first the Chx10$^+$ neurons' behavior *in vitro* as a homogeneous population, and then in combination with spinal motor neurons to determine if they could form a reticulospinal circuit *in vitro* and what functional form such a connection would take.

Figure 15. Isolation, culture, and electrophysiology of HB9$^+$ motor neurons.
a, Timeline schematic of differentiation, isolation and culture of HB9::GFP$^+$ neurons. **b-c** Sample FACS plots and thresholds for isolation of GFP$^+$ neurons. ***b,*** Cells sorted from HB9::GFP$^+$ stem cell derived embryoid bodies (6 DIC), GFP$^+$ cells indicated in box ***c,*** embryoid bodies derived from non-transgenic ES cells. ***d***, fluorescent photomicrograph of sorted HB9::GFP$^+$ neurons, 16 days in culture (DIC), yellow arrowheads indicate neurons. **e-f** Comparison of the response of ***e***, unsorted and ***f***, sorted HB9::GFP$^+$ neurons (bottom panels) to injections of 20, 30, and 40pA current (top panels). **g-h** Response of ***g***, unsorted and ***h***, sorted HB9::GFP$^+$ neurons (bottom panels) to voltage step injection of -90 to 30mV (top panels, result for -10 to 30mV injections shown) (7 DIC). Sodium current (I_{Na}) was calculated at each injected voltage step by subtracting the steady state current response (•) from the initial current minimum (o) (formula shown in insert in *i*). ***i***, I-V plot of Na^+ currents for sorted and unsorted HB9::GFP$^+$ neurons calculated from the voltage clamp experiment results shown in *G* and *H*. ***j,*** Spontaneous activity of unsorted (top panel) and sorted (bottom panel) HB9::GFP$^+$ cells at 13 DIC.

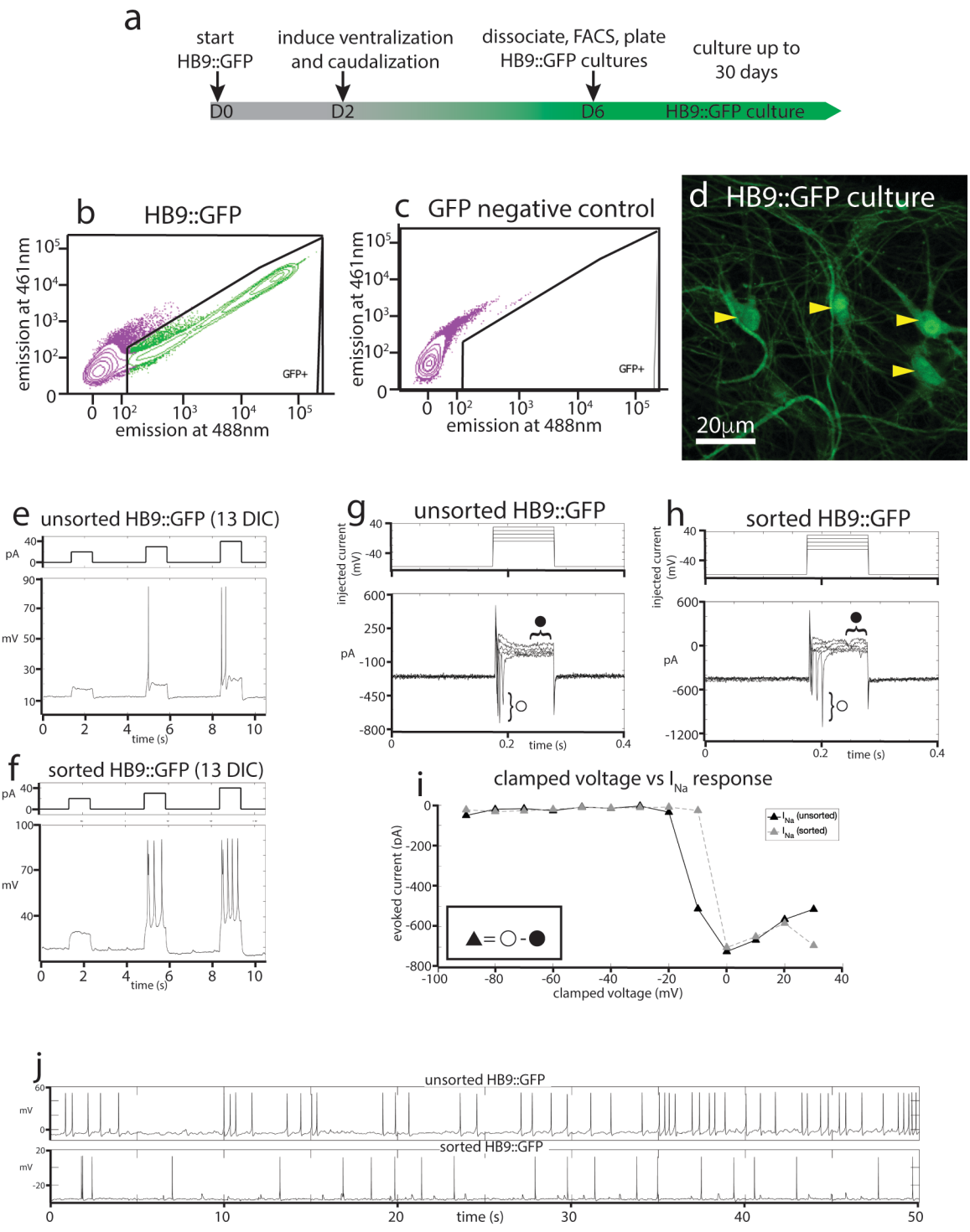
a
start HB9::GFP
induce ventralization and caudalization
dissociate, FACS, plate HB9::GFP cultures
culture up to 30 days
D0
D2
D6
HB9::GFP culture
b HB9::GFP
emission at 461nm
emission at 488nm
GFP+
c GFP negative control
d HB9::GFP culture
20μm
e unsorted HB9::GFP (13 DIC)
pA
mV
time (s)
f sorted HB9::GFP (13 DIC)
g unsorted HB9::GFP
injected current (mV)
h sorted HB9::GFP
i clamped voltage vs I_{Na} response
I_{Na} (unsorted)
I_{Na} (sorted)
evoked current (pA)
clamped voltage (mV)
▲= ○ - ●
j
unsorted HB9::GFP
sorted HB9::GFP
mV
time (s)

We dissected and dissociated the hindbrains from embryonic Chx10::CFP$^{+/-}$ mice at E12.5 (figure 16a) and used FACS to isolate the CFP^{+} population, using hindbrains taken from wildtype (WT) Swiss Webster E12.5 mouse embryos as a negative control for CFP expression (figure 16b,c). The hindbrains contained 2-3% Chx10::CFP^{+} neurons, and sorting enriched this population to >95%. These CFP^{+} neurons were then cultured on a layer of cortical astrocytes, which is known to improve the development and long-term viability of neuron cultures (Wang 1994, Maher 1999, Boehler 2004) (figure 16d).

To assess the electrophysiological development of sorted Chx10^{+} neurons, we used whole cell patch clamp to record the spontaneous activity of single cells in parallel cultures at different ages ranging from 1 to 30 days in culture. For Chx10^{+} hindbrain neurons, the measured membrane capacitance was 22.75±2.9pF, membrane resistance was 787.27±105.1MΩ, access resistance was 29.01±3MΩ, and membrane voltage was -22.6±3.8mV. We found that Chx10^{+} hindbrain neurons developed spontaneous electrophysiological activity after 5 days in culture. This activity started off as random trains of spikes, but gradually became organized into robust, regular bursts after 10 days and this pattern of activity continued throughout the remaining lifetime of the cultures (figure 16e). This demonstrate that even when removed from the intact reticular formation with its descending inputs and diversity of other cell types, Chx10^{+} hindbrain neurons develop intrinsic activity that could potentially pattern a reticulospinal circuit.

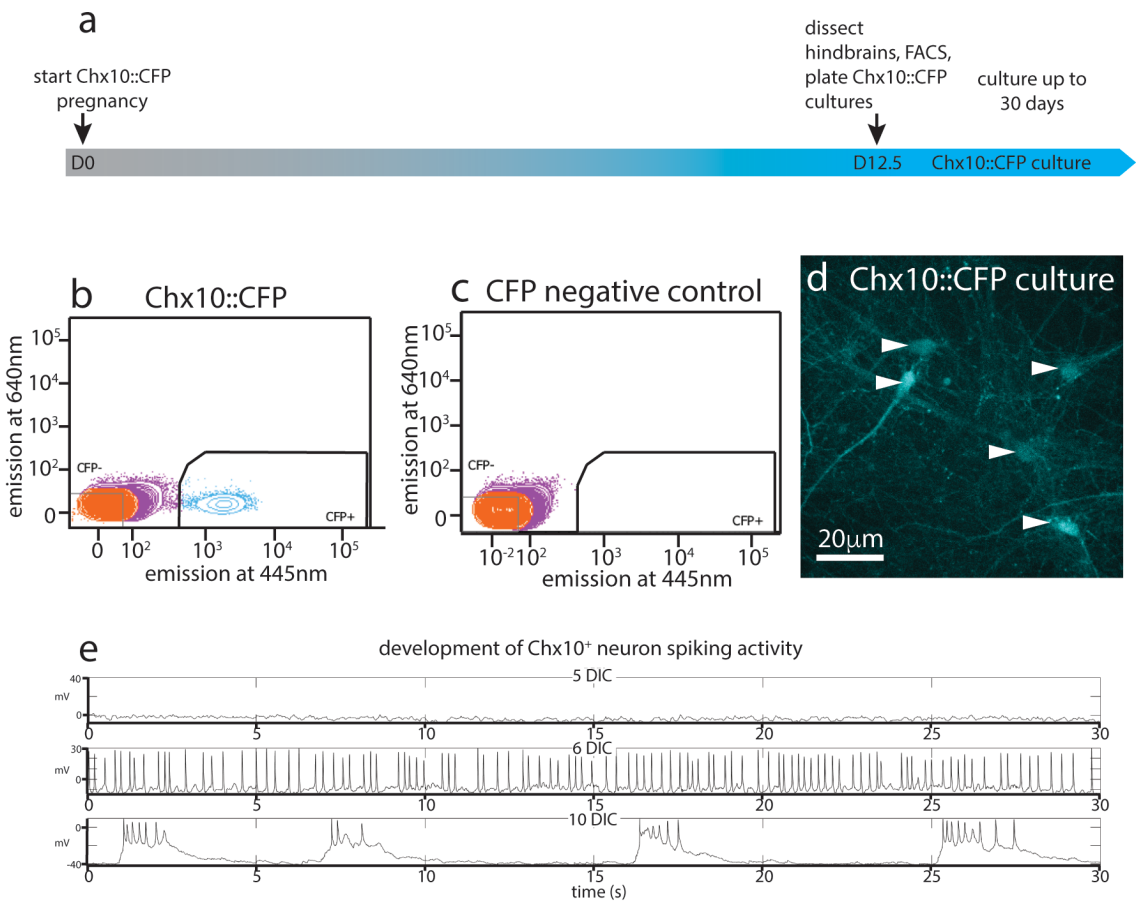

Figure 16. Isolation, culture, and electrophysiology of Chx10^{+} hindbrain neurons.

a, timeline schematic of the generation, isolation, and culture of Chx10::CFP^{+} hindbrain neurons.

b-c Sample FACS plots and thresholds for isolation of CFP^{+} neurons. ***b,*** CFP^{+} neurons from embryonic hindbrains of Chx10::CFP^{+} mice and ***c,*** Swiss Webster mice.

d, Fluorescent photomicrograph of sorted Chx10::CFP^{+} neurons, 10 DIC, white arrowheads indicate neurons. ***e***, Spontaneous activity of sorted Chx10::CFP^{+} neurons at 5 DIC (top), 6 DIC (middle) and 10 DIC (bottom).

4.3.2 Motor and Chx10 neuron cultures develop distinct patterns of network activity

Having established that motor neurons and $Chx10^+$ hindbrain neurons develop spontaneous electrophysiological activity at the single cell level, we sought to determine if cultures of either cell type, which are composed almost exclusively of excitatory neurons and astrocytes could generate spontaneous patterns of network activity, whether these patterns would organize into network bursts, and if there were any cell-type specific differences in such activity.

To record the activity of multiple neurons at different time points, we cultured sorted $HB9^+$ motor neurons on multi-electrode arrays (MEAs) containing a grid of 64 extracellular recording electrodes (MultiChannel systems). We recorded their spontaneous activity daily over 30 days, starting from the day after plating. We found that on their own, without astrocytes, sorted $HB9^+$ motor neurons did not develop any spontaneous activity on the MEA (n = 6) (figure 17). However, when these neurons were cultured on a confluent layer of astrocytes, they gradually developed robust network activity that remained stable over a month of recording (n = 14). We note that astrocytes cultured on their own did not develop spontaneous activity when recorded on MEAs (n = 3), although we did observe spontaneous calcium flux in astrocyte cultures visualized with the calcium sensitive dye Rhodamine3 (figure 18a). These glial calcium waves were easily distinguishable from the calcium activity generated by neurons due to their much slower time course (figure 18b-d). In subsequent calcium imaging experiments of neuron/astrocyte cocultures, we effectively subtracted the calcium activity of astrocytes by normalizing the recording to a smoothing spline baseline.

The activity of $HB9^+$ motor neuron/astrocyte cultures was not well coordinated, even among neighboring recording electrodes (figure 19a,b). Furthermore, the mean spike rate calculated across all of the active channels of the $HB9^+$ motor neuron cultures was found to fluctuate around a single mean (figure 19c).

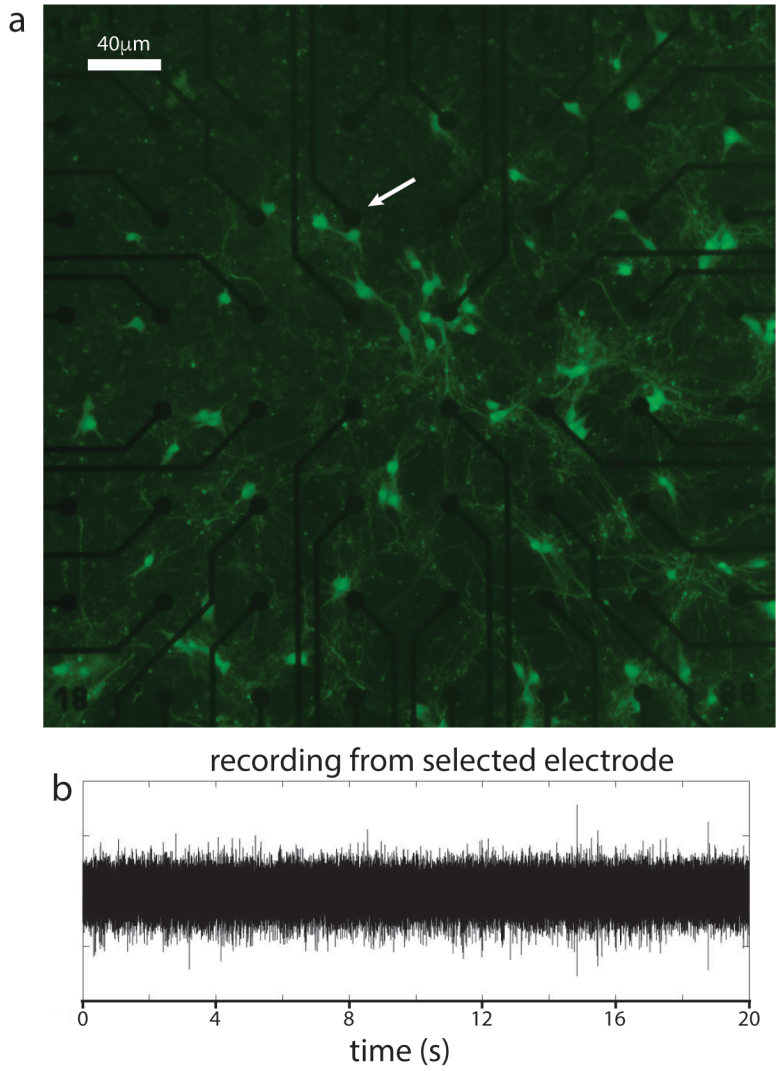

Figure 17. Sorted HB9^{+} motor neurons do not develop spontaneous activity on their own. ***a***, sorted HB9^{+} neurons cultured on a multi-electrode array develop complex morphology and axonal outgrowth (8 days in culture). ***b***, recorded activity from the electrode indicated by the white arrow in *a*. No spontaneous activity could be detected, despite this electrode's proximity to several motor neurons.

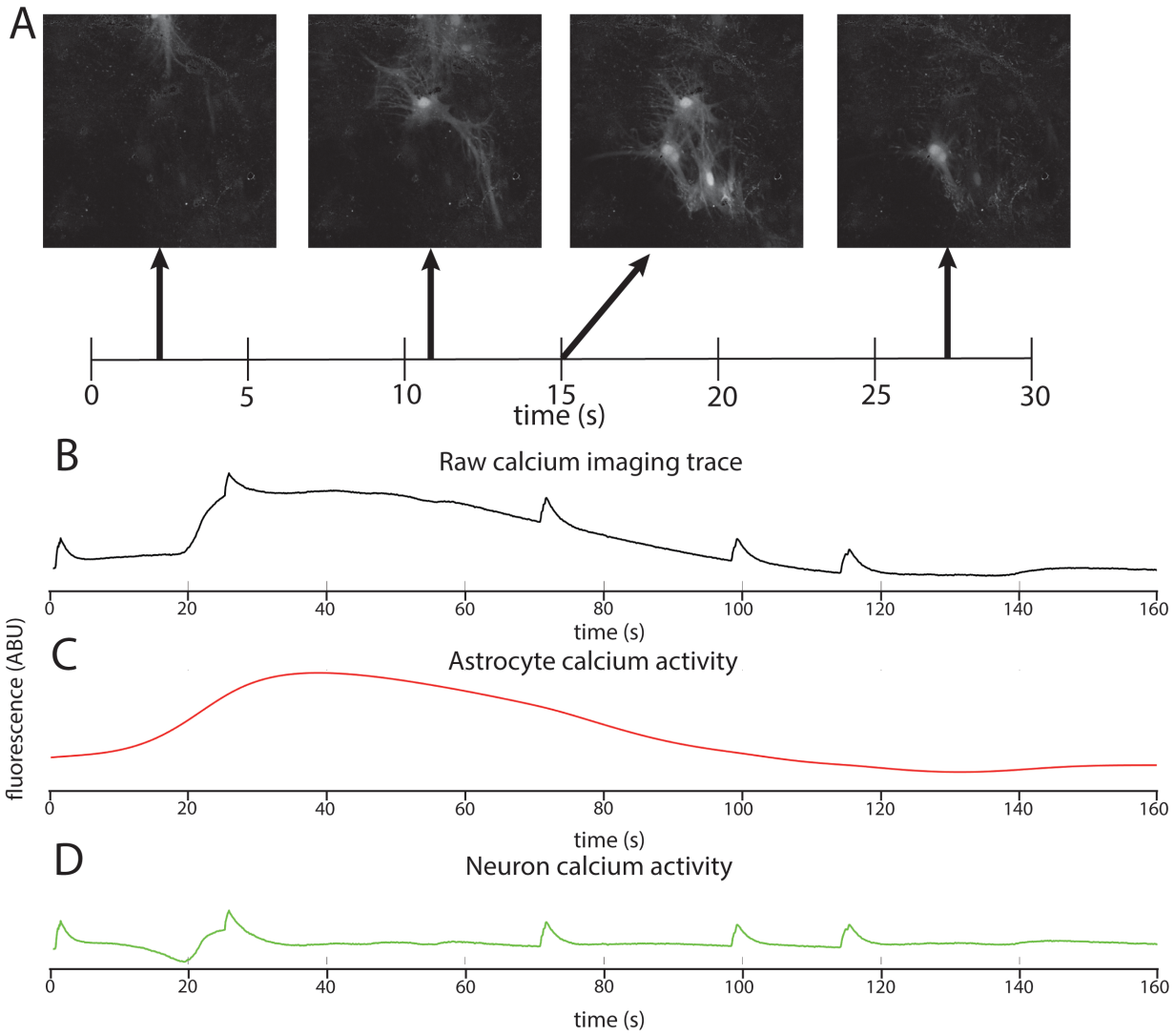

Figure 18. Glial calcium waves

a. Time course of a calcium wave propagating across an astrocyte culture. ***b***, raw quantification of calcium activity of a spiking neuron with overlapping astrocyte, ***c***, calcium activity of astrocyte from *b* , ***d***, calcium activity of neuron from *b*.

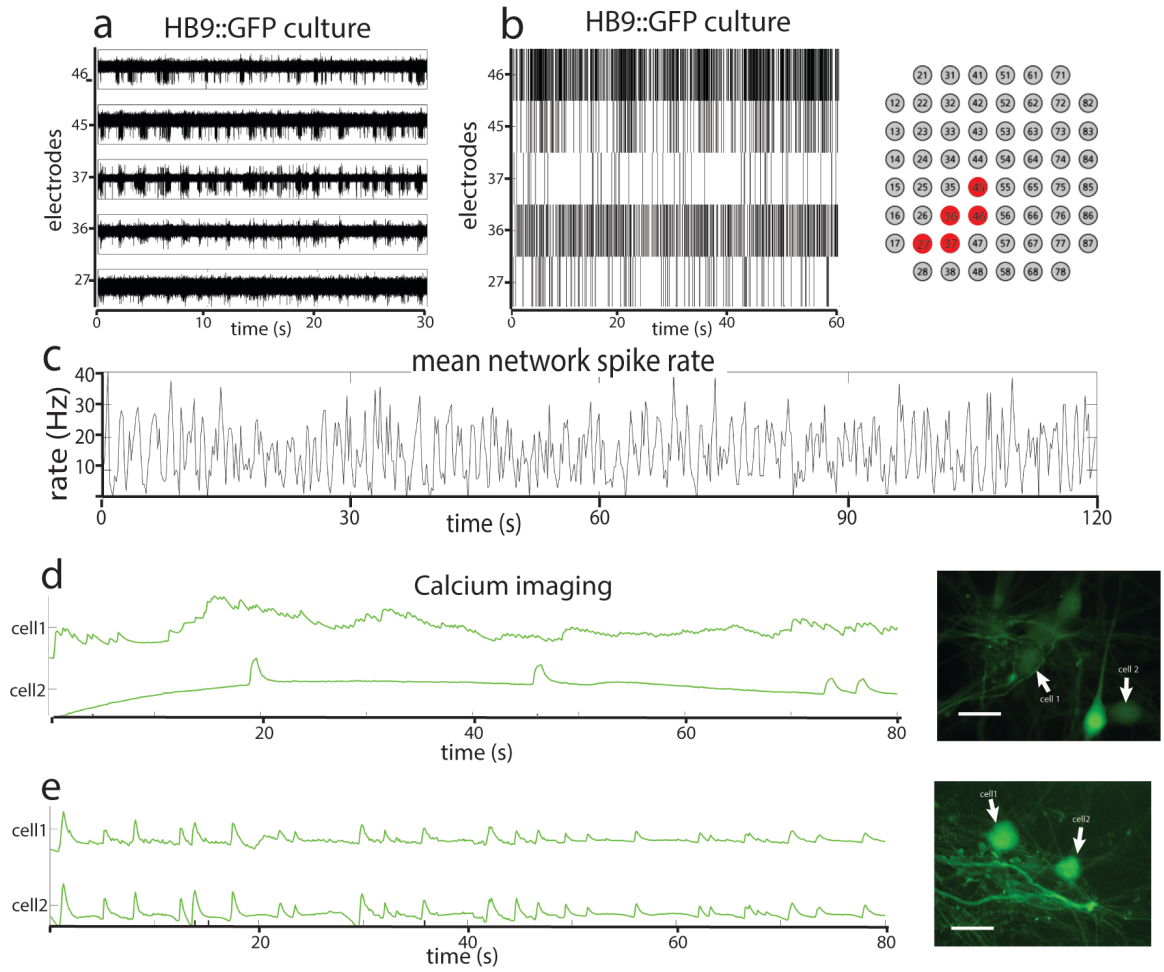

Figure 19. Activity of motor neurons *in vitro*

a-b Examples of five typical actively spiking neurons from a multi-electrode array (MEA) recording of sorted HB9::GFP^{+} motor neurons (18 DIC), both as ***a***, high-pass filtered MEA data and ***b***, raster plot (locations of electrodes indicated in red on right panel). ***c***, Mean spike rate of entire HB9::GFP^{+} motor neuron culture from a,b.

d-e Quantification of calcium-sensitive Rhodamine3 dye fluorescence in the cell bodies of HB9::GFP^{+} motor neurons ***d***, 19 DIC, ***e***, 32 DIC. Scale bars are 20μm.

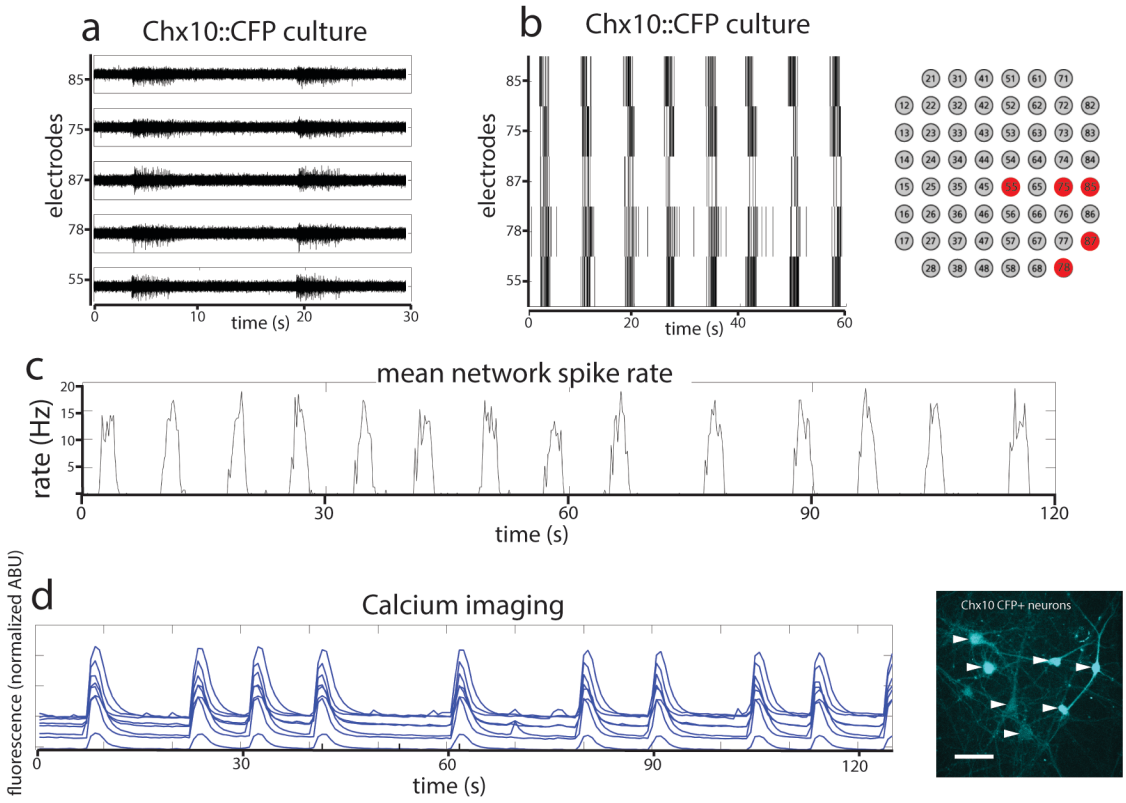

Figure 20. Activity of Chx10^{+} hindbrain neurons *in vitro*

a-b Examples five typical actively spiking neurons from a multi-electrode array (MEA) recording of sorted Chx10::CFP^{+} neurons (5 DIC) as ***a***, high-pass filtered MEA data and ***b***, raster plot (locations of electrodes on array in red on right panel). ***c***, Mean spike rate of entire Chx10::CFP^{+} neuron culture from f,g. ***d***, Calcium imaging of Chx10::CFP^{+} neurons (10 DIC), scale bar is 20μm.

When we used the calcium-sensitive dye Rhodamine3 to assess $HB9^+$ motor neuron activity with single cell resolution, we observed randomly distributed calcium spikes that did not always occur in synchrony between neighboring neurons (figure 19d), though in more mature cultures their calcium activity did display some synchrony between neighboring neurons (figure 19e). The mean correlation coefficient between spike rates across the $HB9^+$ motor neuron cultures was 0.15 ± 0.17 ($p = 0.15$). This value did not significantly deviate from 0, indicating that there was no appreciable correlation between the activity of neurons in the network.

When we cultured $Chx10^+$ hindbrain neurons on MEAs with a confluent layer of astrocytes, we observed the emergence of spontaneous activity with these neurons as well. This activity differed from that observed in the motor neurons in that the $Chx10^+$ neurons did develop robust and coordinated network bursts (figure 20 a-c). Very few spikes occurred outside of these sharply delineated bursting periods. The time between bursts (inter-burst interval) varied between 2 and 10 seconds throughout the lifetime of the cultures, with no apparent long-term trend. We observed the same sort of robust network bursts in $Chx10^+$ hindbrain neuron cultures with calcium imaging (figure 20d). The vast majority of the CFP^+ neurons identified in the field of view participated in these simultaneous bursts with no discernible time delay.

4.3.3 $Chx10^+$ neurons impose their activity patterns on motor neurons in co-culture

Despite their common glutamatergic identity, we observed that $HB9^+$ motor and $Chx10^+$ hindbrain neurons develop distinct patterns of spontaneous network activity. If these two cell types fail to form functional connections to one another *in vitro*, these patterns of activity should remain unchanged in co-culture, but if a unidirectional function connection forms between $Chx10^+$ and $HB9^+$ motor neurons, we might expect to see one activity pattern dominate in co-culture. To test these possibilities, we cultured the two cell types together as a mixed population on multi-electrode arrays and recorded their spontaneous activity daily over 30 days. Such co-

cultures indeed develop spontaneous bursts of comparable time scale and duration to pure $Chx10^+$ cultures, though some neurons continue to have residual spiking activity between network bursts that resembles $HB9^+$ motor neuron culture activity (figure 21a,b). When the overall network activity was measured by averaging spike rates across all active electrodes however, the Chx10-like network bursts predominated (figure 21c).

In order to determine which cell type participates in the cultures' network bursts, we used calcium imaging to obtain single cell resolution recordings of the co-culture. We found that neighboring $HB9^+$ motor and $Chx10^+$ neurons both participate in network burst events (figure 21d). Some $HB9^+$ motor neurons in co-culture also have brief, non-coordinated calcium spiking events that occur between the larger bursts (figure 21e).

Of the total number of $Chx10^+$ neurons recorded in calcium imaging experiments of the co-culture (n = 125), about 12% were spiking (n = 16), 51% were bursting (n = 64), 14% were spiking and bursting (n = 17), and the remaining 22% had no apparent spontaneous calcium activity (n = 28). By comparison, of the total number of $Chx10^+$ neurons recorded by calcium imaging in Chx10-only culture (n = 483), 64% were bursting (n = 312), 1.4% were spiking and bursting (n = 7), 34% had no spontaneous activity (n = 164), and no identified neurons had spiking activity.

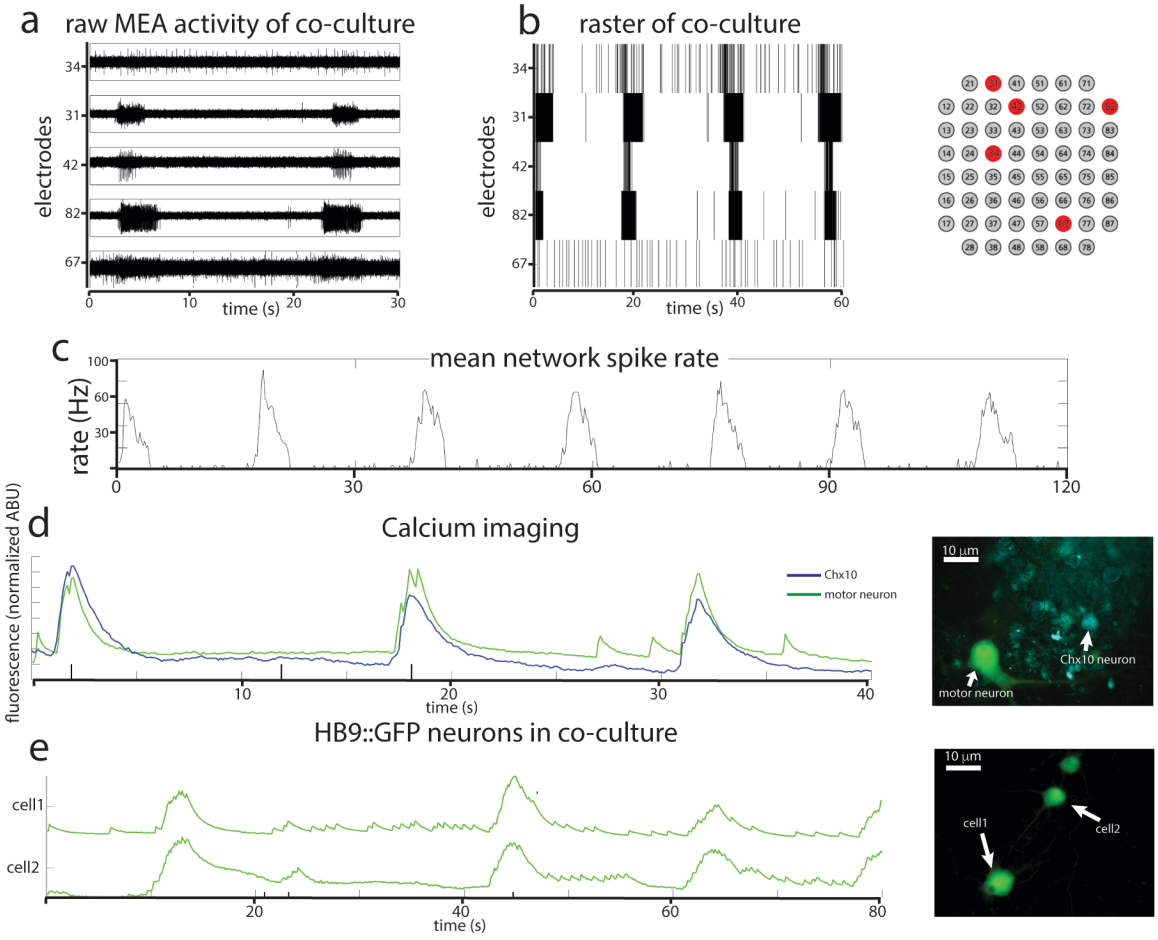

Figure 21. In reticulospinal co-culture, Chx10^{+} neurons drive patterned motor neuron activity.

a-b Example of a multi-electrode array (MEA) recording of HB9::GFP^{+}/Chx10::CFP^{+} neuron co-culture (8 DIC), both as ***a***, high-pass filtered MEA data and ***b***, raster plot (locations of electrodes indicated in red on right panel). ***c***, Mean spike rate of entire co-culture from *a*,*b* over the course of 120 seconds.

d-e Calcium imaging of neurons in co-culture. ***d***, Normalized calcium-sensitive fluorescence intensity over time in co-cultured HB9::GFP^{+} and Chx10::CFP^{+} neurons participating in coordinated bursts. ***e***, Normalized calcium-sensitive fluorescence intensity of two HB9::GFP^{+} neurons from co-culture (Chx10::CFP^{+} neurons not pictured) participating in network bursts.

Of the total number of $HB9^+$ neurons recorded in calcium imaging experiments of the co-culture (n = 67), about 20% were spiking (n = 13), 20% were bursting (n = 13), 43% had a combination of spikes and bursts (n = 29), and 18% had no activity (n = 12). By comparison, of the total number of $HB9^+$ neurons recorded by calcium imaging in motor neuron cultures (n = 176), 46% had spiking activity (n = 81), 1% had spiking and bursting activity (n = 2), 52% were inactive (n = 93), and no identified neurons had bursting activity.

4.3.4 Motor and Chx10 network activity are AMPA receptor-dependent processes

The spontaneous, coordinated activity we observed in $Chx10^+$ and $HB9^+$ motor neuron cultures could be the product of intrinsic pacemaker properties of these neurons or an emergent property of the network that is dependent on synaptic transmission. To distinguish between these alternatives, we applied a panel of synaptic blockers targeting AMPA receptors, NMDA receptors, and $GABA_A$ receptors, while recording from the cultures on MEAs to observe changes in spontaneous activity. The blockers used included the AMPA receptor antagonist CNQX, the NMDA receptor antagonist AP5, and the $GABA_A$ receptor antagonist bicuculline. Washing in the $AMPA_R$ antagonist CNQX on cultures of spiking $HB9^+$ motor neurons caused a gradual decrease in activity to about 40% of initial levels (figure 22a, e). There was a significant relationship between drug dose and spike rates (linear mixed effects model: $\beta = -0.04$, $p = 2.65 \times 10^{-63}$). Similarly, CNQX application resulted in a significant decrease in the activity of $Chx10^+$ neurons to about 40% of the initial rate (figure 22b, f) ($\beta = -0.021$, $p = 8.61 \times 10^{-15}$). The application of CNQX to reticulospinal co-cultures caused certain cells to abruptly stop bursting (figure 22c). Other neurons that participated in network bursts in baseline conditions gradually became decoupled from the network bursts and fired tonically for a brief period before also being silenced during CNQX application (figure 22d). The average response of co-cultured

neurons to CNQX application reflects this transient increase in activity followed by eventual inhibition (figure 22g) (β = -0.012, p =0.0015).

We repeated the CNQX drug application on $Chx10^+/HB9^+$ co-cultures and used calcium imaging with Rhodamine3 to visualize the activity of the culture prior to and after application of 40μM CNQX. Despite a loss of network bursting activity, we observed that some $HB9^+$ neurons in the co-culture continued to have spontaneous spiking activity in the presence of a blocking concentration of CNQX (figure 22h).

We also tested the effects of the NMDA receptor antagonist AP5 on all three cultures (figure 23) and found that there was no significant relationship between blocker dose and spike rates during AP5 wash-in (linear mixed effects model for: $HB9^+$ neurons, β = 0.0005 p = 0.23, $Chx10^+$ neurons, β = 0.004 p = 0.25, co-culture, β = 0.006 p = 0.24). The $GABA_A$ receptor blocker bicuculline also had no significant effect on $Chx10^+$ hindbrain neurons, motor neurons, or reticulospinal cultures (figure 24) (linear mixed effects model for: $HB9^+$ neurons, β = 0.0003 p = 0.54; $Chx10^+$ neurons, β = 0.0026 p = 0.34; co-culture,β = 0.0057 p = 0.13).

Figure 22. Spontaneous activity in reticulospinal cultures is an $AMPA_R$-dependent process.
a-d, Examples of high-pass filtered MEA recordings of spiking neurons during wash-in of a 200μM solution of the $AMPA_R$ blocker CNQX at 50μL/min (final CNQX concentration 20μM), orange bars show time course of blocker wash-in. ***a***, Neuron from HB9::GFP^+ culture, ***b*** neuron from Chx10::CFP^+ culture.

c-d, examples of two different kinds of responses to CNQX of neurons from HB9::GFP^+/Chx10::CFP^+ coculture, ***c***, neuron from coculture that is immediately inhibited by CNQX, ***d***, neuron from coculture that switches from bursting to tonic spiking upon CNQX application.

e-g, Normalized mean responses of all neurons recorded from electrodes with activity to CNQX wash-in, ***e*** HB9::GFP^+ cultures (n = 3), ***f*** Chx10::CFP^+ cultures (n = 3), ***g*** HB9::GFP^+/Chx10::CFP^+ cocultures (n = 4).

h-j, Calcium imaging of coculture ***h***, bursting prior to CNQX application, ***i***, inhibited by application of 40 μM CNQX, and ***j***, recovering bursting after washout of CNQX. $HB9^+$ neurons indicated with in photomicrographs with yellow arrowheads, $Chx10^+$ neurons with white arrowheads.

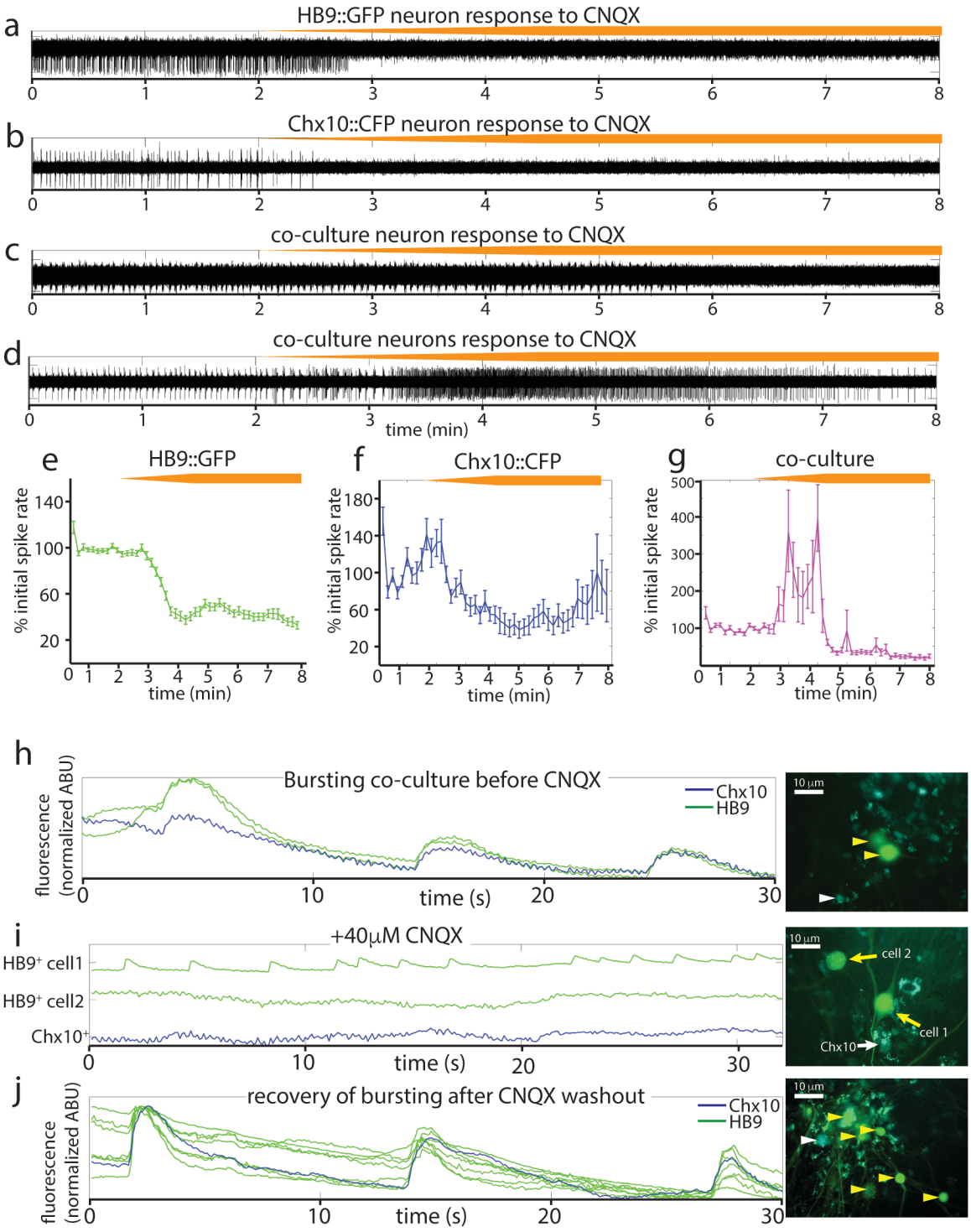
a
HB9::GFP neuron response to CNQX
b
Chx10::CFP neuron response to CNQX
c
co-culture neuron response to CNQX
d
co-culture neurons response to CNQX
time (min)
e
HB9::GFP
% initial spike rate
time (min)
f
Chx10::CFP
% initial spike rate
time (min)
g
co-culture
% initial spike rate
time (min)
h
Bursting co-culture before CNQX
Chx10
HB9
fluorescence (normalized ABU)
time (s)
10 µm
i
+40µM CNQX
HB9+ cell1
HB9+ cell2
Chx10+
time (s)
10 µm
cell 2
cell 1
Chx10
j
recovery of bursting after CNQX washout
Chx10
HB9
fluorescence (normalized ABU)
time (s)
10 µm

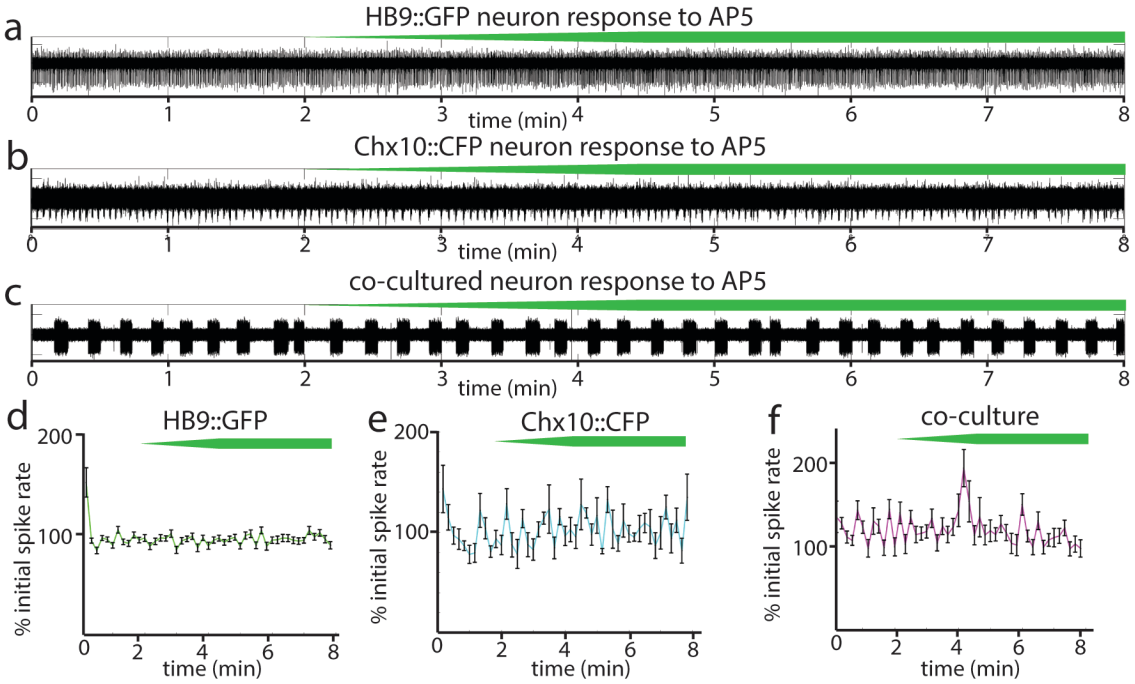

Figure 23. Responses of reticulospinal cultures to $NMDA_R$ blocker.

a-c Examples of high pass filtered MEA recordings of spiking neurons during wash-in of a 500µM solution of $NMDA_R$ blocker AP5 at 50µL/min (final AP5 concentration 50µM), green bars show approximate time course of AP5 wash-in. ***a***, Neuron from HB9::GFP^+ culture, ***b*** neuron from Chx10::CFP^+ culture, ***c*** neuron from HB9::GFP^+/Chx10::CFP^+ co-culture.

d-f, Normalized mean responses of all recorded neurons to AP5 wash-in, ***d*** HB9::GFP^+ cultures (n = 3), ***e*** Chx10::CFP^+ cultures (n = 3), ***f*** HB9::GFP^+/Chx10::CFP^+ co-cultures (n = 4).

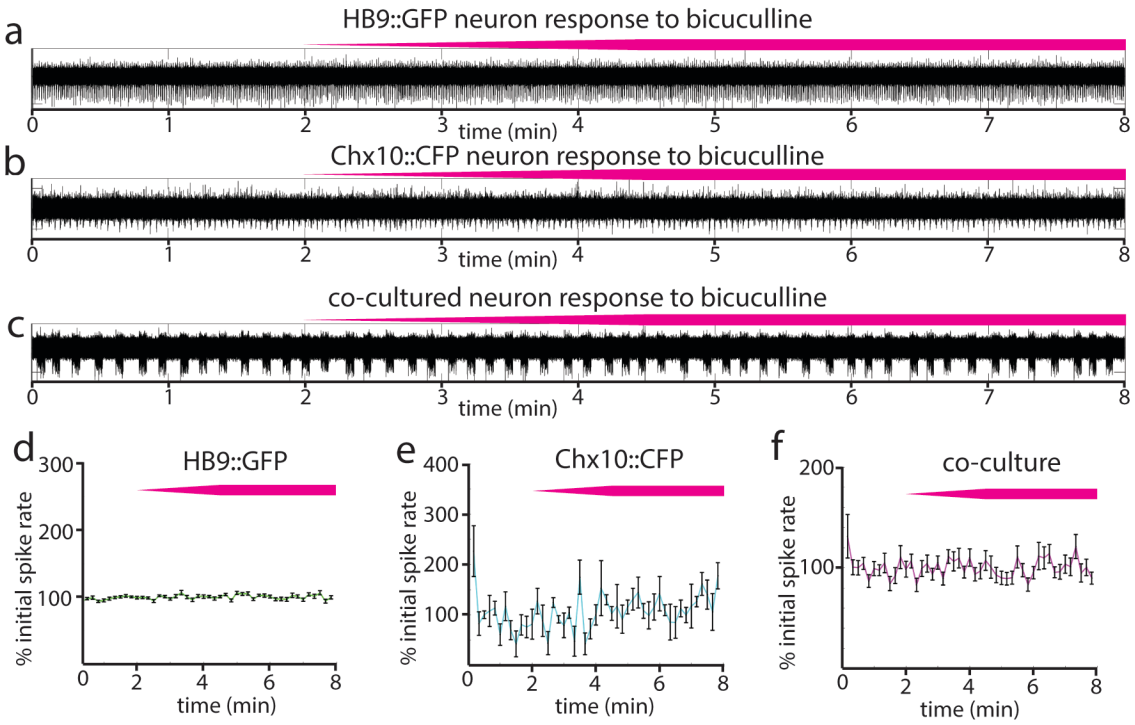

Figure 24. Responses of reticulospinal cultures to $GABA_AR$ blocker.

a-c Examples of high pass filtered MEA recordings of spiking neurons during wash-in of a 600µM solution of $GABA_AR$ blocker bicuculline at 50µL/min (final bicuculline concentration 60µM), magenta bars show time course of bicuculline wash-in. ***a***, Neuron from HB9::GFP^+ culture, ***b*** neuron from Chx10::CFP^+ culture, ***c*** neuron from HB9::GFP^+/Chx10::CFP^+ co-culture. **d-f** Normalized mean responses of all recorded neurons to bicuculline wash-in, ***d*** HB9::GFP^+ cultures (n = 3), ***e*** Chx10::CFP^+ cultures (n = 3), ***f*** HB9::GFP^+/Chx10::CFP^+ co-cultures (n = 4).

4.3.5 The effects of arousal neuromodulators on the reticulospinal circuit

The hindbrain reticular formation is known to be innervated densely by the orexinergic and noradrenergic systems that play important roles in mediating behavioral arousal throughout the brain (Jones 1985, Peyron 1998). Given that these neurons drive changes in locomotion, in which both $Chx10^+$ and motor neurons play an important part, we tested whether the cultures of these cells are able to respond to arousal neuromodulators. Thus, we tested the effects that the orexins, orexin A and orexin B, as well as the α_1 adrenoreceptor agonist L-phenylephrine have on $Chx10^+$ hindbrain neurons and the reticulospinal cultures.

We administered orexin A to $Chx10^+$ neurons while recording their membrane potentials using whole-cell patch clamp. Approximately 10% of the cells tested (n = 37) depolarized in response to local OxA application, whereas OxA application had a hyperpolarizing effect on 10% of the $Chx10^+$ neurons tested (figure 25 a,b). When $Chx10^+$ neurons were similarly tested for their response to Orexin B using whole cell patch clamp, we found that approximately 20% of the recorded neurons (n = 38) depolarized in response to OxB application, but that none had a hyperpolarizing response to OxB (figure 26 a,b).

Despite finding that some $Chx10^+$ neurons respond to the orexins, we found that neither orexin A (figure 25 d,g) nor orexin B (figure 26 d,g) had any effect on the spontaneous activity of $Chx10^+$ networks recorded on MEAs (linear mixed effects model OxA $\beta = 0.03$ $p = 0.18$, OxB $\beta = 0.032$ $p = 0.032$) or on co-cultured reticulospinal networks (figure 24 e, h, m, p) (linear mixed effects model OxA $\beta = 0.022$ $p = 0.08$, OxB $\beta = 0.002$ $p = 0.74$). Thus, the relatively small subpopulation of orexin-responding $Chx10^+$ neurons that we identified from patch clamp experiments were not sufficient to tune the spontaneous activity of the entire network.

Predictably, motor neurons did not respond to OxA application (figure 25 c ,f) (linear mixed effects model $\beta = -0.003$ $p = 0.23$). A modest positive effect of OxB on motor neurons

was observed in a few cases (n = 1) (linear mixed effects model $\beta = 0.107$ $p = 3.7e\text{-}40$), but this effect was not consistent across multiple cultures (n = 2) (linear mixed effects model $\beta = -0.005$ $p = 0.67$) (figure 26 c,f).

When we tested the effects of the α_1 adrenoreceptor agonist L-phenylephrine on $Chx10^+$ and motor neuron cultures, we observed divergent effects of this neuromodulator on both cell types. L-phenylephrine application drove a decrease in the inter-burst interval of about 33% of all active channels from $Chx10^+$ cultures (n = 15) (figure 27 a, c). In motor neurons on the other hand, L-phenylephrine drove a change in spiking activity from the characteristic loosely organized bursts to tonic, regular spiking in about 48% of active channels on MEAs (n = 56) (figure 27 e-f, i).

When we applied L-phenylephrine to reticulospinal cultures, we observed divergent effects on putative $Chx10^+$ and motor neurons in the culture. $Chx10^+$ neurons in the coculture, so classified because they immediately halted bursting when the $AMPA_R$ blocker CNQX was applied in a previous experiment, responded to L-phenylephrine by decreasing their inter-burst interval, much like $Chx10^+$ neurons alone (figure 27 b, d). Motor neurons in coculture, so classified because they had a transient period of tonic spiking following application of CNQX in a previous experiment, tended to stop adhering to network bursts when L-phenylephrine was applied and instead began to fire with tonic regularity, much like motor neurons cultured on their own (figure 27 g-h, j).

Figure 25. Responses of reticulospinal cultures to orexin A

a-b Examples of Chx10$^+$ neurons that response to orexin A application (1μM) (orange/yellow bars). ***a***, a Chx10$^+$ neuron that depolarizes in response to OxA, about 10% of all Chx10$^+$ neurons tested had an excitatory response to OxA (n = 37). ***b***, a Chx10$^+$ neuron that hyperpolarizes in response to OxA, about 10% of all Chx10$^+$ neurons tested had an inhibitory response to OxA. **c-e** Examples of high pass filtered MEA recordings of spiking neurons during wash-in of a 50μM solution of orexin A at 50μL/min (final OxA concentration 5μM), orange bars show approximate time course of OxA wash-in. ***c***, Neuron from HB9::GFP$^+$ culture, ***d***, neuron from Chx10::CFP$^+$ culture, ***e***, neuron from HB9::GFP$^+$/Chx10::CFP$^+$ co-culture.

f-h, Normalized mean responses of all recorded neurons to OxA wash-in (orange bar), ***f*** HB9::GFP$^+$ cultures (n = 3), ***g*** Chx10::CFP$^+$ cultures (n = 3), ***h*** HB9::GFP$^+$/Chx10::CFP$^+$ co-cultures (n = 2).

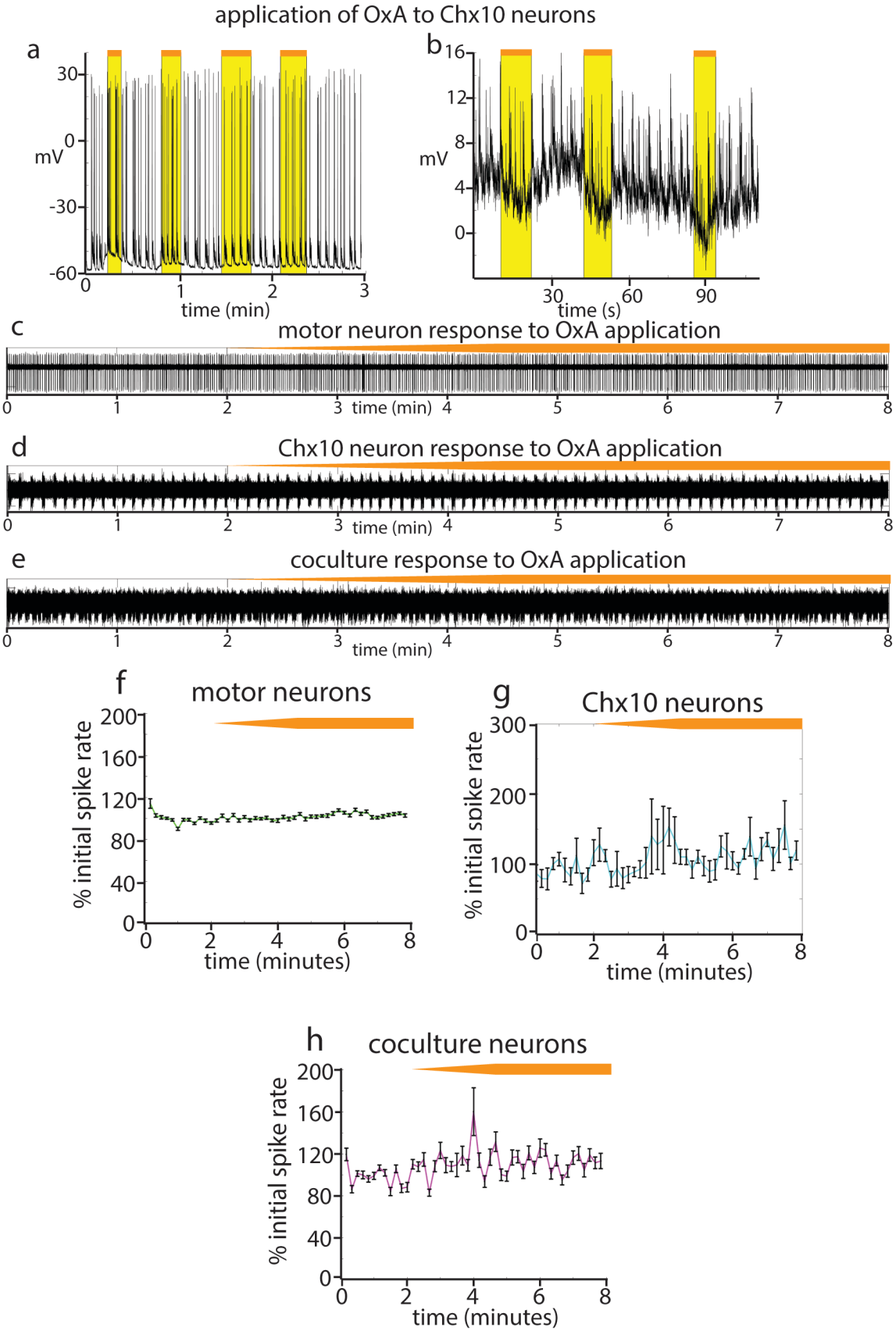
application of OxA to Chx10 neurons
a
30
0
mV
-30
-60
0
1
2
3
time (min)
b
16
12
8
mV
4
0
30
60
90
time (s)
c
motor neuron response to OxA application
0
1
2
3
time (min)
4
5
6
7
8
d
Chx10 neuron response to OxA application
0
1
2
3
time (min)
4
5
6
7
8
e
coculture response to OxA application
0
1
2
3
time (min)
4
5
6
7
8
f
motor neurons
% initial spike rate
200
160
120
80
40
0
0
2
4
6
8
time (minutes)
g
Chx10 neurons
% initial spike rate
300
200
100
0
0
2
4
6
8
time (minutes)
h
coculture neurons
% initial spike rate
200
160
120
80
40
0
0
2
4
6
8
time (minutes)

Figure 26. Responses of reticulospinal cultures to orexin B

a-b, examples of Chx10$^+$ neurons that depolarize in response to orexin B application (1μM) (orange/yellow bars). About 20% of all Chx10$^+$ neurons tested had an excitatory response to OxB, the remaining 80% did not respond to OxB application (n = 38).

c-e Examples of high pass filtered MEA recordings of spiking neurons during wash-in of a 50μM solution of orexin B at 50μL/min (final OxB concentration 5μM), orange bars show approximate time course of OxB wash-in. ***c***, Neuron from HB9::GFP$^+$ culture, ***d***, neuron from Chx10::CFP$^+$ culture, ***e***, neuron from HB9::GFP$^+$/Chx10::CFP$^+$ co-culture.

f-h Normalized mean responses of all recorded neurons to OxB wash-in (orange bar). ***f*** *upper panel*: HB9::GFP$^+$ cultures that do not respond to OxB wash-in (n = 2), *lower panel*: HB9::GFP$^+$ culture that had an excitatory response to OxB wash-in (n = 1). ***g***, Chx10::CFP$^+$ cultures (n = 3), ***h*** HB9::GFP$^+$/Chx10::CFP$^+$ co-cultures (n = 2).

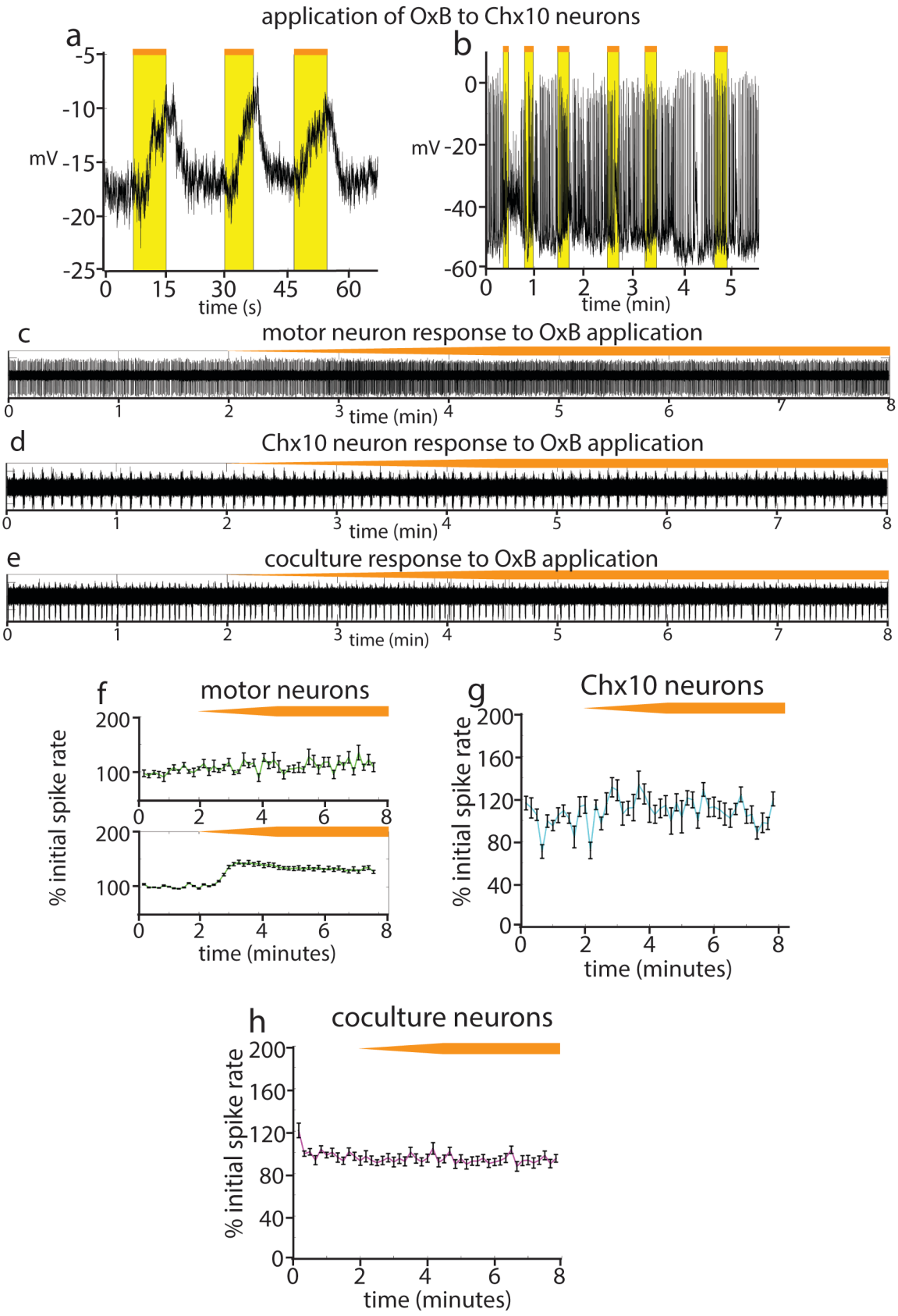
application of OxB to Chx10 neurons
a
mV
time (s)
b
mV
time (min)
c
motor neuron response to OxB application
time (min)
d
Chx10 neuron response to OxB application
time (min)
e
coculture response to OxB application
time (min)
f
motor neurons
% initial spike rate
time (minutes)
g
Chx10 neurons
% initial spike rate
time (minutes)
h
coculture neurons
% initial spike rate
time (minutes)

Figure 27. Responses to reticulospinal cultures to adrenergic α_1 receptor agonist L-phenylephrine.

a-b, examples of high pass filtered MEA recordings of neurons that increase their bursting rate in response to wash-in of a 3mM solution of L-phenylephrine at 50μL/min (final concentration 300μM), orange bars show approximate time course of L-phenylephrine wash-in. ***a***, Neuron from Chx10::CFP^+ culture, ***b***, neuron from HB9::GFP^+/Chx10::CFP^+ co-culture. ***c***, inter-burst interval of the $Chx10^+$ neuron from *a* decreases as L-phenylephrine is washed in (orange bar). ***d***, inter-burst interval of the co-culture neuron from *b* also decreases as L-phenylephrine is washed in.

e-h, examples of high pass filtered MEA recordings of neurons that switch from irregular or bursting activity to tonic spiking in response to L-phenylephrine application. ***e***, neuron from HB9::GFP^+ culture prior to L-phenylephrine application. ***f***, same neuron from *e* after L-phenylephrine wash-in (final concentration 500μM). ***g***, neuron from HB9::GFP^+/Chx10::CFP^+ co-culture prior to L-phenylephrine application. ***h***, same neuron from *g* after L-phenylephrine wash-in (final concentration 300μM). ***i***, spike rate of neuron from *e* and *f* over the course of L-phenylephrine wash-in (orange bar shows time course). ***j***, spike rate of neuron from *g* and *h* over the course of L-phenylephrine wash-in (orange bar).

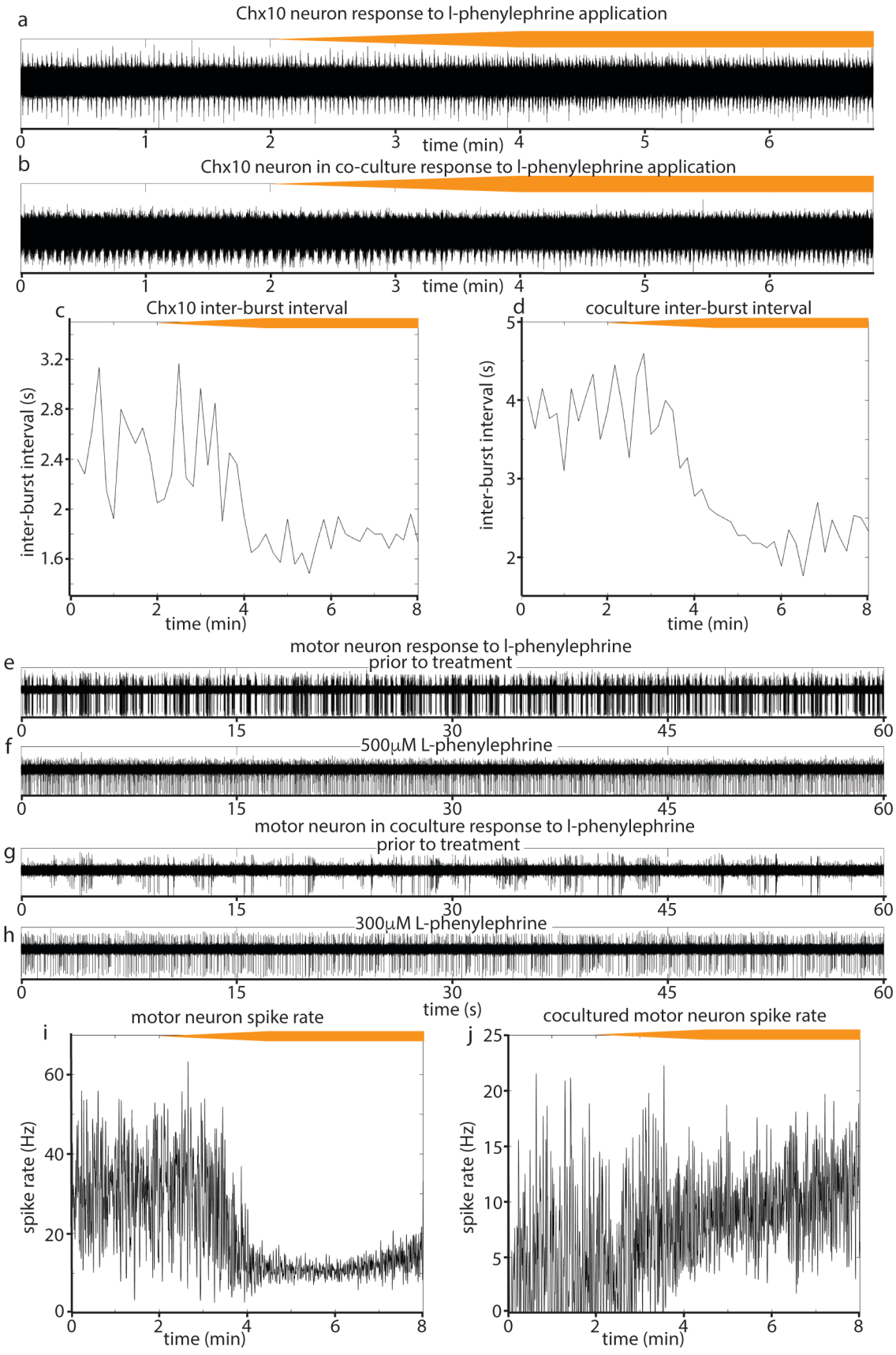
a
Chx10 neuron response to l-phenylephrine application
time (min)
b
Chx10 neuron in co-culture response to l-phenylephrine application
time (min)
c
Chx10 inter-burst interval
inter-burst interval (s)
time (min)
d
coculture inter-burst interval
inter-burst interval (s)
time (min)
motor neuron response to l-phenylephrine
e
prior to treatment
f
500μM L-phenylephrine
motor neuron in coculture response to l-phenylephrine
g
prior to treatment
h
300μM L-phenylephrine
time (s)
i
motor neuron spike rate
spike rate (Hz)
time (min)
j
cocultured motor neuron spike rate
spike rate (Hz)
time (min)

4.4 Discussion

4.4.1 Effect of cell sorting on electrophysiology of the isolated cells

FACS-sorted stem-cell derived $HB9^+$ motor neurons develop complex morphology and electrical excitability *in vitro* (Uzel 2016, Yang 2013, Haidet-Phillips 2011, Wichterle 2002), but it is unclear whether the nature of their electrical responses was altered by the significant amount of shear force that occurs during sorting. Our results on the electrophysiology of both sorted and unsorted $HB9^+$ neurons are consistent with prior measurements of the emergence of excitability in cultures of unsorted stem-cell derived motor neurons (Miles 2004). $HB9^+$ neurons cultured for 7 to 14 days *in vitro* following differentiation respond to a current injection step with a continuous spike train, express a voltage-gated Na^+ current (I_{Na}) in response to voltage step, and develop spontaneous spike trains. FACS sorting was found to have no significant effect on any of these electrophysiological features. Thus, FACS did not appear to alter the excitability of $HB9^+$ spinal motor neurons. In addition, the presence of other neuronal subtypes and progenitors did not have an impact on these aspects of $HB9^+$ neuron development, indicating that they are at least partially determined by cell type identity.

We also used FACS to isolate Chx10::CFP^+ neurons from mouse embryonic hindbrains, which constitute about 3% of all hindbrain cells. Like $HB9^+$ motor neurons, sorted $Chx10^+$ cells developed spontaneous spike trains *in vitro*, which suggests that the sorting process did not irrevocably damage their intrinsic excitability. After 10 days in culture, these spike trains changed into regular rhythmic bursts of activity, something we did not observe for the cultured $HB9^+$ motor neurons. While there are no *in vitro* studies on unsorted hindbrain $Chx10^+$ neurons, this behavior is consistent with the observation that a closely related population of spinal V2a neurons develops spontaneous rhythmic activity following FACS isolation and reaggregation into three-dimensional “circuitoids” (Sternfeld 2017).

Taken together, these experiments demonstrate the viability of FACS for the isolation of molecularly defined neuronal subtypes and their subsequent long-term culture.

4.4.2 Cell type specific patterns of activity in cultures of sorted neurons

Several prior studies have arranged neurons on multielectrode arrays in very specific patterns (Maher 1999, Wheeler 2010), but not defined subtypes. The random patterning of molecularly defined cells on our arrays allowed us to explore whether there is a consistent influence of cell type on network behavior, regardless of network architecture.

Sorted $HB9^+$ motor neurons grow a dense network of projections in the dish, however culturing these neurons as a purified population was not sufficient for the development of spontaneous activity in these cultures, even after a month *in vitro*. When we modified our cultures to incorporate a basal astrocyte layer, the resulting neuronal networks developed spontaneous activity.

Other studies have demonstrated that astrocytes provide an essential support role for the survival and development of cultured neurons (Wang 1994, Boehler 2007), including motor neurons (Ullian 2004). One way that astrocytes mediate such an effect is by removing excess glutamate to prevent excitotoxicity (Rothstein 1996, Swanson 1997). Adding astrocytes to our cultures thus supports the survival and development of the $HB9^+$ neurons without introducing other neuronal cell types that could alter network activity.

We did not observe any spontaneous activity in a series of parallel MEA recordings of cultures containing only astrocytes, though these cultures had some slow waves of calcium activity. These calcium waves were consistently reported in astrocyte culture by various groups and do not directly contribute to recorded electrophysiological activity (Scemes 2006).

The primary firing pattern of $HB9^+$ neurons co-cultured with astrocytes in this system was uncoordinated spike trains. This contrasts with a previous study where culturing unsorted $HB9^+$ neurons resulted in the emergence of coordinated network bursts (Jenkinson 2017). Jenkinson *et al's* cultures additionally contained a minority of $GAD1^+$ GABAergic inhibitory interneurons. Studies of network bursts in cultured cortical neurons have demonstrated that blocking GABA currents causes network burst synchronization to fall apart, suggesting a key role for inhibitory interneurons in this process (Li 2007). The discrepancy in the activity patterns observed between the two motor neuron culture conditions suggests that inhibitory cell types also contributed meaningfully to the generation of network bursts in $HB9^+$ cultures.

By contrast, we found that $Chx10^+$ neurons isolated by FACS and cultured on a confluent layer of astrocytes developed robust and highly coordinated network bursting activity. Our results from calcium imaging highlighted in figure 20 indicate that virtually all $Chx10^+$ neurons participate in simultaneous network bursts. This behavior sharply contrasts with that of neurons in the $HB9^+$cultures that, despite being adjacent to one another, did not appear to have any coordination between their spontaneous calcium spikes.

4.4.3 Chx10-like pattern of activity is dominant in co-culture

Recordings from the $Chx10^+/HB9^+$ co-culture indicate that $Chx10^+$ neurons impose their rhythmic bursting phenotype on adjacent $HB9^+$ motor neurons (figure 21d). In this way, we were able to induce motor neurons to participate in network bursts by exposing them only to excitatory stimulation. Purified cultured $HB9^+$ motor neurons did not coordinate their spontaneous calcium spikes despite being adjacent to each other. Thus, $HB9^+$ motor neurons do not require GABAergic cells to fire in burst-like pattern, but they appear to require patterned input from another cell type. In contrast, $Chx10^+$ hindbrain neurons are able to generate their

own patterns of activity without need for exogenous cell types besides astrocytes. In summary, our results indicate that when cultured with astrocytes, electrically excitable cell types develop different spontaneous patterns of activity that appear to be cell type dependent.

Our observation that Chx10$^+$ neurons are able to impose patterned activity on motor neurons is consistent with their *in vivo* function of driving rhythmic behaviors like hindlimb locomotion and respiration. The strong rhythmicity that we observed in *in vitro* cultures of hindbrain Chx10$^+$ neurons in the absence of external excitatory drive may itself be a particularly important feature of these neurons in driving rhythmic behaviors during early development before other motor control systems have fully formed. This would be consistent with the finding that ablation of hindbrain Chx10$^+$ neurons is maximally impactful on respiratory rhythms in newborn mice and that normal respiratory rhythms gradually reassert themselves as the mice grow older (Crone 2012).

4.4.4 The Chx10/motor neuron coculture recapitulates aspects of reticulospinal circuits

Our finding that hindbrain Chx10$^+$ neurons can impose rhythmic patterning on co-cultured motor neurons has implications for the study and modeling of reticulospinal circuits, different aspects of which are currently being examined by multiple groups (Sternfeld 2017, Oueghlani 2018, Pivetta 2014).

In rodents, hindbrain Chx10$^+$ neurons receive inputs from the mesencephalic locomotor region (MLR) and their activation is associated with bouts of locomotion (Bretzner 2013). These neurons been implicated as a locomotor stop signal, since optogenetically stimulating Chx10$^+$ neurons in the rostral medulla halts ongoing locomotion (Bouvier 2015). Populations of reticulospinal neurons with a similar “stop” signal function have also been identified in the lamprey (Juvin 2016). This function is thought to be governed by synaptic inputs from the MLR rather than intrinsic properties of the reticulospinal neurons themselves, an idea that is supported

by the recent observation that simulating certain regions of the lamprey MLR halts ongoing locomotion as well (Gratsch 2019).

In addition to their involvement in hindlimb locomotion, hindbrain Chx10^{+} neurons appear to play a role in regulating respiratory rhythm. Total ablation of all Chx10^{+} neuron populations in the brainstem and spinal cord has lethal effects on respiratory rhythm (Crone 2008). Chx10^{+} neurons of the medial reticular formation have projections to the pre-Bötzinger complex and have been found to regulate respiratory rhythms in newborn mice (Crone 2012).

Unlike in rodents, where hindbrain Chx10^{+} neurons contact premotor networks within the spinal cord (Bouvier 2015), in the zebrafish hindbrain Chx10^{+} neurons directly contact spinal motor neurons. Selective stimulation of these neurons evokes swimming (Kimura 2013). An analogous population of neurons in *Xenopus* tadpoles within the Chx10^{+} dorsoventral hindbrain also provides patterned excitatory input directly to motor neurons that drives sensory-evoked swimming before other motor control systems have developed (Soffe 2009, Li 2019).

Since we are both lacking the full complement of other interneuron subtypes and their specific patterns of connectivity in dissociated coculture, we are unable at this time to recapitulate the full level of complexity of the Chx10^{+} reticulospinal locomotor control circuit,. Thus, it can be argued that the circuit created by our *in vitro* co-cultures replicates the basic circuitry found in fish and amphibians rather than the more complex murine system, where hindbrain Chx10^{+} neurons project to other intermediary motor control circuits and mediate more diverse effects on locomotion and respiratory rhythm. It would be interesting to determine whether the emergent properties of Chx10^{+} neurons from these species differ from the mouse, and how incorporating additional reticulospinal cell types would alter patterns of activity.

4.4.5 Synaptic properties driving the emergence of network bursts

Our results from applying a panel of synaptic blockers targeting AMPA, NMDA, and $GABA_A$ receptors to spontaneously active $HB9^+$ and $Chx10^+$ neuron cultures (figures 22-24) show that the $AMPA_R$ blocker CNQX effectively blocked all bursts in $Chx10^+$ cultures and significantly decreased the activity in $HB9^+$ neuron cultures. This is consistent with the observation that spinal motor neurons cultured *in vitro* form glutamatergic synapses that are entirely blocked by CNQX (Ullian 2004). CNQX application similarly eradicates spontaneous network bursting in cultures of spinal $Chx10^+$ neurons that are otherwise insensitive to glycine and GABA antagonists (Sternfeld 2017).

These findings also suggest that the rhythmicity of $Chx10^+$ neurons is an emergent property of the network rather than a cell-autonomous feature of this cell type. This contrasts with true pacemaker neurons, such as those of the pre-Bötzinger complex, where bursts are intrinsic to individual cells, and therefore insensitive to the same cocktail of synaptic blockers (Chevalier 2016). Furthermore, the finding that CNQX also blocks motor neuron activity suggests that these neurons form functional synapses onto one another, even though their resultant activity is not as exquisitely synchronized as with $Chx10^+$ neurons. Thus, it appears that even the same $AMPA_R$-dependent mechanism can generate drastically different phenotypes within two different cell types.

In addition to bursts being an emergent property of the $Chx10^+$ culture, we also observed that the coculture exhibited an emergent property that was not present in cultures of individual subtypes. When we applied CNQX to the $Chx10^+/HB9^+$ coculture some recorded neurons switched from rhythmic bursting to a transient period of tonic spiking before gradually becoming quiescent. A potential explanation of this observation is that $HB9^+$ neurons within the culture revert to their native tonic spiking phenotype in the absence of the driving influence of network

bursts. This is consistent with our calcium imaging data in which we identified $HB9^+$ neurons in coculture that continued to have calcium spikes even in the presence of a dose of CNQX that effectively disrupted network bursts (figure 22).

Cultured neurons are known to use many different mechanisms to generate rhythmic bursting activity (Golowasch 1999, Marder 2001). In bursting cultures that contain inhibitory interneurons, $GABA_A$ currents play a key role in network synchronization and burst rate. But whereas in some cases bicuculline application causes network synchronization to completely fall apart (Li 2007), in other rhythmically active networks, bicuculline drives a significant increase in burst frequency (Black 2017, Jenkinson 2017, Zhang 2009, Lonardoni 2017). We observe that although inhibition is vital for balancing the excitability of glutamatergic neurons, inhibitory interneurons are not necessary for the generation of rhythmic activity among excitatory neuron networks. In lieu of inhibitory interneurons, the astrocytes present in our cultures could provide an important check on runaway glutamatergic excitation that allows for patterned activity to arise in $Chx10^+$ neuron cultures. Astrocytes are known to express the Na^+-dependent glutamate transporters GLAST and GLT-1 and thus maintain a low level of extracellular glutamate in neuronal cultures that prevents excitotoxicity (Rothstein 1996, Swanson 1997).

In rhythmically active cultures of glutamatergic neurons, NMDA receptors have been found to be important for mediating underlying spike synchronization, while AMPA receptor activation provides synaptic drive that fuels overall activity (Lonardoni 2017). The broad silencing of spontaneous network bursts that we observed following application of the $AMPA_R$ blocker CNQX is consistent with others' results on cultures of bursting spinal motor circuitoids (Sternfeld 2017), ventral horn neurons (Zhang 2009), and cortical neurons (Bonzano 2006).

More puzzling is the lack of effect that the $NMDA_R$ blocker AP5 had on any of our cultures. Perhaps among the motor neurons, which had a low degree of synchrony to begin with,

$NMDA_R$-dependent mechanisms play a very minimal role in spontaneous network activity. Electrical coupling is important for coordinating the activity of a subset of spinal $Chx10^+$ interneurons (Ha 2018), so it is possible that the related hindbrain $Chx10^+$ population employs a similar mechanism to synchronize activity. We observed that CNQX application stopped $Chx10^+$ network bursts, but that this inhibition was abrupt and not accompanied by any breakdown in burst structure. This is consistent with the hypothesis that AMPA receptor activation drives overall network activity without affecting synchronization.

4.4.6 A subset of $Chx10^+$ neurons is modulated by orexins

The reticular formation is a target of orexinergic innervation originating from the lateral hypothalamus (Peyron 1998). We found that for about 10% of $Chx10^+$ hindbrain neurons, orexin A (OxA) application resulted in depolarization of their membrane potential while in another 10% this resulted in membrane potential hyperpolarization. orexin B (OxB) application, on the other hand, caused about 20% of recorded $Chx10^+$ neurons to depolarize and we did not observe any cases in which OxB application resulted in $Chx10^+$ membrane potential hyperpolarization. OxA has an equal affinity for Ox1 and Ox2 receptors, while OxB has a 10-fold greater specificity for Ox2 over Ox1 receptors (Sakurai 1998). Given the divergent effects that OxA and OxB have on $Chx10^+$ neurons, we hypothesize that Ox1R activation results in $Chx10^+$ neuron membrane hyperpolarization while Ox2R activation causes membrane depolarization, but more detailed experiments are needed to confirm this result. Activation of these two orexin receptors is known to have different behavioral effects; Ox1 receptors are associated with the maintenance of arousal and wakefulness whereas Ox2 receptors mediate responses to environmental stimuli (Sears 2013).

Despite the fact that a subset of $Chx10^+$ neurons respond to the orexins, neither OxA nor OxB administration had an effect on the overall network activity of the neurons recorded on the

MEA (figure 25-26). As our patch clamp results demonstrate, the majority of Chx10$^+$ neurons are insensitive to the orexins. These neurons' contributions to network activity appear to be sufficient to overwhelm those of the relatively small subpopulation of orexin-sensitive Chx10$^+$ neurons. However, within an intact nervous system that retains a specific wiring pattern and complement of additional interneuron subtypes, this subset of orexin-sensitive Chx10$^+$ neurons likely plays a more outsize role in relaying orexin arousal signals to spinal locomotor circuits. This result demonstrates that there remains significant molecular diversity even within the relatively constrained population of Chx10$^+$ hindbrain neurons, further exploration of which could shed more light on their relationship with arousal neuromodulators and behavioral role in the intact nervous system.

The response of motor neurons to orexin application was more variable. For the most part, these neurons did not respond to either OxA or OxB, but in one culture we observed a consistent increase in spiking activity in response to OxB administration. Orexinergic neurons are known to contact a wide range of motor control systems and OxB$^+$ terminals have been found adjacent to orofacial motoneuron pools (Zhang 2002, Hu 2015). So, it is possible that the positive effect of OxB that we observed in this isolated case was due to the presence of a small but prominent population of motor neurons with a more cervical identity in this culture.

4.4.7 The role of norepinephrine in the Chx10$^+$ reticulospinal circuit

Both motor and Chx10$^+$ neurons changed their spontaneous activity patterns in response to the α_1 adrenoreceptor agonist L-phenylephrine. L-phenylephrine caused spiking motor neurons to switch from a pattern of irregular bursting and occasional spiking to a more regular tonic spike train with concomitant decrease in spike rate variability (figure 27). Chx10$^+$ neurons, on the other hand, responded to L-phenylephrine by increasing their burst rate but otherwise not altering the temporal pattern of their activity.

Norepinephrine is an important arousal neuromodulator that selectively amplifies the gain of sensory evoked signals in the brain (Berridge 2003, Bouret 2005, Mather 2016). That a subset of hindbrain Chx10$^+$ neurons respond to the noradrenergic receptor agonist L-phenylephrine suggests that this reticulospinal population integrates arousal-related information in its descending locomotor commands. High frequency stimulation of the noradrenergic locus coeruleus has been found to cause reversible behavioral arrest in mice (Carter 2010), which is consistent with downstream activation of the Chx10$^+$ reticulospinal circuit and its proposed role as a locomotor stop signal (Bouvier 2015).

We also observed that upon exposure to L-phenylephrine, motor neurons enter a state of tonic activation. Activation of the α_1 adrenoreceptor is known to increase motor neuron excitability and enhance their tendency to enter a state of bistability (Conway 1988, Lee 1999). When a neuron is in a bistable state, a transient burst of excitation is sufficient to yield long-lasting activation that can only be reversed by subsequent inhibitory input. Because our cultures lack this inhibition, motor neurons stimulated by synaptic connections to their neighbors are prompted to enter a state of tonic excitation that persists for the duration of L-phenylephrine exposure.

In the reticulospinal co-culture condition, we observed that some neurons respond to L-phenylephrine by increasing their burst rate, much like the Chx10$^+$ cultures, while others responded like motor neurons by switching from bursting to tonic firing. This suggests that the coculture condition does not alter each cell type's native response to L-phenylephrine. Furthermore, it appears that the state of enhanced excitability that L-phenylephrine induces in putative motor neurons is sufficient to overcome the network bursting of the reticulospinal culture, thereby causing the motor neurons that were previously bursting in time with their Chx10$^+$ neighbors to enter a state of tonic activation in which they are effectively desensitized to

any additional excitatory input (figure 27g-h). Thus, although excitatory neurons are able to generate network bursts in the absence of inhibitory interneurons, some source of inhibition is required in order to stabilize the network in the face of chemical perturbation.

4.5 Conclusions and outlook

In this study, we demonstrated that $HB9^+$ spinal motor neurons and $Chx10^+$ hindbrain reticulospinal neurons develop cell type-specific patterns of network activity *in vitro* and that in a co-culture of the two cell types, the $Chx10^+$ pattern of activity dominates. Our results show that even with a simplified reticulospinal culture that consists of randomly interconnected $Chx10^+$ and $HB9^+$ motor neurons, we can recreate some important functions of reticulospinal $Chx10^+$ neurons in driving rhythmic motor activity.

A significant portion of spinally projecting hindbrain $Chx10^+$ neurons are localized to the medullary gigantocellular nucleus (NGC) (Bretzner 2013, Bouvier 2015). We identified subpopulations of hindbrain $Chx10^+$ neurons that modulate their activity in response to orexins and the noradrenergic agonist L-phenylephrine, suggesting that NGC reticulospinal projections play a role in mediating arousal-induced locomotion. This finding constitutes important evidence that the NGC not only receives arousal related inputs from the periphery, but also sends an arousal signal directly to spinal motor effectors to drive rapid changes in behavior, thereby acting as a neuronal substrate for generalized arousal.

The suprachiasmatic nucleus (SCN) of the hypothalamus transmits a circadian sleep switch signal to the orexinergic lateral hypothalamus. We speculate that one way that such circadian signals are relayed from the SCN to spinal cord locomotor circuits is by way of the orexin-sensitive reticulospinal NGC neurons that we identified in this study. In the next chapter, we seek to explore this link between circadian rhythms and generalized arousal *in vivo* by using a high throughput assay that measures the voluntary motor activity of freely behaving mice.

Chapter 5. Circadian transitions in Generalized Arousal

5.1 Introduction

Generalized arousal (GA) is operationally defined as a behavioral state characterized by increases in (i.) voluntary motor activity, (ii.) sensitivity to sensory stimuli, and (iii.) emotional reactivity (Pfaff 2006). A series of behavioral assays that take this definition into account have been used to measure changes in GA in rodents following various manipulations (Arrieta-Cruz 2007). In the GA assay developed by Arrieta-Cruz *et al*, a mouse's total voluntary motor activity was measured using an automated home cage monitoring system that calculates the number of infrared beam crossings in the horizontal and vertical directions over a 24-hour time period. This same system was also used to measure motor responses to different kinds of sensory stimuli, including a tactile air puff stimulus, exposure to a benzaldehyde solution olfactory stimulus, and vestibular stimulation via rotation of the entire home cage on an orbital shaker. Emotional reactivity was then assessed using a fear conditioning paradigm in which a foot shock was paired with various contextual cues in a test chamber separate from the home cage.

This sort of three-pronged approach was found to be more sensitive to changes in GA than the standard SHERPA screen for neurological phenotype changes (Rogers 1997). Weil *et al* demonstrated that it is possible to selectively breed mice with high and low arousal as measured by this behavioral paradigm, suggesting that this measure of GA has a heritable, genetic basis (Weil 2010). The GA assay has been further used to study the effects of anoxia, food restriction, and sex hormone administration on GA (Arrieta-Cruz 2007, Shelley 2007, Chu 2015). Notably, these studies found significant differences in arousal behaviors across the circadian cycle, particularly in measures of voluntary motor activity.

Of the three measures of GA applied in this paradigm, the voluntary motor activity assay is most easily and readily assessed across individuals. Typically, motor activity in rodents is assayed using running wheels. However, as a source of environmental enrichment, running

wheels can introduce sometimes-confounding variability into circadian data. Mice allowed access to running wheels display a shorter free running circadian period (τ) than activity-restricted individuals (Edgar 1991, Koteja 2000, Yasumoto 2015). The diameter of the running wheel used has been found to have an effect on total motor activity and phase delay in response to a light pulse (Deboer 2000). Wheel running in rodents is also considered to be a model of aerobic exercise in humans, a behavior only indirectly correlated with behavioral arousal. Thus, the home cage monitoring of infrared beam crossings used here is supposed to provide a more accurate estimate of an animal's level of arousal than the running wheel assay.

The aforementioned studies using Arrieta-Cruz's GA assay paradigm measured changes in voluntary motor activity over hours and days, but this same assay has also been used to examine behavior on a much finer timescale. Even during active periods, mouse behavior is characterized by bursts of high motor activity followed by brief rest periods. Proekt *et al* determined that these rest times follow a power law distribution that is consistent with a scale-invariant process occurring near the critical point of a behavioral transition (Proekt 2012). This study demonstrates just some of the richness of information available from the automated home cage motor behavior monitoring assay, which can be run on a large cohort of individuals for weeks at a time.

The voluntary motor activity of C57BL/6J mice kept in a schedule of 12 hours of light followed by 12 hours of darkness reveals clear differences in the amount of spontaneous activity during the light phase when the animal is resting, and the dark phase when the animal is usually active (Antle 2016). During the light phase mouse behavior is dominated by sleep dynamics, whereas their behavior during the dark phase is consistent with a critical point near a behavioral transition (Proekt 2012). This suggests that the animal is in a state of low GA during the light phase, and high GA during the dark phase. Therefore, we conclude that the increases and

decreases in motor activity observed when the lights turn off and on correspond to generalized arousal transitions.

In this study we developed an algorithm that applied unbiased selection criteria to distinguish between these low arousal and high arousal states, smoothed the highly granular behavioral data, and found that the behavioral transitions between these two states took on a sigmoidal shape that could be fit to a logistic function using only three parameters. Such parameterization allows us to take a more nuanced look at voluntary motor activity that, in addition to measuring the gross motor output, also takes into account the timing of the behavioral transition onset and the slope of said transition. This equation was robust across individuals and could be applied to both the light-to-dark and dark-to-light transitions, suggesting that the underlying process is time reversible.

We applied this analysis to motor activity data from mice maintained in constant darkness, gonadectomized mice, and mice maintained on a "five and dime" schedule meant to emulate naval watch schedules that have been implicated in several recent high profile accidents at sea (CNN), with five hours of darkness followed by ten hours of light, and asked whether our parameterization paradigm could detect more subtle changes in the GA of these individuals compared to controls.

5.2 Methods

5.2.1 Animal Subjects

Experiments used 64 C57BL/6J mice, 8-9 weeks of age. Mice were individually housed with food and water *ad libitum*. Animals were grouped into experimental cohorts and were placed in different light/dark conditions, which consisted of (1.) the control condition, a regular 12:12 hour light/dark cycle with lights on at 7 pm (n = 48), (2.) total darkness (DD) (n = 8), and (3.) a "five and dime" 5/10 hour dark/light cycle (n = 8). 24 mice kept in the regular light

dark/cycle underwent castrations (n = 8), ovariectomies (n=8), or sham surgeries (n = 8) after 6 weeks to assess the effects of reduced testicular and ovarian hormones on the behavioral transition between the light and dark periods. All surgical procedures were performed under isoflurane anesthesia (2-5% in 100% O_2). All animal procedures and protocols were approved by the Rockefeller Institutional Animal Care and Use Committee.

5.2.2 Behavioral Analysis

Generalized Arousal Assay Chambers.

We used the VersaMax monitor system paired with a VersaMax analyzer (AccuScan Instruments Inc) to automatically collect motor activity data for singly housed mice continuously over 6-8 weeks by detecting infrared beam breaks from a set of 48 horizonal and vertical sensors distributed in a 1cm grid across an acrylic cage, as described in Arrieta-Cruz et al (2007). Measures of movement were recorded and analyzed using a 3D home cage monitoring system, which allowed for the use of a maximum of 32 specially constructed GA assay chambers.

Measuring Motor Activity.

Three parameters for motor activity were collected using the VersaMax software (version 3.41). These are horizontal activity (HACTV), the number of horizontal sensor beam interruptions in 60 seconds, total distance (TOTDIST), the continuous distance traveled in cm in 60 seconds, and vertical activity (VACTV), the number of vertical sensor beam interruptions in 60 seconds. Motor activity was monitored automatically, and the recordings were analyzed on a daily and weekly basis. Prior to testing each behavioral condition, each mouse was kept for 6-9 weeks in the control condition (12-hour light/dark), followed by 6 additional weeks in their respective experimental condition where applicable. In this way, each individual served as its own internal control, apart from 8 pre-gonadectomized mice from the Jackson Laboratory (JAX). Since the measure of VACTV is contaminated by animals reaching for water and is thereby a

less reliable indicator of arousal, we focused on the measure of HACTV for all subsequent analyses.

5.2.3 Light/Dark Cycles

To set the times for the light/dark cycle we used a 24-hour TORK digital time switch with 14 on-off possibilities for precision control of the lighting in each individual cage (TORK ES101A/ES103A/ES120A, Tork Inc). Both transitions, from lights on to lights off (L to D) and from lights off to lights on (D to L), were assessed where applicable.

Regular Light/Dark. Lights were scheduled to turn on at 7 pm and off at 7 am each day for the duration of the experiment. The 24-hour cycle allowed these settings to carry over into the following weeks without disturbance.

Total Darkness (DD). Mice were first kept in the regular light/dark 12:12 cycle for 5 weeks. They were then switched to DD for 5 weeks, during which the digital time switch was kept off. Afterwards, they were reverted to a regular light/dark 12:12 cycle for another 5 weeks to examine recovery.

"Five and Dime". As in the DD experiment, mice were first kept in the regular light/dark 12:12 cycle for 5 weeks. Using the same 24-hour digital time switch, the 14 on-off times were set such the lights remained on for 10 hours and off for 5 hours. This 15-hour cycle was intended to emulate one of the U.S. Navy's most common watch rotations, the "five and dime" watch rotation, one of many traditional watch schedules that disregard the body's natural circadian rhythm (Shattuck 2016). After 5 weeks on the "five and dime" cycle, mice were reverted to a regular light/dark 12:12 cycle for another 5 weeks to examine recovery.

5.2.4 Gonadectomies

4 C57BL/6J female mice were ovariectomized (OVX) and 4 C57BL/6J male mice were castrated (CAS). 4 C57BL/6J female mice and 4 C57BL/6J male mice underwent sham

operations, as well. All mice were kept in the regular light/dark 12:12 cycle in the generalized arousal assay for 6 weeks prior to surgery, then another 6 weeks following surgery. Additionally, in order to compare the fidelity of the impact of gonadectomies on the behavioral transition, 8 mice that had undergone ovariectomies and castrations with the Jackson Laboratory (JAX) were also assayed in the regular light/dark 12:12 cycle for 6 weeks. Similar results allowed for combining and averaging the two gonadectomized groups during analysis.

5.2.5 Data analysis

Equation and Curve-Fitting

Data were collected on a weekly basis, converted to excel spreadsheets, and analyzed in Matlab (see github.com/abubnys/GA_behavior_curvefits for specific scripts used). For each experimental condition, the raw HACTV and TOTDIST data for each mouse was smoothed using a spline function to reduce the impact of random noise. Then, the active period corresponding to the dark phase was identified algorithmically as a continuous period of 300 minutes in which the smoothed motor activity is greater than the standard deviation of the motor activity over the entire 24-hour period, taking into account brief breaks in activity that were less than 150 minutes long. For each behavioral transition from the inactive phase to the active phase we fit the interval of smoothed data from the last local minimum prior to the transition to the first local maximum following the transition. For each behavioral transition from the active phase to the inactive phase we fit the interval of smoothed data from the last local maximum prior to the transition to the first local minimum following the transition. Fitting was performed to a logistic sigmoid function (equation 4) by iterating through combinations of values for parameters t, k, and L to minimize the root mean squared error (rmse). These curve-fit parameters were then compared between experimental cohorts using a two-sample t-test. All curve-fit parameters are reported as cohort means with standard error.

Equation 4. $f(t) = \frac{L}{1+e^{-k(t-t_0)}}$

Actograms and Photoperiod Calculations

For each experimental condition, 48-hour actograms for individual mouse behavior over the duration of the experiment were generated to visualize the timing of circadian shifts in arousal. Sleep-wake behavioral transitions were algorithmically identified in these plots as described above and linear regression was performed using a linear polynomial function to fit these points to a line. The photoperiod corresponds to the slope of this line (τ). Actogram and photoperiod analysis was performed in Matlab (see github.com/abubnys/GA_actograms for specific scripts used).

5.3 Results

5.3.1 Circadian transitions can be fit to a logistic sigmoid function

The voluntary motor activity of eight male C57BL/6J mice kept on a 12-hour LD schedule (12 hours of light followed by 12 hours of darkness) was measured as the number of infrared beam breaks occurring over 60s intervals over 6 weeks of recording. Raw data for an individual mouse averaged over 24 hours shows a significant increase in voluntary motor activity corresponding with the onset of the dark phase and a subsequent decrease in activity when the lights turn back on (figure 28a).

To fit this data to a sigmoidal curve for each individual day's worth of data for each mouse, we smoothed the raw data using a spline function and algorithmically detected the active period in each 24-hour block of recording. For each behavioral transition from the inactive phase to the active phase (low/high), we took the smoothed data from the last local minimum prior to the transition to the first local maximum following the transition as the basis for curve fitting (figure 28b). For each behavioral transition from the active phase to the inactive phase (high/low), we used the smoothed data from the last local maximum prior to the transition to the

first local minimum following the transition as the basis for curve fitting to a logistic sigmoid function (figure 28c).

The relationship between each of the three parameters in equation 4 and the shape of the resulting sigmoidal curve is illustrated in figure 28d. The slope of the curve is defined by the parameter k, the height of the curve is defined by the parameter L, and the transition onset time is defined by the parameter t. The mean root mean squared error (rmse) for the sigmoidal fits of the low/high transition was 4.51 cm moved, with the majority of transitions fitting the logistic sigmoid function with an rmse between 1 and 3. For subsequent analyses, we excluded any curve fits that had an rmse greater than 5 on the basis that these were poor matches to the data.

Figure 28. Curve fitting of behavioral transitions in mouse voluntary motor activity.
a, example of the motor activity of a mouse over 24 hours. Mean motor activity averaged over one week of recording (——), motor activity after smoothing using a spline function (——), dark period corresponds to grey background. ***b***, to calculate the low/high arousal transition, the motor activity (——) stretching from an hour before to an hour after the lights turned off was smoothed using a spline function (°°°°) and then fit to a three-parameter logarithmic function that minimized the root mean squared error (——). ***c***, to calculate the high/low arousal transition, the motor activity in the hour immediately after the lights turned on was smoothed and fit to a logarithmic function as in *b*. ***d***, the logistic function that was fit to the behavioral transitions has one constant t_0, the starting point of the behavioral transition, and the three parameters that describe the shape of the curve. The parameter t describes the transition onset time, k describes the transition slope, L describes the height of the curve.

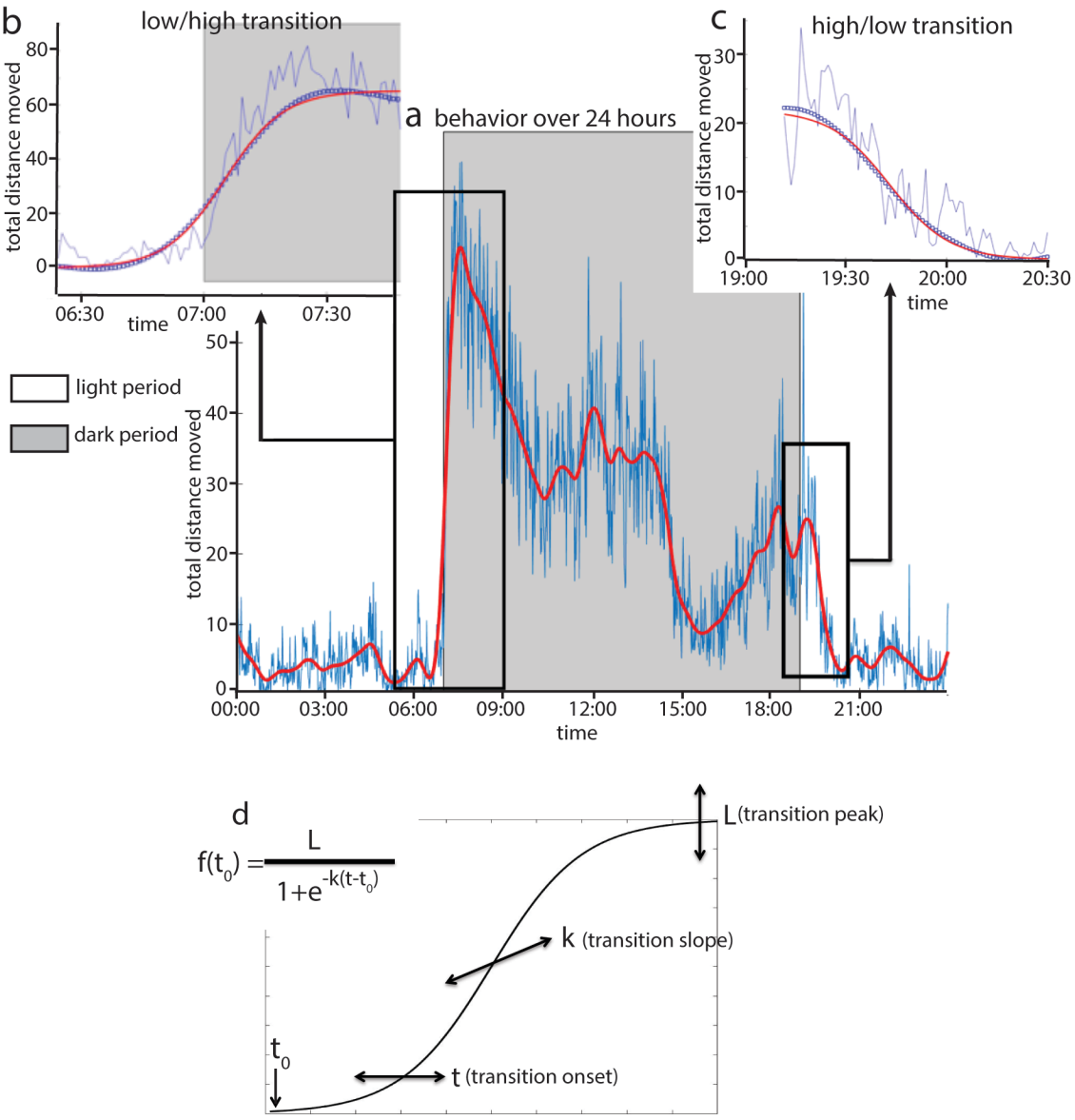
b
low/high transition
total distance moved
time
c
high/low transition
total distance moved
time
a behavior over 24 hours
light period
dark period
total distance moved
time
d
L(transition peak)
k (transition slope)
t (transition onset)

5.3.3 Comparison of low/high and high/low arousal transitions

We took the total horizontal motor activity of mice kept in 12-hour LD and fit the low/high and high/low transitions in this data to see if these transitions conformed to the sigmoidal form and whether the shape of the sigmoid was symmetric for each type of transition. There is some variability among individuals, but overall their low/high transitions (figure 29a) and high/low transitions (figure 29b) for four representative individuals from this group conform to the sigmoidal shape. We then sought to determine whether these two behavioral transitions were similar by comparing the parameters for the sigmoidal fits within the full cohort of eight mice tested.

After excluding any fits that had an rmse greater than 5, we found that both the high/low and low/high transitions could be fit to the logistic sigmoid function, and that the rmse for high/low fits was slightly but significantly higher than for the low/high fits (mean low/high rmse: 2.11±0.114 , mean high/low rmse: 3.18±0.104, two sample t-test p-value: 1.08×10^{-11}) (figure 29c). The transition onset *t* was not significantly different between the low/high and high/low transitions (mean low/high *t*: 4.44±0.57, mean high/low *t*: 3.64±0.74, p-value: 0.39), indicating that the onset of transition following behavioral maximum/minimum was the same for both kinds of transitions (figure 29d). The transition slope *k* was significantly higher for high/low than low/high (mean low/high *k*: 0.14±0.004, mean high/low *k*: 0.16±0.005, p-value: 3.014×10^{-4}), indicating that the high/low transition was steeper than low/high (figure 29e). The transition peak *L* was significantly lower for high/low than low/high (mean low/high *L*: 142.3±6.45, mean high/low *L*: 116.7±4.56, p-value: 0.0015), indicating that the maximal activity at the start of the high/low transition was lower than that at the end of the low/high transition (figure 29f).

Figure 29. Time reversibility of behavioral transitions of mice in 12-hour LD.
a, the low/high transitions of four individual mice at the onset of the dark phase follow a sigmoidal curve (°°°°) that can be fit to the logistic function (—). ***b***, the high/low transitions of the four mice from *a* at the onset of the light phase follow the same sigmoidal curve (°°°°) in reverse that can be fit to the logistic function (—).

c-f comparison of the parameters of the curve fits from low/high versus high/low transitions. ***c***, the minimized root mean squared error (rmse) is significantly lower for the curve fits of low/high transitions. ***d***, the transition onset parameter (t) is the same for both transition types. ***e***, the transition slope (k) is significantly lower for the high/low transition. ***f***, the transition peak (L) is significantly lower for high/low transition.

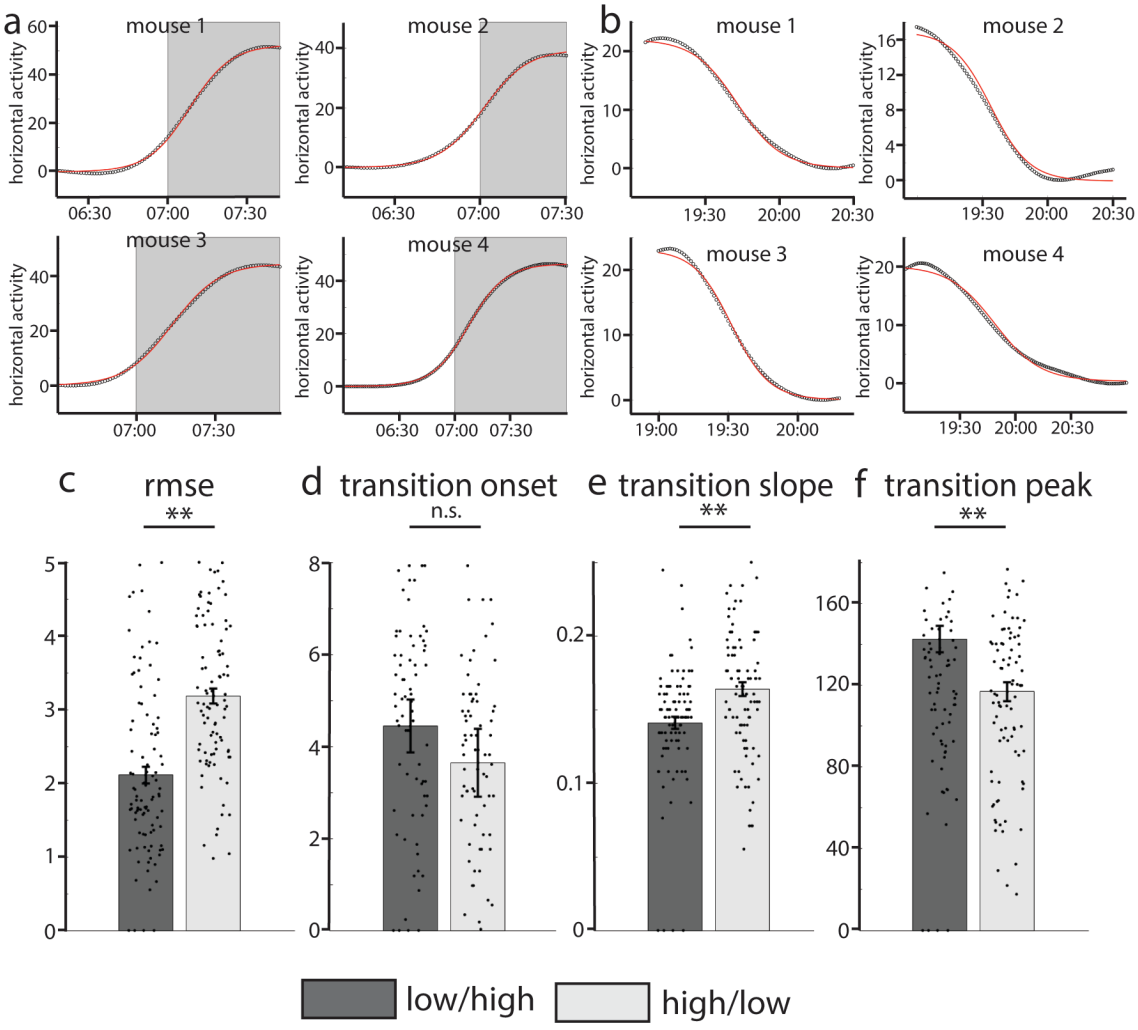
a
mouse 1
mouse 2
mouse 3
mouse 4
horizontal activity
06:30
07:00
07:30
b
mouse 1
mouse 2
mouse 3
mouse 4
horizontal activity
19:00
19:30
20:00
20:30
c rmse
**
d transition onset
n.s.
e transition slope
**
f transition peak
**
low/high
high/low

5.3.4 Behavioral transitions in constant darkness

The sigmoidal shape of the arousal transitions in voluntary motor activity of mice kept in a 12-hour LD schedule could be driven by the sudden changes in lighting conditions when the lights turn on and off at the end of a simulated "day". In order to determine whether the circadian transitions of mice could be modeled by the logistic sigmoid function in the absence of light entrainment, we measured the voluntary motor activity of mice kept in constant darkness for six weeks and analyzed their low/high behavioral transitions using the same methods as described above.

When mice were kept in 12-hour LD, they had much higher levels of voluntary motor activity during the dark period than during the light period when they would typically be asleep. When this regime was switched to constant darkness, the mice retained this same pattern of sleeping and waking and the switch between sleeping and waking phases was still readily distinguishable. There was some individual variability in the free-running circadian period during the six weeks of constant darkness. Some mice retained a circadian period close to 24 hours that meant that their wake times did not shift significantly over the course of the constant darkness experiment (figure 30a), whereas other individuals' wake times gradually shifted to an earlier time each day, indicating that their free-running circadian period was somewhat less than 24 hours (figure 30b). However, overall the free-running period of the cohort of mice tested did not deviate significantly from 24 hours (paired sample t-test p-value: 0.29).

The algorithmically detected arousal transitions for mice in constant darkness (DD) conformed to the sigmoidal form. However, the shape of this curve differed when the mice were kept in constant darkness conditions compared to 12-hour LD (figure 30c). The transition onset t was significantly higher for mice in DD (mean LD t: 5.58±0.46, mean DD t: 8.004±0.5, two sample t-test p-value: 0.0014), indicating a delay in transition onset (figure 30d). The transition

slope *k* was not significantly different across both conditions (mean LD *k*: 0.136±0.003, mean DD *k*: 0.134±0.003, p-value: 0.5881) (figure 30e). The transition peak *L* was significantly lower for mice in DD (mean LD *L*: 150±5.64, mean DD *L*: 98.9±3.25, p-value: 3.67e-16) (figure 30f). This was consistent with the significant decrease in overall horizontal distance moved for mice in DD (mean LD horizontal activity: 72±0.19, mean DD horizontal activity: 38.9±0.1, p-value: 0).

Figure 30. Arousal transitions in mice kept in constant darkness.

a,b, actograms of two individual mice over the course of the experiment, mice were kept on a 12-hour light-dark schedule (LD) for five weeks, then switched to constant darkness (DD) for 5 weeks, then switched back to LD for 5 weeks. They retained defined active and sleep periods in DD, but for the individual in *b*, the start time of the active period shifted to an earlier time each day, indicating a free-running circadian period less than 24 hours. ***c***, mean low/high transition for a mouse in LD (—) versus DD (—).

d-f comparison of the parameters of the curve fits for high/low in LD versus constant darkness. ***d***, the transition onset (t) is significantly lower for mice in LD. ***e***, the transition slope (k) is the same under both conditions. ***f***, the transition peak (L) is significantly lower for mice in constant darkness.

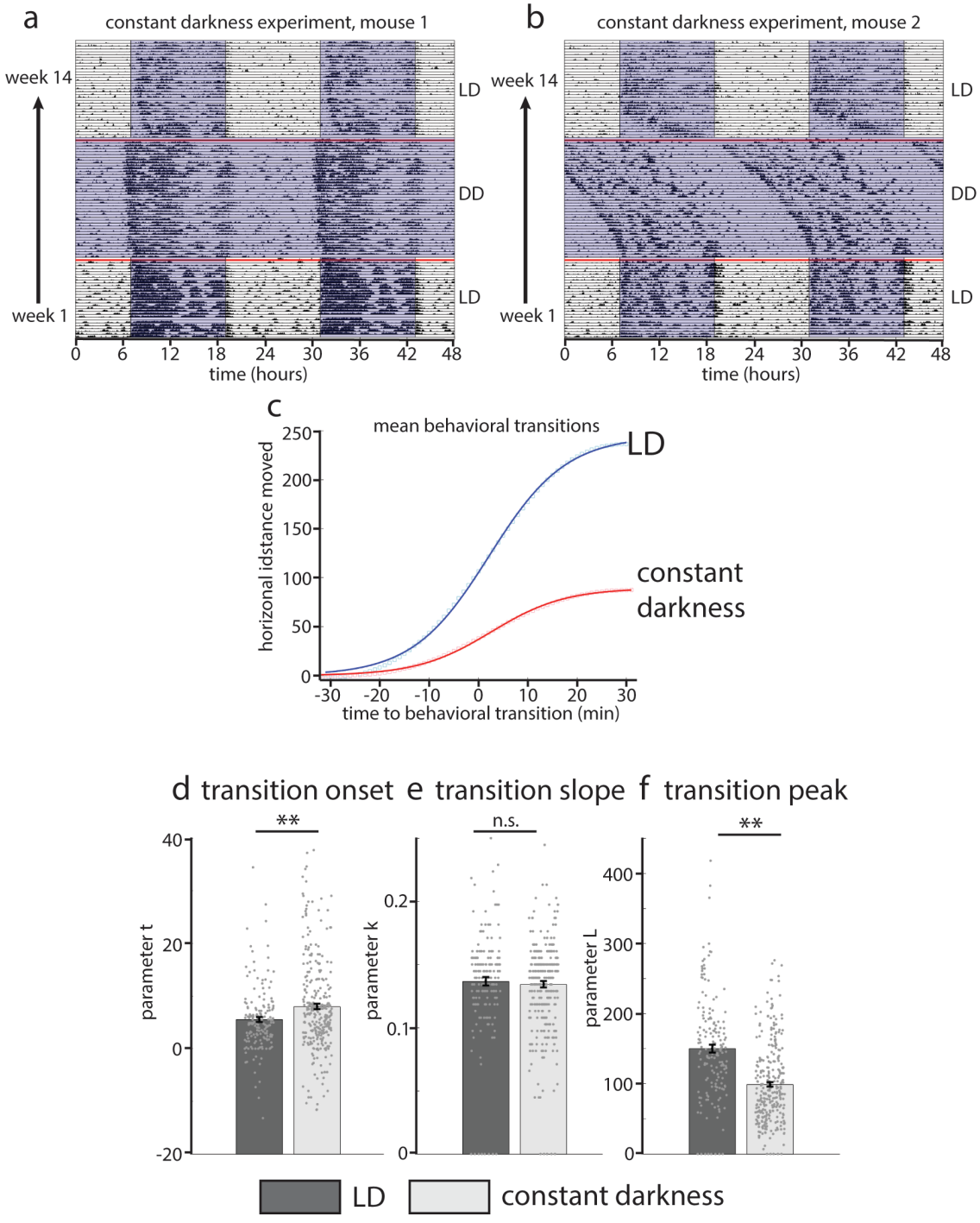
a
constant darkness experiment, mouse 1
week 14
week 1
LD
DD
LD
0 6 12 18 24 30 36 42 48
time (hours)
b
constant darkness experiment, mouse 2
week 14
week 1
LD
DD
LD
0 6 12 18 24 30 36 42 48
time (hours)
c
mean behavioral transitions
horizonal idstance moved
250
200
150
100
50
0
LD
constant darkness
-30 -20 -10 0 10 20 30
time to behavioral transition (min)
d transition onset
e transition slope
f transition peak
parameter t
40
20
0
-20
**
parameter k
0.2
0.1
0
n.s.
parameter L
400
300
200
100
0
**
LD
constant darkness

5.3.5 Effect of gonadectomy on behavioral transitions

Sex hormones are known to play a role in generalized arousal. Gonadectomies of male and female mice reduce running wheel activity, while knockout of the estrogen receptor ERα reduces arousal responses to sensory stimuli (Garey 2003, Daan 1975). We performed a series of gonadectomies and sham surgeries on male and female mice and used our curve fitting of voluntary motor activity paradigm to measure the effect that these treatments have on their low/high transitions when kept in 12-hour LD.

The full cohort of male and female mice had a significantly smaller mean low/high transition curve after gonadectomy (GNX) compared to their behavior prior to surgery (intact) (figure 31a). Breaking this observation down further, the transition onset *t* was significantly higher after gonadectomy (mean intact *t*: 5.29±0.347, mean GNX *t*: 7.39±0.297, two sample t-test p-value: 5.62e-5) (figure 31b). The transition slope *k* was not significantly different after gonadectomy (mean intact *k*: 0.142±0.002, mean GNX *k*: 0.139±0.002, p-value: 0.312) (figure 31c). The transition peak *L* was significantly lower after gonadectomy (mean intact *L*: 148.25±3.8, mean GNX *L*: 77.89±1.73, p-value: 6.37e-69) (figure 31d). By contrast, sham surgery did not have a significant effect on the low/high behavioral transitions for the mixed gender cohort of mice (figure 31e). All three of the parameters for the sigmoidal curve fits had no significant change following sham surgery; transition onset *t* mean intact: 5.52±0.38, mean sham: 5.44±0.83, p-value: 0.944, transition slope *k* mean intact: 0.141±0.002,mean sham: 0.146±0.005, p-value: 0.368, transition peak *L* mean intact: 158.69±4.58,mean sham: 149.15±10.28, p-value: 0.439 (figure 31f-h).

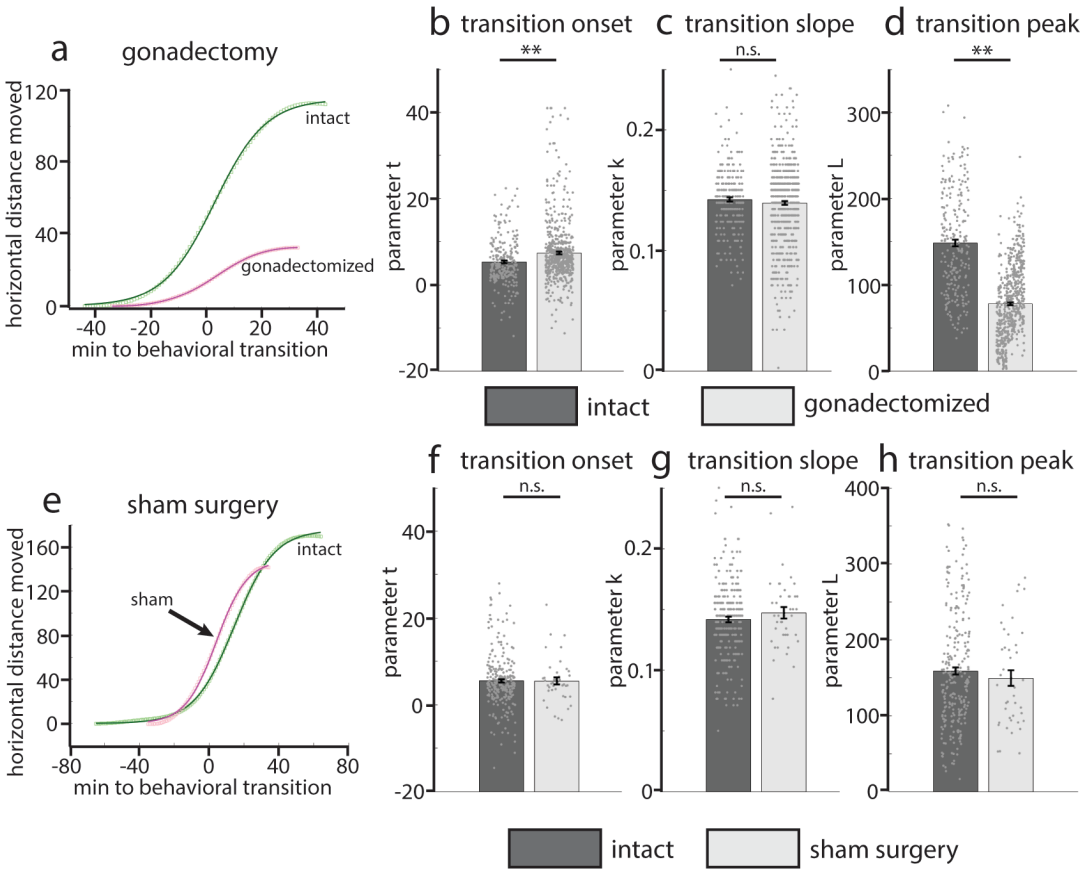

Figure 31. The effects of gonadectomy on low-to-high arousal transitions in a mixed gender cohort.

a, the mean low/high transition for mice prior to (—) and following (—) gonadectomy. **b-d**, comparison of the parameters of the curve fits for low/high in intact (before surgery) and gonadectomized mice. ***b***, the transition onset (*t*) is significantly higher in gonadectomized individuals. ***c***, the transition slope (*k*) is unchanged following gonadectomy. ***d***, the transition peak (*L*) is significantly lower in gonadectomized individuals.

e-h analysis of the effects of sham surgery on low/high transitions. ***e***, the mean low/high transition for mice prior to prior to (—) and following (—) sham gonadectomy surgery. ***f***, the transition onset (*t*), ***g***, transition slope (*k*), and ***h*** transition peak (*L*) are all unchanged by sham surgery.

We did not observe significant differences between males and females prior to gonadectomy (figure 32a). The sigmoidal fit parameters for the males versus the females were as follows: transition onset *t* mean females: 5.37±0.44, mean males: 5.22±0.54, p-value: 0.831, transition slops *k* mean females: 0.144±0.002,mean males: 0.139±0.003, p-value: 0.128, transition peak *L* mean females: 152.54±5.35,mean males: 144.02±5.41, p-value: 0.264 (figure 32b-d). After gonadectomy, there were no significant sex differences in the transition onset *t* (mean female *t*: 8.168±0.71, mean male *t*: 8.027±0.62, p-value: 0.88) (figure 32f). There were also no significant sex differences in the transition slope *k* (mean female *k*: 0.14±0.004, mean male *k*: 0.138±0.004, p-value: 0.702) (figure 32g). However, the transition peak *L* was significantly higher in gonadectomized males than in females (mean female *L*: 48.32±2.74, mean male *L*: 66.09±2.98, p-value: 1.55e-5) (figure 32h).

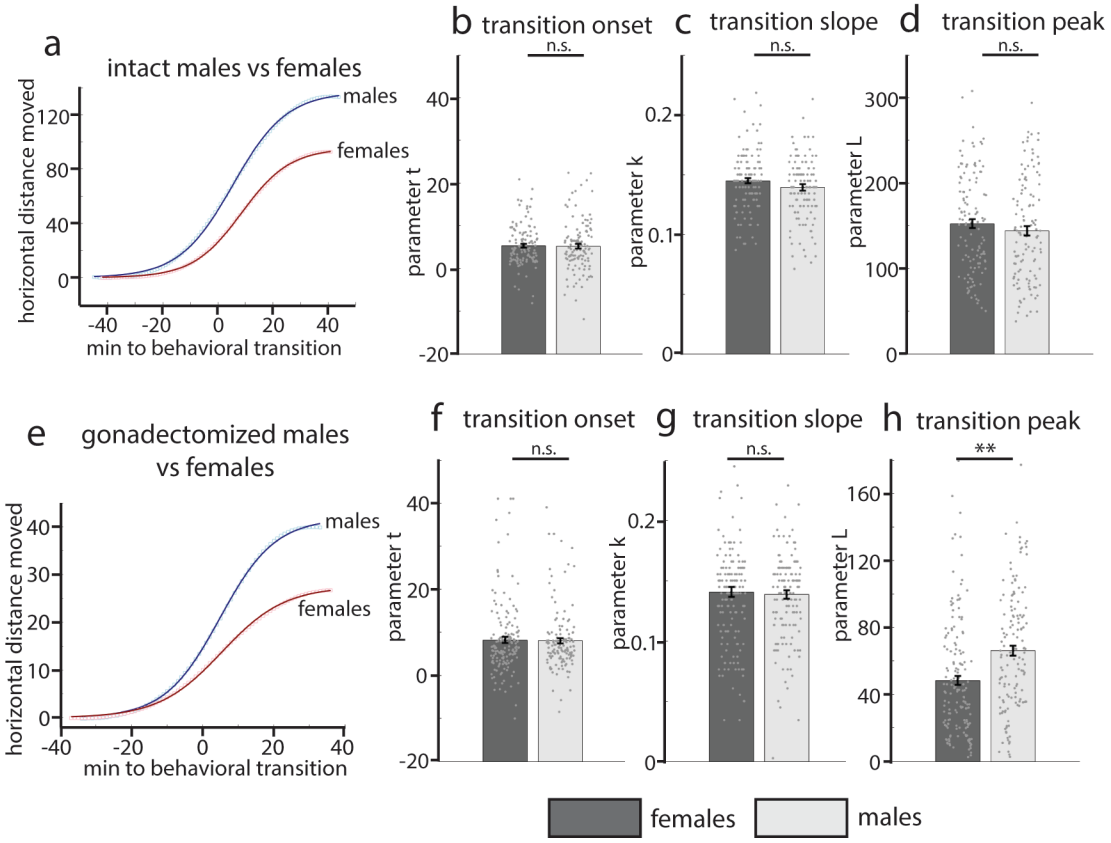

Figure 32. Sex differences in the low-to-high arousal transition prior to and after gonadectomy.

a-d, sex differences between intact male (—) and female (—) mice. ***a***, the mean low/high transition for male (—) and female (—) mice. ***b***, the transition onset (*t*), ***c***, transition slope (*k*), ***d***, transition peak (*L*) are the same between males and females.

e-h, sex differences between gonadectomized male (—) and female (—) mice. ***e***, the mean low/high transition for male (—) and female (—) mice after surgery. ***f***, the transition onset (*t*) and ***g***, transition slope (*k*) are the same between males and females. ***h***, the transition peak (*L*) is significantly lower for gonadectomized females than males.

5.3.6 Behavioral transitions in a "five and dime" schedule

The "five and dime" (5/10) schedule adopted by the US navy has been implicated in a number of accidents at sea in recent years (CNN). We subjected mice to this schedule of 10 hours of light followed by 5 hours of darkness and assessed their low/high transitions to ask whether this kind of schedule would have significant impacts on the behavioral transitions of mice that are adapted to a 24-hour circadian day.

Compared to mice kept on a 12/12 schedule (figure 33a), the voluntary motor activity patterns of mice kept on the 5/10 schedule are disrupted and do not align with the onset of dark periods (figure 33b). However, actograms of the activity of mice on the 5/10 schedule reveal that their motor behavior still retains an underlying periodicity (figure 33c,d). The circadian period of mice on the 5/10 schedule was measured to be approximately 24.87±0.08 hours. This is significantly higher than the free-running period of mice kept in constant darkness (mean period in DD: 23.97±0.04, two sample t-test p-value: 6.72×10^{-6}) (figure 33e).

On the other hand, when we fit the low/high behavioral transitions of mice on the 5/10 schedule to the logistic sigmoid function, they were fairly similar in shape to the transitions of mice on a 12/12 schedule (figure 33f). There were no significant differences in transition onset t (mean t in 5/10: 5.66±0.41, mean t in 12/12: 4.97±0.43, p-value: 0.373) (figure 33g). The transition slope k was slightly smaller for mice on the 5/10 schedule (mean k in 5/10: 0.138±0.002, mean k in 12/12: 0.149±0.006, p-value: 0.0189) (figure 33h), as was transition peak L (mean L in 5/10: 134.63±3.87, mean L in 12/12: 155.395±7.3, p-value: 0.0104) (figure 33i).

Figure 33. Arousal transitions in mice on a "five and dime" schedule.

a, raw data for the horizontal activity of a mouse kept on a 12/12 schedule shows active periods aligned with the dark phase (grey shading). ***b***, raw data for the same mouse from *c* kept on a 5/10 schedule shows dysregulation of active periods. ***c-d***, actograms of two individual mice over the course of the experiment, mice were kept on a 12/12 hour LD schedule for 5 weeks, then switched to a 5/10 schedule of 5 hours of darkness followed by 10 hours of light for 5 weeks, then switched back to 12/12 LD for 5 weeks. ***e***, the mean low/high transition for mice on a 12/12 schedule (—) versus a 5/10 schedule (—). ***f***, the mean circadian period for mice in 5/10 was close to 25 hours, which is significantly higher than the free-cycling circadian period of mice kept in constant darkness. ***g***, the low/high transition onset (t) was not significantly different for mice on a 5/10 schedule compared to 12/12. ***h***, the transition slope (k), and ***i*** the transition peak (L) were significantly lower for mice on the 5/10 schedule.

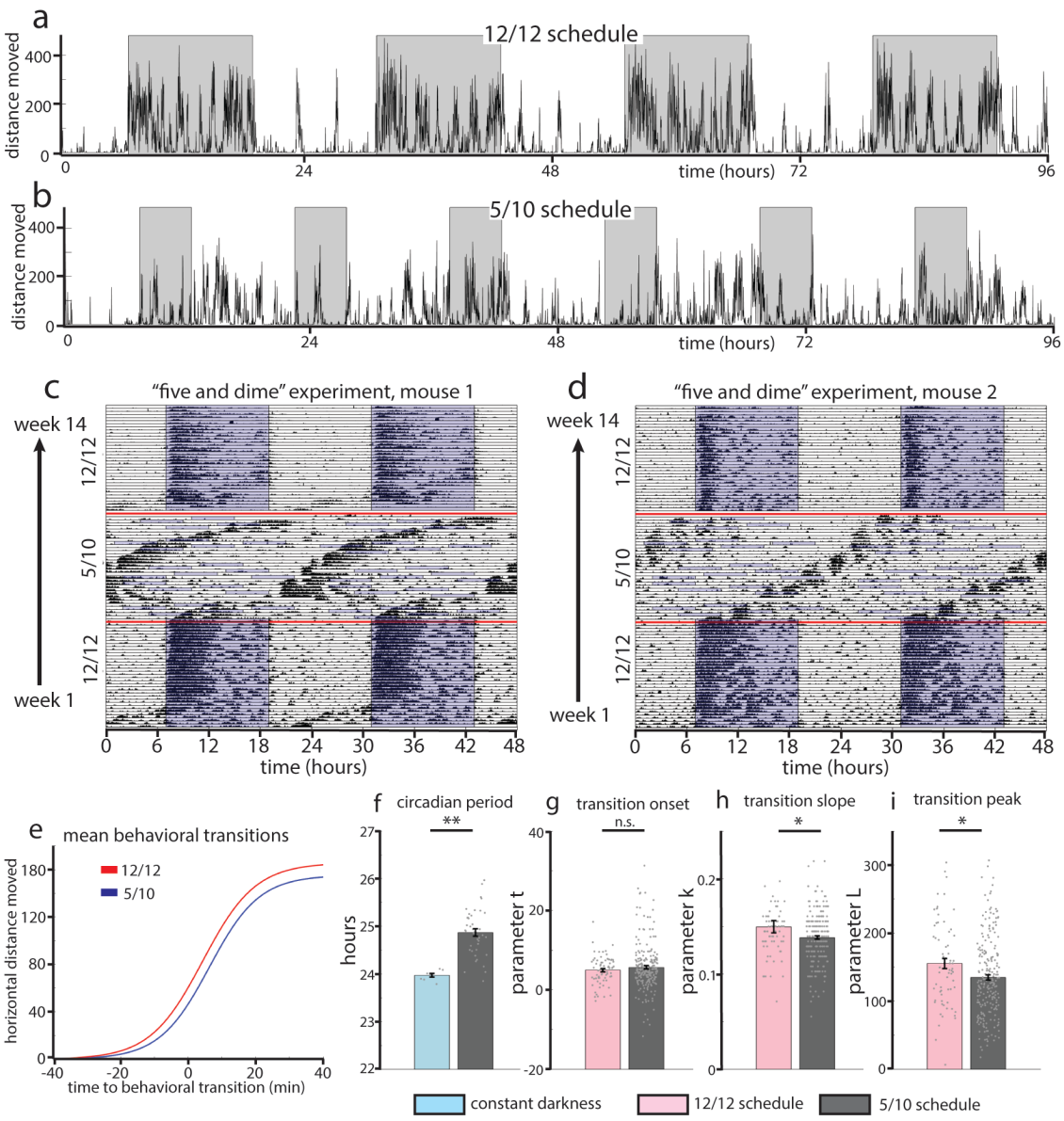
a
12/12 schedule
distance moved
400
200
0
0
24
48
time (hours)
72
96
b
5/10 schedule
distance moved
400
200
0
0
24
48
time (hours)
72
96
c
"five and dime" experiment, mouse 1
week 14
week 1
12/12
5/10
12/12
0
6
12
18
24
30
36
42
48
time (hours)
d
"five and dime" experiment, mouse 2
week 14
week 1
12/12
5/10
12/12
0
6
12
18
24
30
36
42
48
time (hours)
e
mean behavioral transitions
12/12
5/10
horizontal distance moved
180
120
80
40
0
-40
-20
0
20
40
time to behavioral transition (min)
f
circadian period
**
hours
27
26
25
24
23
22
g
transition onset
n.s.
parameter t
40
20
0
-20
h
transition slope
*
parameter k
0.2
0.1
0
i
transition peak
*
parameter L
300
200
100
0
constant darkness
12/12 schedule
5/10 schedule

5.4 Discussion

5.4.1 Arousal transitions can be fit to a logistic sigmoid function

The voluntary motor activity of nocturnal rodents like mice can be reliably differentiated into two phases, a period of high motor activity that happens at night and a period of quiescence that happens during the day. Mouse behavior during the active phase is consistent with a high level of generalized arousal, with the corollary that behavior during the quiescent phase corresponds to a low arousal state (Pfaff 2006, Proekt 2012). We hypothesize that circadian and endocrine manipulations known to affect generalized arousal drive changes in the dynamics of this endogenous transition between the low and high arousal states.

After smoothing noisy behavioral data, algorithmically identified behavioral transitions from low-to-high arousal and high-to-low arousal states could be fit to a logistic sigmoidal function with three parameters that describe the onset, slope, and amplitude of the transition curve. This curve fitting paradigm remained reliable across individuals and for the transitions from both low-to-high arousal states (low/high) and high-to-low arousal states (high/low), suggesting that the same fundamental process underlies these two behavioral transitions.

Although both the low/high transition that happens at the onset of the dark phase and the high/low transition that happens when the lights turn back on could be reliably fit to a sigmoidal curve, there were notable differences in the shape of these two behavioral transitions as measured by the curve fitting parameters used for each. Figure 29 illustrates that although the transition onset parameter t is the same for both transitions, the transition peak L was significantly lower for the high/low transition, while the slope k was significantly higher. If the high/low transition were merely the time reversed version of the low/high transition, we might expect that the slope of these transitions (k) would be the same even if the animal were starting at

a lower level of initial activity (*L*). So, our results suggest that slightly different processes underlie these two kinds of arousal transitions.

5.4.2 Removing photic cues affects arousal transitions

Photic cues are important for entraining circadian rhythms across many systems (Hastings 2018). When mice are kept on a schedule with alternating 12-hour blocks of light and darkness, their behavioral transitions closely align to the lighting schedule, which provides an important arousal cue. Switching the mice from a schedule with 12 hours of light and 12 hours of darkness (LD) to constant darkness (DD) did not affect the fidelity of the fit of the low/high transition to the three-parameter logistic sigmoid function. Thus, we can attribute the observed transition to underlying circadian influences rather than the arousing influence of the lights switching on and off. Although some individual mice had a shorter free-running period in DD (figure 30b), the average free-running circadian period of mice in DD was 23.9, not significantly different from mice in 12-hour LD. This data is consistent with other studies that show that the free running period of mice without running wheel access is close to 24 hours (Edgar 1991).

Even though they still conformed to the sigmoidal form, the low/high transitions of mice in DD had a distinctly different shape from their behavior in LD (figure 30c). In the absence of photic cues, there is a dramatic decrease in the magnitude transition peak *L* and also a more modest increase in the transition onset *t*. Notably, the actual slope of the transition *k* remained unchanged between both conditions. This suggests that the processes underlying *L* and *t* are dependent on photic cues whereas the arousal transition slope *k* is determined by some other mechanism independent of such cues.

5.4.3 Gonadectomy affects arousal transitions in a non sex-specific way

The effects of sex hormones on circadian behavior and generalized arousal are well documented. Changes in the mean, duration, and circadian period of running wheel activity in female mice are linked to their estrous cycle (Wollnik 1988) and gonadectomy of male and female nocturnal rodents causes a decrease in total motor activity that can be partially restored by the administration of testosterone and estradiol (Iwahana 2008, Blattner 2015). The changes in low/high transitions that we observed in mice following gonadectomy were broadly consistent with these findings. Gonadectomy induced a decrease in the transition peak *L* in males and females, with ovariectomized females exhibiting a greater effect than castrated males. Treatment also induced a significant increase in the transition onset *t* relative to intact mice, though this effect was not found to be sex specific. The slope of the transition *k* was unchanged by gonadectomy.

Castrated males generally exhibit a greater decrease in total running wheel activity than females (Kuljis 2013). Our finding that changes in *L*, a parameter that is related to total motor activity, were greater for females than males following gonadectomy seems to be at odds with this established view. However, the effects of gonadectomy on motor activity are not equally distributed across the circadian cycle. Male castration has been found to decrease the amount of activity at active bout onset, while subsequently increasing the activity peak that occurs towards the end of the active bout (Daan 1975). Furthermore, the majority of established findings on sex differences in circadian behavior were performed using running wheels, which only take into account voluntary exercise rather than total motor behavior as we have.

In addition to its dramatic effects on arousal activity peak, we also found gonadectomy to significantly increase the transition onset parameter, *t*. There are no sex differences in this parameter before or after gonadectomy. The behavioral basis for this parameter is not as clear as

that for *L*. Castration has been found to negatively impact the precision of active period onset to the start of the dark phase in males (Kuljis 2013). However, intact males have generally been found to have a greater precision of active period onset than females, a finding that is not reflected in the *t* of intact males and females in our study. So, it is likely that this parameter reflects some more complex aspect of behavior.

5.4.4 A five-and-dime schedule alters the timing, but not the shape of arousal transitions

Excessive fatigue has been cited as a contributing factor in up to 80% of naval accidents at sea (Cordle 2013). This issue has received increased attention recently in light of two high profile collisions involving the USS Fitzgerald and USS John S McCain in the summer of 2017. The "five and dime" shift work schedule traditionally adopted by the US Navy, in which five-hour watch shifts alternate with ten hour "off" periods during which sailors are expected to attend to all personal matters and get sufficient rest, has been found to be highly detrimental to vigilance and morale (Shattuck 2016). Because this schedule does not align with the 24-hour day, sailors are obliged to sleep at different times of day, resulting in reported fatigue and difficulty sleeping even when the amount allotted rest time is theoretically sufficient.

When we subjected mice to this kind of "five and dime" schedule, we found that their circadian transitions never aligned with the enforced schedule, even after five weeks (figure 33a,b). Instead, the mice entered a state of free-cycling behavior with a period approximately 24.8 hours long. This is significantly different from the intrinsic period of mice kept in constant darkness, which in our assay was close to 24 hours. Such phase shifting of mice on the 5/10 cycle is more consistent with a model of chronic jet lag. Humans have been found to undergo phase shifts of approximately 1 hour per day in response to jet lag, much like the mice in our experiment (Wever 1980). Following a return to the typical 12/12 schedule mice quickly

recovered their cycle alignment to the light and dark periods, indicating no long-term detrimental effects of the 5/10 schedule on circadian cycling.

Although the timing of circadian arousal transitions was strongly impacted under the 5/10 schedule, the overall shape of the low/high transitions remained remarkably intact (figure 33g). The transition onset *t* was unchanged by the 5/10 schedule, while there was a modest decrease in the transition slope *k* and the peak *L*. This shift in the arousal transition shape is notably different from that observed for mice in DD, which have a very dramatic decrease in *L* and a shift in *t*, but no change to the slope *k*. Our data suggests that even though mice in 5/10 do not adhere to photic cues, their behavior is nonetheless affected by the changes in lighting conditions that mice in DD are not exposed to.

Other studies investigating the health and behavioral effects of disrupted circadian schedules reveal that even though mice maintained on a 10/10 LD schedule do not experience significant sleep deprivation, their sleep quality and timing is nonetheless disturbed (Phillips 2015). The 10/10 schedule was also found increase immune vulnerability to environmental stress, drive weight gain, change leptin levels and increase the insulin/blood glucose ratio, and cause atrophy of the dendritic spines of pyramidal neurons of the prefrontal cortex along with associated decreases in cognitive flexibility and emotional control (Karatsoreos 2011). Mice exposed to repeated six-hour phase advances that model chronic jet lag experience a similar increase in immune system vulnerability to endotoxic shock despite no apparent sleep loss (Castanon-Cervantes 2010). Thus, even though we did not observe significant changes in the structure of the sleep-wake transition of mice in 5/10, it is likely that this schedule does drive other kinds of adverse immune, metabolic, and cognitive changes. It would be particularly interesting to compare how animals on the 5/10 schedule perform on cognitive tasks administered during their enforced dark phase versus their high arousal periods. We speculate

that cognitive ability is probably decreased across the board relative to 12/12 controls, but perhaps the mice in 5/10 would perform slightly better on tasks administered during their endogenous high arousal periods, thereby highlighting the importance of generalized arousal in behavioral outcomes.

5.5 Conclusions and outlook

In this study, we took voluntary motor activity data collected from mice in the same generalized arousal assay employed in previous studies and used it to examine transitions between low and high arousal states (Arrieta-Cruz 2007, Proekt 2012). We found that despite the intrinsic noisiness of the behavioral data, these arousal transitions have an underlying lawfulness to them that fit a logistic equation for a sigmoidal curve with only three parameters.

This is the first time that the change in behavior across the "phase transition" in arousal and activity, from the low activity state during the light period to the high activity state after the lights go out, has been described mathematically. Our results show that even a compact function such as equation 4 can provide a useful tool for analyzing the dynamics of behavioral arousal. The close adherence of the behavioral data to the theoretical curve means that there are fundamental units of behavior which submit to precise mathematical description.

Many biological processes, especially those associated with the growth of individuals or populations, adhere to a sigmoidal curve (Pearl 1920, Morrison 1997, Tjorve 2002, Chow 2011, Lampl 2012). Such curves can be divided into two phases, an initial period characterized by an exponential growth rate, and then a second asymptotic period of slowing and ultimate cessation of growth. This sigmoidal shape reflects the tendency of biological systems to move between relatively stable equilibrium states stabilized by either by the existence of a local energy minimum or environmental constraints. In the case of the arousal transitions described in this chapter, the sigmoidal curve likely captures the mouse's transition between two relatively stable

states, a low arousal state characterized by very little motor output, and a high arousal state characterized by faster and more frequent bouts of locomotor activity. Perhaps the sigmoidal shape of the transition between these two states reflects the progressive recruitment of motor output units, either among midbrain locomotor control regions like the MLR and NGC, or at the level of the spinal cord. Since there is a finite pool of such motor effectors, motor activity will ultimately taper off at some value determined by the physical and energetic constraints of the system, thereby generating the asymptotic shape of the sigmoid.

Of the three parameters in this equation that describe the arousal transition, we found that the curve height *L* was most sensitive to changes in behavioral conditions. Both constant darkness and gonadectomy drove robust decreases in *L* relative to control 12-hour light-dark conditions. Despite the dramatic differences in the shape of the arousal transitions of these mice, the slope of the transition *k* remained unchanged. One potential explanation for this finding is that different behavioral processes underlie the aspects of arousal transitions that are described by these two parameters.

Mechanisms for the normal transition of arousal and activity from light to dark periods clearly involve outputs from the suprachiasmatic nucleus (SCN) of the hypothalamus, responsible for light-gated circadian rhythms (Pauls 2016) which impact neurons in the lower brainstem reticular formation crucial for the initiation of many behaviors. Several routes serve to transmit signals from the SCN, including humoral signals (Silver 1996), but likely the strongest route is through the subparaventricular zone (SPZ) in the hypothalamus (Vujovic 2015), because SPZ axons impact the "sleep switch" (Saper 2001, 2005) and orexin neurons. In turn, orexin neurons project to medullary reticular formation neurons, which express orexin receptors (Martin 2011, Tabansky 2018, Bubnys, Pfaff and Tabansky, unpublished data). Some of these medullary reticular formation neurons are responsible for the initiation of locomotion (Peterson 1979,

Bretzner 2013, Capelli 2017), while other brainstem neurons regulate speed of locomotion (Caggiano 2018).

We hypothesize that the circuits involved in the initiation and speed of locomotion underlie the behavioral expression of the slope and maximum amplitude of the arousal transition, as quantified by the parameters k and L in our logistic sigmoidal equation. If this were the case, selectively manipulating the brainstem neurons that initiate locomotion may induce changes in k while leaving other aspects of the transition unaffected.

Through these experiments, we demonstrate how evolution has compressed a large amount of physiology into a compact equation. Future studies will hopefully shed more light onto how different aspects of arousal circuitry contribute to this mathematical description.

5.5.1 Robustness and generalized arousal

Given the fundamental role of generalized arousal in driving behavior, it is perhaps no surprise that the circadian arousal transitions that we quantified here are largely insensitive to environmental and endocrine disruption. The hindbrain circuits that underlie arousal are highly conserved and redundant to ensure that the failure of any one component of the system is not systemically catastrophic. We see similar concepts of robustness emerge in the *in vitro* and *in silico* components of this work as well.

In the cell culture study, we demonstrated that hindbrain Chx10^{+} neurons have intrinsic rhythmicity even when cultured outside of the context of the intact nervous system and its specific complement of cell types and connectivity. This suggests that these neurons could continue to mediate rhythmic behaviors like hindlimb locomotion and respiration even in the absence of other upstream or downstream behavioral control systems. Indeed, hindbrain Chx10^{+} neurons are among the first locomotor control systems to develop in the newborn zebrafish and provide important locomotor drive for sensory evoked escape behavior (Kimura 2013). Even

though we found that blocking AMPA receptors silences these neurons, the actual patterning of $Chx10^{+}$ neurons' bursts did not fall apart so much as get silenced for the duration of the block, which suggests that the mechanism governing the temporal patterning of bursts in these neurons is highly robust. This pattern of network bursting was also found to remain relatively stable throughout the lifetime of the culture.

Although we did not interrogate robustness in our modeling experiments *per se*, we did see evidence that some of our results are insensitive to variability in circuit connectivity. When we modeled the effects of local excitatory and inhibitory connectivity within the nucleus gigantocellularis (NGC) region, we found that we could generate a non-linear Yerkes-Dodson relationship between arousing sensory input and behavioral responsiveness even when the connectivity within the NGC was randomly assigned. This suggests that merely the existence of local connectivity within the NGC is sufficient to affect the responsiveness of the arousal system, without needing to specify any sort of precise wiring scheme or complex computational function within this region. We are currently working on building models of this arousal circuit that incorporate error and variability in both the wiring pattern and connection strengths between neurons in order to see how much error can be tolerated before the Yerkes-Dodson relationship falls apart for a given ratio of local excitation to inhibition.

5.5.2 Themes common to this entire work

Although the insights we derived from modeling arousal systems are largely theoretical and require further experimental characterization, we can draw some parallels between the *in silico* aspects of this work and the *in vitro* studies. We found that about one third of reticulospinal $Chx10^{+}$ neurons increase their burst rate upon application of a noradrenergic agonist, suggesting that these neurons have functional connectivity to the noradrenergic Locus Coeruleus. In parallel modeling experiments, we demonstrated that having recurrent connectivity

between the NGC and noradrenergic Locus Coeruleus (LC) resulted in the LC retaining a greater influence over spinal cord activation than the NGC/generalized arousal pathway. The modeling in this case provides a plausible explanation for why the LC-to-NGC connection exists and what functional role it plays, and provides a framework for designing future behavioral and neuroanatomical experiments.

Another insight gained from our modeling efforts is that adding extra sources of descending corticospinal control yields a circuit that is less responsive to generalized arousal signals propagated via the reticulospinal tract. Similarly, when we applied the noradrenergic agonist to Chx10/motor neuron cocultures, this additional source of descending motor control eroded the power that Chx10 neurons had over motor neuron activity. While under baseline conditions, Chx10 neurons imposed their bursting pattern of activity on neighboring motor neurons, the noradrenergic agonist effectively severed this connection and caused motor neurons to switch from bursting to tonic spiking.

Lastly, our results from model four in chapter two suggest that the NGC needs to function as an integrator of many diverse inputs both from the environment and midbrain arousal systems in order to rapidly disseminate a generalized arousal signal to the rest of the nervous system. Our experiments with the hindbrain $Chx10^{+}$ neurons suggest that even this molecularly and spatially restricted population is functionally diverse. Only about a third of these neurons respond to the noradrenergic agonist, while another twenty percent respond to orexin A or orexin B. Of the neurons that responded to orexin A, about half depolarized while the other half underwent membrane hyperpolarization upon orexin application. Preliminary single cell RNAseq analysis of the hindbrain $Chx10^{+}$ population also indicates that it can be further subdivided into up to eight separate clusters (Bubnys, Pfaff and Tabansky, unpublished data). The apparent molecular diversity of hindbrain $Chx10^{+}$ neurons means that, as a whole, these neurons can respond to a

wider array of potential stimuli than a more homogeneous population might. However, further neuroanatomical characterization of the input-ouput structure of this population is required to determine whether the NGC is indeed integrating all of its inputs equally.

Continued logical explorations of the generalized arousal system using CNS modeling techniques are likely to suggest parameters for future electrophysiological experiments, both in cell culture and the intact nervous system. For instance, future work with reticulospinal circuits on MEAs of the sort we have constructed could incorporate more complex geometries and barriers that allow hindbrain $Chx10^{+}$ and motor neurons to be cultured as spatially segregated but interacting populations, or additional spinal cord interneuron cell types such as inhibitory V0 or V1 neurons. Ultimately, the equation achieved by mice initiating activity through the transition from light to dark shows quantitative features which modeling and cell culture work must eventually match before we can have a full understanding of generalized arousal's role in behavior.

5.6 Summary

We used three very different approaches to ask the question: how does the hindbrain reticular formation drive the behavioral changes associated with a highly aroused state? Each of these approaches comes with its own strengths and caveats. Through *in silico* computational modeling of arousal, we demonstrated how each of five neuroanatomical features of the NGC arousal circuit contributes to its function. We then used *in vitro* cell culture methods to demonstrate that a population of reticulospinal NGC neurons can directly pattern spinal motor neuron activity, and that subsets of these neurons are responsive to other arousal circuits driven by orexin and norepinephrine. Finally, we used an *in vivo* behavioral assay to demonstrate that circadian transitions in arousal level follow a lawful structure that can be described by a relatively simple mathematical formula that holds true across individuals and conditions. Taken

together, these studies all demonstrate in their own way the vital role that generalized arousal plays in generating and regulating locomotor drive.

APPENDIX

1) **CNS control file for model 1:**

```
TITLE control cards model 1
*******
SIMDATA "/home/avb/Desktop/simulations/NGC2/SIMDATA/trial.gd"
SAVE RESPONSES SVITMS = N
*******
* This is the region that receives the stimulus
*******
REGION "Arousing sensory input" AIN 10 10 Y=1 X=4.5 W=5 H=5 grids=1 KRP=B
CELLTYPE AIN 1 pt=0 st=49 RF=SPIKE KCTP=E
DECAY omega1=1 omega2=0.8
PARAMS ETHI=0 ETLO=0
NOISE 0-25, SIGMA=0, FRAC=1
REFRACTORY PERIOD 1 PSDST=0 OPT=A

REGION "nucleus gigantocellularis" NGC 10 10 Y=7 X=4.5 W=5 H=5 grids=1 KRP=B
CELLTYPE NGC 1 pt=30 st=49 RF=SPIKE KCTP=E
DECAY omega1=1 omega2=1
MODUL AIN AIN MT=0 MSCL=1
MODUL LCR LCR MT=0 MSCL=0,1
PARAMS ETHI=0 ETLO=0
REFRACTORY PERIOD 1 PSDST=0 OPT=A

REGION "locus coeruleus" LCR 10 10 Y=7 X=11.5 W=5 H=5 grids=1 KRP=B
CELLTYPE LCR 1 pt=30 st=49 RF=SPIKE KCTP=E
DECAY omega1=1 omega2=1
MODUL NGC NGC MT=0 MSCL=0,1
PARAMS ETHI=0 ETLO=0
NOISE 0-50, SIGMA=0, FRAC=1
REFRACTORY PERIOD 1 PSDST=0 OPT=A

REGION "motor input to CPG" MTR 10 10 Y=13 X=4.5 W=5 H=5 grids=1 KRP=B
CELLTYPE MTR 1 pt=30 st=49 RF=SPIKE KCTP=E
DECAY omega1=1 omega2=0.8
MODUL NGC NGC MT=0 MSCL=1
MODUL LCR LCR MT=0 MSCL=1
PARAMS ETHI=0 ETLO=0
REFRACTORY PERIOD 1 PSDST=0 OPT=A

REGION "flexor" FLX 10 10 Y=19 X=1 W=5 H=5 grids=1 KRP=B
CELLTYPE FLX 1 pt=120 st=49 RF=SPIKE KCTP=E
DECAY omega1=1 omega2=1
MODUL MTR MTR MT=0 MSCL=1
MODUL EIN EIN MT=0 MSCL=-1 OPT=S
PARAMS ETHI=0 ETLO=0
REFRACTORY PERIOD 1 PSDST=0 OPT=A

REGION "flexor inhibition" FIN 10 10 Y=26 X=1 W=5 H=5 grids=1 KRP=B
```

```
CELLTYPE FIN 1 pt=30 st=49 RF=SPIKE KCTP=E
DECAY omega1=1 omega2=1
MODUL FLX FLX MT=0 MSCL=1
PARAMS ETHI=0 ETLO=0
REFRACTORY PERIOD 1 PSDST=0 OPT=A

REGION "extensor" EXT 10 10 Y=19 X=8 W=5 H=5 grids=1 KRP=B
CELLTYPE EXT 1 pt=120 st=49 RF=SPIKE KCTP=E
DECAY omega1=1 omega2=1
MODUL MTR MTR MT=0 MSCL=1
MODUL FIN FIN MT=0 MSCL=-1 OPT=S
PARAMS ETHI=0 ETLO=0
REFRACTORY PERIOD 1 PSDST=0 OPT=A

REGION "extensor inhibition" EIN 10 10 Y=26 X=8 W=5 H=5 grids=1 KRP=B
CELLTYPE EIN 1 pt=30 st=49 RF=SPIKE KCTP=E
DECAY omega1=1 omega2=1
MODUL EXT EXT MT=0 MSCL=1
PARAMS ETHI=0 ETLO=0
REFRACTORY PERIOD 1 PSDST=0 OPT=A
*******
* setting up the cycle card
*******
CYCLE 1 100 4 PLOT=SC
*******
END
```

2) Results for simulations of model 1.1 (number of CPG burst cycles evoked by each combination of AIN and LCR input)

	LCR stimulation	0	5	10	15	20	25	30	35	40	45	50
AIN stimulation												
0		0	2	6	6	11	12	12	12	12	12	20
5		0	2	6	6	11	12	12	12	12	12	20
10		12	13	15	14	15	18	18	18	18	18	20
15		6	7	6	11	11	13	13	13	13	13	20
20		6	8	12	6	12	11	11	11	11	11	20
25		11	11	9	12	11	11	11	11	11	11	20

3) Results for simulations of model 1.2 (number of CPG burst cycles evoked by each combination of AIN and LCR input)

	LCR stimulation	0	5	10	15	20	25	30	35	40	45	50
AIN stimulation												
0		0	2	6	6	11	12	12	12	12	12	20
5		0	8	6	6	11	12	12	12	12	12	20
10		5	12	13	14	13	12	12	12	12	12	20
15		6	10	13	14	13	12	12	12	12	12	20
20		6	11	13	13	14	12	12	12	12	15	20
25		11	12	13	13	11	12	12	12	12	12	20

4) Results for simulations of model 1.3 (number of CPG burst cycles evoked by each combination of AIN and LCR input)

	LCR stimulation	0	5	10	15	20	25	30	35	40	45	50
AIN stimulation												
0		0	2	6	6	11	12	12	12	12	12	20
5		0	2	6	6	11	12	12	12	12	12	20
10		12	12	14	15	14	14	14	14	14	14	20
15		6	6	6	10	13	12	12	12	12	12	20
20		6	6	6	6	11	13	13	13	13	13	20
25		11	11	11	11	11	14	14	14	14	14	20

5) Results for simulations of model 1.4 (number of CPG burst cycles evoked by each combination of AIN and LCR input)

	LCR stimulation	0	5	10	15	20	25	30	35	40	45	50
AIN stimulation												
0		0	2	6	6	11	12	12	12	12	12	20
5		0	6	6	11	11	12	12	12	12	12	20
10		5	7	10	10	10	12	12	12	12	12	20
15		6	6	10	11	13	12	12	12	12	12	20
20		6	6	6	10	13	12	12	12	12	13	20
25		11	11	11	11	11	12	12	12	12	12	20

6) CNS control file for model 2:

TITLE control cards for model 2

```
*******
PARAMS NOPLOT
*******
SAVE RESPONSES SVITMS = N
*******
* This is the region that receives the stimulus
*******
REGION “Arousing sensory inputs" AIN 10 10 Y=7.5 X=1 W=5 H=5 grids=1 KRP=B
CELLTYPE AIN 1 RF=SPIKE pt=120 nt=0 st=49 KCTP=E
DECAY omega2=1
NOISE &snn, SIGMA=0, FRAC= 1.0

REGION "Nucleus Gigantocellularis" NGC 10 3 Y=7.5 X=10 W=5 H=5 grids=1 KRP=B
CELLTYPE GAA 1 RF=SPIKE pt=120 nt=0 st=49 KCTP=E
DECAY omega2=1
MODUL AIN AIN MT=0 MSCL=1
CELLTYPE GAB 1 RF=SPIKE pt=120 nt=0 st=49 KCTP=E
DECAY omega2=1
MODUL AIN AIN MT=0 MSCL=1
CELLTYPE GAC 1 RF=SPIKE pt=120 nt=0 st=49 KCTP=E
DECAY omega2=1
MODUL AIN AIN MT=0 MSCL=1

REGION "Limbic system" LIS 10 10 Y=7.5 X=30 W=5 H=5 grids=1 KRP=B
CELLTYPE LIS 1 RF=SPIKE pt=120 nt=0 st=49 KCTP=E
DECAY omega2=1
NOISE 0-50, SIGMA=0, FRAC= 1.0

REGION "Motor control areas" MCR 10 10 Y=7.5 X=20 W=5 H=5 grids=1 KRP=B
CELLTYPE MCR 1 RF=SPIKE pt=120 nt=0 st=49 KCTP=E
DECAY omega2=1
MODUL LIS LIS MT=0 MSCL=1
MODUL NGC GAA MT=0 MSCL=0,1
MODUL NGC GAC MT=0 MSCL=0,1

REGION "CPG input" CIN 10 10 Y=1 X=20 W=5 H=5 grids=1 KRP=B
CELLTYPE CIN 1 RF=SPIKE pt=120 nt=0 st=49 KCTP=E
DECAY omega2=1
MODUL MCR MCR MT=0 MSCL=1
MODUL NGC GAB MT=0 MSCL=0,1
MODUL NGC GAC MT=0 MSCL=0,1
*******
CYCLE 1 20 4 PLOT=SC
*******
END
```

7) results for simulations of model 2.1 (number of trials that elapse before CIN reaches spike threshold)

	LIS stimulation	0	2	4	6	8	10	12	14	16	18	20	22	24	26	28	30	32	34	36	38	40	42	44	46	48	50
AIN stimulation																											
0		80	36	24	20	18	16	16	15	15	14	14	14	14	13	13	13	13	13	13	13	13	13	13	13	13	13
2		42	32	24	20	18	16	16	15	15	14	14	14	14	13	13	13	13	13	13	13	13	13	13	13	13	13
4		30	25	20	19	18	16	16	15	15	14	14	14	14	13	13	13	13	13	13	13	13	13	13	13	13	13
6		26	21	19	16	15	15	15	14	14	14	14	14	14	13	13	13	13	13	13	13	13	13	13	13	13	13
8		24	19	18	15	14	13	13	13	13	13	13	13	13	12	12	12	12	12	12	12	12	12	12	12	12	12
10		22	17	16	15	13	12	12	12	12	11	11	11	11	11	11	11	11	11	11	11	11	11	11	11	11	11
12		22	17	16	15	13	12	12	12	12	11	11	11	11	11	11	11	11	11	11	11	11	11	11	11	11	11
14		21	16	16	14	13	11	11	11	11	11	11	11	11	10	10	10	10	10	10	10	10	10	10	10	10	10
16		21	16	16	14	13	11	11	11	11	11	11	11	11	10	10	10	10	10	10	10	10	10	10	10	10	10
18		20	15	15	14	13	11	11	10	10	10	10	10	10	10	10	10	10	10	10	10	10	10	10	10	10	10
20		20	15	15	14	13	11	11	10	10	10	10	10	10	10	10	10	10	10	10	10	10	10	10	10	10	10
22		20	15	15	14	13	11	11	10	10	10	10	10	10	10	10	10	10	10	10	10	10	10	10	10	10	10
24		20	15	15	14	13	11	11	10	10	10	10	10	10	10	10	10	10	10	10	10	10	10	10	10	10	10
26		19	14	14	13	12	11	11	10	10	9	9	9	9	9	9	9	9	9	9	9	9	9	9	9	9	9
28		19	14	14	13	12	11	11	10	10	9	9	9	9	9	9	9	9	9	9	9	9	9	9	9	9	9
30		19	14	14	13	12	11	11	10	10	9	9	9	9	9	9	9	9	9	9	9	9	9	9	9	9	9
32		19	14	14	13	12	11	11	10	10	9	9	9	9	9	9	9	9	9	9	9	9	9	9	9	9	9
34		19	14	14	13	12	11	11	10	10	9	9	9	9	9	9	9	9	9	9	9	9	9	9	9	9	9
36		19	14	14	13	12	11	11	10	10	9	9	9	9	9	9	9	9	9	9	9	9	9	9	9	9	9
38		19	14	14	13	12	11	11	10	10	9	9	9	9	9	9	9	9	9	9	9	9	9	9	9	9	9
40		19	14	14	13	12	11	11	10	10	9	9	9	9	9	9	9	9	9	9	9	9	9	9	9	9	9
42		19	14	14	13	12	11	11	10	10	9	9	9	9	9	9	9	9	9	9	9	9	9	9	9	9	9
44		19	14	14	13	12	11	11	10	10	9	9	9	9	9	9	9	9	9	9	9	9	9	9	9	9	9
46		19	14	14	13	12	11	11	10	10	9	9	9	9	9	9	9	9	9	9	9	9	9	9	9	9	9
48		19	14	14	13	12	11	11	10	10	9	9	9	9	9	9	9	9	9	9	9	9	9	9	9	9	9
50		19	14	14	13	12	11	11	10	10	9	9	9	9	9	9	9	9	9	9	9	9	9	9	9	9	9

8) results for simulations of model 2.2 (number of trials that elapse before CIN reaches spike threshold)

	LIS stimulation	0	2	4	6	8	10	12	14	16	18	20	22	24	26	28	30	32	34	36	38	40	42	44	46	48	50
AIN stimulation																											
0		80	36	24	20	18	16	16	15	15	14	14	14	14	13	13	13	13	13	13	13	13	13	13	13	13	13
2		36	30	24	20	18	16	16	15	15	14	14	14	14	13	13	13	13	13	13	13	13	13	13	13	13	13
4		24	24	18	15	14	13	13	13	13	13	13	13	13	12	12	12	12	12	12	12	12	12	12	12	12	12
6		20	20	15	14	13	11	11	10	10	10	10	10	10	10	10	10	10	10	10	10	10	10	10	10	10	10
8		18	18	14	13	12	11	11	10	10	9	9	9	9	8	8	8	8	8	8	8	8	8	8	8	8	8
10		16	16	13	11	11	10	10	9	9	9	9	9	9	8	8	8	8	8	8	8	8	8	8	8	8	8
12		16	16	13	11	11	10	10	9	9	9	9	9	9	8	8	8	8	8	8	8	8	8	8	8	8	8
14		15	15	13	10	10	9	9	9	9	8	8	8	8	8	8	8	8	8	8	8	8	8	8	8	8	8
16		15	15	13	10	10	9	9	9	9	8	8	8	8	8	8	8	8	8	8	8	8	8	8	8	8	8
18		14	14	13	10	9	9	9	8	8	8	8	8	8	7	7	7	7	7	7	7	7	7	7	7	7	7
20		14	14	13	10	9	9	9	8	8	8	8	8	8	7	7	7	7	7	7	7	7	7	7	7	7	7
22		14	14	13	10	9	9	9	8	8	8	8	8	8	7	7	7	7	7	7	7	7	7	7	7	7	7
24		14	14	13	10	9	9	9	8	8	8	8	8	8	7	7	7	7	7	7	7	7	7	7	7	7	7
26		13	13	12	10	8	8	8	8	8	7	7	7	7	7	7	7	7	7	7	7	7	7	7	7	7	7
28		13	13	12	10	8	8	8	8	8	7	7	7	7	7	7	7	7	7	7	7	7	7	7	7	7	7
30		13	13	12	10	8	8	8	8	8	7	7	7	7	7	7	7	7	7	7	7	7	7	7	7	7	7
32		13	13	12	10	8	8	8	8	8	7	7	7	7	7	7	7	7	7	7	7	7	7	7	7	7	7
34		13	13	12	10	8	8	8	8	8	7	7	7	7	7	7	7	7	7	7	7	7	7	7	7	7	7
36		13	13	12	10	8	8	8	8	8	7	7	7	7	7	7	7	7	7	7	7	7	7	7	7	7	7
38		13	13	12	10	8	8	8	8	8	7	7	7	7	7	7	7	7	7	7	7	7	7	7	7	7	7
40		13	13	12	10	8	8	8	8	8	7	7	7	7	7	7	7	7	7	7	7	7	7	7	7	7	7
42		13	13	12	10	8	8	8	8	8	7	7	7	7	7	7	7	7	7	7	7	7	7	7	7	7	7
44		13	13	12	10	8	8	8	8	8	7	7	7	7	7	7	7	7	7	7	7	7	7	7	7	7	7
46		13	13	12	10	8	8	8	8	8	7	7	7	7	7	7	7	7	7	7	7	7	7	7	7	7	7
48		13	13	12	10	8	8	8	8	8	7	7	7	7	7	7	7	7	7	7	7	7	7	7	7	7	7
50		13	13	12	10	8	8	8	8	8	7	7	7	7	7	7	7	7	7	7	7	7	7	7	7	7	7

9) results for simulations of model 2.3 (number of trials that elapse before CIN reaches spike threshold)

	LIS stimulation	0	2	4	6	8	10	12	14	16	18	20	22	24	26	28	30	32	34	36	38	40	42	44	46	48	50
AIN stimulation																											
0		80	36	24	20	18	16	16	15	15	14	14	14	14	13	13	13	13	13	13	13	13	13	13	13	13	13
2		32	27	24	20	18	16	16	15	15	14	14	14	14	13	13	13	13	13	13	13	13	13	13	13	13	13
4		20	18	15	14	14	13	13	13	13	13	13	13	13	12	12	12	12	12	12	12	12	12	12	12	12	12
6		16	15	13	11	10	10	10	10	10	10	10	10	10	10	10	10	10	10	10	10	10	10	10	10	10	10
8		14	13	12	10	9	8	8	8	8	8	8	8	8	8	8	8	8	8	8	8	8	8	8	8	8	8
10		12	11	10	9	8	7	7	7	7	6	6	6	6	6	6	6	6	6	6	6	6	6	6	6	6	6
12		12	11	10	9	8	7	7	7	7	6	6	6	6	6	6	6	6	6	6	6	6	6	6	6	6	6
14		11	10	9	8	8	6	6	6	6	6	6	6	6	5	5	5	5	5	5	5	5	5	5	5	5	5
16		11	10	9	8	8	6	6	6	6	6	6	6	6	5	5	5	5	5	5	5	5	5	5	5	5	5
18		10	9	8	8	7	6	6	5	5	5	5	5	5	5	5	5	5	5	5	5	5	5	5	5	5	5
20		10	9	8	8	7	6	6	5	5	5	5	5	5	5	5	5	5	5	5	5	5	5	5	5	5	5
22		10	9	8	8	7	6	6	5	5	5	5	5	5	5	5	5	5	5	5	5	5	5	5	5	5	5
24		10	9	8	8	7	6	6	5	5	5	5	5	5	5	5	5	5	5	5	5	5	5	5	5	5	5
26		9	8	8	7	6	6	6	5	5	4	4	4	4	4	4	4	4	4	4	4	4	4	4	4	4	4
28		9	8	8	7	6	6	6	5	5	4	4	4	4	4	4	4	4	4	4	4	4	4	4	4	4	4
30		9	8	8	7	6	6	6	5	5	4	4	4	4	4	4	4	4	4	4	4	4	4	4	4	4	4
32		9	8	8	7	6	6	6	5	5	4	4	4	4	4	4	4	4	4	4	4	4	4	4	4	4	4
34		9	8	8	7	6	6	6	5	5	4	4	4	4	4	4	4	4	4	4	4	4	4	4	4	4	4
36		9	8	8	7	6	6	6	5	5	4	4	4	4	4	4	4	4	4	4	4	4	4	4	4	4	4
38		9	8	8	7	6	6	6	5	5	4	4	4	4	4	4	4	4	4	4	4	4	4	4	4	4	4
40		9	8	8	7	6	6	6	5	5	4	4	4	4	4	4	4	4	4	4	4	4	4	4	4	4	4
42		9	8	8	7	6	6	6	5	5	4	4	4	4	4	4	4	4	4	4	4	4	4	4	4	4	4
44		9	8	8	7	6	6	6	5	5	4	4	4	4	4	4	4	4	4	4	4	4	4	4	4	4	4
46		9	8	8	7	6	6	6	5	5	4	4	4	4	4	4	4	4	4	4	4	4	4	4	4	4	4
48		9	8	8	7	6	6	6	5	5	4	4	4	4	4	4	4	4	4	4	4	4	4	4	4	4	4
50		9	8	8	7	6	6	6	5	5	4	4	4	4	4	4	4	4	4	4	4	4	4	4	4	4	4

10) CNS control file for model 3:

```
TITLE control cards model 3
*******
PARAMS NOPLOT
*******
SIMDATA "/home/avb/Desktop/simulations/IT3/SIMDATA/trial.gd"
*******
SAVE RESPONSES SVITMS = N
*******
* This is the region that receives the stimulus
*******
REGION "Arousing Sensory Inputs" AIN 10 10 Y=7.5 X=1 W=5 H=5 grids=1 KRP=B
CELLTYPE AIN 1 RF=SPIKE pt=120 nt=0 st=49 KCTP=E
DECAY omega2=1
NOISE 0-30, SIGMA=0, FRAC= 1.0

REGION "Nucleus Gigantocellularis" NGC 10 5 Y=7.5 X=10 W=5 H=5 grids=1 KRP=B
CELLTYPE GAA 1 RF=SPIKE pt=120 nt=0 st=49 KCTP=E
DECAY omega2=1
MODUL AIN AIN MT=0 MTLO=0 MSCL=1
CONNTYPE NGC GAA 20 RUVC, MEAN=1, SIGMA=0, PP=0,0.4,1 , NRX=10, NRY=5
CELLTYPE GAB 1 RF=SPIKE pt=120 nt=0 st=49 KCTP=E
DECAY omega2=1
MODUL AIN AIN MT=0 MTLO=0 MSCL=1
CONNTYPE NGC GAB 20 RUVC, MEAN=1, SIGMA=0, PP=0,0.4,1 , NRX=10, NRY=5

REGION "Limbic system" LIS 10 10 Y=7.5 X=30 W=5 H=5 grids=1 KRP=B
CELLTYPE LIS 1 RF=SPIKE pt=120 nt=0 st=49 KCTP=E
DECAY omega2=1
NOISE 0-30, SIGMA=0, FRAC= 1.0

REGION "Motor control areas" MCR 10 10 Y=7.5 X=20 W=5 H=5 grids=1 KRP=B
CELLTYPE MCR 1 RF=SPIKE pt=120 nt=0 st=49 KCTP=E
DECAY omega2=1
MODUL LIS LIS MT=0 MTLO=0 MSCL=1
MODUL NGC GAA MT=0 MTLO=0 MSCL=1

REGION "CPG input" CIN 10 10 Y=1 X=20 W=5 H=5 grids=1 KRP=B
CELLTYPE CIN 1 RF=SPIKE pt=120 nt=0 st=49 KCTP=E
DECAY omega2=1
MODUL MCR MCR MT=0 MTLO=0 MSCL=1
MODUL NGC GAB MT=0 MTLO=0 MSCL=1
*******
* setting up the cycle card
*******
CYCLE 1 20 4 PLOT=SC
*******
END
```

11) results for simulations of model 3.2 (0% excitatory connections) (number of trials that elapse before CIN reaches spike threshold)

	LIS stimulation	0	3	6	9	12	15	18	21	24	27	30
AIN stimulation												
0		80	28	20	17	16	15	14	14	14	13	13
3		55	22	18	16	16	15	14	14	14	13	13
6		47	22	14	12	12	11	11	11	11	10	10
9		44	22	14	11	10	10	9	9	9	9	9
12		43	22	14	11	10	9	9	9	9	8	8
15		42	22	14	11	10	9	8	8	8	8	8
18		41	22	14	11	10	9	8	8	8	7	7
21		41	22	14	11	10	9	8	8	8	7	7
24		41	22	14	11	10	9	8	8	8	7	7
27		40	22	14	11	10	9	8	8	8	7	7
30		40	22	14	11	10	9	8	8	8	7	7

12) results for simulations of model 3.4 (40% excitatory connections) (number of trials that elapse before CIN reaches spike threshold)

	LIS stimulation	0	3	6	9	12	15	18	21	24	27	30
AIN stimulation												
0		80	28	20	17	16	15	14	14	14	13	13
3		80	19	17	16	16	15	14	14	14	13	13
6		80	22	11	10	10	10	10	10	10	10	10
9		80	22	15	8	8	7	7	7	7	7	7
12		80	22	15	7	7	7	6	6	6	6	6
15		80	22	14	7	6	6	6	6	6	5	5
18		80	21	13	12	6	5	5	5	5	5	5
21		80	21	13	12	6	5	5	5	5	5	5
24		80	21	13	12	6	5	5	5	5	5	5
27		80	22	15	12	11	5	4	4	4	4	4
30		80	22	15	12	11	5	4	4	4	4	4

13) results for simulations of model 3.3 (100% excitatory connections) (number of trials that elapse before CIN reaches spike threshold)

	LIS stimulation	0	3	6	9	12	15	18	21	24	27	30
AIN stimulation												
0		80	28	20	17	16	15	14	14	14	13	13
3		20	17	17	16	16	15	14	14	14	13	13
6		12	10	9	9	9	9	9	9	9	9	9
9		9	7	6	6	6	6	6	6	6	6	6
12		8	6	5	5	5	5	5	5	5	5	5
15		7	5	5	4	4	4	4	4	4	4	4
18		6	4	4	3	3	3	3	3	3	3	3
21		6	4	4	3	3	3	3	3	3	3	3
24		6	4	4	3	3	3	3	3	3	3	3
27		5	4	3	3	2	2	2	2	2	2	2
30		5	4	3	3	2	2	2	2	2	2	2

14) CNS control file for model 4.1:

```
TITLE control cards for model 4-1
*******
SIMDATA "/home/avb/Desktop/simulations/PFC1/SIMDATA/trial.gd"
*******
SAVE RESPONSES SVITMS = N
*******
* This is the region that receives the stimulus
*******
REGION "Arousing Sensory Input" AIN 10 10 Y=7.5 X=1 W=5 H=5 grids=1 KRP=B
CELLTYPE AIN 1 RF=SPIKE pt=120 nt=0 st=49 KCTP=E
DECAY omega2=1
NOISE 0-10, SIGMA=0, FRAC= 1.0

REGION "Nucleus Gigantocellularis" NGC 10 10 Y=7.5 X=10 W=5 H=5 grids=1 KRP=B
```

```
CELLTYPE NGC 1 RF=SPIKE pt=120 nt=0 st=49 KCTP=E
DECAY omega2=1
MODUL AIN AIN MT=0 MSCL=1
MODUL LCR LCR MT=0 MSCL=1

REGION "Limbic System" LIS 10 10 Y=7.5 X=35 W=5 H=5 grids=1 KRP=B
CELLTYPE LIS 1 RF=SPIKE pt=120 nt=0 st=49 KCTP=E
DECAY omega2=1
NOISE 0-50, SIGMA=0, FRAC= 1.0
MODUL LCR LCR MT=0 MSCL=1

REGION "Motor control areas" MCR 10 10 Y=7.5 X=25 W=5 H=5 grids=1 KRP=B
CELLTYPE MCR 1 RF=SPIKE pt=120 nt=0 st=49 KCTP=E
DECAY omega2=1
MODUL LIS LIS MT=0 MSCL=1

REGION "Locus Coeruleus" LCR 10 10 Y=15 X=17.5 W=5 H=5 grids=1 KRP=B
CELLTYPE LCR 1 RF=SPIKE pt=120 nt=0 st=49 KCTP=E
DECAY omega2=1
MODUL NGC NGC MT=0 MSCL=1
MODUL LIS LIS MT=0 MSCL=1

REGION "input to CPG" CIN 10 10 Y=1 X=17.5 W=5 H=5 grids=1 KRP=B
CELLTYPE CIN 1 RF=SPIKE pt=120 nt=0 st=49 KCTP=E
DECAY omega2=1
MODUL NGC NGC MT=0 MSCL=1
MODUL MCR MCR MT=0 MSCL=1
*******
* setting up the cycle card
*******
CYCLE 1 10 4 PLOT=SC
*******
END
```

15) results for simulations of model 4.1 (number of trials that elapse before CIN reaches spike threshold)

	LIS stimulation	0	5	10	15	20	25	30	35	40
AIN stimulation										
0		40	18	13	12	11	10	10	10	10
1		40	17	12	11	10	9	9	9	9
2		36	16	12	11	10	9	9	9	9
3		28	16	11	10	9	8	8	8	8
4		24	14	11	10	9	8	8	8	8
5		21	12	10	9	9	8	8	8	8
6		20	12	9	9	8	8	8	8	8
7		18	11	8	8	7	7	7	7	7
8		18	11	8	8	7	7	7	7	7
9		17	11	7	7	7	6	6	6	6
10		16	11	7	6	6	6	6	6	6

16) CNS control file for model 4.2

```
TITLE control cards for model 4-2
*******
PARAMS NOPLOT
*******
SIMDATA "/home/avb/Desktop/simulations/PFC2/SIMDATA/trial.gd"
*******
SAVE RESPONSES SVITMS = N
*******
* This is the region that receives the stimulus
*******
REGION "Arousing Sensory Input" AIN 10 10 Y=7.5 X=1 W=5 H=5 grids=1 KRP=B
CELLTYPE AIN 1 RF=SPIKE pt=120 nt=0 st=49 KCTP=E
DECAY omega2=1
NOISE &gan, SIGMA=0, FRAC= 1.0
```

```
REGION "Nucleus Gigantocellularis" NGC 10 10 Y=7.5 X=10 W=5 H=5 grids=1 KRP=B
CELLTYPE NGC 1 RF=SPIKE pt=120 nt=0 st=49 KCTP=E
DECAY omega2=1
MODUL AIN AIN MT=0 MSCL=1
MODUL LCR LCB MT=0 MSCL=1

REGION "Limbic system" LIS 10 10 Y=7.5 X=35 W=5 H=5 grids=1 KRP=B
CELLTYPE PFC 1 RF=SPIKE pt=120 nt=0 st=49 KCTP=E
DECAY omega2=1
NOISE &pfn, SIGMA=0, FRAC= 1.0
MODUL LCR LCA MT=0 MSCL=1

REGION "Motor control areas" MCR 10 10 Y=7.5 X=25 W=5 H=5 grids=1 KRP=B
CELLTYPE MCR 1 RF=SPIKE pt=120 nt=0 st=49 KCTP=E
DECAY omega2=1
MODUL LIS LIS MT=0 MSCL=1

REGION "Locus Coeruleus" LCR 10 5 Y=15 X=17.5 W=5 H=5 grids=1 KRP=B
CELLTYPE LCA 1 RF=SPIKE pt=120 nt=0 st=49 KCTP=E
DECAY omega2=1
MODUL NGC NGC MT=0 MSCL=1
CELLTYPE LCB 1 RF=SPIKE pt=120 nt=0 st=49 KCTP=E
DECAY omega2=1
MODUL LIS LIS MT=0 MSCL=1

REGION "Input to CPG" CIN 10 10 Y=1 X=17.5 W=5 H=5 grids=1 KRP=B
CELLTYPE CIN 1 RF=SPIKE pt=120 nt=0 st=49 KCTP=E
DECAY omega2=1
MODUL NGC NGC MT=0 MSCL=1
MODUL MCR MCR MT=0 MSCL=1
*******
* setting up the cycle card
*******
CYCLE 1 10 4 PLOT=SC
*******
END
```

17) results for simulations of model 4.2 (number of trials that elapse before CIN reaches spike threshold)

	LIS stimulation	0	5	10	15	20	25	30	35	40
AIN stimulation										
0		40	18	13	12	11	10	10	10	10
1		40	17	12	11	10	9	9	9	9
2		36	16	12	11	10	9	9	9	9
3		28	16	11	10	9	8	8	8	8
4		24	14	11	10	9	8	8	8	8
5		21	13	10	9	9	8	8	8	8
6		20	12	9	9	8	8	8	8	8
7		18	12	8	8	7	7	7	7	7
8		18	12	8	8	7	7	7	7	7
9		17	11	8	7	7	6	6	6	6
10		16	11	8	7	6	6	6	6	6

18) CNS control file for model 4.3:

```
TITLE control cards for model 4-3
*******
PARAMS NOPLOT
*******
SIMDATA "/home/avb/Desktop/simulations/PFC3/SIMDATA/trial.gd"
*******
*MASTER CELLTYPE KCTP=U
*******
* This is the region that receives the stimulus
*******
REGION "Arousing Sensory Input" AIN 10 10 Y=7.5 X=1 W=5 H=5 grids=1 KRP=B
CELLTYPE AIN 1 RF=SPIKE pt=120 nt=0 st=49 KCTP=E
DECAY omega2=1
NOISE 0-10, SIGMA=0, FRAC= 1.0
```

```
REGION "Nucleus Gigantocellularis" NGC 10 5 Y=7.5 X=10 W=5 H=5 grids=1 KRP=B
CELLTYPE NGA 1 RF=SPIKE pt=120 nt=0 st=49 KCTP=E
DECAY omega2=1
MODUL AIN AIN MT=0 MSCL=1
CELLTYPE NGB 1 RF=SPIKE pt=120 nt=0 st=49 KCTP=E
DECAY omega2=1
MODUL LCR LCR MT=0 MSCL=1

REGION "Limbic System" LIS 10 10 Y=7.5 X=35 W=5 H=5 grids=1 KRP=B
CELLTYPE LIS 1 RF=SPIKE pt=120 nt=0 st=49 KCTP=E
DECAY omega2=1
NOISE 0-40, SIGMA=0, FRAC= 1.0
MODUL LCR LCR MT=0 MSCL=1

REGION "Motor control areas" MCR 10 10 Y=7.5 X=25 W=5 H=5 grids=1 KRP=B
CELLTYPE MCR 1 RF=SPIKE pt=120 nt=0 st=49 KCTP=E
DECAY omega2=1
MODUL LIS LIS MT=0 MSCL=1

REGION "Locus Coeruleus" LCR 10 10 Y=15 X=17.5 W=5 H=5 grids=1 KRP=B
CELLTYPE LCR 1 RF=SPIKE pt=120 nt=0 st=49 KCTP=E
DECAY omega2=1
MODUL NGC NGA MT=0 MSCL=1
MODUL LIS LIS MT=0 MSCL=1

REGION "input to CPG" CIN 10 10 Y=1 X=17.5 W=5 H=5 grids=1 KRP=B
CELLTYPE CIN 1 RF=SPIKE pt=120 nt=0 st=49 KCTP=E
DECAY omega2=1
MODUL NGC NGB MT=0 MSCL=1
MODUL MCR MCR MT=0 MSCL=1
*******
* setting up the cycle card
*******
CYCLE 1 10 4 PLOT=SC
*******
END
```

19) results for simulations of model 4.3 (number of trials that elapse before CIN reaches spike threshold)

	LIS stimulation	0	5	10	15	20	25	30	35	40
AIN stimulation										
0		40	18	13	12	11	10	10	10	10
1		40	18	13	12	11	10	10	10	10
2		40	18	13	12	11	10	10	10	10
3		37	18	13	12	11	10	10	10	10
4		33	16	13	12	11	10	10	10	10
5		30	16	12	12	11	10	10	10	10
6		29	16	12	11	11	10	10	10	10
7		27	16	11	10	10	9	9	9	9
8		27	16	11	10	10	9	9	9	9
9		26	16	11	10	9	9	9	9	9
10		25	15	11	10	9	8	8	8	8

20) CNS control file for model 4.4:

```
TITLE control cards for model 4-5
*******
PARAMS NOPLOT
*******
SIMDATA "/home/avb/Desktop/simulations/PFC4/SIMDATA/trial.gd"
*******
SAVE RESPONSES SVITMS = N
*******
* This is the region that receives the stimulus
*******
REGION "Arousing Sensory Input" AIN 10 10 Y=7.5 X=1 W=5 H=5 grids=1 KRP=B
CELLTYPE AIN 1 RF=SPIKE pt=120 nt=0 st=49 KCTP=E
DECAY omega2=1
```

```
NOISE 0-10, SIGMA=0, FRAC= 1.0

REGION "Nucleus Gigantocellularis" NGC 10 5 Y=7.5 X=10 W=5 H=5 grids=1 KRP=B
CELLTYPE NGA 1 RF=SPIKE pt=120 nt=0 st=49 KCTP=E
DECAY omega2=1
MODUL AIN AIN MT=0 MSCL=1
CELLTYPE NGB 1 RF=SPIKE pt=120 nt=0 st=49 KCTP=E
DECAY omega2=1
MODUL LCR LCB MT=0 MSCL=1

REGION "Limbic system" LIS 10 10 Y=7.5 X=35 W=5 H=5 grids=1 KRP=B
CELLTYPE LIS 1 RF=SPIKE pt=120 nt=0 st=49 KCTP=E
DECAY omega2=1
NOISE 0-40, SIGMA=0, FRAC= 1.0
MODUL LCR LCA MT=0 MSCL=1
MODUL LCR LCB MT=0 MSCL=1

REGION "Motor control areas" MCR 10 10 Y=7.5 X=25 W=5 H=5 grids=1 KRP=B
CELLTYPE MCR 1 RF=SPIKE pt=120 nt=0 st=49 KCTP=E
DECAY omega2=1
MODUL LIS LIS MT=0 MSCL=1

REGION "Locus Coeruleus" LCR 10 5 Y=15 X=17.5 W=5 H=5 grids=1 KRP=B
CELLTYPE LCA 1 RF=SPIKE pt=120 nt=0 st=49 KCTP=E
DECAY omega2=1
MODUL NGC NGA MT=0 MSCL=1
CELLTYPE LCB 1 RF=SPIKE pt=120 nt=0 st=49 KCTP=E
DECAY omega2=1
MODUL LIS LIS MT=0 MSCL=1

REGION "input to CPG" CIN 10 10 Y=1 X=17.5 W=5 H=5 grids=1 KRP=B
CELLTYPE CIN 1 RF=SPIKE pt=120 nt=0 st=49 KCTP=E
DECAY omega2=1
MODUL NGC NGB MT=0 MSCL=1
MODUL MCR MCR MT=0 MSCL=1
*******
* setting up the cycle card
*******
CYCLE 1 10 4 PLOT=SC
*******
END
```

21) results for simulations of model 4.4 (number of trials that elapse before CIN reaches spike threshold)

	LIS stimulation	0	5	10	15	20	25	30	35	40
AIN stimulation										
0		40	18	13	12	11	10	10	10	10
1		40	18	13	12	11	10	10	10	10
2		40	18	13	12	11	10	10	10	10
3		40	18	13	12	11	10	10	10	10
4		40	18	13	12	11	10	10	10	10
5		37	18	13	12	11	10	10	10	10
6		36	18	13	12	11	10	10	10	10
7		34	18	13	12	11	10	10	10	10
8		34	18	13	12	11	10	10	10	10
9		33	18	13	12	11	10	10	10	10
10		32	18	13	12	11	10	10	10	10

22) CNS control file for model 5:

```
TITLE control cards for a model 5
*******
PARAMS NOPLOT
*******
SIMDATA "/home/avb/Desktop/simulations/MAM1/SIMDATA/trial.gd"
*******
SAVE RESPONSES SVITMS = N
*******
* This is the region that receives the stimulus
*******
REGION "Arousing Sensory Inputs" AIN 10 10 Y=7.5 X=1 W=5 H=5 grids=1 KRP=B
CELLTYPE AIN 1 RF=SPIKE pt=120 nt=0 st=49 KCTP=E
DECAY omega2=1
NOISE 0-30, SIGMA=0, FRAC= 1.0
```

```
REGION "Nucleus Gigantocellularis" NGC 10 5 Y=7.5 X=10 W=5 H=5 grids=1 KRP=B
CELLTYPE GAA 1 RF=SPIKE pt=120 nt=0 st=49 KCTP=E
DECAY omega2=1
MODUL AIN AIN MT=0 MSCL=1
CONNTYPE NGC GAA 20 RUVC, MEAN=1, SIGMA=0, PP=0.4, NRX=10, NRY=5
CELLTYPE GAB 1 RF=SPIKE pt=120 nt=0 st=49 KCTP=E
DECAY omega2=1
MODUL AIN AIN MT=0 MSCL=1
CONNTYPE NGC GAB 20 RUVC, MEAN=1, SIGMA=0, PP=0.4, NRX=10, NRY=5

REGION "first limbic input" LIS1 10 10 Y=7.5 X=37 W=5 H=5 grids=1 KRP=B
CELLTYPE LIS1 1 RF=SPIKE pt=120 nt=0 st=49 KCTP=E
DECAY omega2=1
NOISE 0-30, SIGMA=0, FRAC= 1.0

REGION "first motor circuit" MCR1 10 10 Y=7.5 X=27 W=5 H=5 grids=1 KRP=B
CELLTYPE MCR1 1 RF=SPIKE pt=120 nt=0 st=49 KCTP=E
DECAY omega2=1
MODUL LIS1 LIS1 MT=0 MSCL=1
MODUL NGC GAA MT=0 MSCL=0,1

REGION "second limbic input" LIS2 10 10 Y=1 X=37 W=5 H=5 grids=1 KRP=B
CELLTYPE LIS2 1 RF=SPIKE pt=120 nt=0 st=49 KCTP=E
DECAY omega2=1
NOISE 0-30, SIGMA=0, FRAC= 1.0

REGION "second motor circuit" MCR2 10 10 Y=1 X=27 W=5 H=5 grids=1 KRP=B
CELLTYPE MCR2 1 RF=SPIKE pt=120 nt=0 st=49 KCTP=E
DECAY omega2=1
MODUL LIS2 LIS2 MT=0 MSCL=1
MODUL NGC GAA MT=0 MSCL=0,1

REGION "input to CPG" CIN 10 10 Y=1 X=20 W=5 H=5 grids=1 KRP=B
CELLTYPE CIN 1 RF=SPIKE pt=120 nt=0 st=49 KCTP=E
DECAY omega2=1
MODUL MCR1 MCR1 MT=0 MSCL=1
MODUL MCR2 MCR2 MT=0 MSCL=0,1
MODUL NGC GAB MT=0 MSCL=0,1
*******
* setting up the cycle card
*******
CYCLE 1 20 4 PLOT=SC
*******
END
```

23) results for simulation of model 5.1 (number of trials that elapse before CIN reaches spike threshold)

	LIS stimulation	0	3	6	9	12	15	18	21	24	27	30
AIN stimulation												
0		80	28	20	17	16	15	14	14	14	13	13
3		80	19	17	16	16	15	14	14	14	13	13
6		80	22	11	10	10	10	10	10	10	10	10
9		80	22	15	8	8	7	7	7	7	7	7
12		80	22	15	7	7	7	6	6	6	6	6
15		80	22	14	7	6	6	6	6	6	5	5
18		80	21	13	12	6	5	5	5	5	5	5
21		80	21	13	12	6	5	5	5	5	5	5
24		80	21	13	12	6	5	5	5	5	5	5
27		80	22	15	12	11	5	4	4	4	4	4
30		80	22	15	12	11	5	4	4	4	4	4

24) results for simulations of model 5.2 (number of trials that elapse before CIN reaches spike threshold)

	LIS1/2 stimulation	0	3	6	9	12	15	18	21	24	27	30
AIN stimulation												
0		80	22	14	11	10	9	8	8	8	7	7
3		80	18	14	11	10	9	8	8	8	7	7
6		80	18	10	9	9	8	8	8	8	7	7
9		80	17	10	7	7	6	6	6	6	6	6
12		80	17	10	6	6	6	5	5	5	5	5
15		80	17	9	6	5	5	5	5	5	4	4
18		80	16	8	7	5	4	4	4	4	4	4
21		80	16	8	7	5	4	4	4	4	4	4
24		80	16	8	7	5	4	4	4	4	4	4
27		80	16	11	7	6	4	3	3	3	3	3
30		80	16	11	7	6	4	3	3	3	3	3

25) results for simulations of model 5.3 (number of trials that elapse before CIN reaches spike threshold)

	LIS1/2 stimulation	0	3	6	9	12	15	18	21	24	27	30
AIN stimulation												
0		80	22	14	11	10	9	8	8	8	7	7
3		80	18	14	11	10	9	8	8	8	7	7
6		80	18	10	9	9	8	8	8	8	7	7
9		80	17	10	7	7	6	6	6	6	6	6
12		80	17	10	6	6	6	5	5	5	5	5
15		80	17	9	6	5	5	5	5	5	4	4
18		80	16	8	7	5	4	4	4	4	4	4
21		80	16	8	7	5	4	4	4	4	4	4
24		80	16	8	7	5	4	4	4	4	4	4
27		80	16	11	7	6	4	3	3	3	3	3
30		80	16	11	7	6	4	3	3	3	3	3

26) results for simulations of model 5.4 (number of trials that elapse before CIN reaches spike threshold)

	LIS1/2 stimulation	0	3	6	9	12	15	18	21	24	27	30
AIN stimulation												
0		80	22	14	11	10	9	8	8	8	7	7
3		80	22	14	11	10	9	8	8	8	7	7
6		80	22	14	11	10	9	8	8	8	7	7
9		80	22	14	11	10	9	8	8	8	7	7
12		80	22	14	11	10	9	8	8	8	7	7
15		80	22	14	11	10	9	8	8	8	7	7
18		80	22	14	11	10	9	8	8	8	7	7
21		80	22	14	11	10	9	8	8	8	7	7
24		80	22	14	11	10	9	8	8	8	7	7
27		80	22	14	11	10	9	8	8	8	7	7
30		80	22	14	11	10	9	8	8	8	7	7

27) results for simulations of model 5.5 (number of trials that elapse before CIN reaches spike threshold)

	LIS stimulation	0	3	6	9	12	15	18	21	24	27	30
AIN stimulation												
0		80	80	80	80	80	80	80	80	80	80	80
3		22	22	22	22	22	22	22	22	22	22	22
6		14	14	14	14	14	14	14	14	14	14	14
9		11	11	11	11	11	11	11	11	11	11	11
12		10	10	10	10	10	10	10	10	10	10	10
15		9	9	9	9	9	9	9	9	9	9	9
18		8	8	8	8	8	8	8	8	8	8	8
21		8	8	8	8	8	8	8	8	8	8	8
24		8	8	8	8	8	8	8	8	8	8	8
27		7	7	7	7	7	7	7	7	7	7	7
30		7	7	7	7	7	7	7	7	7	7	7

REFERENCES

Adamantidis A, Lecea L De (2008) Physiological arousal : a role for hypothalamic systems. Cell Mol Life Sci 65:1475–1488.

Agostinelli LJ, Ferrari LL, Mahoney CE, Mochizuki T, Lowell BB, Arrigoni E, Scammell TE (2016) Descending projections from the basal forebrain to the orexin neurons in mice. J Comp Neurol 525:1668–1684.

Antle MC, Silver R (2016) Circadian Insights into Motivated Behavior. Curr Top Behav Neurosci 27:137–169 Available at: http://link.springer.com/chapter/10.1007/7854_2011_176.

Arrieta-Cruz I, Pfaff DW, Shelley DN (2007) Mouse model of diffuse brain damage following anoxia, evaluated by a new assay of generalized arousal. Exp Neurol 205:449–460.

Aston-jones G, Cohen JD (2005) An Integrative Theory of Locus Function : Adaptive Gain and Optimal Performance. Annu Rev Neurosci 28:403–450.

Ausborn J, Shevtsova NA, Caggiano V, Danner SM, Rybak IA (2019) Computational modeling of brainstem circuits controlling locomotor frequency and gait. Elife 8.

Bakkum DJ, Chao ZC, Potter SM (2008) Long-term activity-dependent plasticity of action potential propagation delay and amplitude in cortical networks. PLoS One 3.

Barriere G, Tartas M, Cazalets J-R, Bertrand SS (2008) Interplay between neuromodulator-induced switching of short-term plasticity at sensorimotor synapses in the neonatal rat spinal cord. J Physiol 7:1903–1920.

Beier KT, Steinberg EE, Deloach KE, Xie S, Miyamichi K, Schwarz L, Gao XJ, Kremer EJ, Malenka RC, Luo L (2015) Circuit Architecture of VTA Dopamine Neurons Revealed by Systematic Input-Output Mapping. Cell 162:622–634 Available at: http://dx.doi.org/10.1016/j.cell.2015.07.015.

Berridge CW, Waterhouse BD (2003) The locus coeruleus-noradrenergic system: Modulation of behavioral state and state-dependent cognitive processes. Brain Res Rev 42:33–84.

Black BJ, Atmaramani R, Pancrazio JJ (2017) Spontaneous and Evoked Activity from Murine Ventral Horn Cultures on Microelectrode Arrays. Front Cell Neurosci 11.

Blattner MS, Mahoney MM (2015) Changes in estrogen receptor signaling alters the timekeeping system in male mice. Behav Brain Res 294:43–49 Available at: http://dx.doi.org/10.1016/j.bbr.2015.07.060.

Boehler MD, Wheeler BC, Brewer GJ (2007) Added astroglia promote greater synapse density and higher activity in neuronal networks. Neuron Glia Biol 3:127–140 Available at: http://www.journals.cambridge.org/abstract_S1740925X07000440.

Bonzano L, Bove M, Martinoia S (2006) Effects of NMDA and non-NMDA receptors on the dynamic behavior of cultured cortical networks. Neurocomputing 69:1897–1903.

Bouret S, Sara SJ (2005) Network reset: A simplified overarching theory of locus coeruleus noradrenaline function. Trends Neurosci 28:574–582.

Bourgin P, Huitron-Resendiz S, Spier AD, Fabre V, Morte B, Criado JR, Sutcliffe JG, Henriksen SJ, de Lecea L (2000) Hypocretin-1 Modulates Rapid Eye Movement Sleep through Activation of Locus Coeruleus Neurons. J Neurosci 20:7760–7765 Available at: http://www.jneurosci.org/content/20/20/7760.long.

Boutrel B, Kenny PJ, Specio SE, Martin-Fardon R, Markou A, Koob GF, de Lecea L (2005) Role for hypocretin in mediating stress-induced reinstatement of cocaine-seeking behavior. Proc Natl Acad Sci 102:19168–19173.

Bouvier J, Caggiano V, Leiras R, Caldeira V, Bellardita C, Balueva K, Fuchs A, Kiehn O (2015) Descending Command Neurons in the Brainstem that Halt Locomotion. Cell 163:1191–1203 Available at: http://dx.doi.org/10.1016/j.cell.2015.10.074.

Bremer F (1935) Cerveau "isolé" et physiologie du sommeil. C R Soc Biol 118:1235–1241.

Bretzner F, Brownstone RM (2013) Lhx3-Chx10 reticulospinal neurons in locomotor circuits. J Neurosci 33:14681–14692 Available at: http://www.ncbi.nlm.nih.gov/pubmed/24027269.

Brown TG (1913) On the nature of the fundamental activity of the nervous centres; together with an analysis of the conditioning of rhythmic activity in progression, and a theory of the evolution of function in the nervous system. Evolution (N Y) 48.

Caggiano V, Leiras R, Goñi-Erro H, Masini D, Bellardita C, Bouvier J, Caldeira V, Fisone G, Kiehn O (2018) Midbrain circuits that set locomotor speed and gait selection. Nature 553:455–460 Available at: http://www.nature.com/doifinder/10.1038/nature25448.

Calderon DP, Kilinc M, Maritan A, Banavar J, Pfaff DW (2016) Generalized CNS Arousal: an Elementary Force Within the Vertebrate Nervous System. Neurosci Biobehav Rev 68:167–176.

Cape EG, Jones BE (1998) Differential modulation of high-frequency gamma-electroencephalogram activity and sleep-wake state by noradrenaline and serotonin microinjections into the region of cholinergic basalis neurons. J Neurosci 18:2653–2666 Available at: http://www.ncbi.nlm.nih.gov/pubmed/9502823.

Capelli P, Pivetta C, Esposito MS, Arber S (2017) Locomotor speed control circuits in the caudal brainstem. Nature 551:373–377 Available at: http://dx.doi.org/10.1038/nature24064.

Carter ME, Yizhar O, Chikahisa S, Nguyen H, Adamantidis A, Nishino S, Deisseroth K, Lecea L De (2010) Tuning arousal with optogenetic modulation of locus coeruleus neurons. Nat Neurosci 13:1526–1533 Available at: http://dx.doi.org/10.1038/nn.2682.

Castanon-Cervantes O, Wu M, Ehlen JC, Paul K, Gamble KL, Johnson RL, Besing RC, Menaker M, Gewirtz AT, Davidson AJ (2010) Dysregulation of Inflammatory Responses by Chronic Circadian Disruption. J Immunol 185:5796–5805 Available at: http://www.jimmunol.org/cgi/doi/10.4049/jimmunol.1001026.

Castro-alamancos MA, Connors BW (1996) Short-Term Plasticity of a Thalamocortical Pathway Dynamically Modulated by Behavioral State. Science (80-) 272:274–277.

Chevalier M, Toporikova N, Simmers J, Thoby-Brisson M (2016) Development of pacemaker properties and rhythmogenic mechanisms in the mouse embryonic respiratory network. Elife 5.

Chiappalone M, Bove M, Vato A, Tedesco M, Martinoia S (2006) Dissociated cortical networks show spontaneously correlated activity patterns during in vitro development. Brain Res 1093:41–53.

Chow C, Ong K, Dougherty E, Simons SS (2011) Inferring mechanisms from dose-response curves. Methods Enzymol 487:465–483.

Chu X, Gagnidze K, Pfaff D, Ågmo A (2015) Estrogens, androgens and generalized behavioral arousal in gonadectomized female and male C57BL/6 mice. Physiol Behav 147:255–263 Available at: http://dx.doi.org/10.1016/j.physbeh.2015.04.053.

Chung S, Weber F, Zhong P, Tan CL, Nguyen TN, Beier KT, Hörmann N, Chang WC, Zhang Z, Do JP, Yao S, Krashes MJ, Tasic B, Cetin A, Zeng H, Knight ZA, Luo L, Dan Y (2017) Identification of preoptic sleep neurons using retrograde labelling and gene profiling. Nature 545:477–481.

Clements M, Thomas N (2014) High-throughput multi-parameter profiling of electrophysiological drug effects in human embryonic stem cell derived cardiomyocytes using multi-electrode arrays. Toxicol Sci 140:445–461.

Conway BYBA, Hultbornt H, Kiehn O, Mintz I (1988) Plateau potentials in a-motorneurones induced by intravenous injection of L-dopa and clonidine in the spinal cat. J Physiol 405:369–384.

Cordle J, Shattuck N (2013) A Sea Change in Standing Watch. United States Nav Inst Proc 139:34–39 Available at: https://www.usni.org/magazines/proceedings/2013-01/sea-change-standing-watch.

Crone SA, Viemari J-C, Droho S, Mrejeru A, Ramirez J-M, Sharma K (2012) Irregular Breathing in Mice following Genetic Ablation of V2a Neurons. J Neurosci 32:7895–7906 Available at: http://www.jneurosci.org/cgi/doi/10.1523/JNEUROSCI.0445-12.2012.

Crone SA, Quinlan KA, Zagoraiou L, Droho S, Restrepo CE, Lundfald L, Endo T, Setlak J, Jessell TM, Kiehn O, Sharma K (2008) Genetic Ablation of V2a Ipsilateral Interneurons Disrupts Left-Right Locomotor Coordination in Mammalian Spinal Cord. Neuron 60:70–83.

Daan S, Damassa D, Pittendrigh CS, Smith ER (1975) An effect of of castration and testosterone rreplacement on a circadian pacemaker in mice. Proc Natl Acad Sci 72:3744–3747.

Dauth S, Maoz BM, Sheehy SP, Hemphill MA, Murty T, Macedonia MK, Greer AM, Budnik B, Parker KK (2016) Neurons derived from different brain regions are inherently different in vitro: A novel multiregional brain-on-a-chip. J Neurophysiol 117:1320–1341 Available at: http://jn.physiology.org/lookup/doi/10.1152/jn.00575.2016.

de Lecea L, Kilduff TS, Peyron C, Gao X, Foye PE, Danielson PE, Fukuhara C, Battenberg EL, Gautvik VT, Bartlett FS, Frankel WN, van den Pol AN, Bloom FE, Gautvik KM, Sutcliffe JG (1998) The hypocretins: hypothalamus-specific peptides with neuroexcitatory activity. Proc Natl Acad Sci 95:322–327.

Deboer T, Tobler I (2000) Running wheel size influences circadian rhythm period and its phase shift in mice. J Comp Physiol - A Sensory, Neural, Behav Physiol 186:969–973.

Devidze N, Lee AW, Zhou J, Pfaff DW (2006) CNS arousal mechanisms bearing on sex and other biologically regulated behaviors. Physiol Behav 88:283–293.

Dubuc R, Brocard F, Antri M, Fénelon K, Gariépy JF, Smetana R, Ménard A, Le Ray D, Viana Di Prisco G, Pearlstein É, Sirota MG, Derjean D, St-Pierre M, Zielinski B, Auclair F, Veilleux D (2008) Initiation of locomotion in lampreys. Brain Res Rev 57:172–182.

Eban-Rothschild A, Rothschild G, Giardino WJ, Jones JR, De Lecea L (2016) VTA dopaminergic neurons regulate ethologically relevant sleep-wake behaviors. Nat Neurosci 19:1356–1366.

Edelman GM (1993) Neural Darwinism: Selection and reentrant signaling in higher brain function. Neuron 10:115–125.

Edgar DM, Kilduff TS, Martin CE, Dement WC (1991) Influence of running wheel activity on free-running sleep/wake and drinking circadian rhythms in mice. Physiol Behav 50:373–378.

Elias CF, Saper CB, Maratos-Flier E, Tritos NA, Lee C, Kelly J, Tatro JB, Huffman GE, Ollmann MM, Barsh GS, Sakurai T, Yanagisawa M, Elmquist JK (1998) Chemically defined projections linking the mediobasal hypothalamus and the lateral hypothalamic area. J Comp Neurol 402:442–459.

Engel AK, Singer W (2001) Temporal binding and the neural correlates of sensory awareness. trends Cogn Sci 5:16–25.

Ennis M, Aston-Jones G (1988) Activation of locus coeruleus from nucleus paragigantocellularis: a new excitatory amino acid pathway in brain. J Neurosci 8:3644–3657 Available at: http://www.ncbi.nlm.nih.gov/pubmed/3193175.

Esposti F, Signorini MG, Potter SM, Cerutti S (2009) Statistical long-term correlations in dissociated cortical neuron recordings. IEEE Trans Neural Syst Rehabil Eng 17:364–369.

Fantin A, Vieira JM, Plein A, Maden CH, Ruhrberg C (2013) The embryonic mouse hindbrain as a qualitative and quantitative model for studying the molecular and cellular mechanisms of angiogenesis. Nat Protoc 8:418–429 Available at: http://dx.doi.org/10.1038/nprot.2013.015.

Fekete C, Liposits Z (2003) Histamine-immunoreactive neurons of the tuberomammillary nucleus are innervated by α-melanocyte stimulating hormone-containing axons. Generation of a new histamine antiserum for ultrastructural studies. Brain Res 969:70–77.

Ferrari PF, Van Erp AMM, Tornatzky W, Miczek KA (2003) Accumbal dopamine and serotonin in anticipation of the next aggressive episode in rats. Eur J Neurosci 17:371–378.

Fujita A, Bonnavion P, Wilson MH, Mickelsen LE, Bloit J, de Lecea L, Jackson AC (2017) Hypothalamic tuberomammillary nucleus neurons: electrophysiological diversity and essential role in arousal stability. J Neurosci 37:9574–9592 Available at: http://www.jneurosci.org/lookup/doi/10.1523/JNEUROSCI.0580-17.2017.

Garey J, Goodwillie A, Frohlich J, Morgan M, Gustafsson J, Smithies O, Korach KS, Ogawa S, Pfaff DW (2003) Genetic contributions to generalized arousal of brain and behavior. Proc Natl Acad Sci 100:11019–11022.

Gatto G, Goulding M (2018) Locomotion Control: Brainstem Circuits Satisfy the Need for Speed. Curr Biol 28:R254-77 Available at: http://linkinghub.elsevier.com/retrieve/pii/S0960982218301015.

Gielow MR, Zaborszky L (2017) The Input-Output Relationship of the Cholinergic Basal Forebrain. Cell Rep 18:1817–1830 Available at: http://dx.doi.org/10.1016/j.celrep.2017.01.060.

Golowasch J, Casey M, Abbott LF, Marder E (1999) Network stability from activity-dependent regulation of neuronal conductances. Neural Comput 11:1079–1096.

Gompf HS, Aston-jones G (2008) Role of orexin input in the diurnal rhythm of locus coeruleus impulse activity. Brain Res 1224:43–52.

Grätsch S, Auclair F, Demers O, Auguste E, Hanna A, Büschges A, Dubuc R (2019) A brainstem neural substrate for stopping locomotion. J Neurosci 39:1044–1057 Available at: http://www.ncbi.nlm.nih.gov/pubmed/30541913%0Ahttp://www.jneurosci.org/lookup/doi/10.1523/JNEUROSCI.1992-18.2018.

Grillner S, Wallén P, Saitoh K, Kozlov A, Robertson B (2008) Neural bases of goal-directed locomotion in vertebrates-An overview. Brain Res Rev 57:2–12.

Grossman SP (1968) Behavioral and electroencephalographic effects of micro-injections of neurohumors into the midbrain reticular formation. Physiol Behav 3:777–786.

Ha N, Dougherty KJ (2018) Spinal Shox2 interneuron interconnectivity related to function and development. Elife 7.

Haas HL, Sergeeva OA, Selbach O (2008) Histamine in the Nervous System. Physiol Rev 88:1183–1241.

Haas H, Panula P (2003) The role of histamine and the tubermamillary nucleus in the nervous system. Nat Rev Neurosci 4:121–130.

Haensel SM, Mos J, Olivier B, Slob AK (1991) Sex Behavior of Male and Female Wistar Rats Affected by the Serotonin Agonist 8-OH-DPAT. Pharmacol Biochem Behav 40:221–228.

Hägglund M, Borgius L, Dougherty KJ, Kiehn O (2010) Activation of groups of excitatory neurons in the mammalian spinal cord or hindbrain evokes locomotion. Nat Neurosci 13:246–252 Available at: http://www.nature.com/doifinder/10.1038/nn.2482.

Haidet-Phillips AM, Hester ME, Miranda CJ, Meyer K, Braun L, Frakes A, Song S, Likhite S, Murtha MJ, Foust KD, Rao M, Eagle A, Kammesheidt A, Christensen A, Mendell JR, Burghes AHM, Kaspar BK (2011) Astrocytes from familial and sporadic ALS patients are toxic to motor neurons. Nat Biotechnol 29:824–828 Available at: http://www.nature.com/doifinder/10.1038/nbt.1957.

Hasegawa E, Maejima T, Yoshida T, Masseck OA, Herlitze S, Yoshioka M, Sakurai T, Mieda M (2017) Serotonin neurons in the dorsal raphe mediate the anticataplectic action of orexin neurons by reducing amygdala activity. Proc Natl Acad Sci 114:E3526-35 Available at: http://www.pnas.org/lookup/doi/10.1073/pnas.1614552114.

Hasegawa E, Yanagisawa M, Sakurai T, Mieda M (2014) Orexin neurons suppress narcolepsy via 2 distinct efferent pathways. J Clin Invest 124:604–616.

Hastings MH, Maywood ES, Brancaccio M (2018) Generation of circadian rhythms in the suprachiasmatic nucleus. Nat Rev Neurosci 19:453–469 Available at: http://www.nature.com/articles/s41583-018-0026-z.

Hösli L, Tebecis AK, Schönwetter HP (1971) A comparison of the effects of monoamines on neurones of the bulbar reticular formation. Brain Res 25:357–370.

Hu B, Yang N, Qiao QC, Hu ZA, Zhang J (2015) Roles of the orexin system in central motor control. Neurosci Biobehav Rev 49:43–54.

Humphries MD, Gurney K, Prescott TJ (2006) The brainstem reticular formation is a small-world, not scale-free, network. Proc R Soc B 273:503–511.

Inzunza O, Serón-Ferré MJ, Bravo H, Torrealba F (2000) Tuberomammillary nucleus activation anticipates feeding under a restricted schedule in rats. Neurosci Lett 293:139–142.

Iwahana E, Karatsoreos I, Shibata S, Silver R (2008) Gonadectomy reveals sex differences in circadian rhythms and suprachiasmatic nucleus androgen receptors in mice. Horm Behav 53:422–430.

Jenkinson SP, Grandgirard D, Heidemann M, Tscherter A, Avondet M, Leib SL (2017) Embryonic Stem Cell-Derived Neurons Grown on Multi-Electrode Arrays as a Novel In vitro Bioassay for the Detection of Clostridium botulinum Neurotoxins. Front Pharmacol 8.

Jewett KA, Taishi P, Sengupta P, Roy S, Davis CJ (2015) Tumor necrosis factor enhances the sleep-like state and electrical stimulation induces a wake-like state in co-cultures of neurons and glia. Eur J Neurosci 42:2078–2090.

Jones BE, Yang TZ (1985) The efferent projections from the reticular formation and the locus coeruleus studied by anterograde and retrograde axonal transport in the rat. J Comp Neurol 242:56–92 Available at: http://www.ncbi.nlm.nih.gov/pubmed/2416786.

Jones BE (2003) Arousal Systems. Front Biosci 1:438–451.

Jones BE (2004) Activity, modulation and role of basal forebrain cholinergic neurons innervating the cerebral cortex. Prog Brain Res 145:157–169.

Jordan LM, Liu J, Hedlund PB, Akay T, Pearson KG (2008) Descending command systems for the initiation of locomotion in mammals. Brain Res Rev 57:183–191.

Josset N, Roussel M, Lemieux M, Lafrance-Zougba D, Rastqar A, Bretzner F (2018) Distinct contributions of mesencephalic locomotor region nuclei to locomotor control in the freely behaving mouse. Curr Biol 28:1–18 Available at: https://doi.org/10.1016/j.cub.2018.02.007.

Juvin L, Gratsch S, Trillaud-Doppia E, Gariepy JF, Buschges A, Dubuc R (2016) A Specific Population of Reticulospinal Neurons Controls the Termination of Locomotion. Cell Rep 15:2377–2386.

Karatsoreos IN, Bhagat S, Bloss EB, Morrison JH, McEwen BS (2011) Disruption of circadian clocks has ramifications for metabolism, brain, and behavior. Proc Natl Acad Sci 108:1657–1662.

Keenan DM, Quinkert AW, Pfaff DW (2015) Stochastic Modeling of Mouse Motor Activity under Deep Brain Stimulation: The Extraction of Arousal Information. PLoS Comput Biol 11.

Kim LH, Sharma S, Sharples SA, Mayr KA, Kwok CHT, Whelan PJ (2017) Integration of Descending Command Systems for the Generation of Context-Specific Locomotor Behaviors. Front Neurosci 11.

Kimura Y, Satou C, Fujioka S, Shoji W, Umeda K, Ishizuka T, Yawo H, Higashijima SI (2013) Hindbrain V2a neurons in the excitation of spinal locomotor circuits during zebrafish swimming. Curr Biol 23:843–849 Available at: http://dx.doi.org/10.1016/j.cub.2013.03.066.

Koch M (1999) The neurobiology of startle. Prog Neurobiol 59:107–128.

Kocsis B, Varga V, Dahan L, Sik A (2006) Serotonergic neuron diversity: Identification of raphe neurons with discharges time-locked to the hippocampal theta rhythm. Proc Natl Acad Sci

103:1059–1064 Available at: http://www.pnas.org/content/103/4/1059%5Cnhttp://www.ncbi.nlm.nih.gov/pubmed/16418294%5Cnhttp://www.pnas.org/content/103/4/1059.full.pdf%5Cnhttp://www.pnas.org/content/103/4/1059.short.

Korn H, Faber DS (2005) The Mauthner cell half a century later: A neurobiological model for decision-making? Neuron 47:13–28.

Kosse C, Schöne C, Bracey E, Burdakov D (2017) Orexin-driven GAD65 network of the lateral hypothalamus sets physical activity in mice. Proc Natl Acad Sci 114:4525–4530.

Koteja P, Swallow JG, Carter PA, Garland T (2003) Different Effects of Intensity and Duration of Locomotor Activity on Circadian Period. J Biol Rhythms 18:491–501.

Krichmar JL, Reeke GN (2005) The Darwin brain-based automata: Synthetic neural models and real-world devices. In: Modeling in the Neurosciences: From Biological Systems to Neuromimetic Robotics, 2nd ed. (Reeke GN, Poznaski RR, Lindsay KA, Rosenberg JR, Sporns O, eds), pp 613–637. Boca Raton, FL: Taylor & Francis.

Kuljis DA, Loh DH, Truong D, Vosko AM, Ong ML, McClusky R, Arnold AP, Colwell CS (2013) Gonadal- and sex-chromosome-dependent sex differences in the circadian system. Endocrinology 154:1501–1512.

Lampl M (2012) Perspectives on modelling human growth: Mathematical models and growth biology. Ann Hum Biol 39:342–351.

Lee AW, Devidze N, Pfaff DW, Zhou J (2006) Functional genomics of sex hormone-dependent neuroendocrine systems: specific and generalized actions in the CNS. Prog Brain Res 158:243–272.

Lee RH, Heckman CJ (1999) Enhancement of bistability in spinal motoneurons in vivo by the noradrenergic a1 agonist methoxamine. J Physiol:2164–2174.

Lemieux M, Bretzner F (2019) Glutamatergic neurons of the gigantocellular reticular nucleus shape locomotor pattern and rhythm in the freely behaving mouse. PLoS Biol 17:e2003880.

Li W-C, Soffe SR (2019) Stimulation of Single, Possible CHX10 Hindbrain Neurons Turns Swimming On and Off in Young Xenopus Tadpoles. Front Cell Neurosci 13 Available at: https://www.frontiersin.org/article/10.3389/fncel.2019.00047/full.

Li X, Sun J, Chen W, Zeng S, Luo Q (2009) The generation of the synchronized burst in cultured neuronal networks. Proc SPIE, Int Soc Opt Eng 7176 Available at: http://proceedings.spiedigitallibrary.org/proceeding.aspx?articleid=806047.

Li X, Zhou W, Zeng S, Liu M, Luo Q (2007) Long-term recording on multi-electrode array reveals degraded inhibitory connection in neuronal network development. Biosens Bioelectron 22:1538–1543.

Li Y, Zhong W, Wang D, Feng Q, Liu Z, Zhou J, Jia C, Hu F, Zeng J, Guo Q, Fu L, Luo M (2016) Serotonin neurons in the dorsal raphe nucleus encode reward signals. Nat Commun 28.

Lin JS, Sakai K, Vanni-Mercier G, Jouvet M (1989) A critical role of the posterior hypothalamus in the mechanisms of wakefulness determined by microinjection of muscimol in freely moving cats. Brain Res 479:225–240.

Liu C, Xue Y, Liu M-F, Wang Y, Liu Z-R, Diao H-L, Chen L (2018) Orexins increase the firing activity of nigral dopaminergic neurons and participate in motor control in rats. J Neurochem 147:380–394 Available at: http://doi.wiley.com/10.1111/jnc.14568.

Liu Z, Zhou J, Li Y, Hu F, Lu Y, Ma M, Feng Q, Zhang J en, Wang D, Zeng J, Bao J, Kim JY, Chen ZF, El Mestikawy S, Luo M (2014) Dorsal raphe neurons signal reward through 5-HT and glutamate. Neuron 81:1360–1374.

Lonardoni D, Amin H, Di Marco S, Maccione A, Berdondini L, Nieus T (2017) Recurrently connected and localized neuronal communities initiate coordinated spontaneous activity in neuronal networks. PLoS Comput Biol 13 Available at: http://dx.doi.org/10.1371/journal.pcbi.1005672.

Lundberg A (1981) Half-Centres Revisited. In: Regulatory Functions of the CNS Principles of Motion and Organization, pp 155–167.

Maher MP, Dvorak-Carbone H, Pine J, Wright JA, Tai Y-C (1999) Microstructures for studies of cultured neural networks. Med Biol Eng Comput 37:110–118 Available at: http://link.springer.com/10.1007/BF02513276.

Maheswaranathan N, Ferrari S, VanDongen A, Henriquez C (2012) Emergent bursting and synchrony in computer simulations of neuronal cultures. Front Comput Neurosci 6:1–11 Available at: http://journal.frontiersin.org/article/10.3389/fncom.2012.00015/abstract.

Marder E, Bucher D (2001) Central pattern generators and the control of rhythmic movements. Curr Biol 11:R986–R996.

Martin EM, Devidze N, Shelley DN, Westberg L, Fontaine C, Pfaff DW (2011) Molecular and neuroanatomical characterization of single neurons in the mouse medullary gigantocellular reticular nucleus. J Comp Neurol 519:2574–2593.

Martin EM, Pavlides C, Pfaff D (2010) Multimodal sensory responses of nucleus reticularis gigantocellularis and the responses' relation to cortical and motor activation. J Neurophysiol 103:2326–2338 Available at: http://www.pubmedcentral.nih.gov/articlerender.fcgi?artid=2867576&tool=pmcentrez&rendertype=abstract.

Mather M, Clewett D, Sakaki M, Harley CW (2016) Norepinephrine ignites local hotspots of neuronal excitation: How arousal amplifies selectivity in perception and memory. Behav Brain Sci 39.

McBride RL, Sutin J (1976) Projections of the locus coeruleus and adjacent pontine tegmentum in the cat. J Comp Neurol 165:265–284.

McCrea DA, Rybak IA (2007) Modeling the mammalian locomotor CPG: insights from mistakes and perturbations. Prog Brain Res 165:235–253.

Miles GB, Sillar KT (2011) Neuromodulation of vertebrate locomotor control networks. Physiology 26:393–411.

Miles GB, Yohn DC, Wichterle H, Jessell TM, Rafuse VF, Brownstone RM (2004) Functional properties of motoneurons derived from mouse embryonic stem cells. J Neurosci 24:7848–7858.

Minert A, Yatziv S-L, Devor M (2017) Location of the Mesopontine Neurons Responsible for Maintenance of Anesthetic Loss of Consciousness. J Neurosci 37:9320–9331.

Monti JM, Monti D (2007) The involvement of dopamine in the modulation of sleep and waking. Sleep Med Rev 11:113–133.

Morimoto T, Yamamoto Y, Mobarakeh JI, Yanai K, Watanabe T, Watanabe T, Yamatodani A (1999) Involvement of the Histaminergic System in Leptin-Induced Suppression of Food Intake. Physiol Behav 67:679–683.

Morrison LW (1997) The Insular Biogeography of Small Bahamian Cays. J Ecol 85:441–454.

Moruzzi G, Magoun HW (1949) Brain stem reticular formation and activation of the EEG. Electroencephalogr Clin Neurophysiol 1:455–473 Available at: http://linkinghub.elsevier.com/retrieve/pii/0013469449902199.

Olivier B (2015) Serotonin: A never-ending story. Eur J Pharmacol 753:2–18.

Orofino AG, Ruarte MB, Alvarez EO (1999) Exploratory behaviour after intra-accumbens histamine and/or histamine antagonists injection in the rat. Behav Brain Res 102:171–180.

Oueghlani Z, Simonnet C, Cardoit L, Courtand G, Cazalets J-R, Morin D, Juvin L, Barrière G (2018) Brainstem steering of locomotor activity in the newborn rat. J Neurosci 38:7725–7740 Available at: http://www.jneurosci.org/lookup/doi/10.1523/JNEUROSCI.1074-18.2018.

Palva JM, Palva S, Kaila K (2005) Phase Synchrony among Neuronal Oscillations in the Human Cortex. J Neurosci 25:3962–3972.

Parmentier R, Ohtsu H, Djebbara-Hannas Z, Valatx J-L, Watanabe T, Lin J-S (2002) Anatomical, physiological, and pharmacological characteristics of histidine decarboxylase knock-out mice: evidence for the role of brain histamine in behavioral and sleep-wake control. J Neurosci 22:7695–7711 Available at: http://www.ncbi.nlm.nih.gov/pubmed/12196593.

Pauls SD, Honma KI, Honma S, Silver R (2016) Deconstructing Circadian Rhythmicity with Models and Manipulations. Trends Neurosci 39:405–419.

Pearl R, Reed LJ (1920) On the Rate of Growth of the Population of the United States since 1790 and Its Mathematical Representation. Proc Natl Acad Sci 6:275–288.

Peterson B (1979) Reticulospinal Projections to Spinal Motor Nuclei. Annu Rev Physiol 41:127–140.

Peyron C, Tighe DK, van den Pol a N, de Lecea L, Heller HC, Sutcliffe JG, Kilduff TS (1998) Neurons containing hypocretin (orexin) project to multiple neuronal systems. J Neurosci 18:9996–10015.

Pfaff D, Bubnys A, Tabansky I (2017) The brainstem reticular formation and CNS arousal. In: The Brainstem and Behavior, 1st ed. (Lalonde R, ed), pp 1–21. New York: Nova biomedical.

Pfaff DW (2006) Brain Arousal and Information Theory, 1st ed. Harvard University Press.

Pfaff DW, Martin EM, Faber D (2012) Origins of arousal: Roles for medullary reticular neurons. Trends Neurosci 35:468–476.

Pfaff D, Banavar JR (2007) A theoretical framework for CNS arousal. BioEssays 29:803–810.

Phillips DJ, Savenkova MI, Karatsoreos IN (2015) Environmental disruption of the circadian clock leads to altered sleep and immune responses in mouse. Brain Behav Immun 47:14–23 Available at: http://dx.doi.org/10.1016/j.bbi.2014.12.008.

Piper DC, Upton N, Smith MI, Hunter AJ (2000) The novel brain neuropeptide, orexin-A, modulates the sleep-wake cycle of rats. Eur J Neurosci 12:726–730.

Pivetta C, Esposito MS, Sigrist M, Arber S (2014) Motor-circuit communication matrix from spinal cord to brainstem neurons revealed by developmental origin. Cell 156:537–548 Available at: http://dx.doi.org/10.1016/j.cell.2013.12.014.

Pollak Dorocic I, Fürth D, Xuan Y, Johansson Y, Pozzi L, Silberberg G, Carlén M, Meletis K (2014) A Whole-Brain Atlas of Inputs to Serotonergic Neurons of the Dorsal and Median Raphe Nuclei. Neuron 83:663–678.

Portas CM, Bjorvatn B, Ursin R (2000) Serotonin and the sleep/wake cycle: Special emphasis on microdialysis studies. Prog Neurobiol 60:13–35.

Proekt A, Banavar JR, Maritan A, Pfaff DW (2012) Scale invariance in the dynamics of spontaneous behavior. Proc Natl Acad Sci 109:10564–10569.

Qiu MH, Liu W, Qu WM, Urade Y, Lu J, Huang JL (2012) The role of nucleus accumbens core/shell in sleep-wake regulation and their involvement in modafinil-induced arousal. PLoS One 7.

Reeke GN (2016) Modeling Neuronal Systems. In: Neuroscience in the 21st Century, 2nd ed. (Pfaff DW, Volkow ND, eds). New York: Springer.

Reeke GN, Edelman GM (1987) Selective neural networks and their implications for recognition automata. Intl J Supercomput Appl 1:44–69.

Rogers DC, Fisher EMC, Brown SDM, Peters J, Hunter AJ, Martin JE (1997) Behavioral and functional analysis of mouse phenotype: SHIRPA, a proposed protocol for comprehensive phenotype assessment. Mamm Genome 8:711–713.

Rosenblatt F (1958) The Perceptron: A probabilistic model for information storage and organization in the brain. Psychol Rev 65:386–408.

Rothstein JD, Dykes-Hoberg M, Pardo CA, Bristol LA, Jin L, Kuncl RW, Kanai Y, Hediger MA, Wang Y, Schielke JP, Welty DF (1996) Knockout of Glutamate Transporters Reveals a Major Role for Astroglial Transport in Excitotoxicity and Clearance of Glutamate. Neuron 16:675–686 Available at: papers2://publication/uuid/327F682D-2D03-48C7-A0E6-A57E2CD92157.

Ruarte MB, Orofino AG, Alvarez EO (1997) Hippocampal histamine receptors and conflictive exploration in the rat: Studies using the elevated asymmetric plus-maze. Brazilian J Med Biol Res 30:1451–1461.

Ruivo LMT-G, Baker KL, Conway MW, Kinsley PJ, Gilmour G, Phillips KG, Isaac JTR, Lowry JP, Mellor JR (2017) Coordinated Acetylcholine Release in Prefrontal Cortex and Hippocampus Is Associated with Arousal and Reward on Distinct Timescales. Cell Rep 18:905–917 Available at: http://dx.doi.org/10.1016/j.celrep.2016.12.085.

Rybak IA, Dougherty KJ, Shevtsova NA (2015) Organization of the Mammalian Locomotor CPG: Review of Computational Model and Circuit Architectures Based on Genetically Identified Spinal Interneurons. eNeuro 2 Available at: http://eneuro.sfn.org/cgi/doi/10.1523/ENEURO.0069-15.2015.

Ryczko D, Cone JJ, Alpert MH, Goetz L, Auclair F, Dubé C, Parent M, Roitman MF, Alford S, Dubuc R (2016) A descending dopamine pathway conserved from basal vertebrates to mammals. Proc Natl Acad Sci 113:E2440-9 Available at: http://www.pnas.org/lookup/doi/10.1073/pnas.1600684113.

Sakurai T et al. (1998) Orexins and Orexin Receptors: A Family of Hypothalamic Neuropeptides and G Protein-Coupled Receptors that Regulate Feeding Behavior. Cell 92:573–585.

Saper CB, Fuller PM, Pederson NP, Lu J, Scammell TE (2010) Sleep State Switching. Neuron 68:1023–1042.

Saper CB, Chou TC, Scammell TE (2001) The sleep switch: Hypothalamic control of sleep and wakefulness. Trends Neurosci 24:726–731.

Saper CB, Scammell TE, Lu J (2005) Hypothalamic regulation of sleep and circadian rhythms. Nature 437:1257–1263.

Sara SJ, Bouret S (2012) Orienting and Reorienting : The Locus Coeruleus Mediates Cognition through Arousal. Neuron 76:130–141 Available at: http://dx.doi.org/10.1016/j.neuron.2012.09.011.

Sarkar A, Mei A, Paquola ACM, Stern S, Bardy C, Klug JR, Kim S, Neshat N, Kim HJ, Ku M, Shokhirev MN, Adamowicz DH, Marchetto MC, Jappelli R, Erwin JA, Padmanabhan K, Shtrahman M, Jin X, Gage FH (2018) Efficient Generation of CA3 Neurons from Human Pluripotent Stem Cells Enables Modeling of Hippocampal Connectivity In Vitro. Cell Stem Cell 22:684–697 Available at: http://linkinghub.elsevier.com/retrieve/pii/S1934590918301711.

Scemes E, Giaume C (2006) Astrocyte Calcium Waves: What They Are and What They Do. Glia 54:716–725.

Schiebel ME, Schiebel AB (1967) Anatomical basis of attention mechanisms in vertebrate brains. In: The Neurosciences, a Study Program (Quarton GC, Melnechuk QT, Schmitt FO, eds), pp 577–602. New York: Rockefeller University Press.

Schiff ND, Giacino JT, Kalmar K, Victor JD, Baker K, Gerber M, Fritz B, Eisenberg B, O'Connor J, Kobylarz EJ, Farris S, Machado A, McCagg C, Plum F, Fins JJ, Rezai AR (2007) Behavioural improvements with thalamic stimulation after severe traumatic brain injury. Nature 448:600–603.

Schildge S, Bohrer C, Beck K, Schachtrup C (2013) Isolation and Culture of Mouse Cortical Astrocytes. J Vis Exp:1–7 Available at: http://www.jove.com/video/50079/isolation-and-culture-of-mouse-cortical-astrocytes.

Schultz W, Dayan P, Montague PR (1997) A Neural Substrate of Prediction and Reward. Science (80-) 275:1593–1599.

Schultz W, Stauffer WR, Lak A (2017) The phasic dopamine signal maturing: from reward via behavioural activation to formal economic utility. Curr Opin Neurobiol 43:139–148 Available at: http://dx.doi.org/10.1016/j.conb.2017.03.013.

Schwartz MD, Kilduff TS (2015) The Neurobiology of Sleep and Wakefulness. Psychiatr Clin North Am 38:615–644.

Schwarz LA, Luo L (2015a) Organization of the Locus Coeruleus-Norepinephrine System. Curr Biol 25:R1051-6 Available at: http://www.ncbi.nlm.nih.gov/pubmed/26528750.

Schwarz LA, Miyamichi K, Gao XJ, Beier KT, Weissbourd B, DeLoach KE, Ren J, Ibanes S, Malenka RC, Kremer EJ, Luo L (2015b) Viral-genetic tracing of the input–output organization of a central noradrenaline circuit. Nature 524:88–92 Available at: http://www.nature.com/doifinder/10.1038/nature14600.

Sears RM, Fink AE, Wigestrand MB, Farb CR, De Lecea L, LeDoux JE (2013) Orexin / hypocretin system modulates amygdala- dependent threat learning through the locus coeruleus. Proc Natl Acad Sci 110:20260–20265.

Shannon CE (1948) A Mathematical Theory of Communication. Bell Syst Tech J 27:373–439, 623–656.

Sharples SA, Koblinger K, Humphreys JM, Whelan PJ (2014) Dopamine: a parallel pathway for the modulation of spinal locomotor networks. Front Neural Circuits 8:1–16 Available at: http://journal.frontiersin.org/article/10.3389/fncir.2014.00055/abstract.

Shattuck NL, Matsangas P (2016) Operational assessment of the 5-h on/10-h off watchstanding schedule on a US Navy ship: sleep patterns, mood and psychomotor vigilance performance of crewmembers in the nuclear reactor department. Ergonomics 59:657–664.

Shelley DN, Dwyer ER, Johnson C, Wittkowski KM, Pfaff DW (2007) Interactions between estrogen effects and hunger effects in ovariectomized female mice. I. Measures of arousal. Horm Behav 52:546–553.

Sherman D, Fuller PM, Marcus J, Yu J, Zhang P, Chamberlin NL, Saper CB, Lu J (2015) Anatomical location of the mesencephalic locomotor region and its possible role in locomotion, posture, cataplexy, and Parkinsonism. Front Neurol 6.

Silver R, LeSauter J, Tresco PA, Lehman MN (1996) A diffusible coupling signal from the transplanted suprachiasmatic nucleus controlling circadian locomotor rhythms. Nature 382:810–813.

Singer W (1999) Neuronal Synchrony : A Versatile Code for the Definition of Relations? Neuron 24:49–65.

Smetana R, Juvin L, Dubuc R, Alford S (2010) A parallel cholinergic brainstem pathway for enhancing locomotor drive. Nat Neurosci 13:731–738 Available at: http://www.nature.com/doifinder/10.1038/nn.2548.

Smith JC, Feldman JL (1987) In vitro brainstem-spinal cord preparations for study of motor systems for mammalian respiration and locomotion. J Neurosci Methods 21:321–333.

Soffe SR, Roberts A, Li WC (2009) Defining the excitatory neurons that drive the locomotor rhythm in a simple vertebrate: Insights into the origin of reticulospinal control. J Physiol 587:4829–4844.

Soscia D, Belle A, Fischer N, Enright H, Sales A, Osburn J, Benett W, Mukerjee E, Kulp K, Pannu S, Wheeler E (2017) Controlled placement of multiple CNS cell populations to create complex neuronal cultures. PLoS One 12 Available at: http://dx.doi.org/10.1371/journal.pone.0188146.

Sporns O, Gally J a, Reeke GN, Edelman GM (1989) Reentrant signaling among simulated neuronal groups leads to coherency in their oscillatory activity. Proc Natl Acad Sci U S A 86:7265–7269.

Steckler T, Sahgal A (1995) The role of serotonergic-cholinergic interactions in the mediation of cognitive behaviour. Behav Brain Res 67:165–199.

Steininger TL, Alam NM, Gong H, Szymusiak R, Mcginty D (1999) Sleep – waking discharge of neurons in the posterior lateral hypothalamus of the albino rat. Brain Res 840:138–147.

Sternfeld MJ, Hinckley CA, Moore NJ, Pankratz MT, Hilde KL, Driscoll SP, Hayashi M, Amin ND, Bonanomi D, Gifford WD, Sharma K, Goulding M, Pfaff SL (2017) Speed and segmentation control mechanisms characterized in rhythmically-active circuits created from spinal neurons produced from genetically-tagged embryonic stem cells. Elife 6.

Strecker RE, Nalwalk J, Dauphin LJ, Thakkar MM, Chen Y, Ramesh V, Hough LB, McCarley RW (2002) Extracellular histamine levels in the feline preoptic/anterior hypothalamic area during natural sleep-wakefulness and prolonged wakefulness: an in vivo microdialysis study. Neuroscience 113:663–670.

Swanson RA, Liu J, Miller JW, Rothstein JD, Farrell K, Stein BA, Longuemare MC (1997) Neuronal regulation of glutamate transporter subtype expression in astrocytes. J Neurosci 17:932–940.

Tabansky I, Liang Y, Frankfurt M, Daniels MA, Harrigan M, Stern S, Milner TA, Leshan R, Rama R, Moll T, Friedman JM, Stern JNH, Pfaff DW (2018) Molecular profiling of reticular gigantocellularis neurons indicates that eNOS modulates environmentally dependent levels of arousal. Proc Natl Acad Sci 115:E6900-9 Available at: http://www.pnas.org/lookup/doi/10.1073/pnas.1806123115.

Tan KR, Yvon C, Turiault M, Mirzabekov JJ, Doehner J, Labouebe G, Deisseroth K, Tye KM, Luscher C (2012) GABA neurons of the VTA drive conditioned place aversion. Neuron 73:1173–1183.

Tartas M, Morin F, Barriere G, Goillandeau M, Lacaille J-C, Cazalets J-R, Bertrand S (2010) Noradrenergic modulation of intrinsic and synaptic properties of lumbar motoneurons in the neonatal rat spinal cord. Front Neural Circuits 4 Available at: http://journal.frontiersin.org/article/10.3389/neuro.04.004.2010/abstract.

Taylor NE, Van Dort CJ, Kenny JD, Pei J, Guidera JA, Vlasov KY, Lee JT, Boyden ES, Brown EN, Solt K (2016) Optogenetic activation of dopamine neurons in the ventral tegmental area induces reanimation from general anesthesia. Proc Natl Acad Sci 113:12826–12831 Available at: http://www.pnas.org/lookup/doi/10.1073/pnas.1614340113.

Teles-Grilo Ruivo LM, Baker KL, Conway MW, Kinsley PJ, Gilmour G, Phillips KG, Isaac JTR, Lowry JP, Mellor JR (2017) Coordinated Acetylcholine Release in Prefrontal Cortex and Hippocampus Is Associated with Arousal and Reward on Distinct Timescales. Cell Rep 18:905–917 Available at: http://dx.doi.org/10.1016/j.celrep.2016.12.085.

Tikhonov M, Bialek W (2016) Complexity of generic biochemical circuits : topology versus strength of interactions. Phys Biol 13.

Tjorve E (2003) Shapes and functions of species-area curves: a review of possible models. J Biogeogr 30:827–835.

Tjorve E (2003) Shapes and functions of species-area curves: a review of possible models. J Biogeogr 30:827–835.

Tononi G, Sporns O, Edelman GM (1992) Reentry and the problem of integrating multiple cortical areas: simulation of dynamic integration in the visual system. Cereb cortex 2:310–335.

Torrealba F, Riveros ME, Contreras M, Valdes JL (2012) Histamine and motivation. Front Syst Neurosci 6.

Trofimova I, Robbins TW (2016) Temperament and arousal systems: A new synthesis of differential psychology and functional neurochemistry. Neurosci Biobehav Rev 64:382–402 Available at: http://dx.doi.org/10.1016/j.neubiorev.2016.03.008.

Trujillo CA, Gao R, Negraes PD, Chaim IA, Domissy A, Vandenberghe M, Devour A, Yeo GW, Voytek B, Muotri AR (2018) Nested oscillatory dynamics in cortical organoids model early human brain network development. bioRxiv 358622.

Trulson ME, Preussler DW, Howell GA (1981) Activity of substantia nigra units across the sleep-waking cycle in freely moving cats. Neurosci Lett 26:183–188.

Uematsu A, Tan BZ, Ycu EA, Cuevas JS, Koivumaa J, Junyent F, Kremer EJ, Witten IB, Deisseroth K, Johansen JP (2017) Modular organization of the brainstem noradrenaline system coordinates opposing learning states. Nat Neurosci 20:1602–1611.

Ullian EM, Harris BT, Wu A, Chan JR, Barres BA (2004) Schwann cells and astrocytes induce synapse formation by spinal motor neurons in culture. Mol Cell Neurosci 25:241–251.

Uzel SGM, Platt RJ, Subramanian V, Pearl TM, Rowlands CJ, Chan V, Boyer LA, So PTC, Kamm RD (2016) Microfluidic device for the formation of optically motor units. Sci Adv 2 Available at: http://advances.sciencemag.org/content/advances/2/8/e1501429.full.pdf.

Valverde F (1961) Reticular Formation of the Pons and Medulla Oblongata. A Golgi Study. J Comp Neurol 116:71–99.

Van Pelt J, Vajda I, Wolters PS, Corner MA, Ramakers GJA (2005) Dynamics and plasticity in developing neuronal networks in vitro. Prog Brain Res 147:173–188.

Vanderwolf CH, Baker GB (1986) Evidence that serotonin mediates non-cholinergic neocortical low voltage fast activity, non-cholinergic hippocampal rhythmical slow activity and contributes to intelligent behavior. Brain Res 374:342–356.

Vinck M, Bosman CA (2016) More Gamma More Predictions : Gamma-Synchronization as a Key Mechanism for Efficient Integration of Classical Receptive Field Inputs with Surround Predictions. Front Syst Neurosci 10.

Vujovic N, Gooley JJ, Jhou TC, Saper CB (2015) Projections from the subparaventricular zone define four channels of output from the circadian timing system. J Comp Neurol 523:2714–2737.

Wagenaar DA, Madhavan R, Pine J, Potter SM (2005) Controlling Bursting in Cortical Cultures with Closed-Loop Multi-Electrode Stimulation. J Neurosci 25:680–688 Available at: http://www.jneurosci.org/cgi/doi/10.1523/JNEUROSCI.4209-04.2005.

Wagenaar DA, Pine J, Potter SM (2006) An extremely rich repertoire of bursting patterns during the development of cortical cultures. BMC Neurosci 7 Available at: http://www.ncbi.nlm.nih.gov/pubmed/16464257.

Wang LC, Baird DH, Hatten ME, Mason CA (1994) Astroglial differentiation is required for support of neurite outgrowth. J Neurosci 14:3195–3207 Available at: http://www.ncbi.nlm.nih.gov/pubmed/8182466.

Watabe-Uchida M, Zhu L, Ogawa SK, Vamanrao A, Uchida N (2012) Whole-Brain Mapping of Direct Inputs to Midbrain Dopamine Neurons. Neuron 74:858–873 Available at: http://dx.doi.org/10.1016/j.neuron.2012.03.017.

Watts DJ, Strogatz SH (1998) Collective Dynamics of "Small-World" Networks. Nature 393:440–442 Available at: http://www.nature.com/doifinder/10.1038/30918.

Weil ZM, Zhang Q, Hornung A, Blizard D, Pfaff DW (2010) Impact of generalized brain arousal on sexual behavior. Proc Natl Acad Sci 107:2265–2270 Available at: http://www.pubmedcentral.nih.gov/articlerender.fcgi?artid=2836695&tool=pmcentrez&rendertype=abstract.

Wever R (1980) Phase shifts of human circadian rhythms due to shifts of artificial Zeitgebers. Chronobiologica 7:303–327.

Wheeler BC, Brewer GJ (2010) Desingning neural networks in culture. Proc IEEE 98:398–406.

Wichterle H, Lieberam I, Porter JA, Jessell TM (2002) Directed differentiation of embryonic stem cells into motor neurons. Cell 110:385–397.

Wisor JP, Nishino S, Sora I, Uhl GH, Mignot E, Edgar DM (2001) Dopaminergic role in stimulant-induced wakefulness. J Neurosci 21:1787–1794.

Wollnik F, Turek FW (1988) Estrous Correlated Modulations of Circadian and Ultradian Wheel-Running Activity Rhytms in LEW/Ztm Rats. Physiol Behav 43:389–396.

Xu M, Chung S, Zhang S, Zhong P, Ma C, Chang WC, Weissbourd B, Sakai N, Luo L, Nishino S, Dan Y (2015) Basal forebrain circuit for sleep-wake control. Nat Neurosci 18:1641–1647 Available at: http://dx.doi.org/10.1038/nn.4143.

Yamanaka A, Beuckmann CT, Willie JT, Hara J, Tsujino N, Mieda M, Tominaga M, Yagami KI, Sugiyama F, Goto K, Yanagisawa M, Sakurai T (2003) Hypothalamic orexin neurons regulate arousal according to energy balance in mice. Neuron 38:701–713.

Yang N, Wang GZ, Wen SY, Qiao QC, Liu YH, Zhang J (2017) Orexin exerts excitatory effects on reticulospinal neurons in the rat gigantocellular reticular nucleus through the activation of postsynaptic orexin-1 and orexin-2 receptors. Neurosci Lett 653:146–151 Available at: http://dx.doi.org/10.1016/j.neulet.2017.05.048.

Yang YM, Gupta SK, Kim KJ, Powers BE, Cerqueira A, Wainger BJ, Ngo HD, Rosowski KA, Schein PA, Ackeifi CA, Arvanites AC, Davidow LS, Woolf CJ, Rubin LL (2013) A Small Molecule Screen in Stem-Cell-Derived Motor Neurons Identifies a Kinase Inhibitor as a Candidate Therapeutic for ALS. Cell Stem Cell 12:713–726 Available at: http://dx.doi.org/10.1016/j.stem.2013.04.003.

Yasumoto Y, Nakao R, Oishi K (2015) Free access to a running-wheel advances the phase of behavioral and physiological circadian rhythms and peripheral molecular clocks in mice. PLoS One 10 Available at: http://dx.doi.org/10.1371/journal.pone.0116476.

Zhang J, Luo P (2002) Orexin B immunoreactive fibers and terminals innervate the sensory and motor neurons of jaw-elevator muscles in the rat. Synapse 44:106–110.

Zhong G, Droho S, Crone SA, Dietz S, Kwan AC, Webb WW, Sharma K, Harris-warrick RM (2010) Electrophysiological Characterization of V2a Interneurons and Their Locomotor-Related Activity in the Neonatal Mouse Spinal Cord. J Neurosci 30:170–182.

Zitnik GA (2015) Control of arousal through neuropeptide afferents of the locus coeruleus. Brain Res 1641:338–350.